UNIVERSITY OF SOUTHAMPTON

Kelvin Force Microscopy of Polymer and Small Molecule Thin-Film Transistors

by

Stephen Bain

A thesis submitted in partial fulfillment for the
degree of Doctor of Philosophy

in the
Faculty of Engineering, Science and Mathematics
School of Physics and Astronomy

December 2011

UNIVERSITY OF SOUTHAMPTON

ABSTRACT

FACULTY OF ENGINEERING SCIENCE AND MATHEMATICS
SCHOOL OF PHYSICS AND ASTRONOMY

Doctor of Philosophy

KELVIN FORCE MICROSCOPY OF POLYMER AND SMALL MOLECULE THIN-FILM TRANSISTORS

by Stephen Bain

By their nature, scanning probe microscopy (SPM) measurements are ideally suited to the study of organic thin-film transistors (TFTs). In Chapter 3 surface potential measurements are made on TFTs made from the polymer pBTTT. The modification of the surface morphology by annealing into the liquid crystalline phase is examined and the separation between crystalline layers is found to be in agreement with the literature.

Kelvin force gradient microscopy (KFGM) measurements provide a very detailed picture of the local potential within the channel of the TFT, allowing for the separation of the device and film mobilities in both the linear and saturation regimes. Once the effects of the contacts are removed, the linear mobility is found to be four times higher than the saturation mobility, although the model that best fits the data assumes a constant mobility. Short channel effects are studied in saturation and an upper bound placed on the magnitude of the channel-length modulation. The contacts are also studied in more detail and it is found that a broad region of the pBTTT film near the contacts shows increased resistance, modulated by the gate voltage.

In Chapter 4, KFGM is applied to TFTs produces with zone-cast TIPS pentacene as the active material. The seemingly uniform linear crystallites are found to exhibit a wide range of different behaviours, resulting in device characteristics based on statistical averages of many crystallites. The AFM is used to define a single-crystal device and this is found to contain two distinct regions of widely divergent mobility. The highest mobility regions imply that the maximum theoretical mobility is much higher than is achieved with zone-casting. Greater control over the crystallisation of the film could result in significant increases in device performance. Scanned gate microscopy measurements are also performed and susceptibility to local gating is linked to the conductivity of the film.

Contents

Abstract iii

List of Figures vii

List of Tables xi

Publications and Conferences xiii

Declaration of Authorship xv

Acknowledgements xvii

Abbreviations xix

Symbols xxi

1 Introduction to organic electronics **1**
- 1.1 Why use organic electronics? 1
- 1.2 The physics of organic transistors 3
  - 1.2.1 Carbon bonding and conjugation 3
  - 1.2.2 Operation of organic thin-film transistors 7
  - 1.2.3 Device performance of OTFTs 12
  - 1.2.4 Charge transport mechanisms in OTFTs 16
    - 1.2.4.1 Polarons 16
    - 1.2.4.2 Hopping Transport 17
    - 1.2.4.3 Multiple trapping and release 18
    - 1.2.4.4 Grain boundary limited transport 19
  - 1.2.5 Contact effects in OTFTs 20
  - 1.2.6 Conclusions 22

2 Scanning Probe Microscopy **23**
- 2.1 The history of scanning probe microscopy 23
- 2.2 Atomic force microscopy 25
  - 2.2.1 Amplitude modulation (tapping mode) AFM 26
  - 2.2.2 Frequency modulation AFM 31

- 2.2.3 Electrostatic force microscopy 33
- 2.2.4 Kelvin Force Microscopy 35
  - 2.2.4.1 The KFGM setup used in this thesis 37
- 2.2.5 SPM Applied to OTFTs 38
  - 2.2.5.1 Surface Potential Measurements of OTFTs 39

3 SPM Studies of pBTTT Films and Thin-Film Transistors 43

- 3.1 pBTTT device preparation 44
- 3.2 Morphology of pBTTT films from AFM 45
- 3.3 Observations of morphology during annealing 49
- 3.4 Investigation of domains with KFGM 52
- 3.5 KFGM imaging of pBTTT thin-film trasnsistors 55
  - 3.5.1 KFGM measurements of the TFT channel: linear regime 58
  - 3.5.2 KFGM measurements of the TFT channel: saturation regime . . . 65
  - 3.5.3 Short-channel effects 72
  - 3.5.4 KFGM measurements of the contacts 76
  - 3.5.5 The effects of measurement on pBTTT TFTs 84
- 3.6 Conclusions from the pBTTT data 86

4 SPM Studies of TIPS Pentacene Thin-Film Transistors 89

- 4.1 Zone-casting and morphology of TIPS pentacene on an organic gate dielectric 91
  - 4.1.1 Morphology of the zone-cast TIPS pentacene film 96
- 4.2 SPM Measurements of a complete TIPS pentacene TFT 99
  - 4.2.1 Contribution of crystallite 0 to Device 1 104
  - 4.2.2 Potential line-scans of crystallites in Domain 1 of Device 1 105
  - 4.2.3 Potential line-scans of crystallites in Domain 2 of Device 1 108
  - 4.2.4 Potential line-scans of crystallites in Domain 3 of Device 1 111
  - 4.2.5 Scanned gate microscopy of Device 1 113
  - 4.2.6 Conclusions from device measurements 113
- 4.3 SPM Measurements of a Single Crystal TIPS pentacene TFT 116
  - 4.3.1 Cutting TIPS pentacene crystallites with the AFM 119
  - 4.3.2 A single crystal TIPS pentacene device 123
  - 4.3.3 Conclusions from Single Crystallite Measurements 131

5 Conclusions and the Future 133

A Stability of pBTTT Thin-film Transistors 137

- A.1 Bias stress stability of pBTTT TFTs 137
- A.2 Environmental stability of pBTTT TFTs 140
- A.3 Conclusions on the ambient stability of pBTTT TFTs 146

Bibliography 149

List of Figures

1.1 The atomic orbitals of carbon. 3
1.2 Bonding structure of benzene. 4
1.3 Comparison of the energy bands in a metal, insulator and semiconductor. 5
1.4 Molecular energy levels with increasing conjugation length. 6
1.5 Structure of oligoacenes and their band gaps. 7
1.6 Schematic of the four common TFT geometries. 8
1.7 Band bending at the OSC/dielectric interface. 9
1.8 Energy level diagrams at metal/OSC interfaces. 10
1.9 Schematic of a TFT operating in the linear and saturation regimes. 11
1.10 Ideal TFT transfer curves in the linear and saturation regimes. 13
1.11 Ideal TFT output curves for varying V_G. 13
1.12 V_G dependent mobility induced by a trap DOS. 19
1.13 Charge injection mechanisms is OTFTs. 21

2.1 Schematic of a light-lever force sensor. 24
2.2 Block diagram of the AFM. 25
2.3 Operating regimes of the AFM. 27
2.4 Unperturbed oscillation of the AFM cantilever. 28
2.5 Effects of tip-sample forces on the AFM resonance. 30
2.6 Tip Q-factors in nitrogen and vacuum. 32
2.7 Calibration curve for an EFGM measurement. 34
2.8 Schematic of Kelvin probe theory. 35
2.9 Comparison of EFM and KFGM. 36
2.10 Schematic diagram of our KFGM setup. 38

3.1 Structure and stacking of C_{16} pBTTT 46
3.2 AFM images of pBTTT before and after annealing 47
3.3 Histogram plots of annealed and non-annealed pBTTT films 48
3.4 ROI analysis of an annealed pBTTT film 49
3.5 DSC plot for C_{16} pBTTT 50
3.6 AFM images of pBTTT morphology during annealing 51
3.7 Linear transfer scan of a pBTTT TFT 53
3.8 KFGM topography, potential and electric field images of a pBTTT TFT . 54
3.9 KFGM potential scans of a 5 μm pBTTT TFT 55
3.10 Channel resistance versus channel length for pBTTT TFTs 56
3.11 Mobility versus channel length for pBTTT TFTs 57
3.12 Topography and KFGM potential image of a linear transfer scan 59
3.13 KFGM potential line-scan showing the linear fitting 60

3.14 Linear transfer scan of a pBTTT TFT measured under nitrogen 61
3.15 Linear transfer scan of a pBTTT TFT taken during KFGM 62
3.16 KFGM potential line-scans extracted from a transfer scan 63
3.17 Device conductance against V_G 63
3.18 Ratios of source and drain contact conductance to that of the channel . . 64
3.19 Device mobility versus channel mobility 64
3.20 Measurement of a KFGM topography and potential line 66
3.21 Saturation transfer scan taken during KFGM 67
3.22 Saturation potential line-scans taken with KFGM 67
3.23 Output plots for a pBTTT TFT measured under nitrogen 72
3.24 Schematic division of the channel into fitted and unfitted regions 74
3.25 Variation of the fitted and unfitted regions with V_G 75
3.26 Width of the constant field region adjacent to the drain electrode 76
3.27 Comparison of KFGM potential line-scans for annealed and non-anealed pBTTT TFTs 77
3.28 Contact and channel resistance for a non-annealed pBTTT TFT 78
3.29 Contact and channel resistance for an annealed pBTTT TFT 79
3.30 KFGM potential line-scans taken from an output plot 79
3.31 I-V characteristics of the left contact of a pBTTT TFT 80
3.32 I-V characteristics of the right contact of a pBTTT TFT 80
3.33 Source contact region width for an annealed pBTTT TFT 82
3.34 Spatial extent of the contacts for $V_G = 0\ V$ 83
3.35 Spatial extent of the contacts for $V_G = -20\ V$ 83
3.36 Linear and saturation transfer scans before and after ambient exposure . . 85
3.37 Effect of increasing measurement times on measured $I_{D,LIN}$ 85

4.1 Molecular structure and packing of TIPS pentacene 90
4.2 Optical microscope image of spin coated TIPS pentacene crystals 92
4.3 Schematic of the zone-caster. 93
4.4 Optical microscope image of zone-cast TIPS pentacene crystals. 93
4.5 Close-up optical microscope image of zone-cast TIPS pentacene crytsallites with optical axis shown. 94
4.6 Standard bottom gate device layout used in preliminary zone-casting work. 95
4.7 KFGM image showing unscreened gate field between crystallites. 97
4.8 Conducting AFM image of a TIPS pentacene device. 98
4.9 Optical microscope image of TIPS pentacene device no. 1. 99
4.10 Transfer scan and mobility for TIPS pentacene device no. 1 100
4.11 Output scans of TIPS pentacene device no.1 101
4.12 Tapping mode AFM image of TIPS pentacene device no. 1. 102
4.13 KFGM Potential image of TIPS pentacene device no. 1. 103
4.14 KFGM Potential line-scan of crystallite 0 of Device 1. 105
4.15 KFGM potential line-scans of the crystallites in Domain 1 of Device 1. . . 107
4.16 KFGM potential line-scans of the crystallites in Domain 2 of Device 1. . . 109
4.17 KFGM potential line-scans of the crystallites in Domain 3 of Device 1. . . 112
4.18 SGM image of TIPS pentacene device no. 1. 114
4.19 Optical microscope image of TIPS pentacene device no. 2. 116
4.20 Tapping mode AFM image of device no. 2. 117

4.21 Transfer scans and mobility for device no. 2. 118
4.22 Output scan for device no. 2. 119
4.23 Tapping mode AFM image of device no. 2 after being cut using the AFM. 120
4.24 EFM phase image of device no. 2 after being cut using the AFM. 121
4.25 EFM phase line-scan across the cutting line. 121
4.26 Linear transfer scan for Device 2 before the final AFM cut. 122
4.27 Linear transfer scan for Device 2 after the final AFM cut. 122
4.28 Transfer scans and mobility of device no. 2 after being cut. 124
4.29 Output scans of Device 2 after being cut. 125
4.30 Tapping mode AFM and KFGM potential images of the uncut crystallite in device no. 2. 126
4.31 KFGM potential line-scans of the uncut crystallite at varying V_G with V_D = -5 V. 127
4.32 KFGM potential line-scans of the uncut crystallite at varying V_G with V_D = +5 V. 128
4.33 Linear transfer scan taken during imaging of the single crystallite. 128
4.34 Comparison of the resistance of the different regions of the crystallite. . . 129
4.35 Local linear mobility of Device 2, Region B vs Device mobility. 129
4.36 SGM image of the single crystallite at $V_G = 0$ V. 130

A.1 pBTTT bias stress measurements taken in dark and light 139
A.2 Threshold voltage shifts for pBTTT devices measured in dark and light . 140
A.3 I_{ON} and I_{OFF} over time for pBTTT devices in nitrogen and ambient conditions 142
A.4 Temperature and humidity data over a 12 day period 143
A.5 I_{ON} and I_{OFF} over time for a pBTTT device at 60 $°C$ 143
A.6 I_{ON} and I_{OFF} over time for four pBTTT devices over eight days 144
A.7 I_{ON} and I_{OFF} over time for a pBTTT device at 40 $°C$ 145

List of Tables

3.1 pBTTT terrace heights from histogram analysis 47
3.2 Comparison of terrace heights from histogram and ROI analysis 48
3.3 Saturation mobility and threshold voltages estimated from the long channel FET model 69
3.4 Saturation mobility and threshold estimated with a field-dependent mobility 71

4.1 Linear mobility values for devices on a single 1 inch zone-cast substrate. There is significant variation in the mobility between devices. This is caused either by variations in the number and orientation of domains or by defects in the TIPS pentacene film. 96

Publications and Conferences

S Bain, D C Smith, N R Wilson, and M Carrasco-Orozco. Kelvin force gradient microscopy of pBTTT transistors in both the linear and saturation electrical regimes. *Applied Physics Letters*, 95(14), 2009. doi: 10.1063/1.3242001

S Bain, N R Wilson, M Carrasco-Orozco, and David Smith. Kelvin probe microscopy of organic thin-film transistors. *Presented at UKSPM Conference, London 2008*

Declaration of Authorship

I, Stephen Bain, declare that the thesis entitled, ‘Kelvin Force Microscopy of Polymer and Small Molecule Thin-Film Transistors’ and the work presented in the thesis are both my own, and have been generated by me as the result of my own original research. I confirm that:

- this work was done wholly or mainly while in candidature for a research degree at this University;
- where any part of this thesis has previously been submitted for a degree or any other qualification at this University or any other institution, this has been clearly stated;
- where I have consulted the published work of others, this is always clearly attributed;
- where I have quoted from the work of others, the source is always given. With the exception of such quotations, this thesis is entirely my own work;
- I have acknowledged all main sources of help;
- where the thesis is based on work done by myself jointly with others, I have made clear exactly what was done by others and what I have contributed myself.
- parts of this work have been published as: S Bain, D C Smith, N R Wilson, and M Carrasco-Orozco. Kelvin force gradient microscopy of pBTTT transistors in both the linear and saturation electrical regimes. *Applied Physics Letters*, 95(14), 2009. doi: 10.1063/1.3242001

Signed: ____________________________________

Date: ____________________________________

Acknowledgements

There are a lot of people who deserve varying degrees of thanks for assisting me during this PhD, as I'm sure is the case for any such project. The lion's share, however, must go to my supervisor David Smith for his – sometimes sorely tested – patience throughout six years of highs and lows and for providing insight and support throughout. The School of Physics and Astronomy, and particularly the dedicated staff in the school office, also deserve credit for giving me the time to complete this project.

I am grateful to Merck Chemicals Ltd. for providing the CASE funding for the project and also for providing me with a succession of industrial contacts, and also for subsequently offering me a job so that I could enjoy the luxuries of food and shelter whilst writing up. Over the course of this work, I have worn out several industrial contacts: First Maxim Shkunov, followed by Michael Cölle and ending with the current survivor Miguel Carrasco-Orozco. Without their support and the resources at their disposal, this project would not have been possible.

None of the SPM measurements in this thesis would have been possible without the patient support and collaboration of Neil Wilson at the University of Warwick. It is no exaggeration to say that without his time and technical knowledge – and also his AFM – this thesis would not exist.

Pawel Misciewicz and Merck are owed further thanks for letting me steal the zone-caster with which all the TIPS pentacene devices were made. The OE chemistry team at Merck also deserve a mention for putting up with my regular requests for materials. Also, the employees who put op with or even assisted my work in their laboratories over the last six years: David Sparrowe in particular but also Paul Brookes, Toby Cull and Warren Duffy.

Psychological support, usually in alcoholic form, was generously provided by members of the group in Physics and Astronomy: Dan Walker, Jason Hyde and James Wilson in particular.

Special thanks to Lana Nanson for proof-reading this whole document, although I take full responsibility for any mistakes that may have crept in since.

Penultimate thanks to my current managers at Merck, Tomas Bäcklund and Mark James for not bothering me *too* often about when I was going to "get that bloody thesis finished."

Finally I must acknowledge my parents for their support and for giving me the encouragement and freedom to get to where I am today, even though they couldn't both be there at the end. I always said I'd get it finished eventually and I think you almost always believed me.

Abbreviations

AFM	**A**tomic **F**orce **M**icroscopy
CPD	**C**ontact **P**otential **D**ifference
EFM	**E**lectric **F**orce **M**icroscopy
EPD	**E**lectro**P**horetic **D**isplay
FET	**F**ield **E**ffect **T**ransistor
HOMO	**H**ighest **O**ccupied **M**olecular **O**rbital
KFM	**K**elvin **F**orce **M**icroscopy
KFGM	**K**elvin **F**orce **G**radient **M**icroscopy
LCD	**L**iquid **C**rystal **D**isplay
LUMO	**L**owest **U**noccupied **M**olecular **O**rbital
MOSFET	**M**etal **O**xide **S**emiconductor **F**ield **E**ffect **T**ransistor
OFET	**O**rganic **F**ield **E**ffect **T**ransistor
OTFT	**O**rganic **T**hin-**F**ilm **T**ransistor
OLED	**O**rganic **L**ight-**E**mitting **D**iode
OPV	**O**rganic **P**hoto**V**oltaic
OSC	**O**rganic **S**emi**C**onductor
PEN	**P**oly**E**thylene **N**aphthalate
PET	**P**oly**E**thylene **T**erephthalate
RH	**R**elative **H**umidity
SAM	**S**elf-**A**ssembled **M**onolayers
SPM	**S**canning **P**robe **M**icroscopy
STM	**S**canning **T**unneling **M**icroscopy
ROI	**R**egion **O**f **I**nterest
TFT	**T**hing **F**ilm **T**ransistor
TLM	**T**ransmission **L**ine **M**ethod

XRD	**X**-**R**ay **D**iffraction

Symbols

A	amplitude	V
d_i	dielectric thickness	m
E	electric field	Vm^{-1}
E_C	conduction band edge	eV
E_F	Fermi level	eV
E_G	band gap	eV
E_H	HOMO level	eV
E_L	LUMO level	eV
E_V	vacuum level	eV
F	force	N
C	capacitance	Fcm^2
f	frequency	Hz
I	current	A
k	force constant	Nm^{-1}
L	channel length	m
m	mass	kg
$n(x)$	number density of charge	m^{-1}
Q	charge	C
Q	quality factor (harmonic motion)	$dimensionless$
R	resistance	Ω
S	subthreshold slope	$V/decade$
t	time	s
T	temperature	K
V	voltage	V
W	channel width	m

z	z-position of the cantilever	m
μ	charge carrier mobility	$cm^2V^{-1}s^{-1}$
ν	carrier drift velocity	ms^{-1}
$\rho(x)$	charge density	Cm^{-1}
ϕ	work function	eV
ϕ	phase shift (harmonic motion)	$^\circ$
ω	angular frequency	rads^{-1}
ω_0	resonance frequency	rads^{-1}

In memory of my Father, Mick Bain

Chapter 1

Introduction to organic electronics

Since any molecule containing carbon is by definition organic, the definition of what constitutes organic electronics could be very broad, including polymer and small molecule organic semiconductors (OSC) and all of the pure forms of carbon: graphene, nanotubes, fullerenes – C_{60}, C_{70} – and even diamond. In practice, the term is generally used to refer only to electronic devices based on conducting or semiconducting organic polymers and small molecules. Since semiconducting polymers were first produced, the field of organic electronics has grown to include organic photovoltaics (OPV) and organic LEDs (OLED) in addition to organic field-effect transistors (OFET).

1.1 Why use organic electronics?

It is highly unlikely that organic electronics will ever replace the crystalline silicon (c-Si) that forms the basis of the high performance electronics industry in integrated circuits for computer processing. The field-effect mobility, μ of c-Si transistors is typically over $1,000$ $cm^2V^{-1}s^{-1}$, which is what allows current CPUs to achieve clock-speeds of up to 4 GHz – based on the fact that switching speed can be approximated by the ratio of mobility to channel length, μ/L^2. By comparison, the performance of even the fastest OFET is very low. The highest reported average mobility is 16.4 $cm^2V^{-1}s^{-1}$ for single crystals inkjet printed using a novel solvent-antisolvent technique[1]. However, this technique is probably a long way from mass-production, so the upper limit of OFET performance is typically quoted as around 5 $cm^2V^{-1}s^{-1}$ for evaporated pentacene devices, with the performance of solution processed small-molecule OFETs at around 2.4 $cm^2V^{-1}s^{-1}$[2].

Whilst the performance of OFETs may not be anywhere near high enough to compete with c-Si, it is more than adequate to match and exceed the performance of amorphous silicon (a-Si), the semiconductor that is used in the driving backplanes for liquid crystal (LCD) and electrophoretic (EPD) displays. A-Si typically exhibits a field-effect mobility of $0.5 - 1\ cm^2V^{-1}s^{-1}$[3], which is sufficient for voltage-driven backplane applications such as LCD and EPD but not for the current-driven backplanes of future OLED devices. To drive up-and-coming OLED devices over large areas the likely inorganic successor is poly-silicon (p-Si), which can achieve up to 10 $cm^2V^{-1}s^{-1}$.

The main advantage that organic electronics has over its inorganic rivals is in low cost and ease of manufacture. Solution processing of devices allows for the use of established large area printing technologies – gravure, flexography, slot-die and screen printing – to quickly deposit uniform layers over large areas, whilst existing industrial inkjet printers can be used to produce devices with very low material usage. The manufacture of organic electronics also places less stringent requirements on the cleanliness of production facilities than for silicon. This is in part due to the scale of the feature sizes involved. The current smallest feature size in microprocessors is 22 nm with dies containing many millions of transistors, placing very stringent requirements on levels of airborne particulates. That said, cleanliness is still important in the manufacture of large-area backplanes for displays.

A further advantage that organic electronics has over, in particular, p-Si is the relatively low temperature of deposition. In general, process temperatures can be kept below 100 $°C$, although higher temperatures may be required for the annealing of liquid-crystalline polymers. In contrast, p-Si typically requires processing at 300 $°C$, making it unsuitable for use on flexible plastic substrates such as Polyethylene naphthalate (PEN) and Polyethylene terephthalate (PET). The ability to use flexible substrates for organic electronics has several benefits. First, it may allow display manufacturers to dispense with the glass backplanes, which are fast becoming incredibly unwieldy – a current Generation 10 glass substrate is $2,880$ x $3,130$ mm[4] and less than 0.7 mm thick! The introduction of plastic substrates also paves the way for flexible, and later rollable displays.

Currently, the most established organic electronics technology is OLED, with evaporated OLED displays based upon a-Si or p-Si backplanes already on the market. OPV is also a very active field of research and development, with solar cell efficiencies breaking 8 %. The first eBook reader based upon an OFET backplane with an e-Ink EPD frontplane was scheduled for release by Plastic Logic in 2010 but was subsequently withdrawn. Despite such setbacks, there are many groups working to develop devices based on OFETs, starting with EPD – which has relatively low performance demands – and then aiming at LCD and ultimately OLED for an all-organic device. Suffice to say, it is an exciting time to be working in the organic electronics field.

1.2 The physics of organic transistors

1.2.1 Carbon bonding and conjugation

As the fundamental constituent of all organic materials, it is the bonding structure of carbon that defines their basic electronic properties. The ground state configuration of carbon is $1s^2 2s^1 2p_x^1 2p_y^1 2p_z^1$ giving it four unpaired electrons in separate $2s$ and $2p$ orbitals, which hybridise to give 4 sp^3 orbitals, making it tetravalent. Figure 1.1 illustrates the structure of of the $1s$, $2s$ (both spherical around the nucleus) and p_z orbitals (made up of positive and negative lobes above and below the nucleus with zero electron density at the centre). The more commonly taught sp^3 hybridisation of these orbitals leads to the familiar tetrahedral orientation as seen, for example, in methane. This is a strong bonding structure as the s and p orbitals interfere constructively to increase electron density near the nucleus.

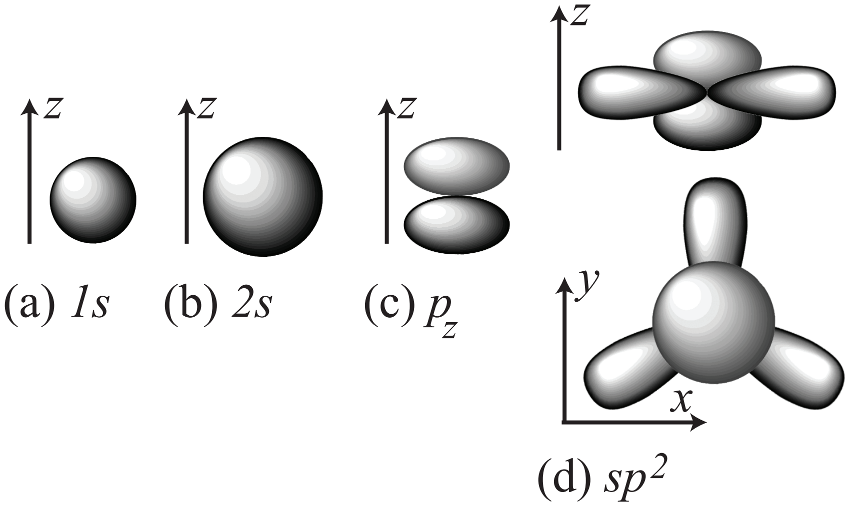

Figure 1.1: Illustration of the surfaces of atomic orbitals: $1s$ (a), $2s$ (b), p_z (c) and hybridised sp^2 (d). Whereas S orbitals are spherical in shape, the p_z orbital has two lobes with a zero probability of finding the electron at the nucleus. The sp^2 orbital results from the hybridisation of one s and two p orbitals and consists of three lobes in the xy-plane at a regular angle of 120° to one another.

The basis of all OSCs, however, is sp^2 hybridisation, in which the $2s$ and the $2p_x$ and $2p_y$ orbitals interfere to create three hybrid orbitals in the xy plane evenly spaced around the nucleus as shown in Figure 1.1(d). The remaining unhybridised $2p_z$ orbital lies perpendicular to the xy plane. This allows each carbon atom to create three σ-bonds with neighbouring carbon or hydrogen atoms, forming the planar backbone of OSC polymers and small molecules. The horizontal overlap of the p_z orbitals of adjacent carbon atoms creates the π-bonds that give OSCs their charge transport capabilities.

Conjugated molecules are traditionally depicted as an alternating series of single and double bonds, as shown for benzene in Figure 1.2(a). A more realistic picture, shown in Figure 1.2(b) is that of the previously mentioned σ-bonds forming the planer ring with its familiar symmetry, and the overlap of the p-orbitals creating delocalised π-electron clouds, indicated with the dotted ring, above and below the plane of the benzene. This difference from the traditional diagram is confirmed as all bond lengths of benzene are equal and lie between the lengths of a single and double bond.

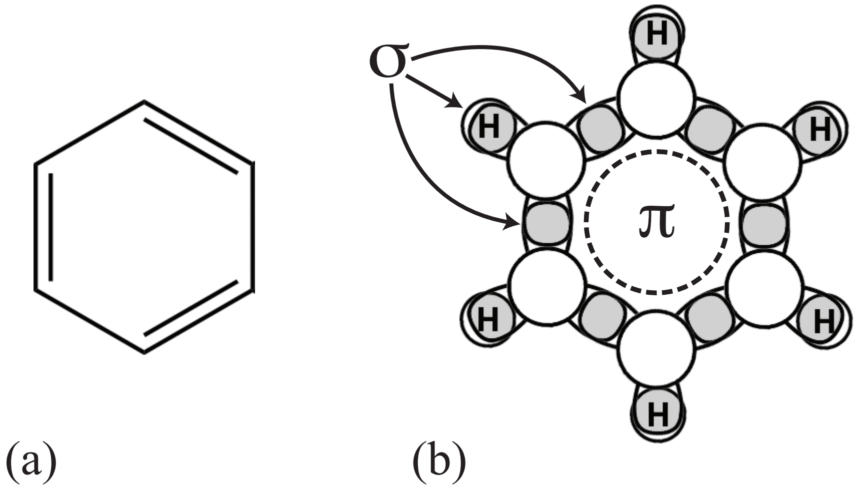

Figure 1.2: The structure of benzene, comparing the traditional structure diagram (a) to a schematic of the atomic orbitals. (b) The traditional structure represents the p_z bonds as alternating single and double bonds, whilst the reality is more nuanced. In (b), adjacent sp^2 orbitals overlap with one another or with the $1s$ orbital of hydrogen to form three σ-bonds leaving the p_z bonds to form a delocalised π-bond (often indicated as a central circle in aromatics), which forms two electron clouds, one above and one below the plane of the benzene ring.

The combination of rigid planar backbone structures and delocalised π-bonds is what allows conjugated molecules to conduct. The π-electron clouds provide states through which charges can pass, either by hopping mechanisms or, if there is significant overlap of π-bonds between adjacent molecules, by a more band-like transport closer to that of crystalline or semi-crystalline inorganic semiconductors. In the past, it was held that a mobility of 0.1 $cm^2V^{-1}s^{-1}$ or lower resulted from hopping transport and above 0.1 resulted from band-like transport, though the boundaries between the two have blurred in recent years.

The easiest way to visualise the band structure of conjugated organic molecules is using frontier orbital theory, which is analogous in many ways to the band theory for crystalline semiconductors, outlined in Figure 1.3. The energy bands in crystalline solids are derived from the energy levels of a single atom in isolation. When a second atom is brought close to the first, the existing energy levels split to form two levels above and below the level of the individual atom. The addition of more and more atoms into an ordered lattice further splits the energy levels into two continuous bands, separated by a gap containing no states, referred to as the band gap, E_G. The upper band is the conduction band as electrons in those states are free to move, whilst the lower band is the valence band, where the electrons are bound to the atoms.

Figure 1.3 outlines the division of materials into metals, insulators and semiconductors based upon the energy levels of their conduction and valence bands. The Fermi level, E_F is effectively the level of the highest energy electron at absolute zero, and it is the position of the valence and conduction bands relative to E_F that determines the properties of the material. In a metal, E_F lies in the conduction band, so there are always free electrons available to carry current if a bias is applied. In both insulators and intrinsic semiconductors, E_F lies within the band-gap so that an electron must be promoted from the valence to the conduction band in order to move freely. The only difference is that E_G for a semiconductor is low enough that the conduction band contains a significant population of thermally excited electrons at room temperature.

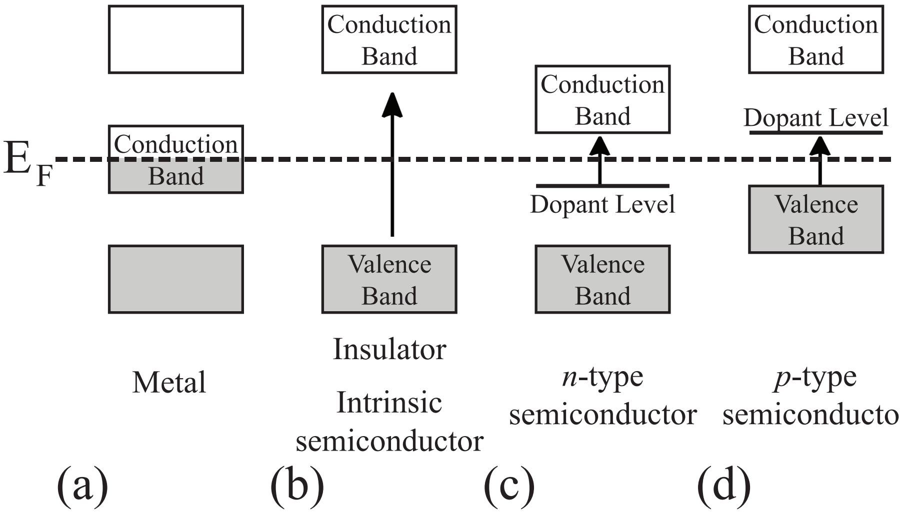

FIGURE 1.3: A comparison of the energy bands of a metal (a), an insulator or intrinsic semiconductor (b), an n-type extrinsic semiconductor (c) and a p-type extrinsic semiconductor. The only difference between an insulator and an intrinsic semiconductor is the size of the band gap. In a semiconductor it must be small enough that electrons can be thermally excited from the valence to the conduction band. In both extrinsic semiconductors the proximity of the dopant levels to the fermi level reduces the effective band gap of the semiconductor. Adapted from [5].

It is common for inorganic semiconductors to be doped with small quantities of electron donating or electron accepting materials to create so-called *extrinsic* semiconductors. The addition of energy levels close to the conduction (n-type) or valence (p-type) bands reduces the effective band-gap, allowing electrons to be more easily promoted to the conduction band in n-type and holes to be promoted to the valence band in p-type semiconductors. This type of doping only really applies to very high purity materials whereas it is common for OSCs to contain equal amounts of n- and p-type dopants, generally referred to as a *compensated* semiconductor.[5] In OSCs, as with polyacetylene, doping is generally used to turn the material from a semiconductor to a metal. In the case of organic semiconductors, where all of the charge is injected from the electrons, the terms n-type and p-type have different meanings.

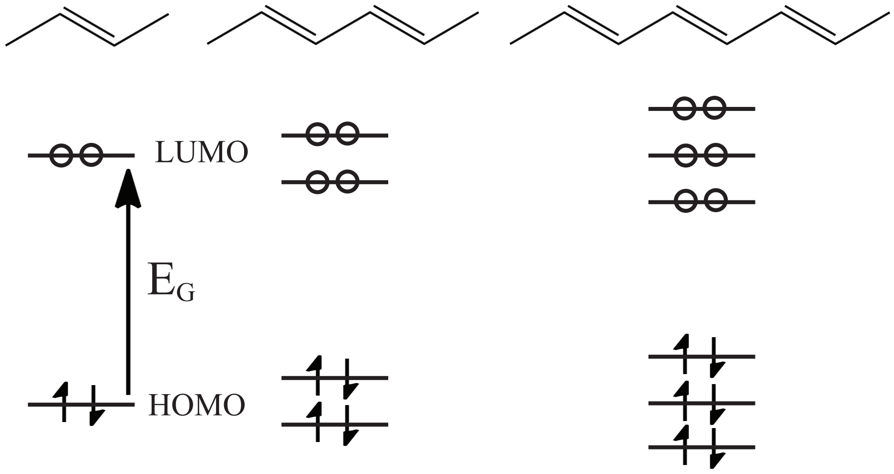

FIGURE 1.4: Illustration of the effect on energy levels of increasing the conjugation length of the molecule. As the conjugation length is increased more elctrons become delocalised and the energy levels split accordingly. As a result, the band gap between the frontier HOMO and LUMO levels is reduced.

With frontier orbital theory, the situation is analogous to that outlined above. All conjugated molecules contain occupied bonding orbitals and unoccupied anti-bonding orbitals. In the case of a single π-bond, as shown in Figure 1.4, there is an energy gap between the highest occupied molecular orbital (HOMO) and the lowest unoccupied molecular orbital (LUMO). As the conjugation length is increased, the delocalisation of the electrons increases, broadening the bands and reducing the band-gap between the HOMO and the LUMO. This frontier orbital band-gap behaves in much the same way as that described above for crystalline solids.

The effective reduction in band-gap with increasing conjugation length is illustrated nicely by Figure 1.5, which shows the experimentally determined band-gaps for four oligoacenes (multiple benzenes bonded together). As the number of benzene rings is increased, the band-gap decreases from 4.35 eV for napthalene to 1.9 eV for pentacene. In the cases of tetracene and pentacene, E_G is low enough that they are good semiconductors. Pentacene is generally regarded as the archetypal small molecule OSC, although its poor solubility means that it must be modified in order to be solution processable. It should be noted here that the reduction of E_G does not continue indefinitely. In the long-chain limit the Peierls distortion ensures that E_G remains finite. Peierls' theorem states that a distortion of the lattice away from perfect periodicity produces additional band-gaps, which is energetically favourable if the energy saved by the addition of the new gaps is greater than that required in the distortion of the lattice.

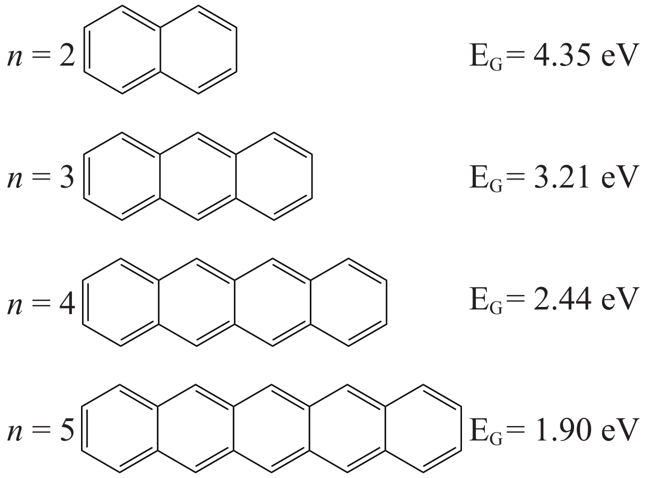

FIGURE 1.5: The structure of four oligoacenes from napthalene (n = 2) to pentacene (n = 5) and their associated band gaps as determined experimentally[6]. The band-gap of napthalene is too great for it to be a viable semiconductor, whilst that of tetracene (n = 4) and pentacene is low enough. Both tetracene and pentacene – and their derivatives – are used as organic semiconductors.

1.2.2 Operation of organic thin-film transistors

The device that forms the basis of the c-Si industry is the metal-oxide-semiconductor field-effect transistor (MOSFET), first proposed by Julius Lilienfeld in 1925. The MOSFET is a three terminal device in which the application of a voltage to one of the electrodes (the gate) induces a conducting channel between the other two (the source and drain) allowing current to flow if a voltage is applied between them. In this manner it can act as a current amplifier though it is predominantly used in digital logic applications.

The device structure that forms the basis of all active matrix display backplanes (found in the majority of modern displays) is the thin-film transistor (TFT). This differs from the MOSFET in its mode of operation (TFTs operate in accumulation, whilst MOSFETS tend to operate in inversion) and also in the manner in which it is constructed. In MOSFETS, the silicon substrate is the semiconductor and is locally doped to form contacts with metal, and more recently p-Si, electrodes. SiO_2 is commonly used as the gate dielectric in MOSFETs. In contrast, TFTs are built up from sequentially deposited (and patterned) thin films upon an inert substrate that plays no part in device operation. Since the most common application of TFTs is in displays where transparency is key, the most common substrate is glass, although organic TFTs (OTFT) are commonly deposited on plastic substrates.

A TFT is effectively a capacitor formed by the metal contact on one side and the OSC on the other side of the gate dielectric. Applying a voltage to the gate electrode induces conducting states at the OSC-dielectric interface allowing a current to flow when charges are injected at the source electrode. The charge induced at the interface is proportional to the gate voltage by $Q = CV$ and so, consequently, is the current that flows between the source and drain.

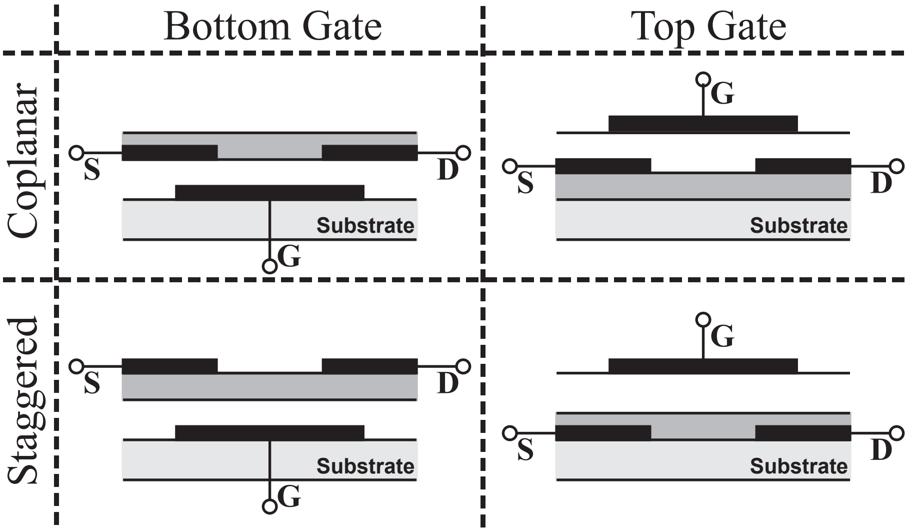

Figure 1.6: Schematic cross-sections of the main TFT configurations with the source (S), drain (D) and gate (G) contacts shown in black, the dielectric in white and the OSC in dark grey. In general, TFTs are either bottom gate (left) in which the OSC is deposited on top of the gate dielectric or top gate (right) where the dielectric is deposited on top of the OSC. Additionally, the source and drain contacts may be deposited on the dielectric side of the OSC, known as coplanar (top), or on the opposite side, known as the staggered configuration (bottom). The bottom gate coplanar geometry is widely used as there is no need to deposit further layers on top of the OSC layer, which can cause damage to some organic films.

There are four basic configurations of OTFT based on the two aspects of the geometry that may be changed, as shown in Figure 1.6. In a bottom gate TFT, the gate electrode and dielectric are deposited first and the OSC is deposited on top. A top gate TFT is basically the same structure but upside-down with the OSC deposited first and the gate dielectric and electrode deposited on top. Each has its own advantages and disadvantages. Solution processed bottom gate devices are easier to make as the gate dielectric may be deposited from a wide range of solvents, whereas the top gate dielectric must be deposited from a solvent that is orthogonal to the OSC layer. In practice, this generally means fluorinated materials deposited from a fluorinated solvent, although vacuum deposited materials are also used. The disadvantage of bottom gate devices is that the OSC layer remains exposed to the atmosphere, requiring additional passivation for long-term stability, whilst the top gate dielectric itself often provides some barrier against contaminants. Either way, for integration into a device stack, further thin-film processing will be required on top of the OTFT.

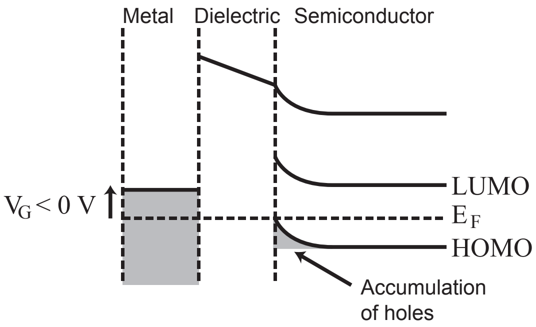

FIGURE 1.7: Band bending at the OSC/dielectric interface for an ideal p-type OTFT with $V_G < 0\ V$. Application of V_G raises the E_F of the metal causing the semiconductor bands to bend upwards as they re-equilibriate. This allows an accumulation layer of holes, injected from the source contact, to form in the first few mono-layers of the OSC.

The second aspect of the geometry that can be changed is the relative position of the source and drain electrodes. If they are deposited in contact with the dielectric – either above or below – they are considered to be coplanar, whilst deposition on the opposite side of the OSC layer from the dielectric is referred to as a staggered geometry. The main consideration here is damage to the OSC layer during deposition of the source-drain electrodes. The predominant metal deposition technology in industry is sputtering, which can cause damage to some OSC films, as can subsequent photolithography and etching processes. For this reason, it is much easier to work either in the bottom gate/coplanar and top gate/staggered geometries. The staggered configuration has been shown to produce devices with lower contact resistances[7] as charge injection to the interface may occur across the whole surface area of the contact rather than solely at the edge of the contact as with the coplanar geometry.

As mentioned above, OTFTs operate in the accumulation mode. Application of a negative voltage to the gate electrode creates an electric field across the dielectric and the OSC near the dielectric interface. This departure from equilibrium is compensated for by a realignment of the Fermi levels of both the gate metal and the OSC, and a resultant energy band bending near the interface, which creates states that can transport holes. This situation is analogous to a p-type MOSFET operating in accumulation, except that in the case of the OTFT all of the holes in the accumulation layer must be injected from the source electrode.

Gold is a commonly used source and drain electrode material as its E_F of 5.1 eV is close to the HOMO level of many OSCs. As a result of this, the energy barrier for the injection of holes is low, as shown in Figure 1.13(a) so it is comparatively easy to inject holes from a gold source electrode into an OSC. In contrast there is a large energy barrier for the injection of electrons, so the majority of OSCs are considered to be p-type. This definition is very different to that for inorganic semiconductors and the two should not be confused.

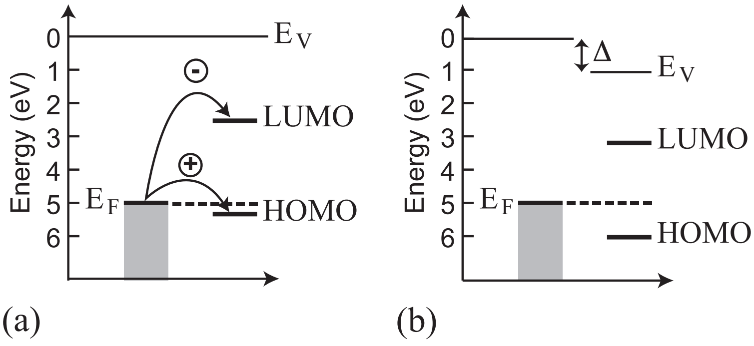

Figure 1.8: Band diagrams of OSC/gold interfaces. In the ideal picture (a), the HOMO level of the OSC is very close to the fermi level of the gold ($E_F \approx 5.1\ eV$) making an Ohmic contact for the injection of holes into the OSC. The comparatively high barrier between E_F and the LUMO level prevents efficient injection of electrons, defining the majority of OSCs as *p-type*. In the more realistic case (b), shown in [8], the interfacial dipole between the metal and the OSC pushes the HOMO level down by as much as 1 eV, significantly increasing the barrier to injection of holes.

It was initially assumed that contacts between gold and a range of OSCs should be Ohmic, as the theoretical energy barrier was typically only a few tenths of an eV. However, this is often not seen to be the case, and UV photoemission spectroscopy has shown that there is in reality a significant barrier between the HOMO level of the OSC and the work-function of the gold contact[8] as shown in Figure 1.8(b). This has been attributed to a dipole barrier between the metal and the OSC, which effectively moves the HOMO level down and increases the barrier to hole-injection. Such a dipole barrier is formed because the electron density in the gold has a tail extending into free space. Deposition of an OSC onto the metal pushes the tail back, reducing the effective work-function of the metal. In real-world devices there are also other factors that can increase the contact resistance, which will be considered in later chapters.

The operation of TFTs can be split into two regimes. In the linear regime, the TFT behaves as discussed above. Application of a negative gate voltage (to a *p*-type device) induces a proportional quantity of holes in the channel, which can then carry a current between source and drain. This general behaviour holds true in situations when the drain bias (in general we will keep the source contact grounded), V_D, is much smaller than the gate bias, V_G. This is known as the linear regime, illustrated in Figure 1.9(a), in which there is no significant lateral variation in charge density between the source and drain electrodes and the drain current I_D increases linearly with V_D.

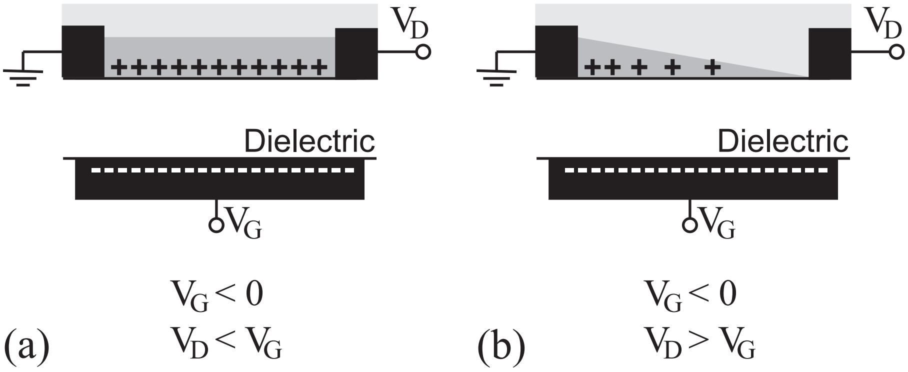

FIGURE 1.9: Illustration of a TFT operating in the linear (a) and saturation (b) regimes with the source contact grounded and negative gate and drain bias. In the linear regime, the magnitude of V_G is much greater than V_D and a uniform sheet of positive charges is formed in the accumulation layer (dark grey). In the saturation regime, the magnitude of V_D exceeds that of V_G so that the local gate bias, and thus the charge density, varies from source to drain. At the drain contact, the charge density is effectively zero, known as the pinch-off point as the current is effectively pinched off and no longer increases with increasing V_D.

When V_D is increased to the point that it exceeds V_G the TFT enters the saturation regime. As V_D is increased, the lateral field becomes large enough to significantly affect the charge density in the channel and a charge density gradient is induced along the channel. This is due to the fact that an increasingly negative V_D reduces the local field across the dielectric at the drain electrode, whilst the drop at the grounded source electrode remains equal to V_G. As V_D equals and then exceeds V_G, the voltage drop across the dielectric at the drain contact becomes zero, resulting in a zero charge density, as shown in Figure 1.9(b). At this point the device is said to be pinched-off as the current is no longer dependent upon V_D, but is limited by the ability of holes to tunnel through the pinch-off region.

It should be noted that the vertical scale in Figure 1.9 is greatly exaggerated, giving the impression that the accumulation layer is much thicker than it is. In reality, charge transport in OTFTs is generally considered to be two-dimensional, with all of the induced charge (CV_G) located at the OSC-dielectric interface. In reality, there is a vertical distribution of charge within the channel[9], but modelling has shown that it does not significantly alter estimates of device performance. Estimates of the effective channel thickness generally fall between 0.1 and 1 nm, which is thinner than a single monolayer of a typical OSC material. For example, the monolayer thickness for the polymer pBTTT, as shown in Chapter 3, is around 2.2 nm. For this reason, we will generally assume two-dimensional charge transport going forward.

1.2.3 Device performance of OTFTs

The two standard electrical measurements typically used to characterise OTFTs are the same as for their inorganic counterparts. A transfer scan is taken by sweeping V_G from the off to the on region whilst maintaining a constant V_D as shown in Figure 1.10. The relative magnitude of V_D compared to V_G determines whether the device is operating in the linear or the saturation regime as described above. V_D in the linear scan (bottom) should be sufficiently small that the OTFT can be considered to operating in the linear regime for the majority of the scan. Likewise, the value of V_D for a saturation transfer scan should be high enough that $V_D > V_G$ across the majority of the scan.

The manner in which a transfer plot is displayed is generally determined by the main parameters one wishes to extract from it. If the on-off ratio (the ratio of $I_{D,ON}$ to $I_{D,OFF}$ and turn-on point are of most interest, then the semi-logarithmic format used in Figure 1.10 is most useful. Typical off-currents vary between 10^{-11} and 10^{-8} A, differences that would be concealed at the zero-line in a linear plot. In practical devices an on-off ratio of greater than 10^5 is generally required. The semi-log plot also emphasises the turn-on point, where the current starts to increase significantly, though not to be confused with the threshold voltage, V_T. If an accurate estimate of V_T is required, then a linear plot will highlight this more effectively.

In standard MOSFET theory, V_T is defined as the value of V_G at the onset of strong inversion[10]. However, OTFTs do not operate in inversion, so V_T can be thought of as a useful fitting parameter and a physically relevant estimate of the transition between the off and on states. In terms of OTFT operation in, for example, backplanes it is the

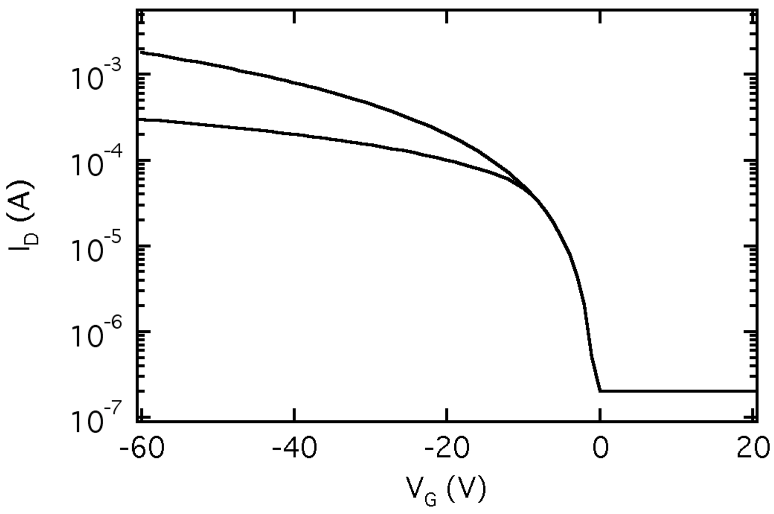

FIGURE 1.10: Ideal transfer curves for $V_D = -5\ V$ (linear, bottom) and $V_D = -60\ V$ (saturation, top) as derived from the MOSFET model for a device with $L = 50\ \mu m$ and $W = 1\ cm$. In this case, a mobility of $\mu = 1\ cm^2V^{-1}s^{-1}$ and a dielectric capacitance of $C = 5 \times 10^{-9}\ F$ were used. Transfer scans are regularly displayed in the semi-logarithmic format as it makes identifying the turn-on point very easy. It also allows for easy estimation of the subthreshold slope.

turn-on point that determines where the on and off voltages are to be set to achieve the required on-off ratio.

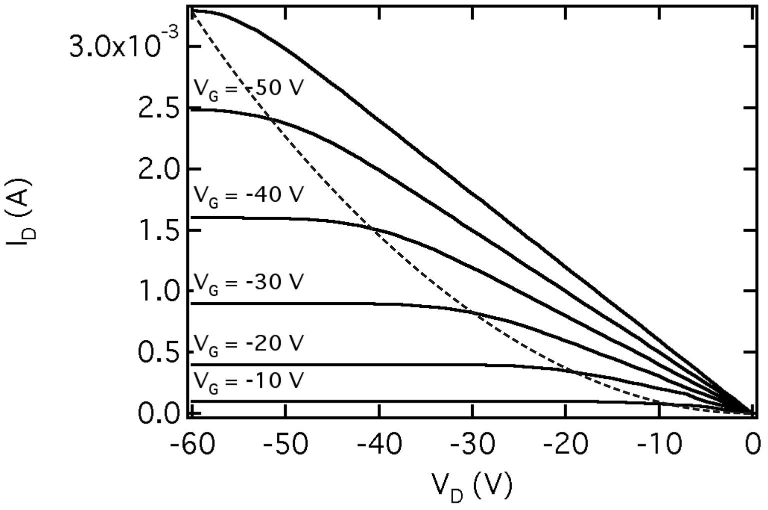

FIGURE 1.11: Ideal output curves derived from the MOSFET model using the same parameters as in Figure 1.10. The point at which the device leaves the linear and enters the saturation regime ($V_D = V_G$) is indicated by the dashed line.

Under ideal conditions, V_T for an OTFT should be zero but in reality this is rarely the case. The origin of a non-zero V_T can be attributed to various sources. If the OSC contains a significant density of shallow trap states then some minimum V_G will be required to fill these states before mobile charges can be injected into the channel.[11] Alternatively, the presence of immobile charges or dipoles at the dielectric surface will shift V_T negative (for positive states) or positive (for negative states).[12] The latter highlights the importance of dielectric choice in manufacturing OTFTs in which the morphology of the subsequently deposited OSC (in the bottom gate devices) was found to depend strongly on the surface quality of the dielectric.[13] A dielectric constant-dependent mobility has also been reported by Stassen et al. for rubrene single-crystal OTFTs.[14]

An output scan is measured by sweeping V_D and holding V_G constant. Typically, output scans are taken for a range of values of V_G as shown in Figure 1.11. Output plots allow the saturation and linear regimes to be clearly distinguished as described by the MOSFET model. V_T will strongly affect the position of the gradual transition from linear to saturation in the output curves, effectively modifying the applied V_G.

So far, we have described how to extract V_T and the on-off ratio, both of which are important in determining device performance. A third parameter that is useful in comparing OTFT performance is the subthreshold slope, S, which is defined by Equation 1.1. In general terms it can be thought of as the inverse of the slope of the semi-log transfer plot in the region just beyond the turn-on point and is usually quoted in units of volts per decade. The smaller the value of S, the sharper the turn on of the transistor and the smaller the difference between the on and off voltages required for reliable device operation. S for OTFTs is often much lower than that for a-Si TFTs due to the presence of traps and interface states, which slow the accumulation of holes in the channel. Despite this, subthreshold slopes of 0.4 $V/decade$[15] or lower have been produced.

$$S = \left[\frac{d(\log I_D)}{dV_G}\right]^{-1} \tag{1.1}$$

The final parameter and the one that, more than any other, is used to benchmark OTFT performance is the field-effect mobility, μ. Physically, μ is defined as the magnitude of the drift velocity per unit applied electric field ($\nu_D = \mu E$). When working with OTFTs, μ is commonly extracted from the device transfer parameters using the standard inorganic MOSFET model in which the drain currents in the linear and saturation regime are defined as:

$$I_{D,LIN} = \frac{W\mu C}{L}[V_G - V_T]V_D \tag{1.2}$$

$$I_{D,SAT} = \frac{W\mu C}{2L}[V_G - V_T]^2 \tag{1.3}$$

where μ is the mobility, L and W the channel length and width respectively, C is the capacitance per unit area of the dielectric and V_G, V_T and V_D are the gate, threshold and drain voltages as discussed above[10]. Re-arragning equations 1.2 and 1.3 gives a value of the device mobility, which we will refer to as μ_{DEV}. This is different from the intrinsic mobility of the OSC, as it will be affected by deviations from the MOSFET model and by the effects of the contacts, device geometry and the dielectric interface.

There are two assumptions implicit in the MOSFET model. The first is that the magnitude of the lateral field along the channel is much lower than the vertical field induced by V_G. This is known as the gradual channel approximation and it is usually achieved by making L much greater than the thickness of the dielectric. Secondly, the model assumes that μ is constant for all of the accumulated holes at all values of V_G and V_D. OTFTs deviate from this model in a number of ways.

For example, Tanase et al. show that for a disordered OSC, the density of holes has a vertical distribution, which tails away from a maximum value at the OSC-dielectric interface.[9] This results in a corresponding maximum mobility at the interface, which decreases with charge density towards the bulk. In practice, the majority of the charge still remains confined to the first monolayer of the OSC[5]. Tanase et al. found that the result of this distribution was a deviation in μ_{DEV} from the MOSFET model of 9%, which still allows for a good estimate of μ_{DEV}.

There are two major factors that generally cause deviations from the MOSFET model, which typically manifest as deviations from a linear fit of I_D (in the linear regime) or $\sqrt{I_D}$ (in saturation). The first is the contact resistance, R_C associated with the source and drain electrodes, which will tend to bend the I_D curve downwards, and the second is a V_G dependent mobility, which will tend to push it upwards as the mobility increases with V_G.[16] The simplest form of the gate dependence, where $\mu = \mu_0 V_G$, is reported by Stallinga et al. for OTFTs based upon sexithiophene.[17]

It should be noted that a third factor, a lateral field dependence of the mobility has also been reported in both polymer[18] and small molecule[19] OTFTs. The effect of the lateral field dependence is to produce a mobility that increases with a reduction in L rather than decreasing as is commonly observed. This behaviour should also be more easily discerned in devices with very low contact resistance as the increasing dominance of the contacts at shorter L would tend to conceal it.

1.2.4 Charge transport mechanisms in OTFTs

Once the effect of the contacts has been removed from the device characteristics either by the transmission line method (TLM)[20–22], four-point measurements[22–24] or using scanning potentiometry[25–27], a V_G dependent mobility is often observed.

The topic of the charge transport mechanism in OSCs is still fairly controversial as several models have been proposed and none found that explain all of the observed effects. The most commonly invoked to deal with V_G dependence of the mobility are models based on multiple trapping and release (MTR), developed for a-Si devices[28] and the variable range hopping model proposed for inorganic materials[29] and later adapted to organics.[30] Additionally, Horowitz et al. link the V_G dependence to a grain-boundary limited transport in the case of polycrystalline OSCs.[31] Before discussing these models it will be useful to first discuss the concept of polarons.

1.2.4.1 Polarons

Although recent reports of the highest performance single-crystal OTFTs with mobilities greater than 10 $cm^2V^{-1}s^{-1}$ have suggested that delocalised band transport is the dominant charge transport mechanism[16], the band model is generally unable to explain the behaviour of organics. The most likely reason for this is that it does not take into account the nature of charges confined to organic molecules. The presence of a charge carrier at a particular site within the solid causes a polarisation of the surrounding region. The outcome is that the charge can no longer be thought of simply as an electron or a hole but as a new charge species: a polaron.

Within organic solids, the polarisation acts upon the π-electron clouds of the OSC molecules (electronic polarisation), upon the nuclei of the molecule harbouring the charge (molecular polarisation) and also upon the molecular lattice itself (lattice polarisation). The key parameters associated with such polarisation are the residence time, τ_{RES}, which is the average time the charge spends on any given molecule and the polarisation time, τ_{POL}, which is the time taken for the polarisation to occur. Order of magnitude estimates can be made for both of these times[32], giving typical values of $\tau_{RES} = 10^{-14}\ s$ and $\tau_{POL} = 10^{-15}\ s$ for an OSC.

A key difference between organic and inorganic semiconductors is that τ_{RES} is typically much less than τ_{POL} for inorganics so that the charges are fast enough that a polarisation cloud never forms. The values for organics show that electronic polarisation is almost always present, resulting in the shifting of the HOMO and LUMO levels as molecules are brought together and discussed in detail by Sato et al.[33] Lattice polarisation occurs on a time-scale slow enough that it is unlikely in organics. For molecular polarisation, τ_{RES} and τ_{POL} are of a similar order, so it is of most interest to us.

The quasiparticle resulting from molecular polarisation is known as the molecular polaron and is made up of the polarization of the intramolecular vibrational modes of the parent molecule combined with any dipole active modes in adjacent molecules, resulting in the formation of polaronic energy levels within the band-gap. Polaronic hopping has been used to explain the gate dependent mobility observed by Brown et al. in OTFTs made from both pentacene and poly(thienylene vinylene) (PTV).[34] The activation energy in this case was equated to the polaron binding energy.

1.2.4.2 Hopping Transport

Hopping models have proven useful in understanding charge transport in disordered organic materials. This is because the dependence of the hopping rate upon temperature goes some way towards explaining the temperature dependence of the mobility in polymers. Transport in this case is based upon the thermally activated tunnelling of charges between localised states. A range of models have been proposed, including the disorder model developed by Bässler,[35] which is based upon three assumptions. First, the polarisation energy of a charge located in a molecule is subject to random fluctuations. Second, that transport occurs due to hopping between localised states, with a Gaussian density of states. Third, the charge transport takes the form of a random walk described by the Miller-Abrahams[29] equation for the hopping rate, ν_{ij}:

$$\nu_{ij} = \nu_0 e^{-\beta \Delta R_{ij}} e^{-\Delta\epsilon_{ij}/kT} \quad for \quad j > i \tag{1.4}$$

where ΔR_{ij} is the distance between occupied site, i, and unoccupied site and j, $\Delta\epsilon_{ij}$ is the energy difference between the sites. ν_0 is a prefactor associated with the frequency of hopping attempts and β represents the overlap parameter of the states i and j.

Vissenberg and Matters[30] applied a variable range hopping (VRH) model with an exponential density of states to the results obtained by Brown et al. for PTV. The VRH takes into account the fact that a distribution of activation energies and hopping distances may be present in a disordered material, allowing for shorter hops at higher activation energy and longer hops at lower activation energy. The V_G dependence of the mobility in the VRH derives from the fact that as V_G is increased, the induced charges occupy localised states with increasingly high energies, thus reducing the activation energy required for a hop to an adjacent state, thus increasing the mobility. They determined the limiting factor in the mobility of an OSC to be the overlap parameter, α, which is related to the separation of the molecules. Given the exponential density of states, providing plenty of states at higher energies, the hopping can be thought of as an activated jump from the Fermi energy to a transport level.

The unsurprising conclusion of applying the VRH is that greater overlap of electronic wavefunctions due to closer and more ordered stacking of the organic molecules is the main route to mobility improvement in OSCs.

1.2.4.3 Multiple trapping and release

The second widely used model for trap-limited transport in OTFTs is MTR. Whilst the VRH model has been successfully applied to disordered materials such as amorphous polymers, MTR can be used to explain the mobility in more ordered OSCs. Typically, it is applied to small molecule OSCs such as pentacene and its functionalised derivatives. The MTR model describes a density of localised trap states within the forbidden band of the semiconductor and close to the transport band. As charges move through the delocalised band, they become trapped in and subsequently thermally released from the localised levels. The only assumptions required for MTR are that trapping takes place instantaneously for any charge that meets a trap and that the release mechanism is thermally activated. The equation relating the effective mobility, μ_{EFF} to the delocalised mobility, μ_0 takes the form:

$$\mu_{EFF} = \mu_0 \alpha e^{-(E_C - E_T)/kT} \tag{1.5}$$

where E_C is the energy at the transport band edge, E_T that of a single trap level and α the ratio of the trap density of states to the density of states at the transport band edge. In reality, the energy distribution of the trap states could take a range of forms, but the key result is a thermally activated mobility. The effect of a distribution of trap states near the transport band edge is shown in Figure 1.12. At equilibrium, the trap states are filled up to the Fermi level and the energy required to release a trapped charge to the transport band, E_C is high. When a voltage is applied to the gate, the induced potential at the OSC-dielectric interface effectively shifts E_F towards the transport band edge, reducing the energy required for a trapped charge to be

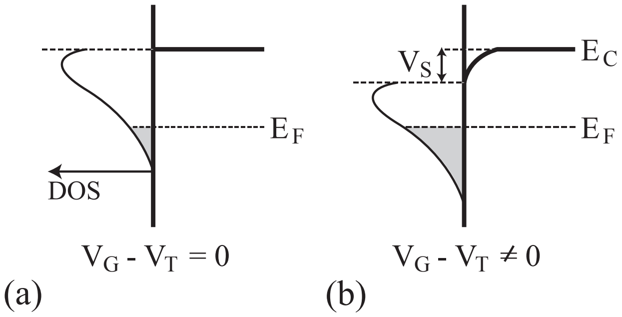

FIGURE 1.12: Illustration of the V_G dependent mobility caused by an energy distributed trap density. Whilst no gate voltage is applied (a), the trap states are filled up to the Fermi level, E_F. When a voltage is applied (b), the potential, V_S, at the OSC-dielectric interface shifts E_F towards the transport band and filling more of the trap states. The distance between the highest filled trap and the conduction level is thus reduced, making trap-release easier and increasing the mobility. Reproduced from [32].

thermally excited into the transport band. This has the effect of increasing the trap-limited mobility with V_G as reported by Völkel et al. for pentacene TFTs[36] and Horowitz et al. with sexithiophene.[37]

1.2.4.4 Grain boundary limited transport

In the case of polycrystalline materials, it has been proposed that the mobility is limited by the grain boundaries.[38] Horowitz et al. developed a further trap-limited charge transport model in which the traps are localised to the grain boundaries within the organic layer.[31] The result is a mobility that emerges from the combination of the high mobility within the grains and the much lower mobility at the grain boundaries as shown in Equation 1.6.

$$\frac{1}{\mu} = \frac{1}{\mu_G} + \frac{1}{\mu_B} \tag{1.6}$$

where μ_G is the grain mobility and μ_B the grain boundary mobility. The model applies so long as the Debye length remains smaller than the average grain size. In the case of sexithiophene reported by Horowitz et al. the Debye length was estimated at 10 nm, a factor of 10 to 100 smaller than the observed grain size. When the Debye length exceeds the grain size, the film can be treated as homogenous and the MTR model was found to apply.

Grain boundaries were also found to be the limiting factor in the mobility of solution processed TIPS pentacene OTFTs produced by Chen et al.[39] By applying a grain boundary limited model to OTFTs with a range of grain sizes, they estimated the mobility in the grain boundary itself to be 5 x 10^{-7} $cm^2V^{-1}s^{-1}$, which was seven orders of magnitude lower than the intrinsic mobility of the TIPS pentacene crystals. It should be noted that in our work on TIPS pentacene, presented in this thesis, we attempt to eliminate the contribution of grain boundaries by producing crystals with a high aspect ratio and a length many times that of the channel.

1.2.5 Contact effects in OTFTs

As implied previously, the contacts are crucial to the performance of an OTFT. It is probably not an exaggeration to say that most OTFTs that have been produced are in some way contact limited and this is certainly true of many polymer TFTs. As the performance of OSCs increases, their relative contribution to the total resistance of the OTFT is reduced and that of the contacts is increased.

When discussing the effects of contact resistance it is often easier to think of the OTFT as three resistors in series, with R_{SOURCE}, R_{CHAN} and R_{DRAIN} the source, channel and drain resistance respectively. Often, R_{SOURCE} and R_{DRAIN} are combined and treated simply as $R_{CONTACTS}$ although this can miss out much of the detail in how the device operates.

Three likely charge injection mechanisms from a metal contact into an OSC are illustrated in Figure 1.13. In all three cases, there is an energy barrier to charge injection due to the difference between the Fermi level, E_F of the metal and the HOMO level, E_H of the OSC. The first case is thermionic emission (a) in which the applied positive bias on the metal electrode gives the holes enough energy to overcome the injection barrier, $E_F - E_H$. At larger interfacial fields, holes may tunnel into the OSC by field emission (b), effectively reducing the injection barrier. Finally, the existence of defect states (c) within the OSC band gap may facilitate charge injection by breaking one large injection barrier down into multiple smaller ones. There is evidence in the literature that charge injection from the source contact is not simply a result of thermionic emission.[40, 41]

In reality, the contact effects in OTFTs may be caused by one or more of a range of phenomena. The first is the already mentioned contact diople in which the adsorption of the OSC layer onto the metal modifies the effective work function of the metal, increasing the barrier to charge injection. To counteract this effect, metal contacts in OTFTs are commonly treated with self-assembled monolayers (SAM)[42] such as pentafluorothiophenol (PFTP), which have their own dipole moment, thus allowing the

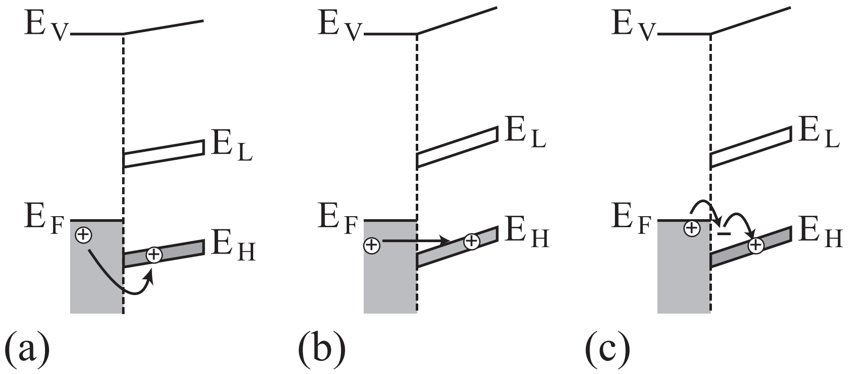

FIGURE 1.13: Band diagram illustrating the different charge injection mechanisms at the metal-OSC interface. Thermionic emission (a) in which the hole must have enough energy to hop over the full potential barrier. Field emission (b) or tunnelling through the potential barrier may occur at high fields. Finally, defect assisted injection (c) occurs if there are mid-gap states present near the electrode via which the holes may enter the OSC.

work function of the electrode to be varied either up or down depending upon the ionisation potential of OSC that will be deposited.

It is also likely, particularly in the bottom-gate co-planar configuration that the crystalline order of the OSC film is disturbed by the presence of the electrodes beneath the film. A film, which may be perfectly crystalline within the channel could be highly disordered in the regions immediately adjacent to the contacts. The disordered region will have a lower mobility than the rest of the channel and may introduce significant numbers of traps at the interface. Such trap populations would slow the injection of electrons from the source into the OSC.

It is also possible that biasing the metal contact may create a depletion region near the electrode, which acts as a diode-like barrier to charge injection. In some cases, this is used as an explanation for the non-linearity of the observed contact resistance[5] and the contacts are sometimes modelled each as a pair of head-to-tail diodes.

Whatever the origin of the contact resistance, the key is to be able to separate the effects of the contacts from those of the channel so that they may be analysed separately. The commonly used techniques are the transmission line method (TLM)[7, 43], the four-probe technique[24, 44] and more recently the kelvin force microscopy (KFM and KFGM) techniques used throughout this thesis.

The techniques themselves are described in more detail in Chapter 3, but in brief the TLM requires the measurement of the device resistance for a series of TFTs with varying L. A linear fit to the plot of R vs L allows for the extrapolation of the $R_{CONTACTS}$, assuming good uniformity between devices. The four probe technique uses specialised device structures in which two additional electrodes are placed within the channel to probe the potential. Knowing the potential at each contact and at two points within the channel allows a fit to be produced that estimates R_{SOURCE} and R_{DRAIN} so long as the device is operating ideally in the linear regime. KFM and KFGM use a conductive AFM tip to probe the local potential at any point in the channel and for any realistic values of V_G and V_D.

1.2.6 Conclusions

In this chapter we introduced the carbon molecule and described how its unique properties allow it to form the basis of all organic semiconductors. The concept of conjugation and the delocalisaiton of charge over π-bonds was discussed in terms of the formation of frontier orbitals analogous to the conduction and valence bands in a traditional inorganic semiconductor. The extraction of the key parameters was covered including threshold voltage, subthreshold slope and the key parameter of mobility. The problems associated with describing the charge transport physics within OSCs were discussed in terms of the competing models that have been applied in the literature. The concept of the polaron as a localised charge within the organic lattice was described before we discussed the VRH model, which has been most successfully used to describe charge transport in amorphous polymer semiconductors. The competing MTR model was discussed in terms of more highly ordered crystalline and polycrystalline OSCs and its utility in explaining the gate voltage and temperature dependence of the mobility in such systems. Whilst progress continues to be made in developing a unified model to describe charge transport in conjugated organic molecules, it is clear that we have not yet reached that goal.

Chapter 2

Scanning Probe Microscopy

2.1 The history of scanning probe microscopy

Atomic force microscopy (AFM) is part of the family of imaging techniques known as scanning probe microscopy (SPM). Over the course of the last two decades, AFM instruments have rapidly developed from experimental devices to ubiquitous instruments in surface-science laboratories world-wide. This is most likely due to their versatility, since the same instrument can be used in different modes to produce sub-nanometre resolution images of surfaces, to probe surface properties such as elasticity or work function, to detect local electric and magnetic fields and to manipulate material at very small scales.

The concept of the AFM traces its origins back to early stylus profilers, which were developed as early as 1929 by Shmalz[45]. With this method, a sharp tip mounted on a flexible cantilever was brought into contact with and drawn across a surface. The deflection of the cantilever was measured via a light beam reflected from a mirror, mounted on the cantilever, onto photographic film. Using this technique profiles could be produced with an effective magnification above 1,000X. However, this technique was susceptible to deformations of the cantilever, either due to reversible torsion of the cantilever from lateral forces or irreversible deformation of the cantilever over long periods.

An early solution, proposed by Becker, was to vibrate the cantilever such that the probe oscillated into and out of contact with the surface, making the cantilever much less susceptible to damage if it comes up against hard or sharp surface features. This idea was further developed by Young et al[46] in 1972 as a non-contact stylus profiler or “Topagrafiner” as it was named. Young’s instrument used a piezo-electric crystal, similar to those used in all modern AFMs, to control the tip-surface separation and relied upon the electron field emission current between a metal tip and conductive sample to control the height.

The first truly scanning probe system was the scanning tunnelling microscope (STM), invented and developed by Binnig and Rohrer in 1981[47, 48] and winning them the Nobel prize in Physics in 1986. The basic method was similar to that of Young et al. but relied upon the electron tunnelling current rather than field-emission. This greatly increased the sensitivity of the instrument, allowing it to be scanned much closer to the surface to produce atomic resolution images. STM is a non-destructive technique as the tip never comes into contact with the sample and energy of the tunnelling "beam" as described by Binnig et al. is as low as 0.1 meV.[48]

However, STM was still not viable with non-conductive samples and could be susceptible to the effects of surface contamination. In order to overcome these limitations, Binnig and Quate developed the AFM in 1986[49]. The prototype AFM used an STM setup and tip to scan the surface but this was soon replaced by the familiar sharp tip mounted on a flexible cantilever used in all AFMs today. The "light-lever" method for measuring tip deflection, similar to the idea of Shmalz and outlined in Figure 2.1, was also employed in subsequent versions of the instrument, allowing for very accurate measurement of the tip deflection.

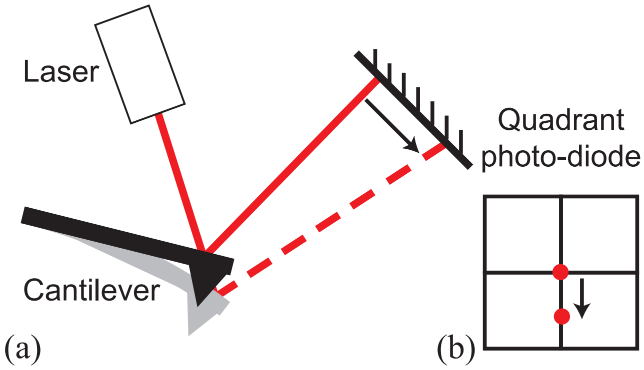

FIGURE 2.1: Schematic diagram of the "light-lever" used to detect tip deflection in many AFMs. A laser (a) is bounced off the reflective back surface of the AFM cantilever onto a photo-diode, which is divided into quadrants (b). In the most basic mode, the output of the upper and lower quadrants is compared and a difference signal is produced such that the signal is zero when no deflection is present. Any deflection of the cantilever will shift the laser spot more into the upper or lower quadrants producing a signal, which is proportional to the tip deflection. This allows the deflection of the tip to be measured very accurately.

Binnig and Quate suggested that a vibrating cantilever might further improve the technique, and the idea was first demonstrated by Martin et al. in 1987[50]. By vibrating the cantilever and using an optical interferometer to measure its position they were able to achieve resolutions better than 10 nm and, by using the intermittent close contact of the probe with the surface, to differentiate between hard and soft surfaces.

In the intervening time, AFMs have not changed significantly. Piezo-electric crystals are still used to control the x, y and z position of a sharp tip above the surface and the "light-lever" is the industry standard for measuring tip deflection. There has, however, been an explosion in the range of techniques applicable to the AFM: lateral force microscopy (LFM), scanning thermal microscopy (SThM), conducting tip AFM (cAFM) and nano-lithography are all possible in the contact regime[51] whilst magnetic force microscopy[52, 53] (MFM), electric force microscopy[54] (EFM) and scanning Kelvin probe microscopy[55] (SKPM) are possible in the non-contact regime.

2.2 Atomic force microscopy

The basic design of the AFM, as outlined in Figure 2.2, consists of a sharp tip at the end of a flexible cantilever – typically between 100 and 500 μm in length and with a stiffness in the range of 0.1 to 50 N/m – mounted on a piezo so that it may be driven to oscillate in the z-direction. This is in turn mounted below a piezo stack, which can be used to accurately control the tip position in three dimensions. A force sensor is the final component of the AFM scanner. Typically this is a "light-lever" sensor, although piezo-electric quartz crystals are also sometimes used.

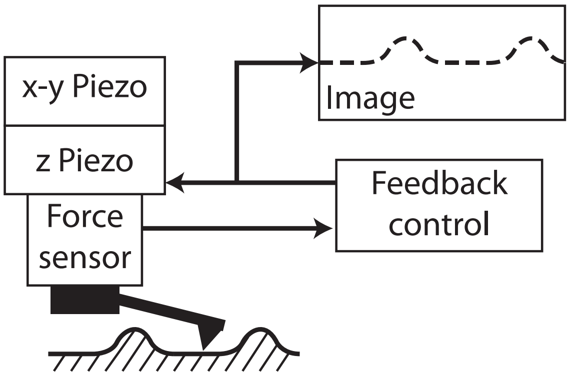

Figure 2.2: Block diagram of the basic AFM setup. A very sharp tip is mounted at the bottom of a stack consisting of x, y and z piezos – to precisely control the position of the tip – and a force sensor. The output of the force sensor, which is proportional to the tip deflection – and so also tip-sample separation – is fed into a feedback control, which adjusts the z-piezo to maintain constant height. The z-piezo height signal is used to generate a profile of the surface. By raster scanning the tip in the $x-y$ direction an image of the sample surface is produced.

In the simplest AFM technique, contact-mode, the tip is brought into direct contact with the surface such that a set-point cantilever deflection – and therefore tip-surface force – is reached. The tip is then raster scanned across the surface of the sample, with a feedback loop using the tip deflection to maintain a constant force by moving the cantilever up and down. The z-motion of the cantilever provides a map of the surface topography, which is recorded. AFM images are typically up to 100 μm in size.

However, the simplicity of the technique is offset by some key disadvantages. Since the tip is effectively dragged across the sample surface there is the potential for either damage to soft samples or for blunting of the tip and twisting of the cantilever caused by impacts with sharp surface features. Furthermore, when imaging samples with varying hardness, the tip will push further into the surface in some places than others, producing unreliable images of the surface topography. For these reasons, dynamic AFM techniques were developed, as described in the following sections.

2.2.1 Amplitude modulation (tapping mode) AFM

Dynamic AFM techniques rely upon an oscillating cantilever to detect the surface of the sample. So called “tapping mode” AFM, often generally referred to as amplitude modulation AFM (AM-AFM) uses relatively large tip oscillation amplitudes, such that the tip comes into contact with – and “taps” – the surface at the bottom of every oscillation. In contrast, non-contact AFM operates exclusively in the attractive regime and is typically performed using frequency modulation AFM (FM-AFM), which provides improved resolution but can only be performed stably under vacuum or in liquids[56]. In principle non-contact AFM can also be performed using amplitude modulation but this is not commonly used. The difference between the techniques is thus not as simple as AM-AFM equals tapping mode and FM-AFM equals non-contact mode although this is a common error.

The different operating regimes of the AFM can best be described by the relationship between force and distance, as shown in Figure 2.3. In contact mode, the tip is in constant contact with the surface and is thus operating in the repulsive regime as the tip-sample force is repulsive. At the other end of the spectrum is FM-AFM, which operates exclusively in the attractive regime. Tapping mode straddles the two regions as the tip generally moves from contact (repulsive) to non-contact (attractive) in the course of every oscillation. AM-AFM is typically performed in air, whilst FM-AFM is typically performed in vacuum. In this thesis, we shall only concern ourselves with AM-AFM, as it is this technique that is used in all of the AFM topography scans presented herein.

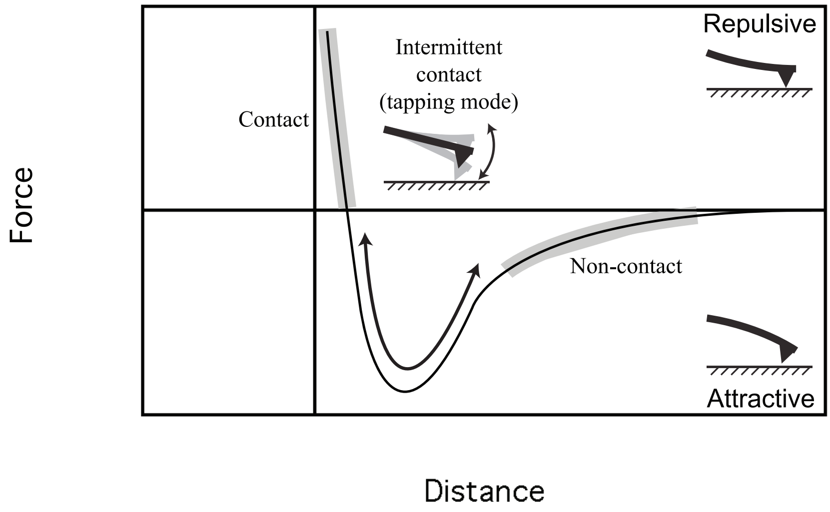

Figure 2.3: Force versus distance from the surface for an AFM tip. When the tip is very far from the surface there is effectively no force acting upon it. As the tip is brought close to the surface, atractive forces – either from the sample itself or from the adsorbed contamination layer on the surface – pull the tip towards the surface, eventually causing the tip to “snap” onto the surface. As the tip moves even closer, repulsive electrostatic forces start to contribute until the tip is in contact and is mechanically pushed upwards by the surface. Contact-mode AFM works exclusively in the repulsive regime and non-contact mode in the attractive regime. Intermittent contact, or tapping mode, AFM works by oscillating the tip through both regimes, tapping the surface at the bottom of each oscillation as indicated by the arrow.

Cantilevers used in AM-AFM are typically fairly stiff – 1 to 50 Nm^{-1} – and are oscillated with amplitudes up to 100 nm. This oscillation is most commonly generated by a piezo-electric actuator, which is driven by an a.c. voltage to produce the tip motion. In some specialised cases a magnetised tip and applied magnetic field can also be used to produce the cantilever oscillation.

Interpreting the results of AM-AFM requires some understanding of the equation of motion for the oscillating cantilever, which in its complete form can be written as:[57]

$$EI\frac{\partial^4 w(x,t)}{\partial x^4} + \mu\frac{\partial^2 w}{\partial t^2} = F(x,t) \tag{2.1}$$

where $w(x,t)$ represents the vertical deflection of the cantilever and E, I and μ are the Young’s modulus, moment of inertia and mass per unit length of the cantilever. Tackling Equation 2.1 is a rather formidable task so most discussions of AM-AFM, including García and Pérez [57], use the following approximate model of a damped, driven harmonic oscillator:

$$m\ddot{z} + kz + \frac{m\omega_0}{Q}\dot{z} = F_{TS} + F_0\cos(\omega t) \tag{2.2}$$

In this case, F_0 and ω are the amplitude and angular frequency of the driving force and Q, ω_0 and k are the quality factor, resonance frequency and force constant of the cantilever in free space, respectively. The F_{TS} term represents all of the tip-sample interaction forces, including van der Waals forces, adhesion forces and mechanical forces from the tip-sample collision.

Let us first consider the cantilever in the absence of tip-sample interactions ($F_{TS} = 0$). For $\omega << \omega_0$, the cantilever will move in phase with the driving frequency as it is the stiffness, k, of the cantilever that dominates. As ω is increased beyond ω_0 inertia begins to dominate over the cantilever stiffness and we should see a small oscillation amplitude 180° out of phase with the drive frequency. This dependence of the amplitude and phase is illustrated in Figure 2.4.

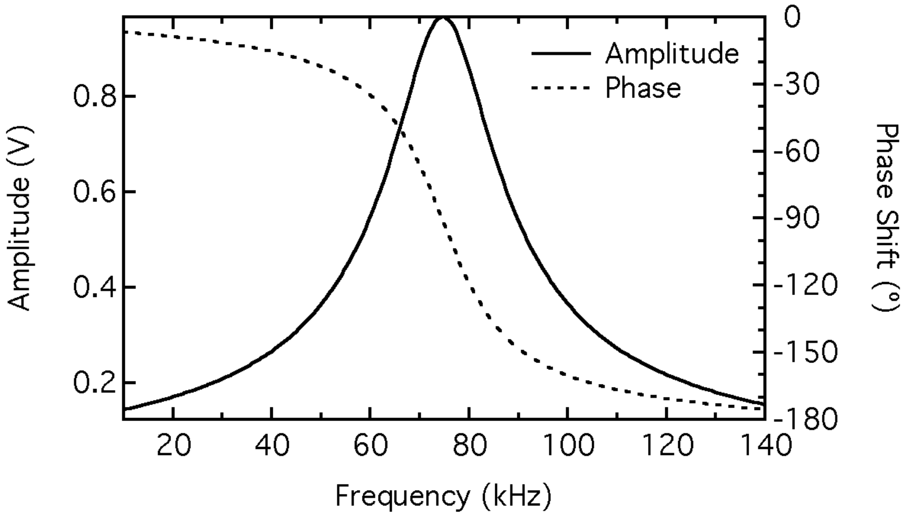

FIGURE 2.4: An ideal cantilever oscillating in free-space at its resonance frequency, ω_0, has the above amplitude and phase response. The phase signal is 0° at $f < \omega_0$, 90° at $f = \omega_0$ and 180° at $f > \omega_0$. Both signals can be used as the feedback control to maintain constant height.

The solution of the damped harmonic oscillator is:

$$z = B\exp(-\alpha t)\cos(\omega_r t + \beta) + A\cos(\omega t - \phi) \tag{2.3}$$

which contains a transient and a steady state solution. At $t = 0$ both components are significant, with the transient term reducing gradually until time $2Q/\omega_0$, when the transient term has fallen by a factor of $1/e$ allowing the steady state solution to prevail.

The steady state solution is a harmonic function with a phase shift relative to the driving force. The amplitude and the phase shift of the oscillation can be calculated by:

$$A(\omega) = \frac{F_0/m}{[(\omega_0^2 - \omega^2)^2 + (\omega\omega_0/Q^2)]^{1/2}} \tag{2.4}$$

$$\tan\phi = \frac{\omega\omega_0/Q}{\omega_0^2 - \omega^2} \tag{2.5}$$

where ϕ is the angle by which the displacement lags behind the driving force. If the cantilever is driven at its resonance frequency $\omega = \omega_0$ and with no damping, Equation 2.4 is reduced to:

$$A_0 = \frac{QF_0}{k} \tag{2.6}$$

The effect of the damping is to change the resonance frequency of the cantilever. The relationship between the damped resonance, ω_R, and the free resonance frequency is given by:

$$\omega_R = \omega_0 \left(1 - \frac{1}{2Q^2}\right)^{1/2} \tag{2.7}$$

The key result of Equation 2.4 is that the amplitude of the oscillation is dependent upon the excitation and effective resonance frequencies of the cantilever. This goes some way towards explaining the experimentally observed dependence of A upon the strength of F_{TS}, which is found to be approximately linear over a broad range of displacements if the correct oscillation amplitude and tip-sample separations are used.[58]

Under the influence of a parabolic tip-surface potential, García and Pérez show that the effective resonance frequency for small z displacements is modified according to:

$$\omega_{EFF} = \left(\frac{k - \partial F_{TS}/\partial z}{m}\right)^{1/2} \tag{2.8}$$

The effect of applying an external force, F_{TS}, is thus to shift the effective resonance frequency of the cantilever, which suggests that the whole resonance peak will be shifted in ω-space. If the cantilever is driven at an off-resonance frequency, ω_{EX}, as shown in Figure 2.5, and the tip is moved closer to the surface, the resultant repulsive forces will have the effect of increasing the effective resonance frequency and, consequently, reducing the measured A at ω_{EX}. Similarly, if the tip is moved further from the surface, the attractive forces will act to reduce the effective resonance, thus increasing the measured A. This is widely known as the slope-detection method.

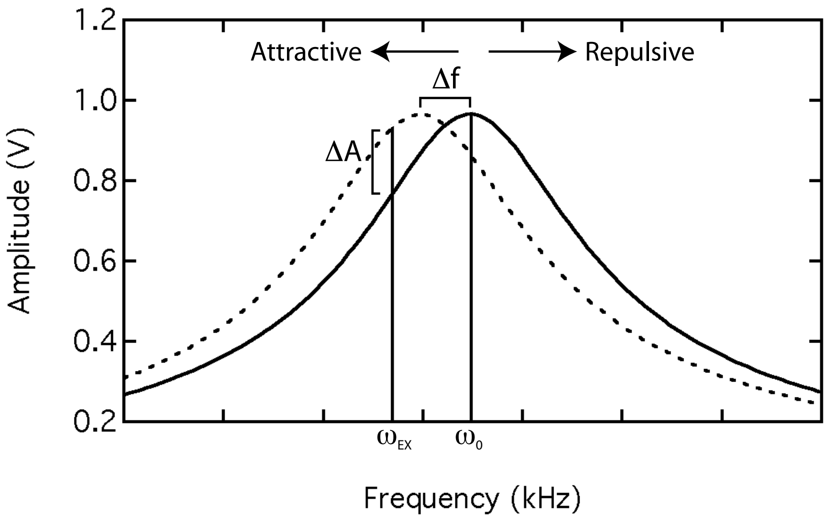

FIGURE 2.5: External tip-sample forces modify the effective spring constant of the cantilever, which in turn shifts the effective resonance frequency away from ω_0. This has the effect of shifting the resonance peak either to lower frequencies, for attractive forces, or to higher frequencies, for repulsive forces. If the cantilever is excited at constant frequency, ω_{EX}, just off-resonance then the shift in resonance will change the amplitude of the oscillation at ω_{EX}. This signal is the basis of AM-AFM. (Reproduced with modifications from [59])

Equation 2.8 shows us that the frequency-shift of the oscillation is dependent not upon the force itself but upon the gradient of the force. This is the basis of frequency modulation AFM (FM-AFM) which is briefly outlined in the following section.

Whether the AM- or FM-AFM is used, the z-piezo is used to adjust the tip height to keep A (or ω) constant by moving the tip up and down, a constant F_{TS} can be maintained allowing the tip to track the surface very closely. It should be noted that the harmonic approximation above is useful in explaining the relationship between the various parameters within the system, but that actual behaviour of the tip is more complex. In Equation 2.8 it was assumed that there is no energy transfer between tip and surface and that $\partial F_{TS}/\partial z$ is independent of z. Equation 2.8 also only applies for small z displacements. The limitations of the harmonic approximation are discussed in more detail elsewhere.[60]

2.2.2 Frequency modulation AFM

Frequency modulation AFM is a non-contact AFM technique in which the distance between the tip and the sample is greater than the amplitude of the cantilever oscillation. In other words, the tip should never come into contact with the sample surface. In principle this allows for more stable imaging as deformations caused to tip and sample by their contact are effectively eliminated. Stiffer cantilevers also tend to be used for FM-AFM as the chance of the tip being pulled into contact with the surface by attractive forces is greatly reduced for higher spring-constants. There is also a benefit to the maximum achievable resolution with higher Q-factor cantilevers, which will be discussed later. Further, by operating the AFM in a vacuum, dissipative forces can be minimised and the effective Q-factor of the cantilever increased as high as 10^5.

It has been shown that the minimum detectable force gradient in slope-detection is given by[50]:

$$\left(\frac{\partial F}{\partial z}\right)_{MIN} = \sqrt{\frac{2k_L k_B T B}{\omega_0 Q \langle z^2_{OSC} \rangle}} \tag{2.9}$$

with $\langle z^2_{OSC} \rangle$ the mean-square amplitude of the driven cantilever oscillation, B the bandwidth and $k_B T$ the ambient thermal energy of the system. Increasing the Q-factor as high as possible might seem to be beneficial from Equation 2.9, however this is not the case for slope-detection.[59] Figure 2.5 shows the steady-state curves, which are only obtained once the system has reached equilibrium after a change in F_{TS} and ω_0. The transition of the system between steady-states can be described by the time constant $\tau = 2Q/\omega_0$, which shows that as Q is increased, the effective bandwidth of the system decreases. There is thus a trade-off between low-Q cantilevers offering a fast response but low sensitivity and high-Q cantilevers with slow response and high sensitivity. The reduced bandwidth and dynamic range of AM-AFM using slope-detection for high Q makes FM-AFM the better option for imaging in vacuum.

The increase in Q that can be achieved simply by imaging in vacuum, thus significantly reducing the damping in the system, is shown in Figure 2.6. Both of the resonance peaks shown are for the same cantilever – a commercially available cantilever with nominal $\omega_0 = 75\ kHz$ – and the only difference is that one is taken under nitrogen at atmospheric pressure whilst the other, much sharper peak, is taken under a vacuum of 10^{-5} Torr. The result is an increase in Q by a factor of 80 from 189 to over 16,000 and this from only a modest vacuum. By optimising the tip and imaging in ultra-high vacuums it is possible to increase the effective Q-factor to 10^5 or higher.

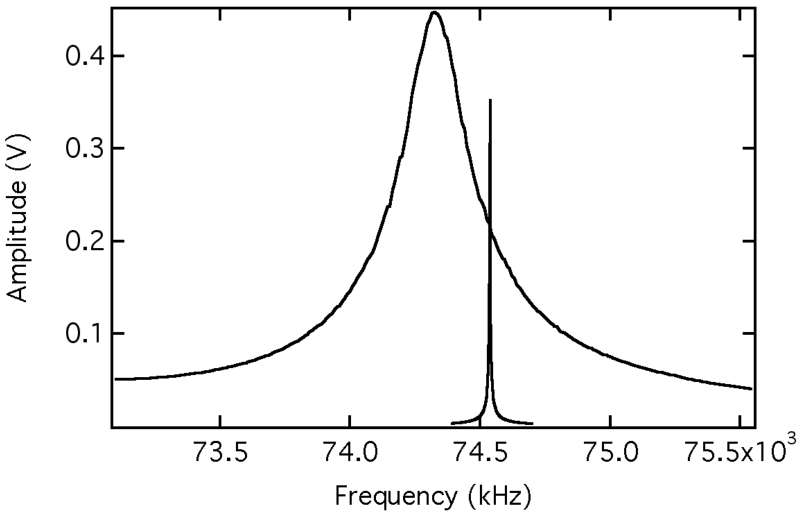

FIGURE 2.6: Resonance curves obtained for a Mikrokasch NSC-18 tip oscillating in a nitrogen atmosphere at ambient pressure and under a vacuum of 10^{-5} Torr. The Q-factors estimated for the tip resonances were 189 and 16,984 under nitrogen and vacuum respectively.

In the FM-AFM regime, the high-Q cantilever is driven close to resonance (which may be different from ω_0 due to F_{TS}) at constant amplitude and changes in $\frac{\partial F}{\partial z}$ are detected as changes in the oscillator frequency. For non-contact AFM, the excitation is applied with a small negative frequency shift. The resonance frequency may be detected by a phase-locked-loop, a digital frequency counter or by some other method. The frequency and amplitude are kept constant by a feedback circuit and automatic gain controller. As the tip is scanned over the surface, a constant $\Delta\omega$ is maintained by varying the tip-sample separation, z, thus generating the topography image.

Albrecht et al.[59] show that the minimum detectable force gradient in the FM mode is given by:

$$\left(\frac{\partial F}{\partial z}\right)_{MIN} = \sqrt{\frac{4k_L k_B T B}{\omega_0 Q \langle z_{OSC}^2 \rangle}} \tag{2.10}$$

which is very similar to Equation 2.9 for slope-detection in AM-AFM. Thus, if the same parameters are used, both techniques may yield essentially the same results. However, in the AM mode, B and Q are not independent parameters so one can only increase Q at the expense of B. In the FM mode, we may increase Q as high as we like and the bandwidth is determined only by the performance of the FM-demodulator. Modern digital phase-locked loop demodulators offer resolutions better than 5 mHz with bandwidths of 500 Hz.[61]

2.2.3 Electrostatic force microscopy

In order to detect the electrostatic forces produced by a sample with a local surface potential, a cantilever must be used that will interact electrostatically. Metal coated tips are commonly used, and indeed are used in much of the work presented in this thesis, although they are not essential. The basic premise of EFM is that applying a voltage to the tip will produce a force, F_{ES}, that is dependent upon the capacitance between tip and sample, which in turn is dependent upon the separation, z, and upon the voltage applied to the tip[54]:

$$F_{ES} = -\frac{1}{2}V^2\frac{\partial C}{\partial z} \tag{2.11}$$

Application of both a d.c. and a sinusoidal a.c. voltage, with frequency ω, to the tip produces a force that can be broken down into three terms.[62] The d.c. component, F_{DC}, is:

$$F_{DC} = -\frac{\partial C}{\partial z}\left(\frac{1}{2}(V_{DC} - CPD)^2 + \frac{V_{AC}^2}{4}\right) \tag{2.12}$$

with V_{DC} the d.c. potential applied to the tip, V_{AC} the a.c. potential and CPD the contact potential difference between the tip and the sample. Equation 2.12 represents a constant bending of the cantilever but is typically of an amplitude below the noise limit of the force sensor [63] so is of little experimental utility. F_ω, the component of the force at ω, is given by:

$$F_\omega = -\frac{\partial C}{\partial z}(V_{DC} - CPD)V_{AC}\sin(\omega t) \tag{2.13}$$

and is dependent upon the same applied potentials as the d.c. component. However, unlike the F_{DC}, F_ω can be isolated by a lock-in amplifier and detected using the same methods as conventional AFM. The final component of the force, $F_{2\omega}$ does not depend upon the surface potential so cannot be used to map the local potential.

$$F_{2\omega} = \frac{\partial C}{\partial z}\frac{V_{AC}^2}{4}\cos(2\omega t) \tag{2.14}$$

$V_{2\omega}$ can, however be used to map the local capacitance variation of a sample, which can be useful in determining local dopant concentrations for example.[64]

As with AFM, EFM may be performed in amplitude modulation, in which the force is detected directly or in frequency modulation (EFGM) in which the force gradient is detected. The frequency shift is approximately proportional to the force gradient as shown in Equation 2.15:

$$\Delta f(\omega) \propto \frac{\partial F_\omega}{\partial z} = \frac{\partial^2 C}{\partial z^2}(V_{DC} - CPD)V_{AC}\sin(\omega t) \tag{2.15}$$

where the symbols have their usual meanings. One of the main drawbacks of conventional EFM is that the long range of electrostatic forces results in significant contributions to the force from the tip cone and cantilever in addition to the tip apex. This results in images that are effectively averaged over a large area and prevents the true local potential from being determined. As EFGM is dependent upon $\frac{\partial^2 C}{\partial z^2}$ rather than $\frac{\partial C}{\partial z}$, the relative strength of the longer range components is reduced, producing a much more local measurement of the potential. This has been likened to an effective sharpening of the tip although the effect is greater than can be achieved that way.[65]

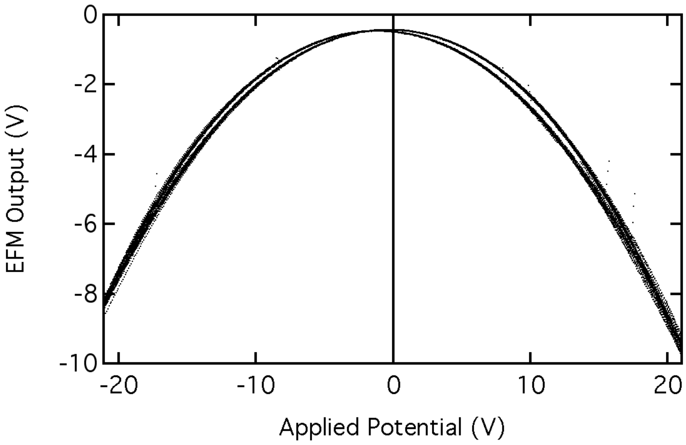

FIGURE 2.7: Calibration curve from an EFGM image taken over a gold contact. A triangular waveform alternating voltage with an amplitude of 20 V was applied to the contact and the EFM signal output recorded for around 20 oscillations. The EFGM output can be seen to be proportional to the square of the applied voltage. It is for this reason that EFGM images require calibration during analysis.

Whilst the force-gradient signal produces more local images of the potential, the measurement is now parabolically dependent upon $V_{DC} - CPD$, which introduces a new problem into interpreting the data as shown in Figure 2.7. It becomes necessary to calibrate the measurement by reference to a series of known surface potentials and to adjust the observed potential accordingly. The easiest way to do this is to scan the tip over a metal electrode with a triangular waveform a.c. voltage applied to it. Over a large number of passes, a good fit can be produced that relates observed to real potentials. A better solution to this problem is to use the Kelvin probe technique, as outlined in the next section.

2.2.4 Kelvin Force Microscopy

Kelvin force microscopy (KFM) was first proposed by Weaver and Abraham in 1991.[66] It is a non-contact SPM technique, similar in most ways to EFM, that relies upon the concept of the Kelvin probe, itself first proposed by Lord Kelvin in the 19th century. The Kelvin probe is a widely used instrument for detecting the contact potential difference between a reference electrode and a sample. A schematic diagram of the technique is shown in Figure 2.8. In the general case, two materials with different work functions are brought into contact, resulting in a flow of electrons from one to the other such that the Fermi levels in the two materials align. The result is a CPD between the two materials, which creates an electric field between them. The CPD is then nulled by application of an external potential, V_C. By definition $V_C = CPD$, which represents the difference in the work functions of the two materials. Using this technique, the work function of a material relative to a known reference electrode can be determined to a high degree of accuracy.

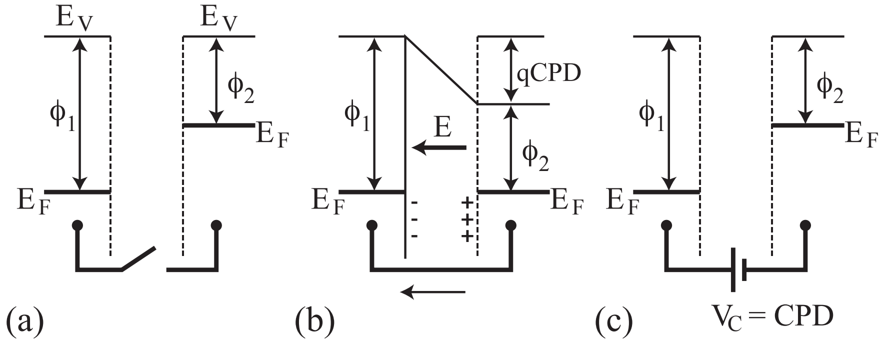

FIGURE 2.8: Schematic diagram of the Kelvin probe method. (a) Initially, the two materials with differing work functions, ϕ_1 and ϕ_2, are not in contact. The vacuum levels are aligned and the work functions simply correspond to the difference between the Fermi levels, E_F and the vacuum level, E_V. (b) As the materials are brought into contact, electrons will flow from material 2 into material 1 until the Fermi levels align. This results in a CPD between the two materials with the charges now present in both materials creating an electric field, E. (c) If an external potential is applied to null the electric field, the the vacuum levels will realign and $V_C = CPD$. Reproduced from [27].

KFM is analogous to the Kelvin probe, although in this case forces rather than currents are sensed. An a.c. potential V_{AC} with frequency ω is applied to the tip and a lock-in amplifier used to detect the forces acting at ω just as with the EFM technique. However, in the case of KFM the d.c. potential V_{DC} is applied using an additional feedback loop so that the tip deflection, and therefore the force, at ω is nulled. The use of a d.c. nulling potential allows for absolute values of the local surface potential to be obtained in both force and force-gradient sensitive techniques, since V_{DC} is known and must be equal to CPD.

As with EFM, it is possible to perform KFM both with reference to the force or the force gradient (KFGM). As discussed earlier, the force gradient signal allows for higher Q cantilevers to be used for imaging in vacuum, but even using the same cantilever at atmospheric pressure yields improved spatial resolution. The benefits of both the Kelvin probe technique and the force gradient signal are most easily explained by a comparison between EFM and KFGM when imaging a working device, as shown in Figure 2.9.

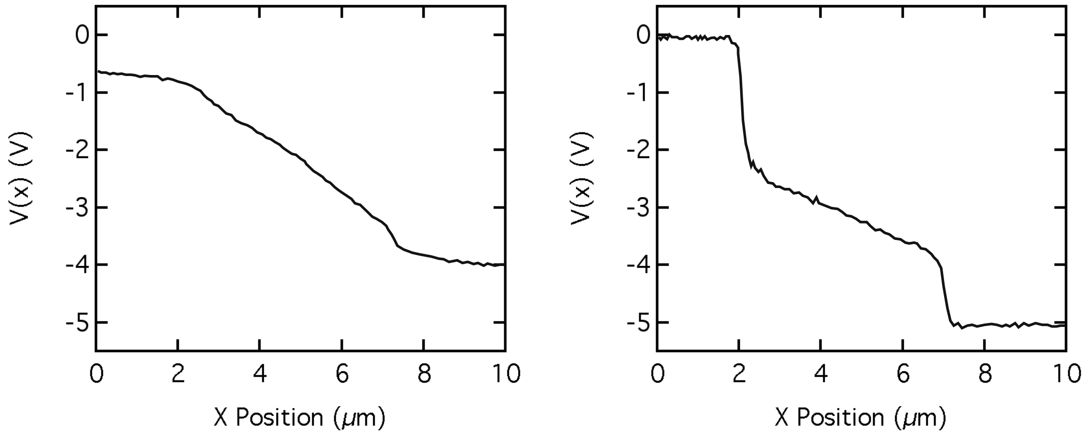

FIGURE 2.9: Two potential line-scans taken of the channel of the same pBTTT TFT using the same tip and an applied V_D of $-5\ V$ but with different techniques. The EFM line-scan (left) does not show the sharp potential drops at the left and right contacts and does not give an accurate value for the potential difference. The line appears as though it has been heavily smoothed due to the contributions to the potential from the cantilever and tip cone, which will overlap adjacent contacts, producing an "averaged" image. In contrast, the KFGM line-scan (right) provides constant values for the potentials at the contacts and the correct potential difference to within 100 mV. The resolution is also greatly improved by the increased locality obtained by detecting the force gradient rather than the force, which significantly reduces the effects of the tip cone and cantilever.

There are two effects at work in producing the differences between the potential line-scans shown in Figure 2.9. The first is that of measuring the force gradient rather than the force, resulting in a much higher lateral resolution and increased locality of the image. The EFM image is visibly "smoothed" and does not produce the correct values for the potential at the contacts. In both cases the potential difference between the electrodes is $-5\ V$ but the observed potential difference in the EFM image is closer to 3.5 V. In general, we were able to obtain potential differences by KFGM to within 50 mV, offset by 20 mV from the applied values.[67] Some offset is expected due to work function differences between the tip and the sample. Martin et al. have shown that under optimal conditions, the potential resolution can be less than 1 mV with spatial resolution $< 100\ nm$.[54] The non-locality of the EFM measurement has also resulted in a slope across the whole image, so that the measured potential, even over uniform metal contacts, is not constant. The second effect is the use of the Kelvin probe technique to obtain absolute surface potential values, thus reducing the need for post processing and the errors that may be introduced. The combination of these two effects in KFGM allows sharp potential drops to be easily measured, facilitating a thorough analysis of the contact resistances.

2.2.4.1 The KFGM setup used in this thesis

The KFGM images used in this thesis were produced using a Veeco Enviroscope AFM connected to two Nanonis OC4 oscillation controllers as shown in Figure 2.10. A home-built voltage source/ammeter was used to control V_D and V_G, and to measure I_D via a DAC and a PC running Labview. All of the images were taken in lift-mode in which a topography line is scanned first, followed by a KFGM line at a fixed lift-height above the surface. A relay connected to one of the switching channels of the AFM allowed the sample voltages and the tip voltage to be switched off when the tapping mode topography lines were being taken. Saturation images were taken using the same setup with the addition of a voltage amplifier to allow for the increased tip voltages up to 60 V. Linear images were taken using a typical lift-height of $30 - 50\ nm$ above the surface, whilst saturation images were taken with a lift-height of 100 nm. This increased lift-height was used to minimise the chances of any tip-surface contact, which might result in a significant current passing through the tip resulting in damage to the AFM.

For low sample voltages, the AFM itself can be used as a voltage source, however the Nanoscope hardware only allows a maximum output range of of -10 to $+10\ V$, which is insufficient to produce the required values of V_G or for V_D in the saturation regime. In cases where higher voltages were required or where a range of values was required in one image the external Labview controlled voltage source was used. For imaging at constant low voltages, for example when performing initial measurements of devices or taking higher resolution images of features within the channel, it is simpler to use the internal voltage sources.

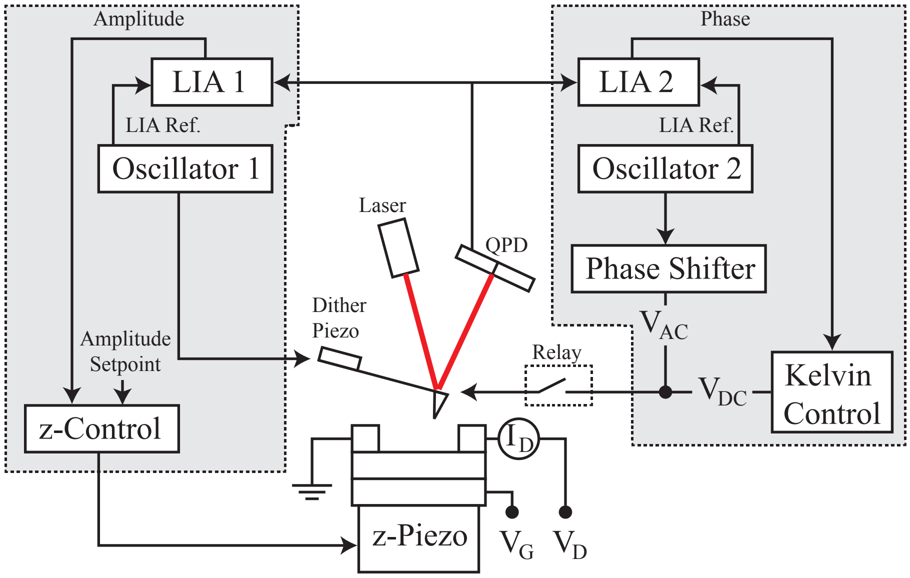

FIGURE 2.10: Schematic diagram of the KFGM apparatus used in this thesis. The grey boxes represent the two external Nanonis OC4 oscillation controllers. The first – on the left – controls the height of the tip via the amplitude of the oscillation just off-resonance versus a user-defined amplitude setpoint. The second applies V_{AC} – 2 to 5 kHz – to the tip and minimises the phase-shift of the tip oscillation at this frequency by applying V_{DC}. V_{DC} is also used to generate the surface potential image.

2.2.5 SPM Applied to OTFTs

AFM is regularly applied to investigate the morphology of organic thin films as it provides a fairly rapid method for characterisation at high resolution. When combined with electrical measurements and techniques such as X-ray diffraction (XRD) it is possible to identify correlations between macroscopic morphology, microscopic molecular ordering and device performance. This is demonstrated clearly by Gundlach et al.[68] who have identified a strong link between the formation of several-μm dendritic grains – seen in the AFM – and a highly ordered single-crystal ordering – identified by XRD – in evaporated pentacene films. Films evaporated more rapidly and at higher temperature, however, exhibited a much more disordered surface morphology, linked to a lack of molecular ordering in the XRD measurements.

Biscarini and coworkers[69] used AFM measurements of evaporated 6T thin films to demonstrate a temperature dependent grain size with a transition to a highly ordered lamellar structure approaching a critical temperature of 200 $°C$. They suggest that the ordering of the films is substrate induced and show that the lamellar spacing is close to the length of a 6T molecule. Similar behaviour, observed in films of octithiophene (8T) using SEM hints at a common behaviour for oligothiophenes.[70] Increased device performance is linked to the increased order and the reduction in number of grain boundaries.

A similar behaviour has been observed by Kline et al.[71] for solution processed devices based on poly(3-hexylthiophene) (P3HT) only in this case it is the molecular weight of the OSC that is the key parameter. It is shown by AFM that the low molecular weight ($3,200\ gmol^{-1}$) forms needle like crystals that show significant local anisotropy and have many well defined grain boundaries. In contrast, the high molecular weight ($36,600\ gmol^{-1}$) films are highly anisotropic and have no obvious grain boundaries. Kline suggests that the high molecular weight P3HT presents fewer grain boundary barriers to charge transport and that the longer chains may provide more conductive bridges between neighbouring domains.

The specific application of AFM to pBTTT TFTs will be discussed in Chapter 3 whilst its application to TIPS pentacene TFTs will be covered in Chapter 4. The above discussion is intended to illustrate that AFM has become a standard tool in the characterisation of OSCs. Aside from the above-mentioned papers, further AFM studies on pentacene have been performed[72] including observations of the influence of an organic gate dielectric on film morphology.[73] It has also been used to study improvements in mobility brought about by solvent-vapour annealing of triethylsilylethynyl anthradithiophene (TES-ADT)[74] and to investigate the effects of thermal annealing on ultra-thin films of 6T TFTs.[75] Observations have also been made of terraced domains in the polymer poly(3,3"'-dialkylquaterthiophene) (PQT)[76] and in the *n*-type OSC N,N'-dipentyl-3,4,9,10-perylene tetracarboxylic dimide[22] showing that such a microstructure is common amongst a range of OSCs.

2.2.5.1 Surface Potential Measurements of OTFTs

The full range of potential-sensitive SPM techniques has been applied to OTFTs ranging from very basic single point potential measurements all the way to KFGM measurements of operating TFTs. The ability to image the surface potential on a the sub-μm length scale that is required can be achieved through no other method. That said, methods vary significantly from study to study, with KFGM being the gold-standard.

At the simplest end of the spectrum, Seshadri and Frisbie[77] connected a conducting AFM tip to a high-impedence electrometer and used it as a static potential probe at fixed points within the channel of a 6T TFT with a $L = 400\ nm$. This produces results very similar to those obtained by conventional four-point electrical measurements but without the need to design a dedicated device architecture to do so. They find that the contact resistance is strongly dependent on both V_D and V_G and that the mobility of the channel is an order of magnitude higher than that of the device once corrected for the contacts. A gate-dependent mobility is also observed.

Phase-EFM is used effectively by Annibale et al.[78] to correlate potential drops within the channel of an ultra-thin-film pentacene TFT. They pointed out the significant improvement in resolution that can be achieved by using the force-gradient instead of the force. Their images require calibration to relate the observed parabolic phase-shift to known surface potentials. The inhomogenous nature of the pentacene film used prevented them from calculating absolute resistance values for the contacts or for the observed grain boundaries, but they do observe that approximately 25% of the potential is dropped at the contacts and that the rest is dropped almost exclusively at the grain boundaries. This result is interesting as it highlights the problems of inhomogeneity when imaging crystalline rather than amorphous films. Their results also add to the body of evidence that in such devices the thin-film microsctructure and domain boundaries play a significant role in limiting device performance. However, their comparison between phase-EFM and KFM ignores the possibility of performing KFGM, which would provide the benefits of both techniques.

The KFM measurements by the group of Sirringhaus and co-workers[25, 41, 79, 80] provide probably the best example of the application of KFM to operating OTFTs in the current literature. These will be discussed further in Chapter 3 in the context of our results, but they will be summarised here. By using KFGM in an ultrahigh vacuum local potential profiles were produced of P3HT, and later poly [(9,9-dioctylfluorene-2,7-diyl)-co-(bithiophene)] (F8T2), TFTs for a range of V_D and V_G covering the linear and saturation regimes. They were able to extract accurate values for the source and drain contact resistances and to estimate the local mobility in the saturation regime. In the case of the polycrystalline F8T2 they show that it is not the domain boundaries but rather the variable conductivity from domain to domain that limits device performance, which they link to the orientation of the F8T2 molecules relative to the channel.[80]

The effect of the contacts on the performance of OTFTs is further studied by Nichols et al. who examined the effect of the contact metal on device performance using KFM.[81] The source contact is found to have the strongest influence on device performance, consistent with the idea that charge injection is the limiting factor. By changing from nickel and palladium to electrodes made from platinum, which has a high work function, they significantly reduced the contact effects and increase the on-current of the TFT. Further evidence for the benefits of using Pt as an electrode metal were shown by Miyazaki et al.[82] using ultrathin Pt electrodes and monolayers of methylquinquethiophene as the OSC. Even at the thickness of a single monolayer, they were able to observe a gradual potential drop across the channel and to identify the resistive barriers associated with the contacts and with defects within the channel.

Puntambekar et al. use KFM to compare the contact resistance in top and bottom contact pentacene TFTs.[26] The resistances of the source and drain contacts, and the channel are extracted using the associated potential drops and I_D. The bottom contact device is shown to be contact limited even at high V_G with the source contact dropping the largest fraction of the potential. In the top contact geometry the channel resistance is dominant at all values of V_G, and at high V_G the device resistance is much lower than bottom contact. This is consistent with the usual assumption that the staggered geometry creates lower contact resistances and thus higher device performance. The contact resistances were found to be very strongly dependent upon the appled V_G and not upon V_D. It is also mentioned that the measured potential drops do not always sum to the applied V_D. Use of KFGM in this instance would be likely to resolve these issues by increasing the locality and resolution of the potential profiles.

The effects of bias stress on poly(triarylamine) (PTAA) TFTs has also been studied using KFM by Mathijssen et al.[83] who observe an increasingly convex potential profile across the channel with increasing bias stress time. This is consistent with a threshold-shift caused by the accumulation of immobile positive charges at the interface caused by the bias stress. The results being that the potential profile shifts from a broadly linear profile to that of a device operating in saturation.

For a review of KFM and KFGM as applied to OSCs, that of Palermo, Palma and Samori[27] covers much of what has been discussed and more besides. They provide a comprehensive introduction to Kelvin probe and to the KFM technique. They also cover a broader range of topics including KFM on inorganic materials and the application of the technique to SAMs, biological molecules and organic photovoltaics.

The above discussion is intended to be a brief overview of the application of KFM and KFGM to OTFTs. Where relevant to our experimental results, further discussion will be provided in the following chapters. The important conclusion here is that, whilst AFM has become a ubiquitous technique in organic electronics research, KFM and KFGM are still not widely reported in the literature despite their applicability and great versatility. We feel that the following experimental results can add a lot to the discussion and provide ample evidence for the utility of KFGM in this field.

Chapter 3

SPM Studies of pBTTT Films and Thin-Film Transistors

Molecular order is crucial to the performance of organic semiconductors. Optimising device preparation to encourage more regular and closer stacking of the conjugated molecules allows for greater overlap between neighbouring π-orbitals, which leads to increased delocalisation of electrons and an associated increase in the charge carrier mobility within the semiconductor layer. In the case of planar conjugated molecules such as poly(2,5-bis(3-alkylthiophen-2-yl)thieno[3,2-*b*]thiophene) (pBTTT) one can take advantage of their liquid crystalline behaviour by annealing them at a temperature above the liquid crystal phase transition and cooling them, preserving the increased crystallinity.

In this chapter, we investigate the behaviour of TFTs made from pBTTT on a SiO_2 dielectric using a range of SPM techniques. In Section 3.2 we observe the morphology of the annealed and non-anealed pBTTT films, finding a lamellar structure somewhat similar to that reported elsewhere and with a spacing of 2.4 nm that is consistent with measurements of the molecular separation in the literature. Having confirmed the structure of the annealed film at room temperature, in Section 3.3 the transient morphology during the annealing process is explored at high temperature, suggesting that the film melts in domains not directly linked to the thin-film microstructure. The possible existence of macroscopic domains is discussed in Section 3.4 with apparent domain-boundaries discovered that are 10 times as resistive as the rest of the film at low V_G.

Section 3.5 covers our KFGM measurements of pBTTT TFTs. In Section 3.5.1 we image the device in the linear regime, performing a complete transfer scan during KFGM, showing that as much as 90% of the source-drain potential is dropped at the contacts, giving a value for the pBTTT film mobility that is 10 times higher than the device mobility. These measurements are extended to the saturation regime in Section 3.5.2 where, by fitting the local potential using the long channel FET model, we are able to show that the saturation mobility only varies very slowly with V_G and that it appears to be around four times lower than the linear mobility. The internal consistency of the data lead us to conclude that this is a real phenomenon. The possibility of channel length modulation in saturation is discussed in Section 3.5.3 and, although it cannot be ruled in or out by our measurements, we can place an upper bound on its extent.

KFGM potential profiles of an annealed and a non-annealed device in Section 3.5.4 show that the strong asymmetry often observed between the source and drain contact resistances only arises after annealing, when the channel resistance has significantly decreased. The increase in mobility achieved by annealing is shown, for pBTTT, to make the difference between the device being contact limited or not contact limited. This is most likely a coincidence of the particular range in which the pBTTT mobility falls. A detailed look at the contacts reveals a V_G dependent variation in their spatial extent within the channel that appears to be a maximum at $V_G = 0\ V$. The I-V behaviour of the contacts also implies a non-diode-like behaviour, contradicting the assumption of Schottky barriers as the main limitation to charge injection.

Finally, the effects of the method of device measurement and transport are covered briefly in Section 3.5.5. We determine that the measured device current may be reduced by as much as 25% by increasing the integration time of the measurement.

3.1 pBTTT device preparation

pBTTT devices were prepared following the procedure outlined by Mculloch et al.[84] Wafers of highly n-doped silicon with a 230 nm thermally grown oxide layer were used as the substrate for bottom gate coplanar TFTs. In this case the substrate itself acts as a common gate for all of the devices so no patterning step is required for the gate electrode. 40 nm thick Cr-Au contacts were defined by photolithography with channel lengths ranging from 2.5 to 20 μm and width 1 cm.

To remove any residues from the photolithography process, the substrates were cleaned in acetone in an ultrasonic bath at $> 30\ ^\circ C$ for 10 minutes, repeated three times with fresh acetone in each case. The substrates were then dried with nitrogen (from liquid N_2 boil-off) before being sequentially cleaned in the sonic bath for 10 minutes in water, acetone and finally isopropyl alcohol (IPA). The final cleaning step was a 10 minute ozone treatment under UV ozone to remove any organics remaining on the surface.

Prior to deposition of the OSC, the substrates were treated with the silylating self-assembled monolayer (SAM) octytrichlorosilane (OTS) by means of immersion in 10 mM solution in toluene at 60 $°C$ for 20 minutes. The SAM treatment has the effect of modifying the naturally hydrophyllic SiO_2 surface by replacing the terminal hydroxyl groups with the less polar alkyl monolayer. [85] Treatment with trichlorosilane monolayers has been shown to increase the contact angle of water with the SiO_2 surface from 10° to as much as 100°. [86] The same study, by Salleo et al. suggests that ordered alkyl chains of the SAM may interlock with those of the OSC, improving out-of-plane ordering and thus the π-π stacking and mobility of the polymer film. We may also speculate that interlocking of the alkyl chains will improve adhesion of the OSC to the dielectric. Immediately after SAM treatment, the substrates were rinsed for a few seconds in hexane, acetone and IPA and transferred to a dry nitrogen glove-box – < 1 ppm of both water and oxygen – for annealing at 110 $°C$ for 10 to 30 minutes.

Solutions of pBTTT were made up to 10 mg/ml in dichlorobenzene (DCB) and spin coated at $3,000$ rpm for 3 minutes in the glove-box. Solutions that initially failed to produce uniform coatings were left on the substrate for up to 30 seconds prior to spinning, which generally resulted in an even coating. In addition it was found that spinning solutions at an elevated temperature (60 $°C$) onto hot substrates tended to produce more reproducable results. The pBTTT films were then annealed at between 100 and 180 $°C$ for 10 minutes depending on the experimental requirements.

After production, devices were stored until use in the dry nitrogen glove-box under dark conditions. The effects of exposure of pBTTT to atmospheric oxygen and water are significant, resulting in a loss in on-current and mobility and increased hysteresis in electrical measurements. Transport between labs for SPM measurements was achieved by means of a short section of 40 mm stainless steel pipe sealed at both ends with KF blanking plates. The effects of transportation on device performance are discussed later in this chapter.

3.2 Morphology of pBTTT films from AFM

The stiff conjugated backbone of pBTTT gives it a clear nematic liquid crystalline phase. In the nematic phase, the polymer backbones align parallel to the substrate surface with the thiophene rings stacked face-to-face, forming terraced lamellar

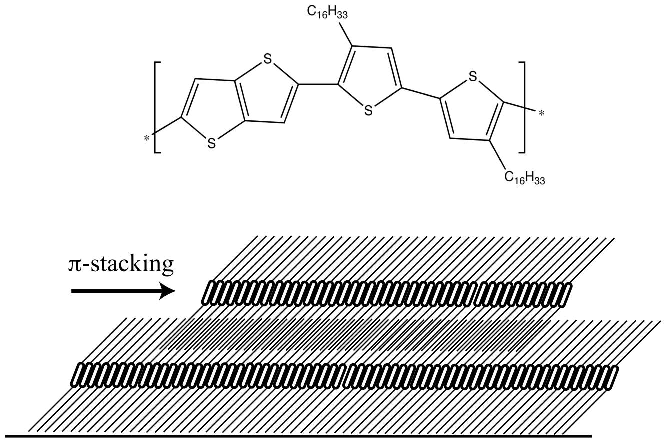

Figure 3.1: Chemical structure of C_{16} pBTTT (top) and schematic of stacked terraces showing the partially interdigitated alkyl side-chains. (bottom) The tilt angles of the backbones (21°) and the alkyl chains (45°) were determined by Kline et al.[87]. The relative sizes of the backbone and alkyl chains are not shown to scale.

structures, which can be observed using AFM. The terraces can extend for hundreds of nanometres with a step-height of ca. 2.2 nm for C_{14} pBTTT.[88]

Figure 3.1 illustrates both the chemical structure of the C_{16} molecule and the arrangement of the molecules within the terraces as determined by Kline et al.[87] using near-edge X-ray fine structure spectroscopy and IR dichroism measurements. In addition, Kline et al determined the tilt angles of the conjugated backbone and the partially interdigitated alkyl chains to be $21\,^{\circ}$ and $45\,^{\circ}$ to the substrate normal respectively.

Our AFM images of spin-coated C_{16} pBTTT films exhibit a similar morphology to that observed by Kline and others,[84, 87] with characteristic terraces formed during annealing. The tapping-mode images in Figure 3.2 illustrate the increase in ordering that occurs during annealing. Before annealing, the film is highly disordered with an apparent grain size of around 20 nm, whilst the film annealed at 180 $^{\circ}C$ has relatively smooth terraces at three distinct step-heights. This is further illustrated with a comparison of the surface roughness averages, R_a, for the two films. The as-spun surface roughness is $R_a = 1.76\ nm$, which reduces to $R_a = 0.99\ nm$ upon annealing.

The presence of terraces at the surface of the pBTTT film is confirmed by plotting the height data as a histogram as in Figure 3.3. The relative terrace heights can be estimated by making a multi-peak Gaussian fit to the histogram, where peak position corresponds to the relative terrace height. Analysis of the as-spun film produces a single, broad Gaussian indicative of a topography randomly disordered around a mean

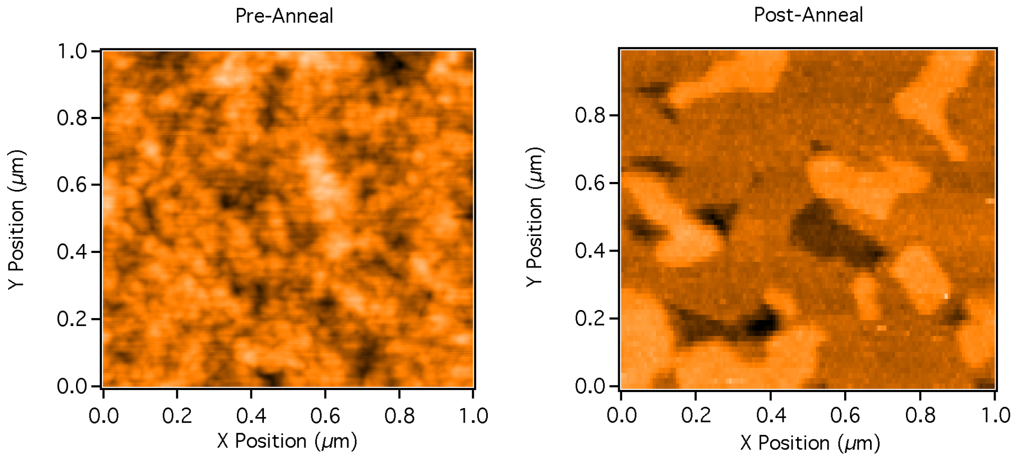

FIGURE 3.2: AFM images of the C_{16} pBTTT film before (left) and after annealing at 180 °C (right). Before annealing the surface is highly disordered with a grain size of approximately 20 nm and a surface roughness average, $R_a = 1.76$ nm. After annealing, the film has re-ordered into flat terraces at three distinct heights with $R_a = 0.99$ nm.

height, whilst the annealed film has three peaks corresponding to the three terrace heights observed in the image. The terrace heights taken from the histogram are shown in Table 3.1 with a comparison of the standard deviation and FWHM obtained from the line-fits. In this case the histogram also shows a strong tendency towards the central terrace height, as approximately 70% of the points fall within the central peak.

	Terrace height (nm)	FWHM	Standard deviation
T_1	5.266	1.295	0.55
T_2	7.389	1.578	0.67
T_3	9.648	1.507	0.64

TABLE 3.1: Terrace heights estimated from the histogram analysis. The more generous estimate of the error, the standard deviation, represents an error of up to 10% in the individual terrace heights. These errors represent the errors in the absolute values of the terrace heights and will, of course, increase significantly when combined in determining the step-height difference (see Table 3.2).

However, the estimated errors as shown in the table, either the FWHM or the standard deviation, are substantial. For a more accurate estimate of the terrace height, the mean heights of selected terrace areas, or regions of interest (ROI), have been calculated - by taking the mean value of the selected points - and compared to adjacent areas at different heights. Figure 3.4 illustrates the ROI analysis, showing the regions selected for analysis. This approach has the advantage of being more local so it is less affected by any bowing or slope in the image that remains after post-processing, which will tend to broaden the Gaussian peaks.

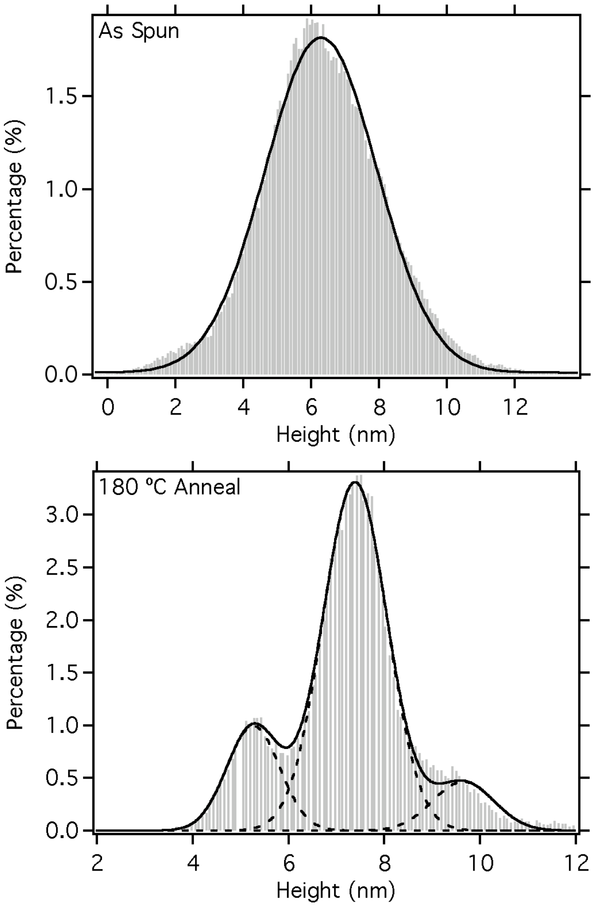

FIGURE 3.3: Histogram plots of the height data for as-spun (top) and annealed (bottom) C_{16} pBTTT films. The individual Gaussian fits (dashed lines) and the combined fits (solid lines) are both shown. The fits themselves are in good agreement with the data and it can be seen that annealing the film results in a narrower overall distribution than for the as spun film, which has a *FWHM* of 3.915. The Gaussian peaks are still relatively broad for the annealed film (see Table 3.1 for the *FWHM* values), but the three distinct terrace heights are clearly discernible by eye.

	Histogram	Error	ROI	Error
T_2-T_1 (nm)	2.123	±0.87	2.222	±0.475
T_3-T_4 (nm)	2.259	±0.93	2.271	±0.501

TABLE 3.2: Comparison of histogram and ROI analyses used for determining the differences between the terrace heights $T_2 - T_1$ and $T_4 - T_3$. After the individual errors are combined, the ROI analysis produces an error of approximately 20%, a significant improvement on the 40% obtained using the histogram method. This is most likely because the ROI method is more localised so contains less error from any bowing or slope in the image.

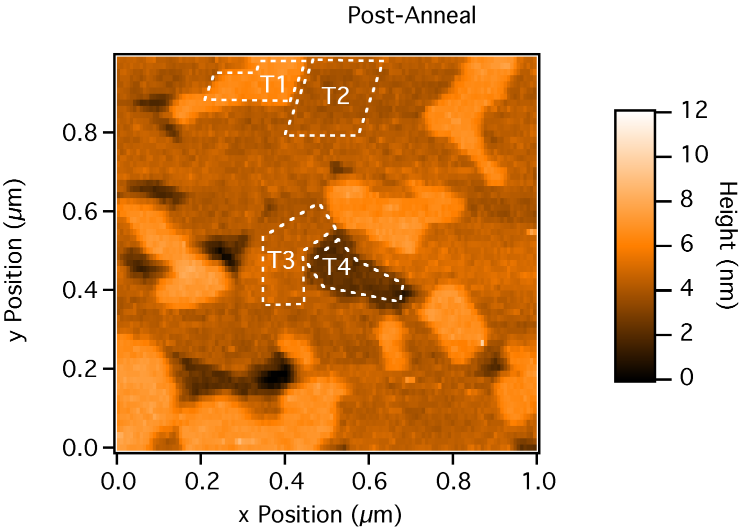

FIGURE 3.4: AFM image of annealed pBTTT with the ROIs shown. The areas T_1 to T_4 used in the analysis are shown. ROI analysis takes the mean height values for adjacent ROIs and subtracts them to produce a more local estimate of the terrace height. This reduces the influence of bowing or slope in the AFM image, which will act to broaden the Gaussian peaks in Figure 3.3.

The step-heights estimated from both histogram and ROI analysis are shown in Table 3.2. The errors have been calculated from the standard deviations of either the Gaussian peak or the ROI combined in quadrature. As expected, the more localised ROI approach increases the precision of the step-height estimate, although the reduced error is still approximately 20%.

Kline and co-workers did not report a direct measurement of the expected lamellar spacing for C_{16} pBTTT. However, their observations of C_{10}-C_{14} pBTTT provide a good linear fit for lamellar spacing vs. alkyl side-chain length. From their observations, the expected step-height for our samples would be ca. 2.4 nm, which agrees with our data to within the error. This agreement, combined with the striking visible similarity between the AFM images is sufficient to conclude that our C_{16} films order during annealing in a similar manner.

3.3 Observations of morphology during annealing

The morphology of planar conjugated polymer films has been extensively studied using AFM and other tools in order to correlate the observed increase in ordering with improved device performance. In the case of AFM measurements, the sample is heated to the anneal temperature and then allowed to cool back to room temperature before images are taken. Increased formation of terraces in pBTTT is observed as the film is annealed past the liquid crystal phase transition, however nothing is learned about the dynamic nature of the process.

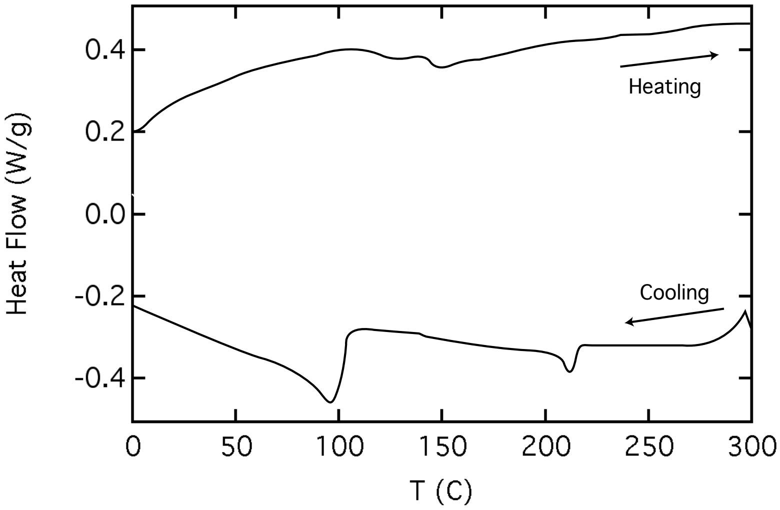

FIGURE 3.5: DSC plot for the C_{16} pBTTT batch used in this section. The heating and cooling rate was 10 $°Cmin^{-1}$. The broad endotherm at around 145 $°C$ shows the liquid crystal phase transition, where we would expect to see changes in morphology occurring.

Differential Scanning Calorimetry (DSC) measurements of the C_{16} pBTTT batch used in this chapter show an endotherm, related to the liquid crystal phase transition at around 145 $°C$ as shown in Figure 3.5. The endotherms in the DSC are not as sharp as those observed for shorter alkyl chain lengths, but we can still safely expect to see changes in surface morphology occurring at around 145 $°C$.

Ideally, one would take AFM images of the same area of the pBTTT film as the temperature is increased through the liquid crystal phase transition. This would allow features in the morphology to be directly correlated to temperature during the formation of individual terraces. However, the effects of increasing the temperature of the film render this impractical. Thermal expansion of the film increases the risk of crashing the AFM tip into the surface, whilst the changing temperature reduces the stability of AFM imaging by both increasing lateral drift and shifting the resonance peak of the cantilever.

Our images of C_{16} pBTTT films during annealing represent the closest practical alternative to the above. A sequence of images was taken using a heated sample stage to control substrate temperature during imaging. A heated cantilever holder was also used in order to minimise the temperature gradient between the tip and the surface and so increase thermal stability. Images were taken at intervals of approximately 10 $°C$. During the temperature ramps, the tip was raised out of contact with the surface. The increased drift experienced at high temperatures, combined with the changes in surface morphology themselves, prevent us from directly correlating specific surface features between images. These thermal instabilities also became severe enough as to prevent any stable imaging at all above around 160 $°C$.

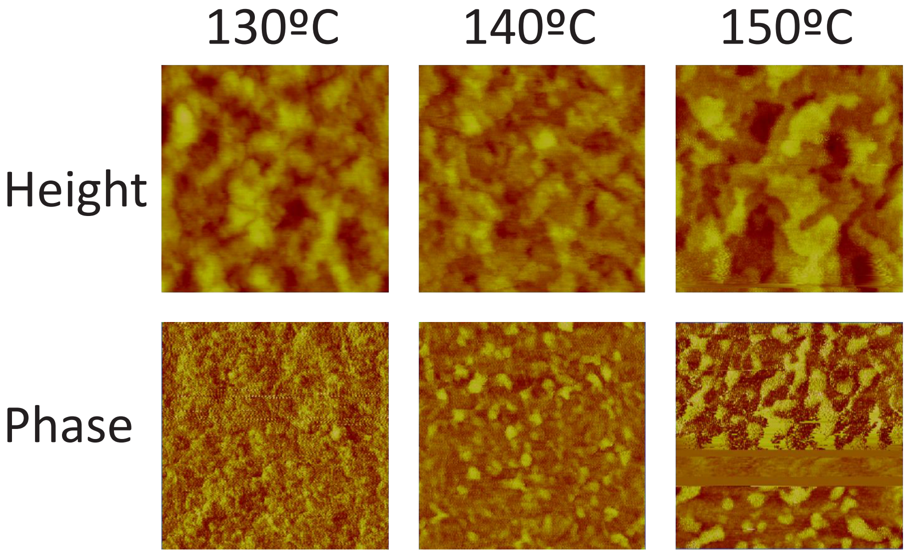

FIGURE 3.6: AFM images showing pBTTT morphology as the temperature passes the 145 $°C$ endotherm. The initial grain size for this sample is larger than that shown in Figure 3.2. As the temperature passes 145 $°C$, the formation of terraces is clearly seen. The phase images also indicate that larger regions with different surface properties are developing on the surface, possibly suggesting regions where the pBTTT film is more crystalline or more amorphous. The large artefacts in the topography and phase images are caused by thermal instabilities in imaging at high temperatures.

The expected change in morphology is clearly seen in the AFM height data shown in Figure 3.6. Despite the reduced image quality from imaging at high temperatures, the terraces become clearly visible in the 150 $°C$ image, which approximately corresponds to the endotherm observed in the DSC. It should be noted that the uncertainty on the quoted temperatures is likely to be around 10 $°C$. The two main sources of the uncertainty were the quality of the thermal contact between heater and substrate, which was made simply using silver paste, and the calibration of the heating stage itself, which did not include a feedback loop.

The images of the phase-shift in Figure 3.6 are also of interest. The scale in these images represents the phase-difference between the excitation signal and the tip-displacement signal and can be qualitatively linked to the material properties of the surface. As the temperature increases, areas of higher and lower phase-shift begin to emerge, showing no obvious correlation to topography.

A quantitative interpretation of the phase-shift is not possible from these images as it is difficult to disentangle the various contributions to the phase-shift. However, the qualitative interpretation can still be informative. Areas of increased phase are likely to be associated with material that is either softer or more adhesive to the tip. Softer material will deform on tip impact, damping the oscillation of the cantilever, whilst adhesion of the tip effectively reduces the spring constant of the cantilever. Both of these effects act to reduce the resonance frequency of the cantilever, effectively increasing the phase-shift. The converse is true for harder or less adhesive material.

The phase-shift images suggest that the film does not melt uniformly on a scale of tens of nm. It is possible that the low phase-shift regions represent more crystalline areas of the film, in which the interchain π-π interactions maintain the crystallinity, whilst the high phase-shift regions represent more amorphous areas where the polymer chains are more tangled. This may be related to the structure of the resultant terraces, but no correlation can be seen in our images. A more detailed exploration of this phenomenon would require higher quality images taken over finer temperature variations and up to higher temperatures, although the problems of thermal expansion and instability would make this challenging.

3.4 Investigation of domains with KFGM

Polarised optical images of planar conjugated polymer dioctylfluorene-bithiophene (F8T2) transistors by Bürgi et al. [80] show the presence of $0.4 - 1\ \mu m$ domains with varying molecular orientation. It is shown using KFM that there are significant lateral conductivity variations between domains, so it can be reasonably concluded that conductivity is linked to molecular orientation relative to the channel. Our measurements of C_{16} pBTTT, and those of Kline et al. on C_{12} and C_{14} pBTTT, show the formation of ordered crystalline domains or lamella. Thus, it is likely that pBTTT also forms domains with distinct molecular orientations. If such domains are related to the lamellar structures in the film, which can extend for hundreds of nanometres, they should in principle be observable using KFGM.

Figure 3.7 shows the linear transfer scan for the TFT, with $L = 5\ \mu m$, $W = 1\ cm$, used in this section. The measurement was made using a custom current-voltage amplifier with the device mounted in the AFM stage under vacuum prior to imaging. V_T as determined from a linear fit to I_D was $+8.16\ V$. KFGM images were made of the middle of the channel, excluding the contacts, at the voltages indicated on the figure (circles).

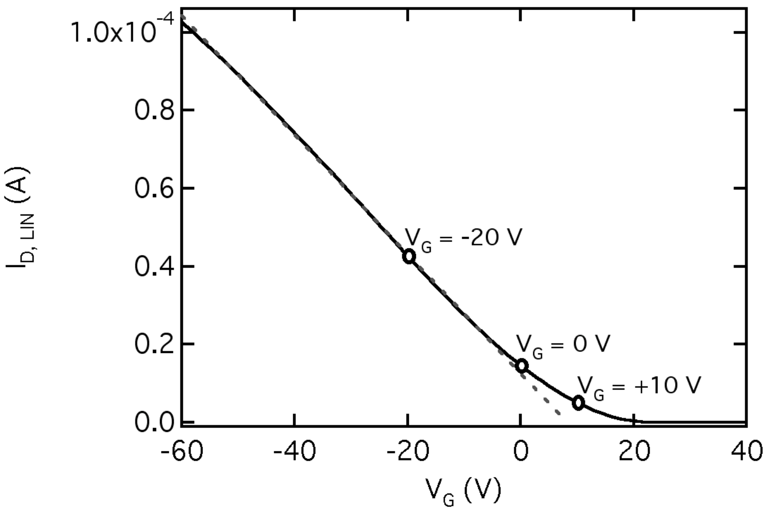

FIGURE 3.7: Linear transfer scan, $V_D = -5\ V$, of the pBTTT transistor used in the KFGM domain measurements. The voltage points corresponding to KFGM images in Figures 3.8 and 3.9 are shown (circles). V_T estimated from the linear fit (dashed line) is +8.16 V, which in this case is in close agreement with the saturation fit. At $V_G = 10\ V$ the device is clearly operating in the subthreshold region, moving into the on state for $V_G = 0$ and $-20\ V$.

KFGM topography and potential maps of the channel taken at $V_G = 10\ V$ are shown in Figure 3.8 (a) and (b) respectively. The drain contact is on the right of the image, parallel to the y-axis. A clear potential step is visible in the potential image at around $x = 2\ \mu m$. The presence of this feature is confirmed in the map of lateral electric field (Figure 3.8 (c)), determined from the derivative -∂V(x)/∂x. The feature extends the full height of the image from top to bottom and appears to continue beyond the bottom edge, giving it a length of at least 1 μm in the y-direction. Superimposing the outline of the step onto the topography image indicates that there is no strong correlation between surface topography and potential so, if this is a domain boundary, it appears to be restricted to the lower lamellae.

We can also use the potential data in Figure 3.8 (b) to investigate the observation by McCulloch at al. that the lowest height regions in films of C_{12} pBTTT represent voids in the thin-film caused by partial dewetting of the formulation during annealing.[84] First, we have not observed such large (up to 400 nm) "voids" in our C_{16} pBTTT films. Second, what small low features we have observed (black areas in Figure 3.8 (a)) are not voids in the film. We can say this with some confidence since we would expect to see some evidence for the un-screened gate potential in the KFGM images of these regions, were they free of pBTTT. This is in contrast to our KFGM images of TIPS pentacene films where areas free of the OSC show a strong effect of the unscreened gate potenetial.

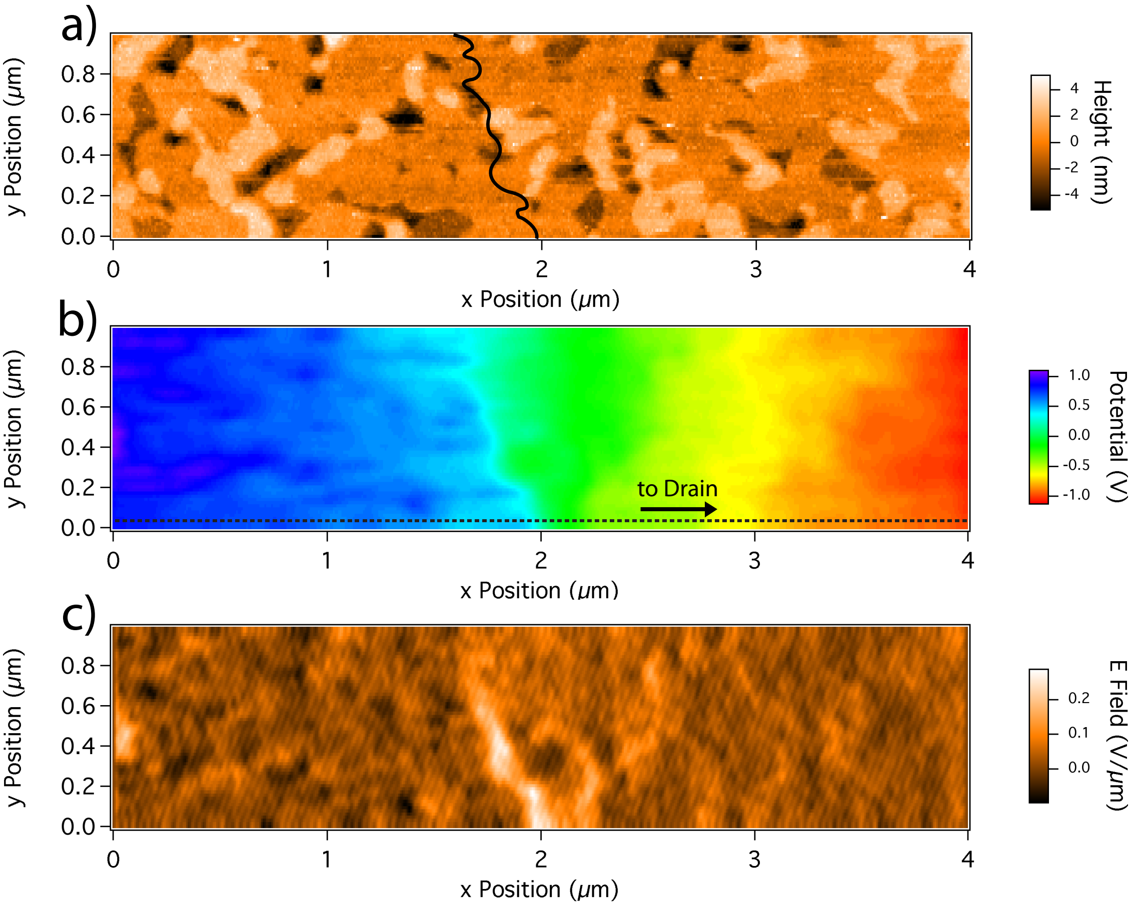

FIGURE 3.8: Topography (a), potential (b) and electric field, $-\frac{\partial V}{\partial x}$, (c) maps across the centre of the channel of a C_{16} pBTTT device with $L = 5\ \mu m$, taken with $V_G = 10\ V$ and $V_D = 5\ V$. The speckle and line artefacts in the AFM image are most likely caused by material adhering to the tip. The potential step clearly visible in (b) and (c) has no obvious correlation to the topography as shown by superimposing it onto (a) (black line).

In Figure 3.9, potential line-scans taken at the same position in the TFT channel for different values of V_G are compared to each other and to the topography (red line). The boundary seen at $V_G = 10\ V$, which is in the subthreshold region as indicated in Figure 3.7, is not visible as the device is turned on. Linear fits to the three distinct regions of the 10 V line estimate the lateral electric field strength as 0.19 $V\mu\text{m}^{-1}$ (left), 2.1 $V\mu\text{m}^{-1}$ (middle) and 0.32 $V\mu\text{m}^{-1}$ (right). The factor of 10 difference between the boundary and the adjacent channel areas suggests that is has a much lower conductivity, although we cannot be quantitative without a local measurement of the current. The width of the boundary region, 300 nm, suggests that we may be looking at a region of disordered material rather than an abrupt boundary, although no feature can be seen in the topography that directly corresponds to this.

As V_G is increased and more mobile charges are injected into the channel, turning the

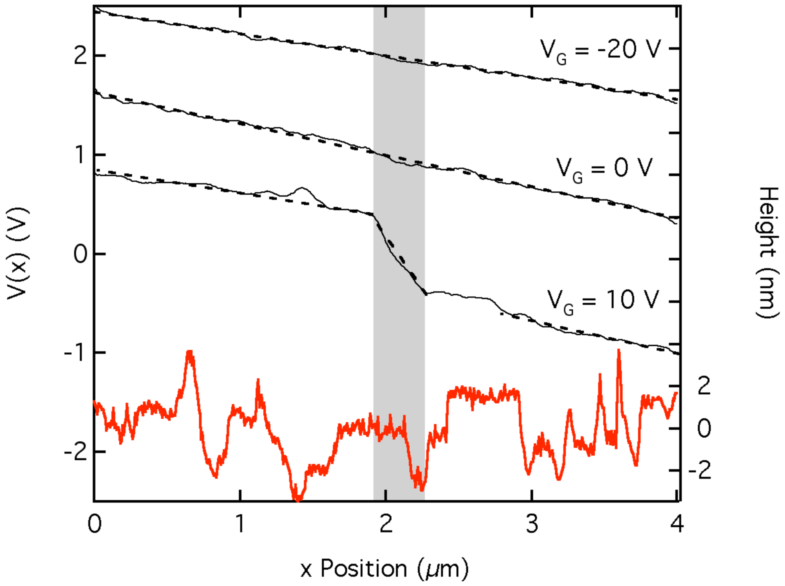

Figure 3.9: KFGM potential line-scans taken along the x-axis at the position shown in Figure 3.8 (b) (dashed line) and offset by 1 V for clarity. Linear fits to the potential are shown (dashed lines). The corresponding topography line-scan is shown in red. The $V_G = 0$ and $-20\ V$ lines are fitted well with a constant electric field strength, whilst the three distinct regions in the $V_G = 10\ V$ line are fitted separately. At $V_G = 10\ V$ two regions, with $E = 0.19$ and $0.32\ V\mu m^{-1}$ respectively, are separated by a 300 nm boundary region (grey box) in which $E = 2.1\ V\mu m^{-1}$, a factor of 10 higher. This is suggestive of a highly resistive grain boundary although such is not reflected in the topography.

device on, the step disappears. This could indicate that it contains trap states that must be filled before the conducting channel can form, so such boundaries may be related to the position of V_T. However, given that these effects only become visible as the device is turned off, they are unlikely to have a significant effect on the device performance when $V_G > V_T$ and the device is turned on.

In conclusion, we have seen limited evidence for domains in C_{16} pBTTT, although unlike those seen by Bürgi et al. in F8T2, they only appear in the subthreshold region. The spatial extent of the observed boundary suggests that it represents an extended region of disordered material, perhaps the type of thread-like disclination that gives nematic liquid crystals their name.

3.5 KFGM imaging of pBTTT thin-film trasnsistors

Modelling of TFTs suggests that in a device with ideal Ohmic contacts all of the resistance should occur at the source contact.[5] Organic TFTs rarely behave ideally and there are many possible factors that can lead to increased contact resistance. As a result, the performance of organic TFTs is strongly reliant upon efficient charge injection from the source contact, and therefore upon contact resistance in general. In many cases, device performance is dominated by the contact effects, particularly at shorter channel lengths.[7] Whilst it is possible to reduce the effects of the contacts by careful selection and surface modification of the contact metal,[40, 89] this is not always practical or successful. In the past, the problem of separating the contribution of the contacts from that of the TFT channel has been approached in a number of ways, each with its own limitations and drawbacks.

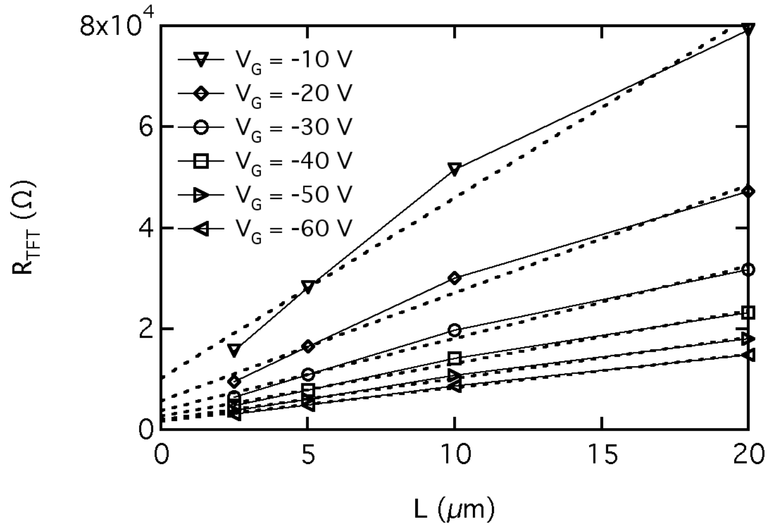

Figure 3.10: R_{DEV} plotted against L for $V_G = -10$ to -60 V with linear fits shown (dashed lines). The total parasistic contact resistance, R_P ($= R_S + R_D$), can be separated from the channel resistance, R_{CHAN}, by extrapolating the fit to $L = 0$. Closer to the off region (more positive V_G) there is a clear departure from the linear fit for the devices with $L = 20$ μm. This inconsistency makes a reliable estimate of R_P for all values of V_G very difficult.

In the linear regime, the contact resistance is often estimated by producing a range of devices with varying channel length, L. Simple electrical measurements can then be used to calculate the device resistance, $R_{DEV} = R_{CHAN} + R_P$, where R_{CHAN} is the resistance of the channel and R_P is the total parasitic resistance form the contacts.[90] Plotting R_{DEV} against L for different values of the gate voltage, V_G, allows for the separation of R_{CHAN} from R_P by means of a linear fit, extrapolated to $L = 0$. Figure 3.10 is an example, albeit over a limited range of L, of such a plot using our pBTTT TFTs measured in a dry nitrogen atmosphere. For this set of devices, with $L = 2.5 - 20$ μm, R_P ranges from 10,131 Ω at V_G = -10 V to 1,624 Ω at $V_G = -60$ V. In comparison, the extracted R_{CHAN} component over the same range of V_G is $3,573 - 665$ $\Omega/\mu m$.

The significance of the contacts to device performance is usually illustrated by plotting the device mobility, μ_{DEV} against L. Linear and saturation μ_{DEV} are calculated from the long channel FET model, as shown in Equations 3.1 and 3.2. It is generally observed that $\mu_{DEV,LIN}$ increases with channel length, as the relative contribution of R_P to R_{DEV} decreases. Plotting the μ_{DEV} for the same devices shown in Figure 3.10 produces the values shown in Figure 3.11. $\mu_{DEV,LIN}$ follows the expected trend, decreasing as L increases, however $\mu_{DEV,SAT}$ *decreases* with increasing L. It is possible that for devices with $\mu_{DEV,SAT}$ in this range – 0.14 to 0.20 $cm^2V^{-1}s^{-1}$ – the effects of increasing electric field with reduced channel length overcome the effects of R_P.

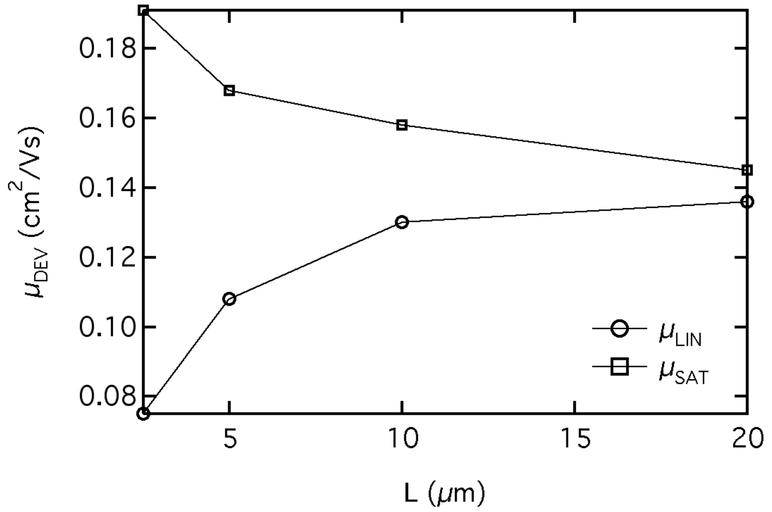

FIGURE 3.11: $\mu_{DEV,LIN}$ (circles) and $\mu_{DEV,SAT}$ (squares) plotted against L. $\mu_{DEV,LIN}$ follows the behaviour of increasing with channel length as would be expected for a contact-limited device, whilst $\mu_{DEV,SAT}$ shows the opposite behaviour. The implication is that R_{CHAN} dominates the device performance in the saturation regime.

$$\mu_{DEV,LIN} = \frac{\partial I_D}{\partial V_G}\frac{L}{WC_iV_D} \tag{3.1}$$

$$\mu_{DEV,SAT} = \left(\frac{\partial\sqrt{I_D}}{\partial V_G}\right)^2\frac{2L}{WC_i} \tag{3.2}$$

Whilst it does allow for the estimation of R_{CHAN}, the above method is both practically and theoretically limited. A large number of devices are required with low device-to-device variation in order to produce reliable fits. This can be problematic for organic semiconductors such as pBTTT, which can be sensitive to small variations in device processing. The main theoretical limitation is that, whilst one can extract R_P, there is no way to separate the individual contributions of the source and drain, R_S

and R_D. Given the importance of the source contact to device performance, this is a major deficiency if the aim is to understand and optimise device performance.

Direct extraction of R_S and R_D for individual devices is also possible using four-point electrical measurements.[23, 24] Such measurements rely upon a linear fit between two points within the channel to estimate the contact resistances, so they are only useful in the linear regime where $V(x)$ can be assumed to drop linearly across the channel. In the saturation regime, where the shape of the potential cannot be assumed, it is impossible to extract reliable values. A further inconvenience is that device geometries incorporating potential probe contacts in the channel must be used.

Similar results to those obtained from four-point measurements can be achieved using simple conducting-tip AFM potentiometry measurements.[77] The potential is probed by contacting a conducting tip to the surface at selected points within the channel and measuring V(x) directly. The data are analysed in much the same way as for four-point measurements and, in theory, as many points can be measured as the experimenter has patience for. However, to produce images at high resolutions ($\lesssim$ 100 nm) would require an unfeasibly large number of individual measurements.

KFGM measurements eliminate all of the above frustrations by allowing the spatial variation of the potential within the channel to be accurately and reliably measured, and for contact effects to be separated from material properties using single measurements on individual devices. The ability to fully characterise a single device makes KFGM particularly suited to studying device-to-device variations. Using KFGM in tandem with automated current-voltage measurements, as described in this section, allows for the full range of voltages in both the linear and saturation regimes to be probed.

C_{16} pBTTT devices with $L = 5$ μm were used throughout this chapter as they provided the best compromise between minimising short-channel effects and reducing measurement times. All measurements were performed either in low vacuum (10^{-4} $torr$) or under nitrogen (from liquid boil-off) in order to minimise any degradation of the pBTTT caused by exposure to the ambient environment.

3.5.1 KFGM measurements of the TFT channel: linear regime

In the linear regime, KFGM measurements were taken over full 10 μm x 10 μm images with between 256 and 512 lines per image. Since the applied V_D was relatively low – -5 V to $+5$ V – stable imaging was possible with a low lift-height of 30 nm. These pBTTT devices also show a good degree of uniformity along the width of the channel, with good agreement between images from different positions in the channel and with different tips. A range of different voltages can thus be applied at different positions in a single image without reducing our confidence in the data.

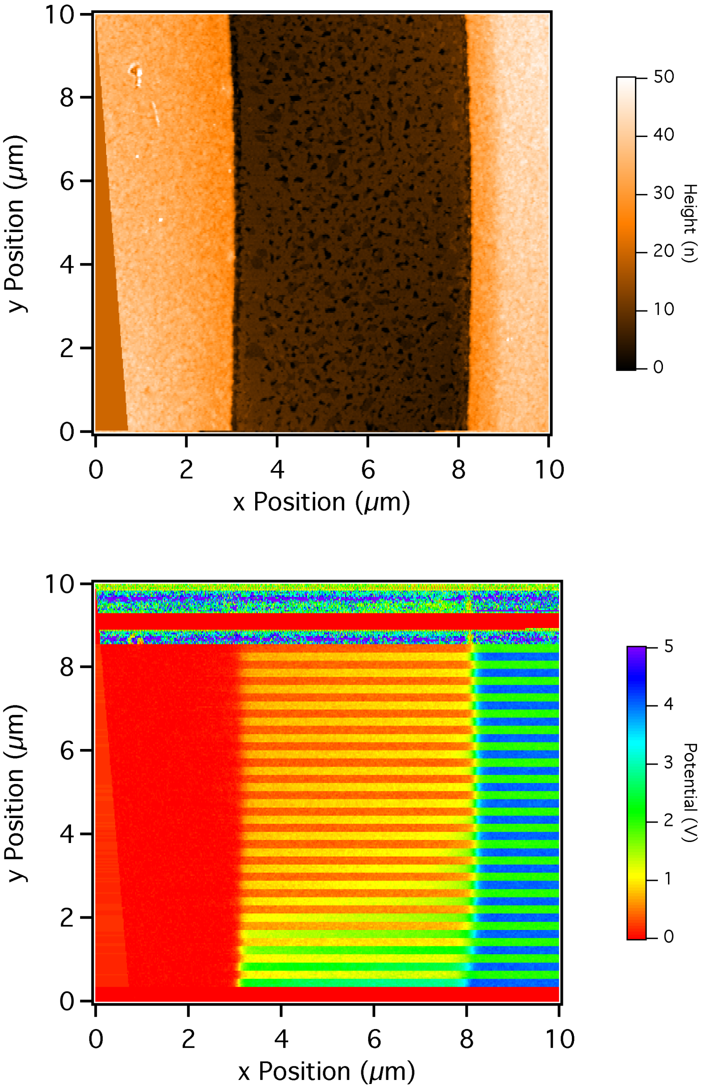

FIGURE 3.12: Tapping mode AFM topography (top) and KFGM potential (bottom) maps showing a linear transfer scan taken from $V_G = 20$ to $-20\ V$ in steps of $2\ V$ with $V_D = 2$ and $4\ V$. Each voltage value was held for 5 lines producing the distinctive stripes in the potential. The images have been offset line-by-line in the x-direction to account for the difference of 5° between the channel edges and the image y-direction. The curvature observed at the channel edges is an artefact most likely caused by lateral drift of the AFM during imaging.

The images in Figure 3.12 show the topography and local potential maps for a transfer scan from $V_G = 20\ V$ to $-20\ V$, alternating between $V_D = 2\ V$ and $4\ V$. Each voltage point is scanned for five lines allowing for mean values to be taken to reduce the effect of noise. The same terraced topography is observed as in the images in Figures 3.2 and

3.8 albeit at lower resolution. Importantly, the mean potential measured at the source electrode equals the applied potential to within the noise. A good confirmation that the device is operating in the linear regime is that the potential line-scans for $V_D = 2\ V$ lie directly on top of those for $V_D = 4\ V$ when scaled up by a factor of two.

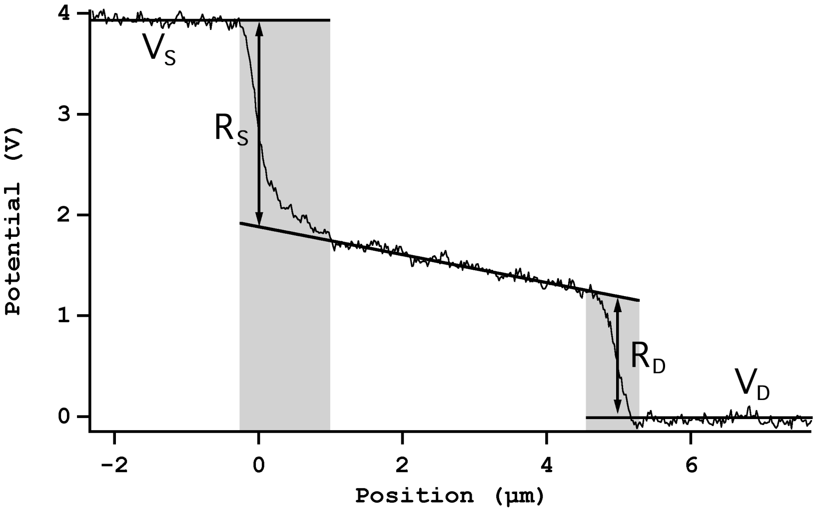

FIGURE 3.13: Example KFGM Line-scan for $V_D = 4\ V$ with linear fits to the channel and contacts shown (solid lines). The extent of the contact regions is highlighted in grey. Values of R_S and R_D were determined by a software macro as the difference between the linear fits to the contact and the channel through the centre of the contact potential drop, as indicated by the arrows.

For each voltage point, a potential line-scan similar to that shown in Figure 3.13 was recorded. This image demonstrates the immediate advantages of using KFGM over more conventional non-SPM methods. The asymmetry between R_S and R_D is clear: the potential dropped at the source (left) contact is almost twice that dropped at the drain (right). The contacts also have a significant spatial extent into the channel; approximately 1 μm at the source contact. These are both striking features that would be missed by simpler methods.

The potentials at each contact, V_S and V_D, were determined by averaging the 50 points adjacent to the contact edge. The potential drops across the contacts were defined as the difference between the contact potential and a linear fit to the channel, taken at the contact edge. The spatial extent of the contacts can vary with V_G so the potential was taken at the middle of the contact to maintain consistency between measurements. The results were found not to be significantly affected by small variations in the position of the measurement point. The device current $I_{D,LIN}$ can then be used with Ohm's law to simply determine the contact resistances, R_S and R_D.

The linear transfer scan, along with $\mu_{DEV,LIN}$ calculated from the long channel FET model, for the pBTTT TFT used in the following section are shown in Figure 3.14.

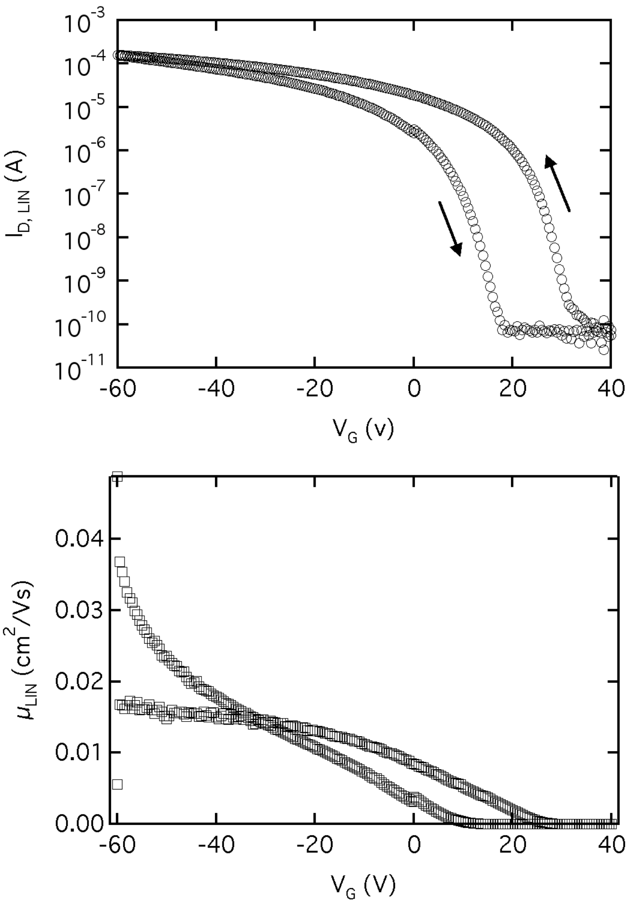

FIGURE 3.14: Linear forward and reverse transfer scan for the C_{16} pBTTT TFT used in this section measured under nitrogen inside the AFM chamber immediately before the KFGM scan. The hysteresis bewteen the forward and reverse scans (see arrows) represents a V_T shift of 20 V. The cause of such hysteresis is generally assigned to short-lived traps at the OSC-dielectric interface, as repeat scans maintain the same shape and similar hysteresis.

The mobility calculated from Equation 3.1 was 1.6×10^{-2} $cm^2V^{-1}s^{-1}$. There is also a significant hysteresis of 20 V between the forward and reverse scans (indicated by the arrows), which is generally attributed to short-lived traps at the OSC-dielectric interface. The scan was taken using the custom I-V amplifier under flowing dry nitrogen immediately before the KFGM measurements were made. The comparable transfer scan, taken as part of the KFGM image at $V_D = 4$ V, is shown in Figure 3.15. V_T determined by a linear fit to I_D closely matches that of the reverse scan in Figure 3.14, which is consistent with the presence of short-lived traps given the longer integration time of the KFGM transfer scan. Along with the good agreement of $I_{D,LIN}$ between the two scans, this suggests that the device is functioning normally during imaging.

During the KFGM image, V_G was scanned from $+20$ V to -20 V in 2 V steps. A

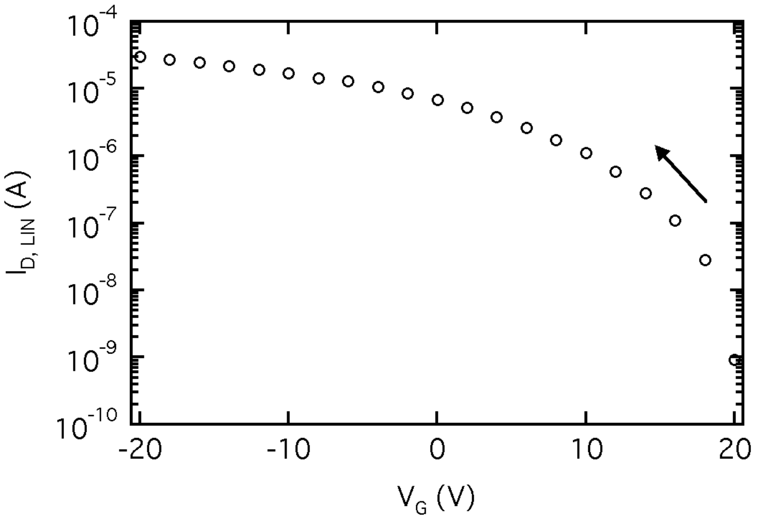

FIGURE 3.15: Forward linear transfer scan at $V_D = 4$ V, for the pBTTT TFT during the KFGM image. The values of $I_{D,LIN}$ are taken using the mean value of the current over the five lines of the KFGM image for each value of V_G representing around a 40 s integration time. V_T as estimated from this transfer scan closely matches that of the reverse scan in Figure 3.14. This is consistent with the existence of short-lived traps, as the longer measurement time ensures that all of the traps are filled.

potential line-scan, averaged over the five lines, was analysed as in Figure 3.13 for each value of V_G. Selected line-scans are shown in Figure 3.16. Even a brief visual inspection of the graph shows that the potential dropped at the source (right) contact clearly increases with V_G whilst that of the drain (left) contact shows an opposite behaviour. We can also see that 90% of the potential is dropped at the contacts when the device is turned on. These are both interesting facts, however the true value of the technique is in the complete analysis.

Using I_D and the voltages dropped across the channel and contact we can calculate the conductance of the channel, G_{CHAN} and that of the contacts, G_S and G_D alongside G_{DEV} for the whole device, as shown in Figure 3.17. Both G_S and G_D are significantly lower than G_{CHAN} although it is the source contact that dominates, to the point that G_S and G_{DEV} are comparable. In fact, there is a remarkable consistency between the behaviours of the three elements in terms of general behaviour. This is highlighted by plotting the ratios of G_S and G_D to G_{CHAN} and to each other, as in Figure 3.18. The ratios are effectively constant from $V_G = 0\ V$ to $-20\ V$, though they begin to diverge as V_G approaches V_T.

Given that only 10% of the potential is dropped across the channel, we would expect μ_{CHAN}, calculated from G_{CHAN}, to be a factor of 10 higher than μ_{DEV} and this is indeed what we see. A comparison of the two mobilities is shown in Figure 3.19, plotted on a log scale to highlight the difference. $\mu_{CHAN} = 0.1\ cm^2V^{-1}s^{-1}$, which is

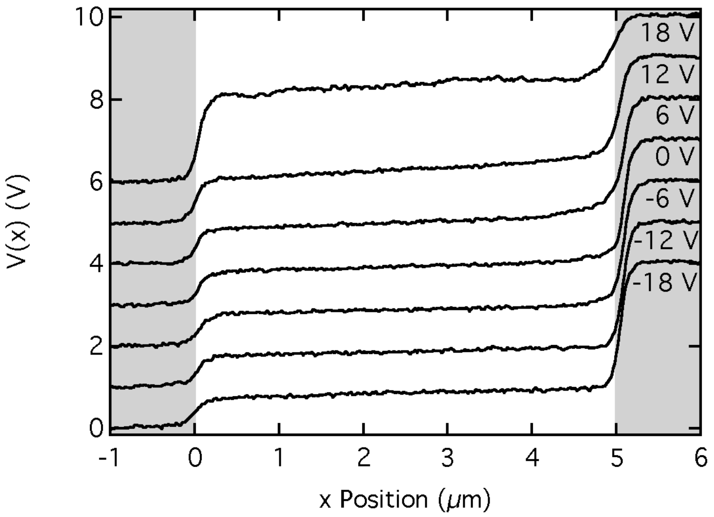

FIGURE 3.16: Selected line-scans in $V(x)$ taken from the KFGM transfer scan image in Figure 3.12 and offset by 1 V for clarity. The source (left) and drain (right) contacts are shown in grey. As V_G is made more negative and the device turns on, the potential drop V_S decreases whilst V_D increases significantly, accounting for the majority of the potential dropped across the device.

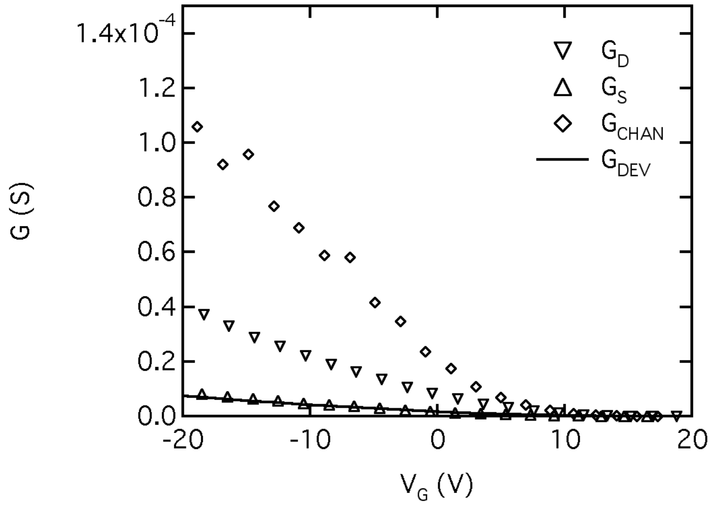

FIGURE 3.17: Device condictance, G_{DEV} (solid line), plotted alongside that of the individual components, G_D (down triangles), G_S (up triangles) and G_{CHAN} (diamonds) as extracted from the transfer KFGM line-scans in Figure 3.16. The component with the lowest conductance, and therefore that which dominates the device performance, is G_S. Thus, G_{DEV} closely follows G_S. All three components show a clear linear behaviour.

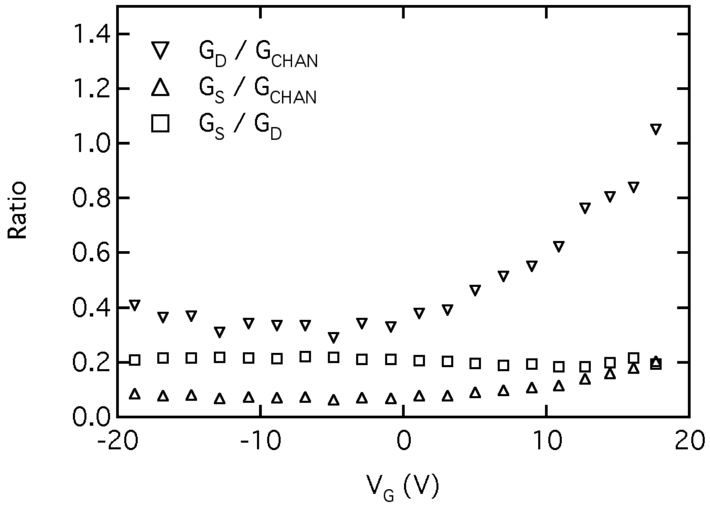

FIGURE 3.18: Ratios of the various device component conductances to one another plotted against V_G. For $V_G < 0\ V$ the components maintain fairly constant values of $G_D/G_{CHAN} = 0.35$, $G_S/G_{CHAN} = 0.07$ and $G_S/G_D = 0.22$ respectively, which is impressive given the order of magnitude differences between G_S and G_{CHAN}. This consistency between the conductance values implies that R_S and R_D arise from the pBTTT within the channel rather than from any diode-like contact effects. See Section 3.5.4 for a more detailed discussion of the contacts.

within a factor of three of the device mobilities observed by McCulloch et al in devices with lower resistance platinum contacts and similar electric fields.[89]

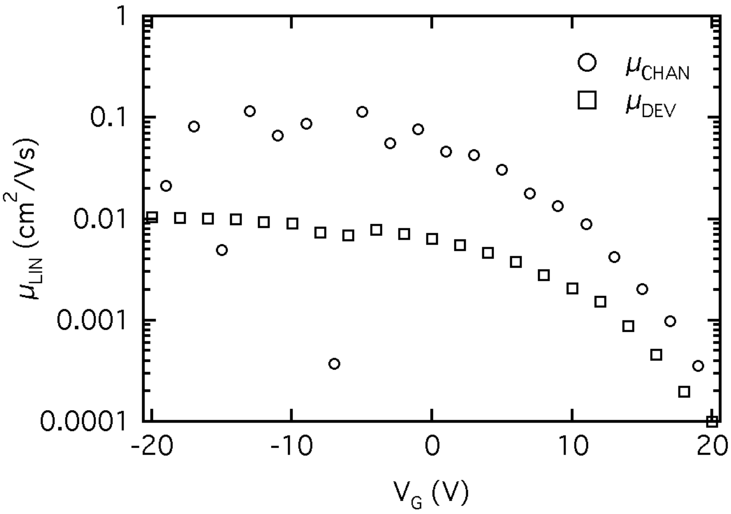

FIGURE 3.19: Comparison of μ_{CHAN} (circles) and μ_{DEV} (squares) plotted against V_G on a logarithmic scale to highlight the differences. $\mu_{CHAN} = 0.11\ cm^2V^{-1}s^{-1}$, which is an order of magnitude larger than μ_{DEV}, as implied by the approximately 90% of the potential that is dropped at the contacts.

The mobility measured in this device is significantly lower than is reported elsewhere in the literature so it should be discussed. The difference can be broadly attributed to two sources. The first is a drop in the device current by a factor of two between the measurements taken in nitrogen prior to transfer and those taken in the AFM. Short term exposure to ambient conditions - in this case around 30 minutes whilst the device was mounted in the AFM - causes an immediate, unrecoverable drop in device performance. The second factor accounting for the lower performance mobility here comes from device preparation. We encountered difficulties in reproducing the reported results for pBTTT, most likely stemming from the unreliability of the OTS treatment, which leads to reduced uniformity of the SAM and thus poorer alignment of the pBTTT molecules and lower mobility. The second factor is not a significant problem since the KFGM measurements allow us to deal with individual devices, regardless of sample-to-sample uniformity. The first factor is more problematic as it could be seen to introduce doubt as to the validity of the measurements. However, the strong internal consistency of the measurements and their agreement with the theory makes a strong case for the integrity of the data.

In the linear regime, the measurements presented above show that standard electrical measurements will tend to seriously underestimate the mobility of the OSC in the TFT channel. Fitting device resistance to channel length by the GTLM can provide an estimate of contact resistance, but this technique cannot be applied to single devices. The accurate determination of R_{CHAN}, R_S and R_D that we have obtained by KFGM provide the only truly reliable value for μ_{CHAN} for a given device, which gives us more meaningful information about the behaviour of the pBTTT itself. Additionally, much more detailed information can be obtained about the contacts themselves, as discussed later.

3.5.2 KFGM measurements of the TFT channel: saturation regime

In the saturation regime, the separation of the electrical characteristics of the channel and contacts with KFGM is more complicated, both technically and theoretically. The increased source-drain voltage, in this case $-60\ V$, increases the likelihood that short delays in the software controlling the voltages will allow the tip to be in contact with the surface at high voltage. The resultant discharge can cause permanent damage to swathes of the channel hundreds of microns wide. On the theoretical side, the channel in saturation can no longer be treated as having a uniform conductivity, so a simple linear fit to the channel potential will no longer suffice to extract the channel mobility.

The technical issue of electrical discharge between tip and surface, which could potentially damage the instrument as well as the device, is resolved by performing the KFGM line-scan with an increased lift-height of 100 nm and by ensuring that the

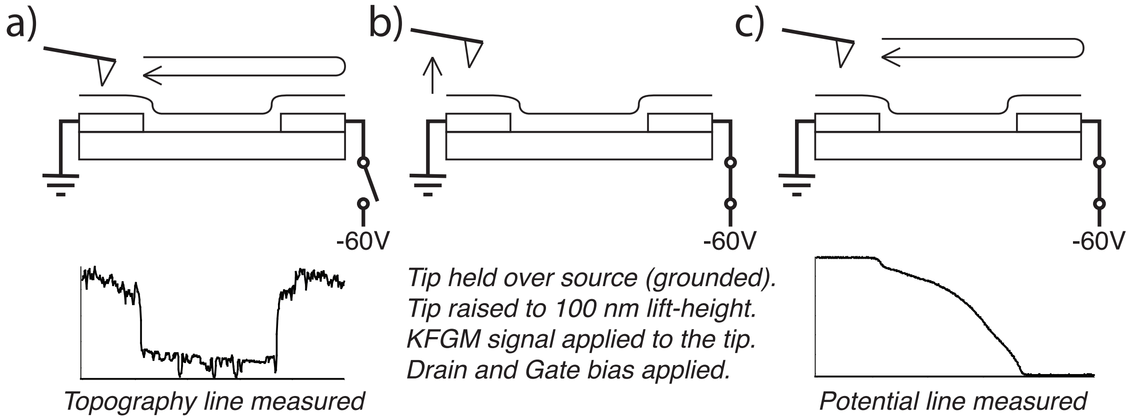

FIGURE 3.20: The process for measuring one saturation KFGM line. The topography is first measured in tapping mode (a) and then the voltages are applied and the tip raised to 100 nm (b) for the KFGM scan in lift-mode (c). It is important that the tip is held over the source (grounded) contact as the voltages are applied as this reduces the chances accidental tip-surface contact caused by the sudden presence of a strong electric field.

voltages are applied to both device and tip whilst it is held above the grounded (source) contact, as shown in Figure 3.20. Slower scanning rates of around 0.25 Hz also significantly reduce the chance of software delays causing the voltages to be applied whilst the tip is in the wrong location.

The saturation transfer plot obtained during KFGM for the same pBTTT device used in the previous section is shown in Figure 3.21. Values were obtained every 6 V with V_G ranging from $+18\ V$ to $-18\ V$. The threshold voltage obtained from a linear fit to $\sqrt{I_D}$ is 13.78 V. The saturation images were taken immediately after the linear images under the same ambient conditions and with the same tip. They can can thus be considered to be comparable with the linear measurements.

Saturation potential line-scans were taken at 6 V intervals of V_G and are shown in Figure 3.22. The potential profile within the channel is clearly super-linear, suggesting a spatially varying charge density as predicted by the long channel FET model in the saturation regime. Qualitatively, these potential profiles appear similar to those obtained by Burgi et al. [80] in the channel of a P3HT TFT. However, unlike Burgi et al., who opt for a gate-dependent model of mobility to best fit their data, our potential profiles are most closely fitted by the long channel FET model assuming a constant, gate-bias independent mobility.

We first assume that the gradual channel approximation holds true since the channel length, L = 5 μm, is significantly larger than the insulator thickness d_i = 230 nm. The current flowing through an element with width W is proportional to W, the charge density, $\rho(x) = en(x)$, and the carrier drift velocity, $\vec{v}$:

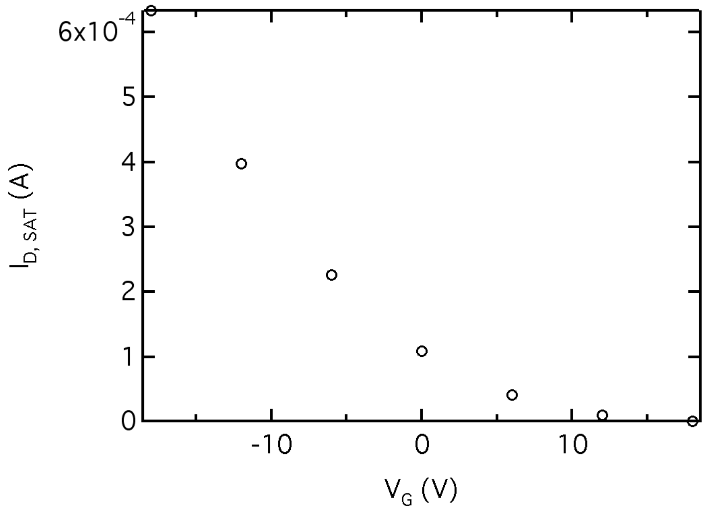

FIGURE 3.21: Saturation transfer scan for $V_D = -60\ V$ taken during the KFGM saturation scan in Figure 3.22. V_T estimated from a linear fit to $\sqrt{I_{D,SAT}}$ is 13.78 V although the limited number of points in the scan add a greater uncertainty to the estimate.

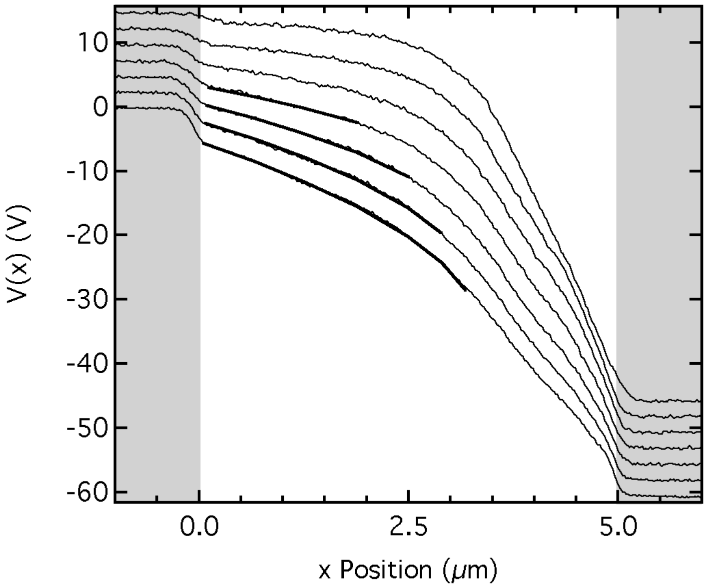

FIGURE 3.22: KFGM saturation potential line-scans from (top to bottom) $V_G = 18$ to $-18\ V$ in 6 V steps with the line-fits obtained using Equation 3.10 shown (heavy black lines). The slope of the potential clearly varies spatially from the source contact into the channel as we would expect from a spatially varying charge density. At the drain contact, there appears to be a region with constant electric field (slope) that grows wider as V_G is made more positive. The fits show good argeement to $V(x)$ up to the point where $V_{G,LOCAL}$ is approximately +10 V.

$$i = Wen(x)|\vec{v}| \tag{3.3}$$

The charge carrier mobility, μ, is simply the ratio of induced drift velocity to the magnitude of the electric field so we can substitute $|\vec{v}| = \mu|\vec{E}|$ into Equation 3.3 to obtain Equation 3.4:

$$i = Wen(x)\mu|\vec{E}| \tag{3.4}$$

In the long channel FET model we assume that the channel and the gate electrode behave as an ideal capacitor with accumulated charge $Q = C_i V'$. The charge density at any point within the channel will, therefore, be dependent upon the effective gate voltage, V', at that point. In our case, we can define V' in terms of the local potential, V(x), and the effective gate voltage $V_G - V_T$:

$$V' = V(x) - V_G + V_T \tag{3.5}$$

The local number density of charge is thus:

$$n(x) = \frac{C_i(V(x) - V_G + V_T)}{e} \tag{3.6}$$

Local electric field can be simply determined from the local potential, V(x), by:

$$\vec{E} = \frac{-\partial V(x)}{\partial x} \tag{3.7}$$

Substituting Equations 3.6 and 3.7 into Equation 3.4 provides us with a more useful form of the equation for current:

$$i = -W\mu C_i(V(x) - V_G + V_T)\frac{\partial V(x)}{\partial x} \tag{3.8}$$

To produce an equation for V(x) we can rearrange Equation 3.8 and integrate over the fitted range of the potential from the start point where $x = x_0$ and $V(x) = V_0$ to the point $(x, V(x))$ as shown.

$$\int_{x_0}^{x} \frac{\partial V(x)}{\partial x}(V(x) - V_G + V_T)dx = \int_{x_0}^{x} \frac{-i}{W\mu C_i}dx \tag{3.9}$$

Solving the integrals in Equation 3.9 and rearranging for V(x) we obtain an equation that we can use to fit to the potential V(x).

$$V(x) = V_G - V_T + \sqrt{(V_0 - V_G + V_T)^2 - G_S(x - x_0)} \tag{3.10}$$

With G_S:

$$G_S = \frac{2i}{WC_i\mu} \tag{3.11}$$

Fitting the saturation potential data from Figure 3.22 using Equation 3.10 with the free parameters V_T and G_S generates the values shown in Table 3.3. The fits are remarkably close to the measured potential, so long as they are restricted to the area of the channel running from the source (left) contact to the point where the local gate voltage $V_{G,LOCAL}$ is approximately +10 V. Extending the fit much beyond this region produces erratic and inconsistent results, suggesting that the behaviour of the rest of the channel is not easily fitted by the long channel FET model. This is to be expected, given that in regions of the channel where $V_{G,LOCAL}$ approaches V_T we should expect the channel to be "off" and that FET theory predicts a depleted pinch-off region near the drain contact.

V_G (V)	V_T (V)	μ_{CHAN}
0	17.24 ± 1.13	0.021
-6	18.49 ± 0.40	0.021
-12	18.63 ± 0.35	0.023
-18	17.32 ± 0.17	0.028

TABLE 3.3: Saturation channel mobility and threshold voltage values estimated from the long channel FET model fitting with Equation 3.10. The non-constrained fitting parameters were V_T and G_S, from which we extract μ_{CHAN}. The values obtained show a good consistency in V_T and show μ_{CHAN} varying slowly with V_G.

Leaving aside the limitations of the fit, the values for V_T and μ_{CHAN} obtained using Equation 3.10 are in fact in good agreement with the values obtained from the electrical measurements in Figure 3.21. The values of μ_{CHAN} show some variation, increasing from 0.021 to 0.028 $cm^2V^{-1}s^{-1}$ for $V_G = 0$ to -16 V, but closely agree with $\mu_{DEV} = 0.028$ $cm^2V^{-1}s^{-1}$ obtained from the transfer scan using Equation 3.2. The values of V_T are broadly consistent with one another and differ from the threshold obtained from the electrical measurements by only a few volts. This variation in V_T could be explained by the difference in measurement speeds between the two measurement types, with the longer KFGM scan allowing more time for accumulation of trapped charges for example. Alternatively, it could simply be that the limited number of points obtained during the transfer scan does not allow for a precise fit.

The two sets of values for μ and V_T were obtained by applying the long channel FET model to different data, so it might initially be unsurprising that they agree with one another. However, we have shown that a local application of the model within the TFT channel in saturation agrees with its general application to the whole device. This is consistent with the observation that in the saturation case only $\sim 10\%$ of the potential is dropped at the contacts compared to the $\sim 90\%$ seen in the linear regime. The mobility in saturation is also predicted to be independent of lateral electric field, so a reduction in field caused by contact resistance should have little effect.

In contrast to the above, Bürgi et al. fit their local potential data using a linearly V_G dependent mobility of the form $\mu = \mu_0 V'$ and obtain a value for μ_0 of 2 x $10^{-5} cm^2 V^{-2} s^{-1}$ that requires only a small threshold shift to fit their data. Substituting $\mu = \mu_0 V'$ into the derivation above produces Equation 3.12. Our saturation data show a slow increase of μ with V_G and our linear data show a farly strong linear dependence so it is worth testing this model as an alternative to the fits above.

$$V(x) = V_G - V_T + \sqrt[3]{(V_0 - V_G + V_T)^3 - \frac{3i}{WC_i\mu_0}[x - x_0]} \tag{3.12}$$

Fitting the $V(x)$ line-scans in Figure 3.22 using Equation 3.12 produces the values shown in Table 3.4. The values obtained from this fit are much less consistent than those we obtained using the long channel FET model. In order to fit the data, values of V_T are required that are both more variable than those we obtained and more than a factor of two greater than the value estimated from the transfer data. Further to this, we were unable to obtain a constant value of μ_0 for the different values of V_G. The best we can say is that the values obtained for μ_{DEV} are of the same order of magnitude as those in Table 3.3.

Having discarded a linearly V_G dependent mobility, we might consider other forms such a mobility might take, however what we would learn from such an endeavour is limited. If the mobility is V_G dependent then it seems to be only weakly so, which might imply agreement with the MTR model for charge transport in OTFTs. To confirm which model is applicable to our devices would require information about the density of states and about trap distributions that cannot be obtained from the KFGM. Without this, and some knowledge of the temperature dependence of the mobility, we cannot decide on any model. What we have shown, however, is that the

V_G (V)	V_T (V)	μ_0	μ_{CHAN}
0	37.26 ± 4.25	2.7 x 10^{-4}	0.01
-6	43.72 ± 2.61	1.9 x 10^{-4}	0.0095
-12	32.67 ± 0.68	4 x 10^{-4}	0.018
-18	34.17 ± 0.49	4 x 10^{-4}	0.021

Table 3.4: μ_{SAT} and V_T values estimated from the linearly V_G-dependent μ used by Bürgi et al.[80] and shown in Equation 3.12. The fitting parameters μ_0 and V_T are shown in columns 2 and 3. In order to closely fit $V(x)$, very high values of V_T must be used that vary significantly from fit to fit and show no agreement with the electrical data. The lack of a consistent value for μ_0 also suggests that a linearly V_G dependent μ is not appropriate in this case.

simplest and most commonly applied model – the long channel FET model – provides a very good fit to our experimental data for $V(x)$ in the saturation regime and that introducing a V_G dependence does not improve the consistency of our results.

Comparing the values we have obtained for $\mu_{CHAN,LIN}$ and $\mu_{CHAN,SAT}$ we see the clear result that the mobility is around a factor of four higher in the linear regime. This is unusual but the internal agreement between electrical and KFGM measurements points to this not being a measurements artefact. This result disagrees with that reported by McCulloch et al. [89] for pBTTT TFTs with platinum electrodes – and also with that of Hamadani et al. using gold contacts[91] – which showed increasing saturation mobility with decreasing channel length and thus increasing lateral field. We should also point out that our own measurements of pBTTT TFTs with $\mu_{DEV,SAT}$ above 1 $cm^2V^{-1}s^{-1}$, taken much earlier in the project also show an increasing saturation mobility with decreasing L. The difference could be due to variation in the quality of the pBTTT layers between the devices used, a conclusion further supported by the differences in μ_{CHAN} obtained by McCulloch et al. after correcting for the contacts.

The MTR model, as applied by Stallinga et al.[17] predicts a mobility that increases with lateral field, which contradicts our observation that saturation mobility is lower than linear mobility. The effects of resistive heating caused by increased power dissipation during saturation measurements would also be expected to lead to a higher mobility in disordered materials.[92] Our results so far do not explain this discrepancy. One possibility is so-called short-channel effects, which can lead to deviations from expected behaviour.

3.5.3 Short-channel effects

As we have shown above, once the performance of the channel are separated from that of the contacts, we directly access $\mu_{DEV,LIN}$ with a simple linear fit and $\mu_{DEV,SAT}$ with the long channel FET model, producing results that are convincingly self-consistent. However, there are aspects of our pBTTT device performance that do not fully obey the model. As is often observed in OTFTs with channel lengths $< 10\ \mu m$,[93–96] our pBTTT devices show a lack of saturation behaviour in output measurements. Figure 3.23 is an example output plot for the device described previously, showing a clear deviation from the behaviour predicted by the long channel FET model in Equations 3.13 and 3.14 for the linear and saturation regimes respectively.

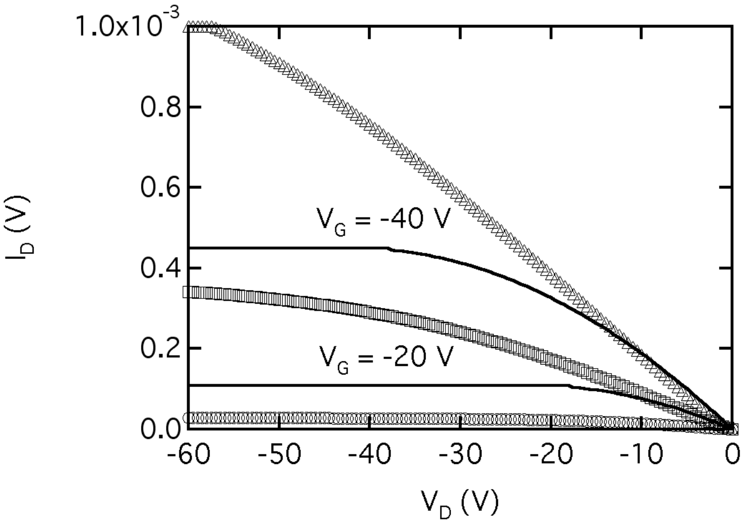

FIGURE 3.23: Output plots for the same pBTTT TFT, measured under nitrogen immediately before the KFGM scan. The measured values for $V_G = 0$ V (circles), $V_G = -20$ V (squares) and $V_G = -40$ V (triangles) are compared to the values calculated from Equations 3.13 and 3.14 (solid lines).

$$I_{D,LIN} = \mu C \frac{W}{L}[V_G - V_T]V_D \tag{3.13}$$

$$I_{D,SAT} = \mu C \frac{W}{2L}(V_G - V_T)^2 \tag{3.14}$$

In these devices, the output current rises linearly at low V_D as expected but deviates from the predicted values by as much as a factor of three for high V_D. Such deviations from ideality are observed in inorganic TFTs if the gradual channel approximation breaks down, resulting from the lateral electric field being comparable to the gate field. Haddock et al. [96] survey instances of long and short channel behaviour in organic

TFTs in relation to the ratio of channel length to gate oxide thickness, L/d_i. Broadly speaking, devices with a high $L/d_i > 30$ behave as long channel devices whilst those with a low $L/d_i < 15$ show short-channel behaviour. For our devices, $L/d_i = 21$, which falls between these two general regions. However, the fact that $E(x) << E(y)$ is still clearly true for our devices suggests that the observed deviations from the long channel FET model are not due to a breakdown of the gradual channel approximation. Chabinyc et al. [94] discuss a number of possible effects, both extrinsic and intrinsic to the device that could explain this non-ideal behaviour.

The first possible explanation is a significant leakage current, I_G, through the 230 nm SiO_2 gate dielectric. I_G was not recorded during the electrical and KFGM measurements used in the preceding sections, however, comparable transfer scans taken immediately after device fabrication under nitrogen show that I_G is at least a factor of 100 lower than I_D. We can think of no plausible mechanism for any breakdown of the gate dielectric between these initial measurements and those presented above so gate leakage can be trivially ruled out.

The other extrinsic factors suggested are charge trapping at the dielectric interface and movement of ionic impurities or chemical degradation of the polymer film. As is the case for Chabinyc et al., we can simply dismiss charge trapping and ionic impurities as these would also affect longer channel devices and we do not observe a similar lack of current saturation for devices with $L = 20\ \mu m$. Finally, whilst we know that our films do show some degradation upon exposure to the ambient atmosphere, this would also equally affect longer channel devices. Additionally, we would expect to see a significant deviation of the channel behaviour from the long channel FET model and this is not observed.

Given that the field-effect mobility in disordered organic systems generally increases with temperature, it is possible that the high biases and currents applied to the device might cause an increased mobility due to resistive heating. However, we can dismiss this as a significant factor for two reasons. The first, as noted by Chabinyc et al., is that the thermal resistivity of Si is very low, so we would not expect local heating to be a problem. The second is that in the linear regime, close to the contacts we see an increase in electric field, corresponding to a local reduction in conductivity. Given that the majority of the potential is dropped at the contacts, this is where the bulk of the resistive heating would be expected to take place, causing an *increase* in local conductivity, which we do not see.

The final explanation suggested by Chabinyc et al., and the one most amenable to investigation using our KFGM data, is that of channel length modulation when the device is operating in pinch-off. The depletion of charge-carriers near the pinch-off region combined with a high lateral electric field favours a bulk conductance in this region. The point in the channel at which transport through the accumulation layer gives way to bulk transport effectively defines a new channel edge, reducing the effective channel length of the device. The point at which this occurs is constrained by the fact that conservation of current must apply throughout the device with $I_{CHANNEL} = I_{BULK}$.

The saturation potential profile within the channel for our pBTTT TFT can effectively be divided into three regions, as shown in Figure 3.24. In the first region, X_{FITTED}, adjacent to the source electrode, the long channel FET model applies and the potential is readily fitted by Equation 3.10. The second region, defined as $X_{UNFITTED}$ covers the bulk of the channel not fitted by Equation 3.10. The third region, $X_{SATURATION}$, immediately adjacent to the drain electrode appears to support a maximum lateral field of $E \approx 30\ V\mu m^{-1}$.

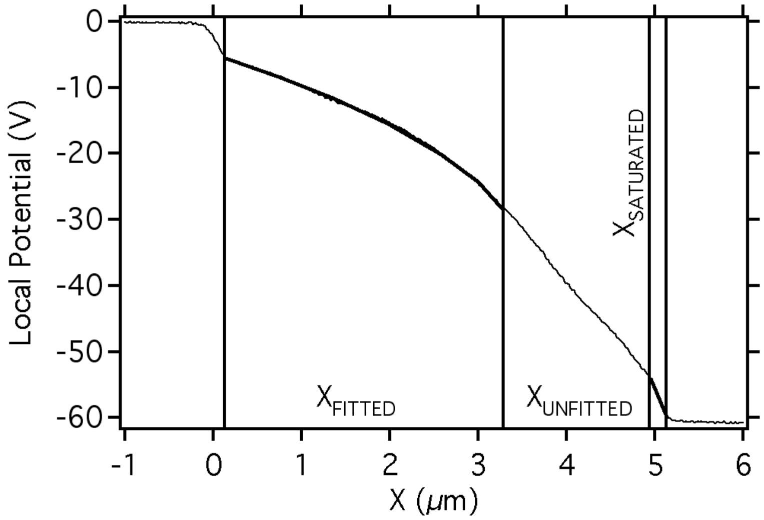

FIGURE 3.24: Example division of the saturation potential profile into three distinct regions where X_{FITTED} is the region in which the FET model applies, $X_{SATURATED}$ corresponds to a region of maximum lateral field near the drain electrode and $X_{UNFITTED}$ covers the remainder of the channel.

The relative extent of each of these regions is plotted against V_G in Figure 3.25. As V_G is increased and the device becomes more saturated, X_{FITTED} decreases with a corresponding increase in $X_{UNFITTED}$. The unfitted region effectively defines the maximum possible extent of the bulk conductance region into the channel. Whilst we only have the limited output electrical data shown in Figure 3.23, we can make an broad comparison between the two data-sets. If we assume that the difference between the observed current and the modelled current in Figure 3.23 is entirely due to shortening of the channel we obtain a width for the bulk region, $L_{BULK} = 1.67\ \mu m$ at

V_G = -18 V, V_D = -60 V. From Figure 3.25 we obtain L_{BULK} = 1.89 μm at V_G = -20 V, V_D = -60 V.

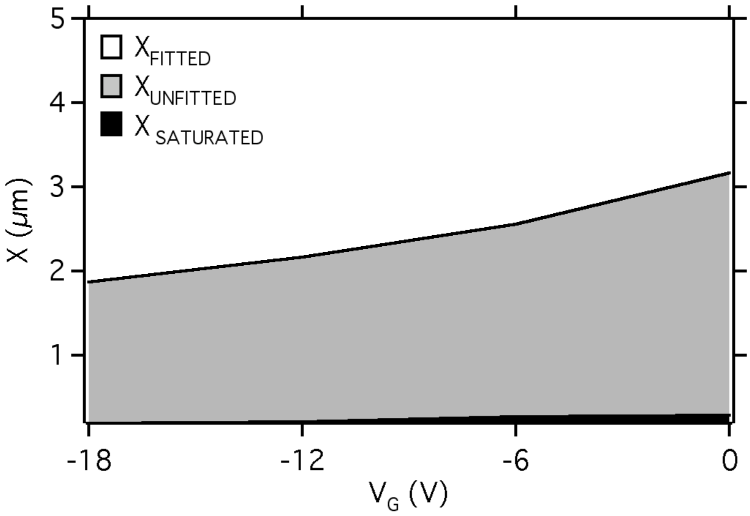

FIGURE 3.25: The spatial extents of X_{FITTED}, $X_{UNFITTED}$ and $X_{SATURATION}$ plotted against V_G for the potential profiles fitted using the long channel FET model.

Thus the estimated channel shortening falls within the unfitted region of the saturation potential, which would allow for the channel modulation suggested by Chabinyc et al. Unfortunately, we do not have a model with which to fit the local potential in this region so can say no more than that our data are consistent with a channel length modulation causing increased current in the saturation regime.

Within the unfitted region of the channel, we have defined $X_{SATURATED}$ as the small region adjacent to the drain electrode that maintains a constant electric field independent of V_G. This appears to suggest that there is a maximum saturated field that can be maintained within the pBTTT film, even with varying local conductivity.

The key claim of Chabinyc et al. that can be investigated using our KFGM measurements is that of channel length modulation caused by a bulk-conductance region at the drain electrode when the device is operating in pinch-off. Our saturation measurements show a region near the drain contact with a constant electric field of $E \approx 30\ V \mu m^{-1}$. This appears to suggest that there is a maximum saturated field that can be maintained in the pBTTT film, although the local conductivity must still increase with increasing V_G.

The width of $X_{SATURATED}$ is estimated in Figure 3.26 as the region over which a linear fit to V(x) applies. As the device becomes more saturated, the width of $X_{SATURATED}$ increases to a maximum value of 664 nm, only accounting for a little over 10% of the channel length. It is possible that this region is related to the width of

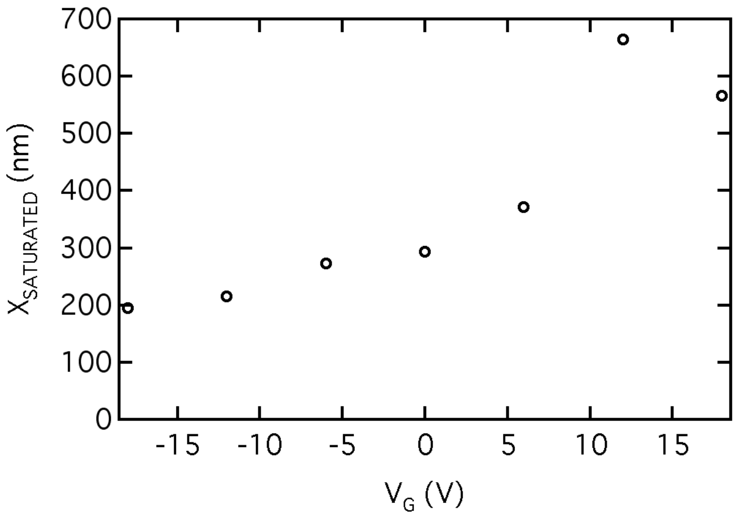

FIGURE 3.26: Width of the constant field region, $V_{SATURATED}$ next to the drain electrode extracted from Figure 3.22 and plotted against V_G. The width of the region decreases steadily from 550 nm to 200 nm as the device is turned on. The spatial extent of the region implies that it is not associated with relatively short range Schottky or dipole barriers.

the pinch-off region itself, with the apparent variation in conductance caused by the pBTTT film only being able to support a maximum field of 30 $V\mu m^{-1}$. However, with no way to directly test this based upon our data, this remains speculation. It is also possible that this region is simply due to a contact resistance, discussed in the next section.

Our KFGM measurements in saturation are consistent with a channel length modulation as proposed by Chabinyc et al. Whilst we cannot directly confirm the hypothesis, it may explain the observed lack of saturation in the output scan and the observed region in the channel where the long channel FET model does not apply. We can certainly say that, based upon our data, channel length modulation is the most likely explanation for our data.

3.5.4 KFGM measurements of the contacts

One of the key conclusions from the data presented earlier in this chapter is that, in the linear regime particularly, the contacts have a significant effect on device performance. Since as much as 90% of the potential dropped across the transistor is dropped at the contacts, it will be informative to examine their behaviour with respect to the applied voltages. The effects of annealing on the behaviour of the contacts will also be investigated. Throughout this section, we will treat the TFT channel as a three part system consisting of a central channel region bracketed by extended source and drain contact regions.

Due to the stability issues inherent to handling pBTTT transistors, it was not possible to take KFGM measurements of the same device before and after annealing, so the data presented in the following comparison are taken from two devices, one annealed at 180 °C for 10 minutes and one not. The level of device-to-device variation was relatively high for these devices, however comparisons of the relative values of resistances and potentials are still valid.

One simple way to estimate the relative contributions of the contacts to device performance between annealed and non-annealed transistors is to plot potential line-scans side by side, as shown in Figure 3.27. Both line-scans are taken at V_G = -20 V and it is immediately clear that, whilst the contacts in the annealed (red) device account for 90% of the device potential, the contacts in the non-annealed (black) device drop only 50% of the applied potential. The source (left) contact is also clearly dominant in the annealed device whereas the contacts in the non-annealed device are symmetrical with no significant additional barrier to charge injection.

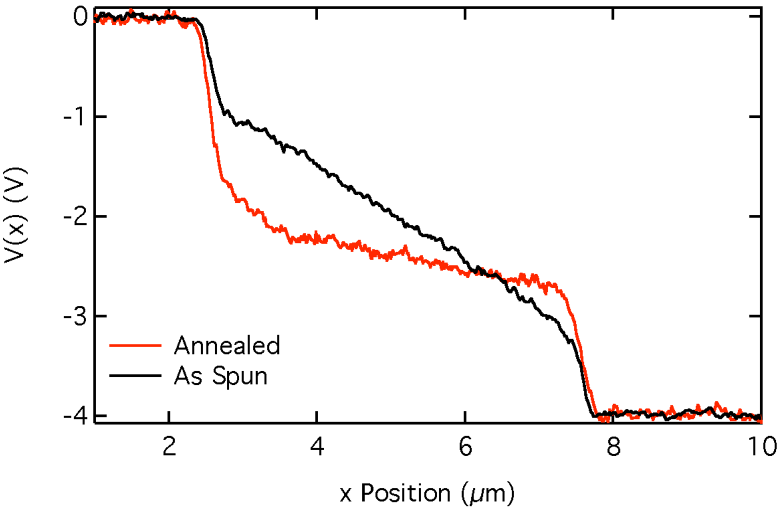

FIGURE 3.27: Comparison of potential line-scans at V_G = -20 V for a non-annealed device (black line) and a device annealed at 180 °C (red line). The annealed device is significantly more contact limited, which is what we would expect if μ_{CHAN} has increased.

Plotting the resistance of the three components against the applied gate voltage provides more information. For the non-annealed device shown in Figure 3.28, the source and drain resistances are similar throughout the "on" region, diverging only at more positive V_G where the linear fit to the channel tends to break down. As suggested by the line-scans, the channel is the single biggest contribution to device resistance.

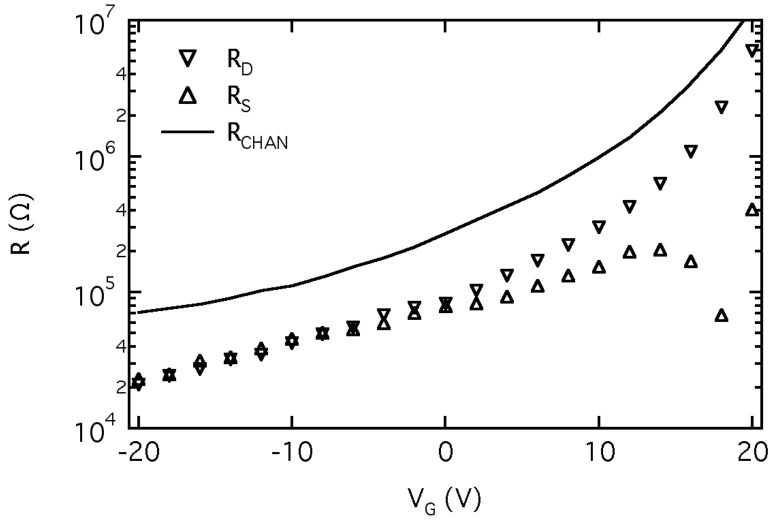

Figure 3.28: R_S, R_D and R_{CHAN} for an as-spun C_{16} pBTTT TFT as a function of V_G. R_S and R_D are approximately equal when V_G is below 0 V as implied by the potential drops in Figure 3.27. Interestingly, R_{CHAN} is the dominant component in this device.

In contrast to this, in the annealed device (Figure 3.29) the source contact makes the greatest contribution to the dropped potential and the channel the smallest. The drop in channel resistance is consistent with the expected increase in the conductivity of the film due to annealing. Interestingly, the dominance of the source contact over device performance also appears to be linked to the annealing step. The contact dipole at the Au/pBTTT interface could be strongly dependent upon the molecular order of the semiconductor at the interface, or it could simply be that the molecular order is disrupted at the contact edge as the device is annealed, creating a significant difference in mobility between the regions near the contacts and in the channel.

As we have shown in KFGM transfer measurements, both the contacts and the channel have a strong dependence upon V_G. Output measurements were also taken of the same device, in which V_D was varied with constant V_G for a range of gate voltages. Figure 3.30 is an example KFGM output measurement, with a lift-height of 30 nm, of the device operating in linear regime and turned on. In this case, the left contact was held at 0 V, with the potential varied on the right contact. Thus, as V_D is cycled from negative to positive, the right contact effectively switches from being the drain to the source. The voltage range of the output measurement is limited by operation at low lift-height in the linear region. In this case, the asymmetry between the source and drain contacts is much more pronounced when the right contact is the source.

Using local potential line-scans such as those in Figure 3.30 along with simultaneous measurements of I_D, we can investigate the I-V characteristics of the contacts. Figures

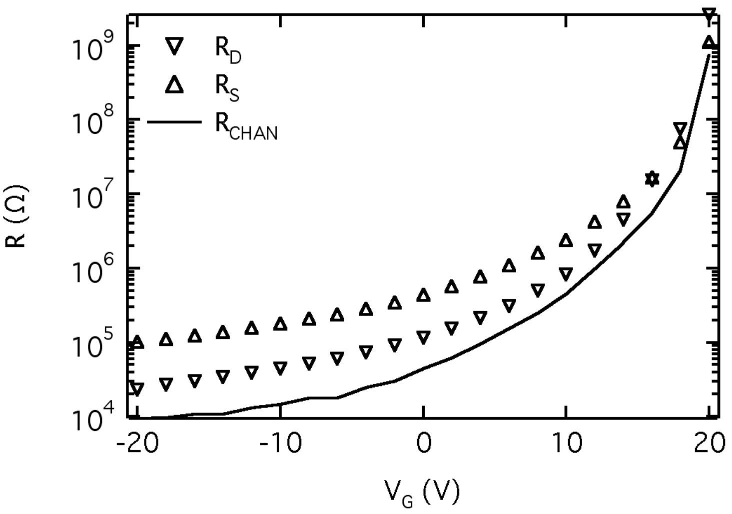

FIGURE 3.29: Contact and channel resistances for an annealed device as a function of V$_G$. In this case it is R_{CHAN} that makes the smallest contribution to the device resistance, with R_S clearly dominant.

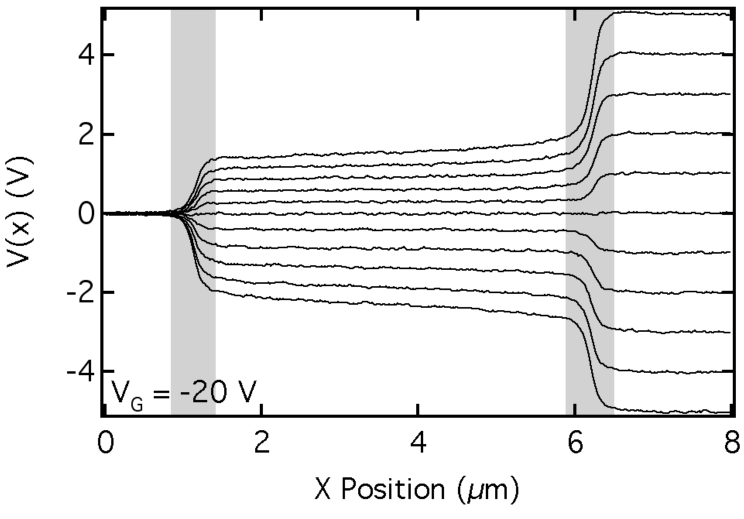

FIGURE 3.30: KFGM line-scans taken from an output scan with $V_G = -20\ V$ and V_D varying from -5 to $5\ V$ in $1\ V$ steps. The source and drain contact regions, in this case defined as the region over which $V(x)$ deviates from the linear fits, are shown in grey. The asymmetry between the source and the drain contact apears to be more pronounced when the right contact is the source.

3.31 and 3.32 show such I-V characteristics for the left and right-hand contacts respectively for a range of V_G. In this case, the device current, I_D is plotted against the voltage drop at the contact, defined as the distance between the point of deviation from a linear fit to the contact and the point of deviation from the linear fit to the channel. The sign of the voltage drop is arbitrary so the regions in which each contact is acting as the source or the drain are indicated.

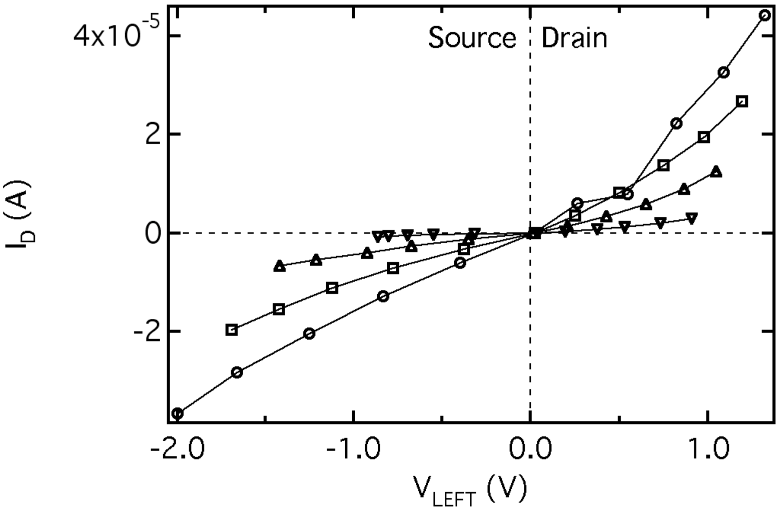

Figure 3.31: I-V characteristic of the left-hand contact of an annealed pBTTT device for $V_G = 10$ V (bottom) to $V_G = -20$ V (top) in steps of 10 V

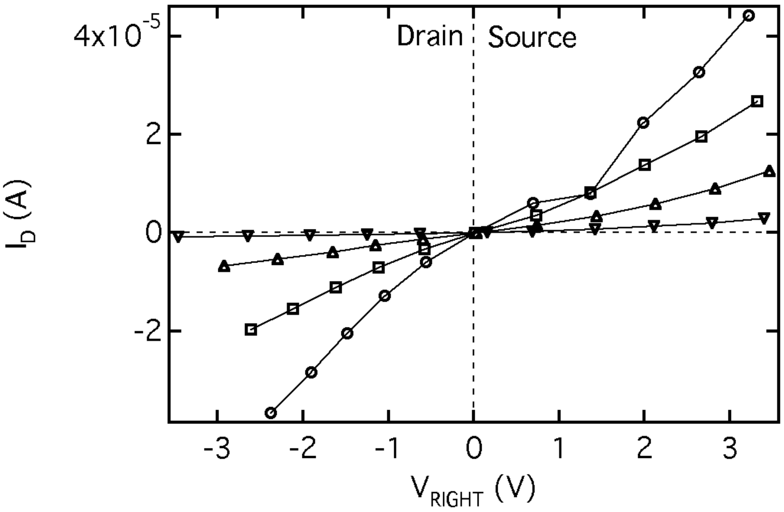

Figure 3.32: I-V characteristic of the right-hand contact of an annealed pBTTT device for $V_G = 10$ V (bottom) to $V_G = -20$ V (top) in steps of 10 V

The I-V profiles of the contacts appear in most cases to be slightly super-linear, possibly suggesting a forward biased diode-like behaviour. It is often assumed that the metal/semiconductor interface at the contacts behaves as a Schottky diode [97], which has the form:

$$I_D = I_0(\exp{(qV/nkT)} - 1) \tag{3.15}$$

with I_0 the reverse-bias saturation current and V the voltage dropped at the contact. However, we were unable to fit the data using the basic Schottky diode model, even with the inclusion of an unrealistically large ideality factor, $n > 20$. The turn-on of the Schottky diode is much sharper than the I-V curves presented here. Neither can we consider the contacts to be simple resistors with respect to V_D, since their resistance varies by as much as a factor of two over a 2 V range. Furthermore, the large spatial extent of the contact potential drop into the channel implies a longer range phenomenon, as discussed next.

Another key feature of the contact potentials that can be easily investigated with KFGM is the spatial extent of the contact potential. In all of the potential line-scans shown in this chapter, the contact region extends into the channel a certain distance. The width of the contact region can be simply defined as the distance between the point where the potential deviates from the linear fit to the contact and the point where it deviates from the linear fit to the channel region. Figure 3.33 shows the source contact width, X_{SOURCE}, for the annealed device plotted against V_G. There is a clear dependence of X_{SOURCE} upon V_G with a peak value around +6 V, which is close to the V_T determined from the transfer scans. No dependence upon V_G is observed for the drain contact, or for either contact in the non-annealed device.

That it is apparently a by-product of the annealing process, suggests that X_{SOURCE} is related directly to the structure of the pBTTT near the contact interface, although it is unlikely to be due to an induced surface dipole as the observed spatial extent is much too large. Its apparent dependence upon V_G suggests that it is affected by the accumulation of charges within the channel, although the peak at 6 V is difficult to explain.

It is often assumed that the metal-organic contacts obey the Mott-Schottky (MS) model, wherein the contacts should be ohmic if the work function of the contact is close to the HOMO level (for a p-type material such as pBTTT) or the LUMO level (for n-type materials). If the work function difference is significant, then the resultant energy barrier strongly inhibits charge injection from the contact. The ionisation potential of pBTTT has been measured as 5.1 eV, suggesting that it should form a good contact with the gold source electrode, which has a work function of around 5.1 eV. Our measurements, and those of others, show that the contact resistance (of the

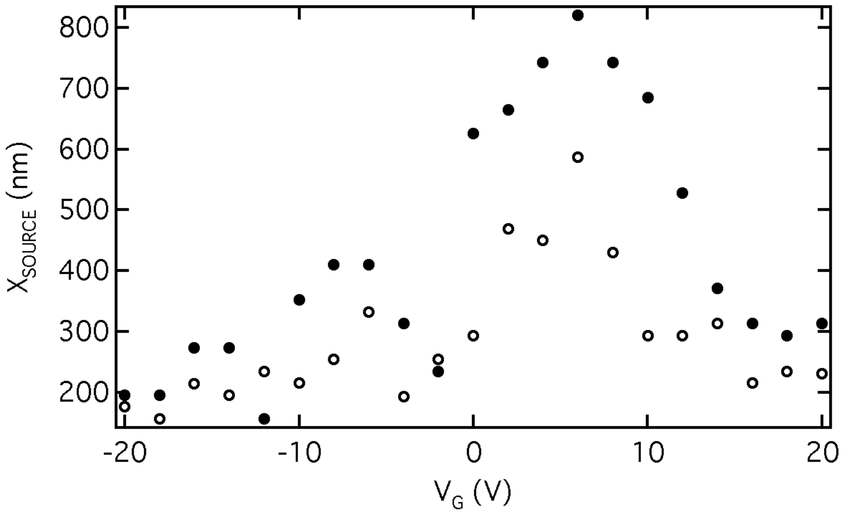

FIGURE 3.33: Estimated source contact width, X_{SOURCE}, for the annealed C_{16} pBTTT TFT with $V_D = 2$ V (open circles) and $V_D = 4$ V (closed circles). Both show a maximum at $V_G = 6\ V$.

order of 10 $k\Omega$ to 100 $k\Omega$) in the on region is much higher than the MS model would suggest.

One possible cause for the increased contact resistance is the formation of a contact dipole, in which the deposition of molecules on the contact surface can act to increase the effective work function of the metal, thus increasing the barrier to charge injection. This would also provide an explanation for the asymmetry between source and drain as charge extraction at the drain would not be hindered. A dipole barrier would not, however, explain the large spatial extent of the contact regions. It is possible that a dipole barrier is present at the contacts, along with some other effect producing the large contact regions. The as spun device shows neither the contact asymmetry nor the large spatial extent of the source contact region observed for the annealed device, suggesting that the annealing process itself is responsible for the formation of the contact regions. It is possible that the presence of the gold electrode hinders the ordering of the pBTTT layers, which are after all a factor of 20 thinner than the gold.

The spatial extent of the contacts also shows some variation with V_D and the KFGM output measurements discussed earlier reveal that this behaviour is not entirely straight-forward. Figure 3.34 shows the contact widths plotted against V_D for $V_G = 0\ V$, when the device is close to off. The source contact – the left contact for negative V_D and the right for positive V_D – is broader for all values of V_D. It also appears that the difference in contact width is much more pronounced when the left contact is made the source, suggesting a possible physical asymmetry between one side

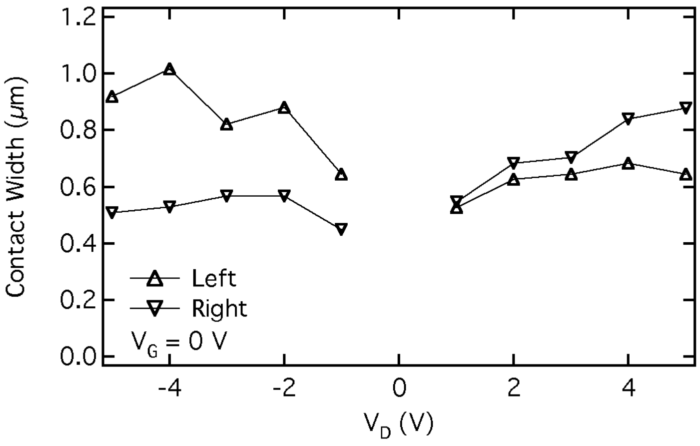

FIGURE 3.34: Estimated contact widths for the left and right contacts for $V_G = 0\ V$. The left contact is grounded.

of the channel and the other. It is also possible that this effect is linked to the differences in local gate created between positive and negative V_D.

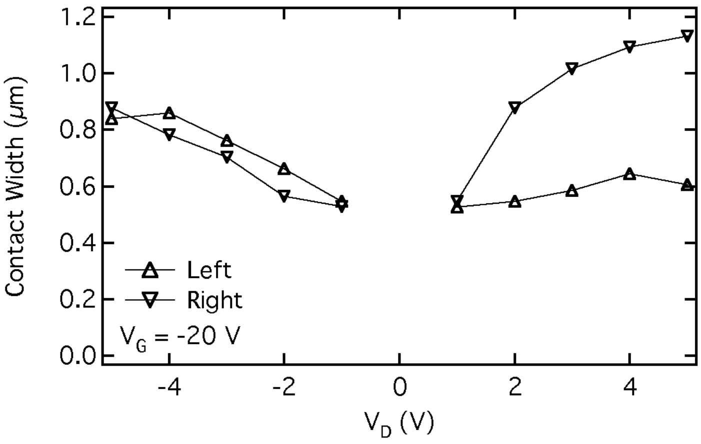

FIGURE 3.35: Estimated contact widths for the left and right contacts for $V_G = -20\ V$. The left contact is kept at 0 V

At $V_G = -20\ V$, as shown in Figure 3.35 when the device is more turned on, the effect seems to be reversed, with the biggest difference between source and drain occurring when the right contact is the source. The gate-dependence of the contact width is also apparent, with the right contact significantly increasing in width when it is made the source.

It seems likely that some variation in the underlying pBTTT layer near the contacts is responsible for the observed variation in contact widths. A strong contact-dipole may also be present, explaining the significant barrier to charge injection at the source, although the extent of this would be swamped by the variations in the pBTTT film. It seems unlikely that any kind of diode-like depletion region is responsible as the width is very large and we would expect such a region to be much narrower. We can also rule out any effect of local heating, as mentioned previously, due to the high potential dropped at the contacts, as this would tend to increase the mobility of the adjacent pBTTT by resistive heating and the contact region clearly shows an increased electric field and thus reduced conductivity at the contact edge.

3.5.5 The effects of measurement on pBTTT TFTs

Both the electrical measurements and KFGM data presented above were taken using a custom-built I-V set-up whilst the devices were inside the AFM chamber. Whilst the internal consistency of these results and their agreement with theory leaves us in no doubt as to their validity, there are some issues surrounding the measurement process and its effect on device performance that need to be addressed. Particularly, there is a factor of four drop in both linear and saturated on-current and mobility between a device measured in nitrogen before transport and when it is measured during the KFGM scan.

As mentioned previously, all of the pBTTT TFTs used in this work were produced and stored for the majority of their lifetimes in a dry nitrogen atmosphere. This is to minimise degradation due to ambient environmental factors, which can be a significant problem for TFTs made using polymers that are sensitive to oxidation, for example. Under nitrogen, the devices are stable over a period of many months. However, in order to transport them to the AFM laboratory and load them into the AFM chamber itself it was necessary to expose them to ambient conditions for short periods of time. The effects of both this exposure to ambient conditions and the measurement set-up used will be explored in this section.

In order to simulate the transport of a pBTTT device and exposure to ambient during preparation for KFGM, a test device was loaded into the transport container - a short length of sealed KF vacuum tubing - and left for 24 hours on the lab bench. It was subsequently exposed to air for 30 minutes to simulate loading into the AFM chamber. Transfer scans, shown in Figure 3.36, taken before and after this simulated transport show a drop in both linear and saturated on-currents of around 20%, as well as an order of magnitude increase in the off-current. However, the observed drop only accounts for around half of the drop in current and mobility that occurred during the experiments, so there must be another factor affecting device performance.

Currents in organic TFTs generally take a short time to reach equilibrium after the gate voltage is changed[98], so it is possible that differences in the speed of the

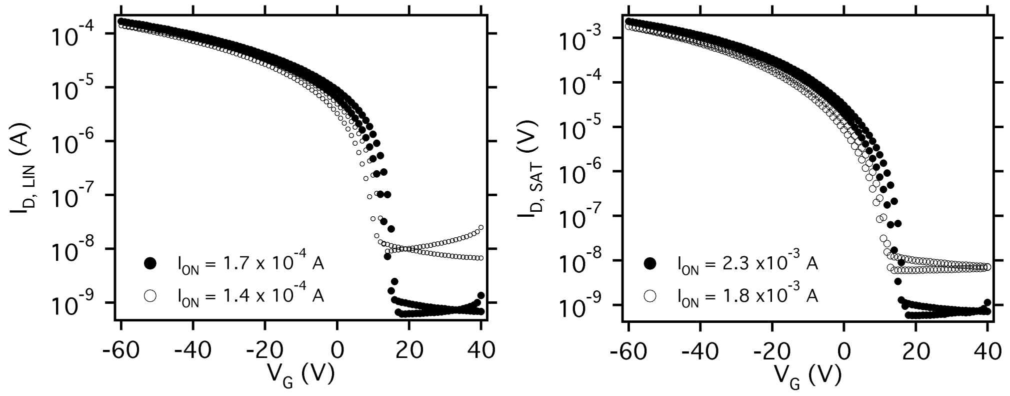

FIGURE 3.36: Linear and saturation transfer scans before (closed circles) and after (open circles) 30 minutes exposure to ambient conditions and 24 hours in simulated transit.

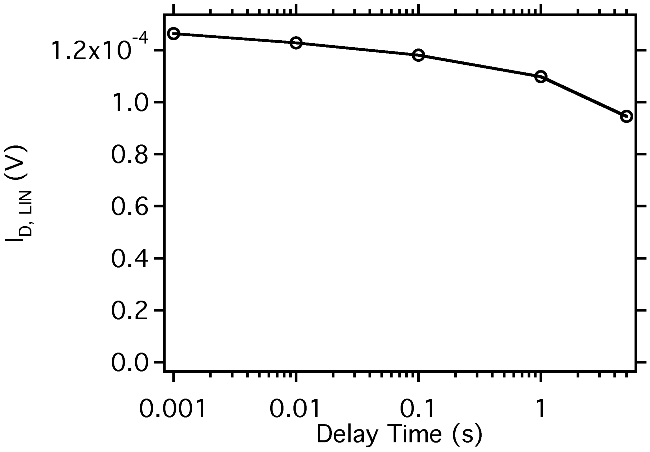

FIGURE 3.37: $I_{D,LIN}$ for a pBTTT TFT with increasing delay time. The drop in current between 1 ms and 5 s is around 25%.

measurements may be a factor although this is typically less than 10 ms. The typical period that V_G was held at each voltage point during a measurement using the Agilent 1455C parameter analyser was 20 ms and this timing was replicated using the AFM I-V amplifier. However, during the KFGM scan, the scan rate was typically 0.25 Hz, which is equivalent to a 4 s delay time at each voltage point. A series of transfer scans were taken with a pBTTT TFT mounted inside the AFM with increasing delay times. Figure 3.37 shows that the linear on-current drops by around 25% as the delay time is increased from 1 ms to 5 s. This can only account for around half of the observed drop in on-current between a standard transfer scan and a KFGM measurement, both taken using the same I-V amplifier. Whilst these measurement issues shouldn't be ignored, neither should they be understood as discrediting our conclusions. Our KFGM data remains internally consistent, agrees with our theoretical expectations and, despite the observed loss of current before and during the KFGM measurements, still follow “typical” OTFT device behaviour.

3.6 Conclusions from the pBTTT data

In this chapter, we began by confirming the lamellar structure of pBTTT observed elsewhere in the literature, with a molecular spacing that is consistent with AFM measurements for varying alkyl chain length. We can conclude from this that our pBTTT films have the same basic morphology as those described by Kline et al. and McCulloch et al. among others. This may not be surprising, but it should be pointed out that the AFM measurements involved in this are comparatively straightforward, allowing for the future prospect of profiling many devices in order to perhaps link morphology to device performance. The importance of image analysis methods was also highlighted, showing that the more localised estimate of terrace height provided by ROI analysis provides more precise values. By using KFGM, we also ruled out the existence of voids in the pBTTT film caused by de-wetting during deposition. This may only be a small detail, but it is illustrative of the additional information that may be obtained by EFM or KFM and no other techniques.

We have also provided tentative proof for the existence of domain boundaries within the pBTTT film, although they only appear strongly as the device is turned off and they only account for a small fraction of the total channel length. However we were able to show that they possess much greater resistivity than the bulk of the pBTTT film, another small but interesting detail that would have been missed by alternative techniques. The wealth of additional detail we may obtain from AFM and KFGM measurements is tantalising in itself, but where the KFGM in particular really comes into its own is in looking at the bigger picture of device performance.

In the work described above on pBTTT TFTs, we have described strongly internally consistent results indicating a pBTTT μ_{CHAN} that varies slowly with V_G but that is, unusually, four times higher in the linear than in the saturation regime. We have shown that the typical device behaviour observed for pBTTT TFTs where the saturation mobility is significantly higher than the linear mobility is caused by the dominance of the contacts in the linear regime, which actually masks the opposite trend in μ_{CHAN}. The KFGM data have allowed the extraction of μ_{CHAN} in the saturation regime, which has not been reliably reported elsewhere. We have also shown μ_{LIN} in our devices to be four times higher than μ_{SAT}, which is in stark contrast to results reported elsewhere. Whilst we are unable to determine the cause of this discrepancy, we can be confident that it is a true phenomenon, something we would have been unable to see without KFGM.

We have also shown much more detail about the behaviour of the local potential within the channel, placing an upper bound on the extent of any channel length modulation and observing an intriguing variation in the width of the contact regions with V_G. We may have been unable, in this case, to determine the mechanism behind the behaviour of the contacts or to come down firmly on one side or the other in determining the charge transport mechanism, but what we have clearly shown is the utility and versatility of KFGM as applied to OTFTs.

With just a single technique, and in the absence of temperature dependent mobility measurements or estimates of trap densities, we have produced valuable and publishable results. We are certain that the addition of KFGM to these and other techniques will provide a much fuller understanding of OTFT behaviour than was previously possible, particularly when applied to crystalline materials, which do not possess the uniformity of amorphous or semi-crystalline OSCs. In the following chapter we apply KFGM, along with other SPM techniques, to just such a material: TIPS pentacene.

Chapter 4

SPM Studies of TIPS Pentacene Thin-Film Transistors

This chapter discusses the deposition by zone-casting and characterisation by electrical and SPM techniques of TFTs made with the small molecule OSC 6, 13-bis (triisopropyl-silylethynyl) pentacene (TIPS pentacene) on a UV cross-linked organic gate dielectric. TIPS pentacene (Figure 4.1(left)) was developed by Anthony et al. [99] as a solution processable variant of the widely reported pentacene molecule, still generally used as the benchmark material in OTFTs. The solid state ordering of TIPS pentacene shows significant improvements over that of unsubstituted pentacene, adopting a 2-dimensional π-stacking arrangement (Figure 4.1(right)) as opposed to the "herringbone" arrangement of unsubstituted pentacene[100].

The 2-D ordering of TIPS pentacene, described by Anthony et al. as a "bricklayer" configuration stems from the tendency of the bulky solubilising groups to push as far apart as possible in the long axis of the pentacene. This has the advantage of reducing the packing distance in the π-stacking direction to lower than that for unsubstitued pentacene (3.47 Å as opposed to 6.27 Å. [99].) In the 10 years since its development, the TIPS pentacene molecule has been widely studied in organic TFTs so cannot be regarded as in any way state of the art. However, the wide body of literature and the easy availability of the molecule itself make it ideal for this work.

In section 4.1, we will describe the zone-casting technique as a method for producing relatively uniform long linear crystals from solution and cover the optical and electrical characterisation of the TIPS pentacene film. We determine the likely orientation of the TIPS pentacene molecules within the crystallites and demonstrate the device-to-device variation observed across one substrate. Following on from this, in Section 4.1.1 we show how KFGM can be used to differentiate between the conductinve and the non

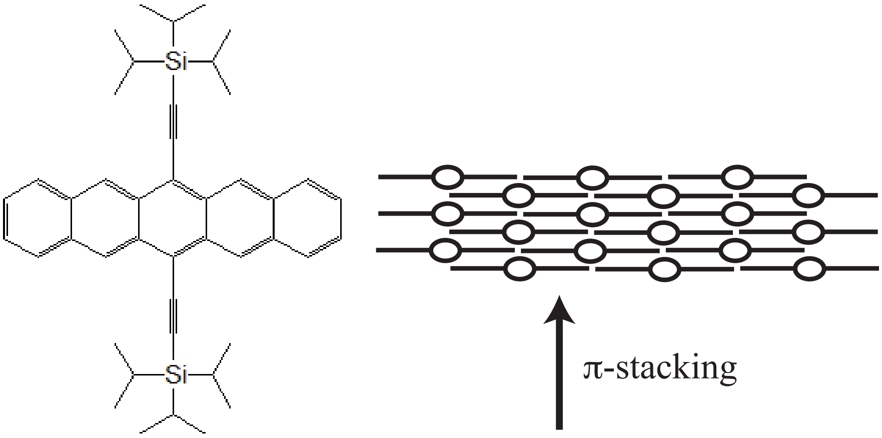

Figure 4.1: Structure of the TIPS pentacene molecule (left) and its crystal packing (right) as viewed along the short axis of the acene. The elipses represent the TIPS solubilising groups attached to the central benzene ring. The bulky TIPS groups interleave, allowing for close packing of the molecules and for each pentacene to π-overlap with two adjacent molecules. This allows for efficient $\pi - \pi$ stacking.

conductive regions of the film by observing the unscreened gate field in the latter. This result is confirmed by conducting-AFM mesurements showing that current is only carried in the linear crystallites themselves.

Section 4.2 covers the characterisation by KFGM of a complete TIPS pentacene TFT with a nominal W of 60 μm. The variations in the potential profiles between the different crystallites are investigated and it is found that the behaviour of the crystallites is far from uniform. We find that there are several distinct forms of the potential profile within crystallites and that some contain resistive physical defects. We also show that some crystallites may connect the source and drain by more convoluted routes, and not solely across the channel. Finally, preliminary scanned gate microscopy (SGM) measurements are presented that may correlate areas that are highly susceptible to local gating by a biased tip with areas of higher resistance. There is however a fundamental limitation of all the measurements in this section: the lack of a quantative measure of the current flowing through each crystallite.

This shortcoming is addressed in Section 4.3 in which a single crystal TIPS pentacene TFT is defined using the AFM to perform nano-lithography with $L = 17$ μm and $W = 5$ μm. Section 4.3.2 describes the electrical and KFGM measurements of the single crystal device, which exhibits a $\mu_{DEV,LIN}$ of 1.1 $cm^2V^{-1}s^{-1}$. The single crystallite is found to contain multiple regions with individual mobilities as high as 2.25 $cm^2V^{-1}s^{-1}$. These regions are shown to be present when either contact is the source, showing that they arise from the physical structure of the TIPS pentacene crystallite itself.

4.1 Zone-casting and morphology of TIPS pentacene on an organic gate dielectric

In the previous chapter, covering pBTTT TFTs, it was shown that on the length scale of a typical TFT (5-20 μm) liquid crystalline polymer films are effectively homogenous and isotropic. That is, the features observed within the films are at the sub-micron scale, well below the channel lengths and widths generally used in devices. Typical small molecule OSC films, on the other hand, may form crystals of up to many microns in length, which in deposition techniques like spin coating and flexographic printing can lead to significant anisotropy that often cannot be easily controlled.

Figure 4.2 is an optical microscope image of a bottom gate TIPS pentacene TFT spin coated at 1,500 rpm from a 2 wt% solution in mesitylene with 1% ethyl benzoate as co-solvent and a 4:1 ratio of TIPS pentacene to an inert polymer binder. The majority of the film consists of fine “feathery” crystals that form during the spinning process and which grow outwards from randomly distributed nucleation points and are up to 100 μm in width. The crystals themselves exhibit significant birefringence suggesting an ordered alignment of molecules whilst the darker material between the crystals appears disordered and does not exhibit any birefringence. The random distribution of both crystal size and disordered – and therefore probably less conductive – material is likely to cause significant device-to-device variation. Even within a single device, any extraction of material mobility is made impossible by the varying orientation of the crystallites within the channel

In region (a) of Figure 4.2 the crystallites cross the channel approximately perpendicular to the source-drain contacts, whereas in region (b) they are close to parallel to the contacts, and even curve back to rejoin the same electrode in some cases. Assuming that the π-stacking direction is related to the crystallite axis, we could expect significant differences in conductivity parallel and perpendicular to the crystallite long axis. Thus we can reasonably expect the mobility in regions (a) and (b) to be significantly different. It is this lack of homogeneity that makes determining the performance of TIPS pentacene in devices more challenging than that of pBTTT devices.

Zone-casting was first reported by Tracz et al. [101] in the manufacture of discotic liquid crystal OSCs and has been used elsewhere to deposit other OSCs.[102] It is of particular interest as it allows for the introduction of a significant degree of controlled film anisotropy and an increase in homogeneity. With this technique, as shown in Figure 4.3, the OSC formulation is deposited from a narrow slot at temperature T_S and speed S_S – controlled by a syringe – onto a substrate that is drawn beneath it on

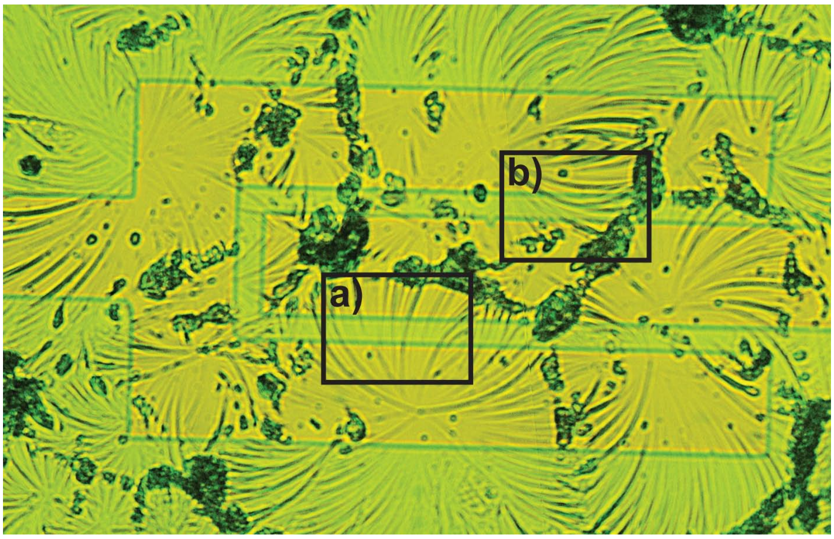

FIGURE 4.2: Optical microscope image of a spin coated TIPS pentacene TFT. The bulk of the film is formed of large disordered crystals consisting of crystallites growing radially from various nucleation points on the substrate. The crystallites in region (a) cross the channel approximately perpendicular to the contacts, whilst those in region (b) appear parallel to the contacts.

a table at temperature T_T and speed S_T. By varying T_S and T_T it is possible to control the evaporation rate of the solvent and by varying S_S and S_T, the volume of formulation deposited per surface area can also be controlled. If the many possible variations in formulation are taken into consideration - bulk solvent, co-solvent, total solids content and fraction of inert binder - then there is a vast parameter space to explore in order to optimise crystal growth.

Figure 4.4 shows a typical zone-cast TIPS pentacene device with channel length $L = 10\ \mu m$ and width $W = 1000\ \mu m$ zone cast from the same formulation used for the sample in Figure 4.2 onto a cross-linked organic gate dielectric with 40 nm thick gold source and drain electrodes. The casting direction is indicated on the image and it is clear that the crystallites grow exclusively within around 20° of the casting direction; that is the direction in which the substrate was scanned beneath the casting slot. In this case, the width of the crystallites varies from 5 μm to 15 μm. Also visible in Figure 4.4 are regular “knee”-like features along the edges of the crystallites. The observed irregularity in our TIPS pentacene crystals is in marked contrast to the much more homogenous crystals reported for zone-casting of discotic liquid crystal OSCs.[103] This may be caused by the different packing schemes for the molecules used, rather than any differences in equipment and processing. These features exhibit a constant angle relative to the crystal direction, suggesting that they are related to the crystal structure of the TIPS pentacene itself. They are also often associated with

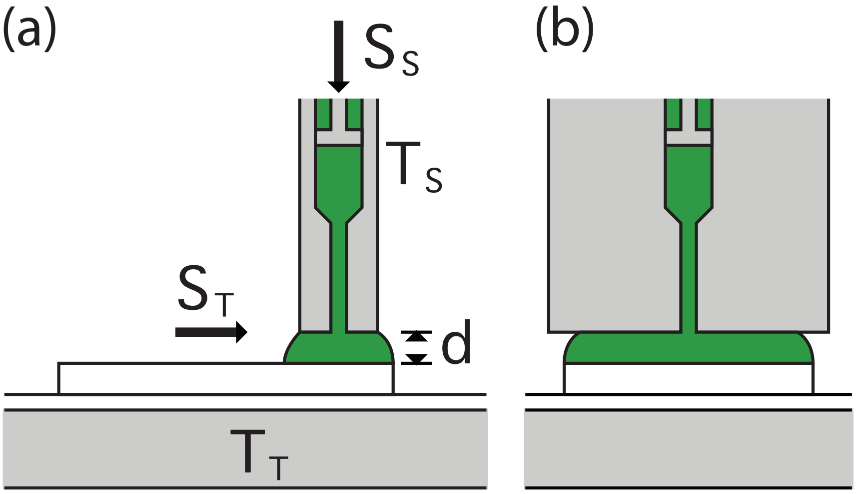

FIGURE 4.3: Schematic diagram of the zone-caster with side (a) and end (b) elevations shown. A syringe holding the formulation is kept at temperature T_S and pushed out at speed S_S, from a wide head. Generally S_S only needs to be sufficient to maintain a miniscus across the width of the substrate. The substrate is held at temperature T_T on the sliding table, which is moved under the head at speed S_T.

the edges of the source and drain contacts, which is to be expected as discontinuities in surfaces tend to strongly affect crystal growth in solution.

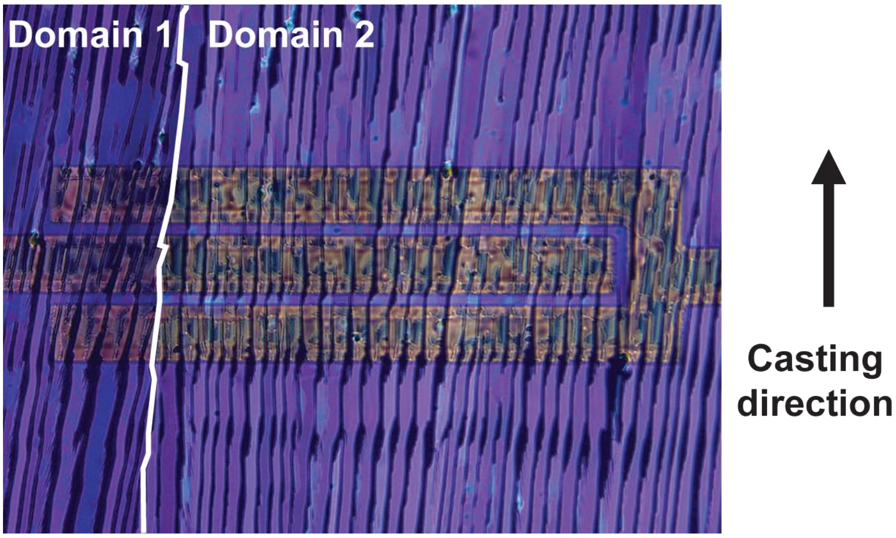

FIGURE 4.4: Optical microscope image of a zone-cast TIPS pentacene device with $W = 1000\ \mu m$ with the casting direction shown. The angle at which the crystals are deposited is typically within 20° of the casting direction. In this image, there are two domains with opposite molecular alignment indicated by their optical axes and the angle of the "knees" to the crystallite long axis.

Figure 4.5 shows an enlargement of a typical zone-cast TIPS pentacene film in which the crystallites run across a 10 μm TFT channel. Polarised optical microscopy of the film shows that the optical axis of the TIPS pentacene film is parallel and perpendicular to the “knee” features. The strong birefringeance exhibited by the TIPS pentacene crystallites confirms that the molecules are aligned parallel to one another as shown by Anothony et al. [99]. That the optical axis runs parallel to the ’knee’ features strongly suggests that the molecules are aligned parallel to these features. The “knee” features are formed at an angle of 50° to the long axis of the crystallites, so in this image the TIPS pentacene molecules are most likely aligned at an angle of 35° to the channel, which is not ideal assuming that charge transport is most efficient in the π-stacking direction.

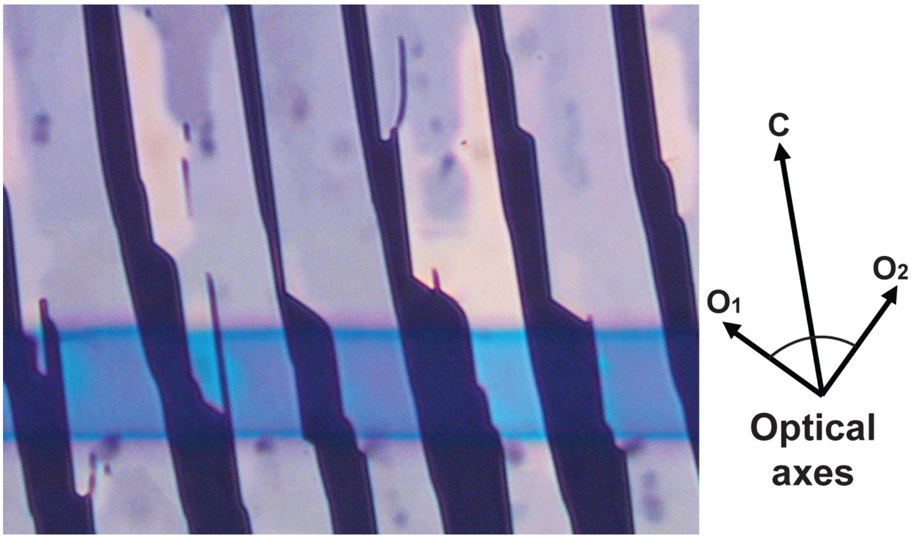

Figure 4.5: 100x optical microscope image of a zone-cast TIPS Pentacene device. The optical axes determined from polarised optical microscopy is shown as either O_1 or O_2, parallel with the “knee” features at the crystallite edges.

There are two possible configurations of crystallite, in which the molecules are aligned at 50° and −50° to the long axis. This behaviour is similar to that seen by Headrick et al. [104] in TIPS pentacene crystals deposited using the “hollow pen” method in which a capillary tube is used to drag a very small meniscus of OSC formulation across the substrate. The linear crystals produced bear some resemblance to our zone-cast crystals insofar as they have a very high aspect ratio. Importantly, by measuring μ_{DEV} parallel and perpendicular to the long-axis, they observed that the mobility was sometimes higher parallel to the deposition and sometimes higher perpendicular. They conclude that this is caused by two orthogonal molecular alignments relative to the deposition direction, as we have inferred from the optical images presented here.

The crystallites grow in domains of parallel molecular orientation, as shown in Figure 4.4, whilst the long axis for adjacent domains can vary by as much as ±20°. The very close alignment of the zone-cast crystallites within domains suggests that uniformity within the channels of individual devices should be greatly improved. However, individual devices may still contain two or three domains with differing orientation, so device-to-device variation is still an issue. Figure 4.6 shows the standard layout of devices on a one inch substrate as used thus far and for developing the techniques used later in this chapter. Each group of 22 devices (including one capacitor) shares a common gate line, labelled A - F and the channels run perpendicular to the gate lines. Typically zone-casting was performed with the casting direction parallel to the gate lines so that the crystals cross the channels as shown in Figure 4.4.

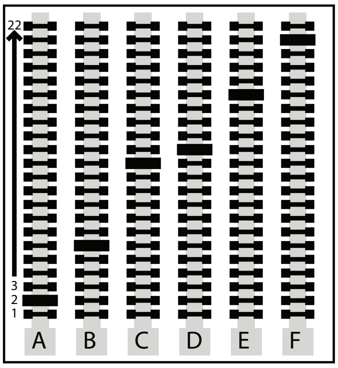

Gate lines: *A - F*

Devices: *1 - 22*
1: L = 20 μm
2: L = 10 μm
3: L = 50 μm
...
20: L = 10 μm
21: L = 50 μm
22: L = 20 μm

FIGURE 4.6: Schematic diagram showing the standard bottom gate device layout used in all of the preliminary zone-casting work discussed above. The one inch substrate consists of six common gate lines each with 22 devices alternating between $L = 10$, 20 and 50 μm and one capacitor pad. All of the devices have $W = 1,000$ μm.

Table 4.1 shows the linear mobility values extracted from the first 20 devices on gate lines B to E on a typical zone-cast substrate. In the table, capacitors are denoted by "–", whilst "NA" indicates a device that either shorted – due either to defects in the gate dielectric or gold contacting source to drain – or did not show transistor behaviour. The spread of mobility values is large, ranging from $\mu_{LIN} = 0.012$ to 0.496 $cm^2V^{-1}s^{-1}$. There is a tendency for the mobility to be higher towards the upper and right sides of the substrate.

This device-to-device variation in itself is not a problem for KFGM, as we have shown that the strength of the technique is in extracting the material performance from individual devices. The issue is simply the number of crystallites in each device. It would be prohibitively time consuming to determine whether the performance of every crystallite was identical, leaving aside the problem of multiple domains within a sample. As we show in the rest of this chapter, devices with narrower channel widths are required in order to attempt a realistic extraction of the material performance.

20 (10 μm)	NA	NA	NA	NA
19 (20 μm)	0.375	0.279	NA	NA
18 (50 μm)	0.436	0.343	NA	NA
17 (10 μm)	0.296	NA	0.286	–
16 (20 μm)	0.274	0.281	0.344	0.389
15 (50 μm)	0.141	0.304	0.432	0.496
14 (10 μm)	0.251	0.176	0.278	0.308
13 (20 μm)	0.140	0.221	–	0.354
12 (50 μm)	0.310	–	0.418	0.377
11 (10 μm)	0.123	0.225	0.327	0.226
10 (20 μm)	0.291	0.235	NA	0.050
9 (50 μm)	0.316	0.295	0.470	0.317
8 (10 μm)	0.216	0.232	0.332	NA
7 (20 μm)	0.252	0.232	0.324	NA
6 (50 μm)	–	0.193	0.349	0.305
5 (10 μm)	0.171	0.118	0.012	0.361
4 (20 μm)	0.107	0.063	0.216	0.288
3 (50 μm)	0.138	0.058	0.255	0.272
2 (10 μm)	0.086	NA	0.066	0.249
1 (20 μm)	0.103	0.054	0.085	NA
	B	C	D	E

Table 4.1: Linear mobility values for devices on a single 1 inch zone-cast substrate. There is significant variation in the mobility between devices. This is caused either by variations in the number and orientation of domains or by defects in the TIPS pentacene film.

4.1.1 Morphology of the zone-cast TIPS pentacene film

In the previous section the optical birefringence was used to determine that the long linear crystallites in zone-cast films of TIPS pentacene formulations are formed from the crystalline TIPS pentacene and not from the amorphous, and insulating, binder material. This assumption can be further confirmed by KFGM and other SPM techniques. Figure 4.7 is a KFGM image of a small region of the device shown in Figure 4.4 with the drain contact grounded and $V_S = 5\ V$, $V_G = 20\ V$. Parts of two crystallites can be seen in the image and there are significant differences between the two. The uppermost crystallite shows significant steps in the potential parallel to the optical axis, indicating fractures or boundaries between parts of the crystallite. The lower crystallite appears relatively homogenous with equipotentials approximately parallel to the source-drain contact edges. Such significant differences between two randomly selected crystallites are suggestive of significant variation between crystallites throughout the device.

In addition to demonstrating the differences between crystallites in the zone-cast TIPS pentacene film, Figure 4.7 also provides the first evidence that the material in between

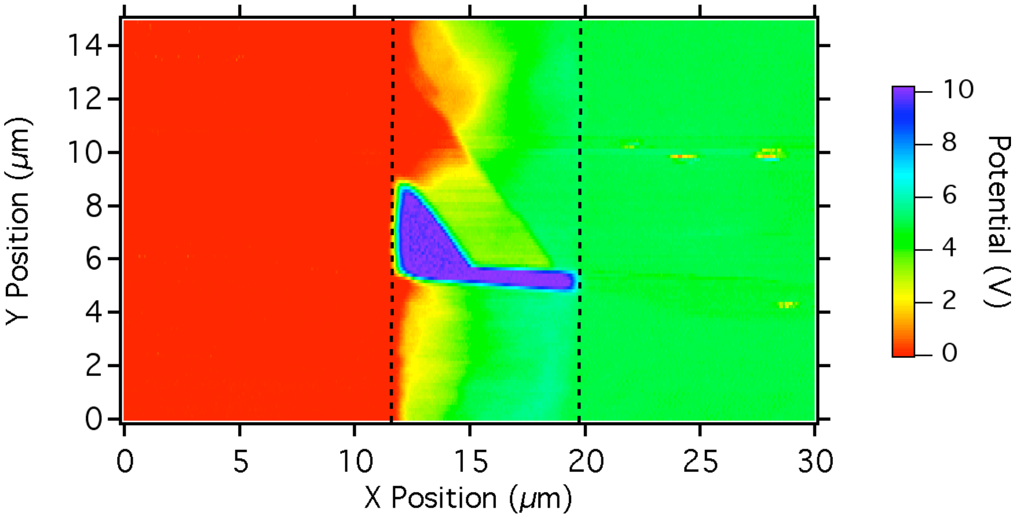

FIGURE 4.7: KFGM image taken of a small region of the channel of the device in Figure 4.4 with the channel indicated by the dashed lines. The drain (left) contact is held at 0 V whilst $V_S = 5\ V$ and $V_G = 20\ V$. The purple region between the two crystallites has a local potential of 10 V, which comes from the unscreened gate field.

the crystallites is indeed very highly resistive. The local potential at the surface of the TIPS pentacene crystallites varies smoothly between the values at the source and drain contacts, whilst the potential in between is around 10 V. This indicates that the KFGM is detecting the gate field through the dielectric, which would only be possible if there is no significant charge present at the dielectric interface to screen the gate. This strongly suggests that any material deposited between the crystallites is the inert polymer binder.

Figure 4.8 shows a conducting tip AFM (cAFM) image of a section of the channel of another TIPS pentacene TFT with $V_G = 0\ V$ and $V_{TIP} = -2.5\ V$. In cAFM a conducting tip is used in contact mode so that it is in electrical contact with the surface of the sample. A potential difference is applied between the tip and the sample and the resulting current is recorded. Thus, every point in the image represents the current flowing from the tip at that point to the source contact. It is difficult from our cAFM image to make any quantitative inferences about charge transport or crystallite structure, however, we can see that the current when in contact with the crystallites themselves is approximately 1 nA, whereas it is negligible in the areas between crystallites. This confirms our hypothesis that the crystallites are formed from the conductive TIPS pentacene with inert binder or dielectric in-between. We cannot speculate about the presence of binder beneath the crystallites from SPM imaging.

We should take a moment to discuss the image quality in Figure 4.8, as there are a number of imperfections present. The blank lines crossing the crystallites are most

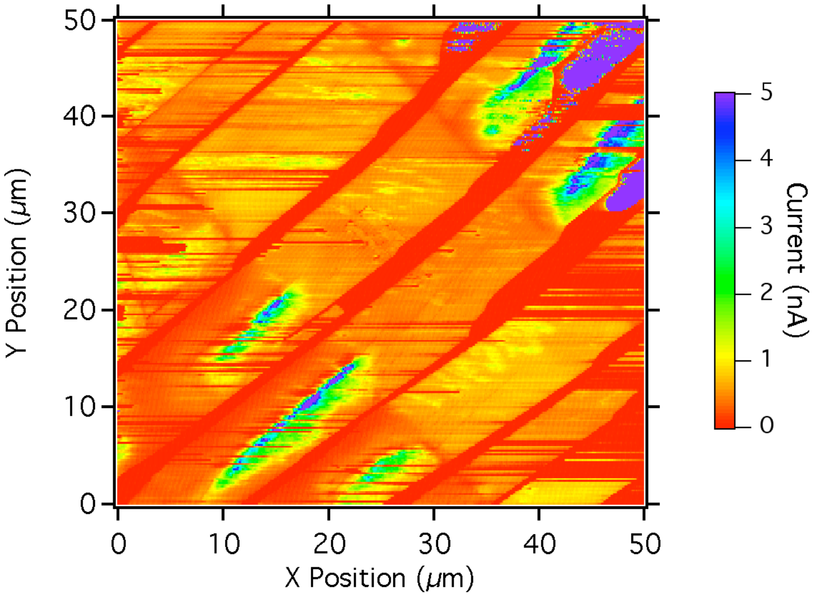

Figure 4.8: Conducting AFM (cAFM) image of a region of a TIPS pentacene device with a tip bias of $-2.5\ V$ and $V_G = 0\ V$. A current of 5 nA flows between the tip and the source contact whilst the tip is in contact with the crystallites, whilst the current in the regions between the crystallites is below the sensitivity of the current-voltage amplifier.

likely caused by the tip picking up material from the sample surface and dropping it elsewhere, temporarily increasing its resistance and thus reducing the current. This is a common problem when performing contact-mode AFM imaging of soft materials. The high-current artefacts over the contacts at the top-right and bottom-left of the image occur where the TIPS pentacene crystallites are thinner over the contacts, reducing the access resistance and allowing current to flow either directly into the source or from drain-to-source across the full width of the channel. Both of these will result in a much higher current flowing from tip to source.

4.2 SPM Measurements of a complete TIPS pentacene TFT

As was shown in the previous section, the TIPS pentacene films exhibit both significant inhomogeneity and anisotropy. Initial KFGM and cAFM images have shown that the areas between the crystallites do not contribute significantly to charge transport, at least when the device is in the on state. Thus, in any given device as much as 10% of the channel area – which may vary as a fraction of W across the channel – may be made up of non-conductive material. Whilst this does not pose a problem for measurements of device performance, it does increase the challenges of measuring the intrinsic mobility of TIPS pentacene itself. Whereas with pBTTT TFTs we could rely on uniformity over thousands of microns of channel width, any electrical measurements of TIPS pentacene will necessarily have to be local, that is we should be able to quantify where in the device the current is flowing.

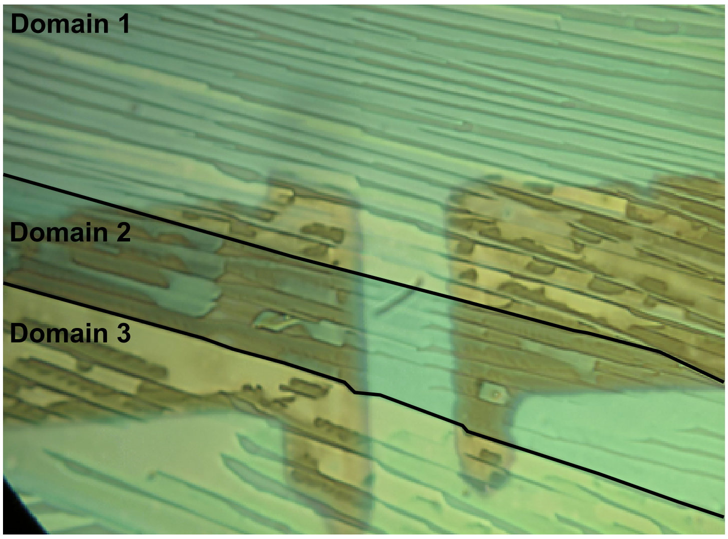

Figure 4.9: Optical microscope image of the TIPS pentacene device used in this section. Based on the known channel length of 20 μm, the width was estimated as 60 μm. The improvised nature of the shadow mask is clear from the irregular shape of the gold contacts.

The first step towards achieving this is to produce devices with dimensions small enough to be imaged by AFM in their entirety. To achieve this, an existing shadow mask was modified by hand to produce source-drain contacts with $L \approx 20\ \mu m$ and $W \approx 60\ \mu m$. Devices were then zone cast at 75 $\mu m/s$ onto bottom gate substrates so that the crystallites aligned approximately perpendicular to the channel.

An optical image of the device investigated in this section is shown in Figure 4.9. From a visual inspection there appear to be 13 crystallites crossing the channel at an angle of 19° to the channel edge normal, which is $\approx 20°$ away from the casting direction. Even with an estimated channel width of only 60 μm, this device exhibits three clear domains within the channel as distinguished both by the orientation of the "knees" and the associated optical axes. Domains 1 and 3, at the top and bottom of the channel as shown in Figure 4.9, show one orientation whilst domain 2, in the centre of the channel shows the perpendicular orientation.

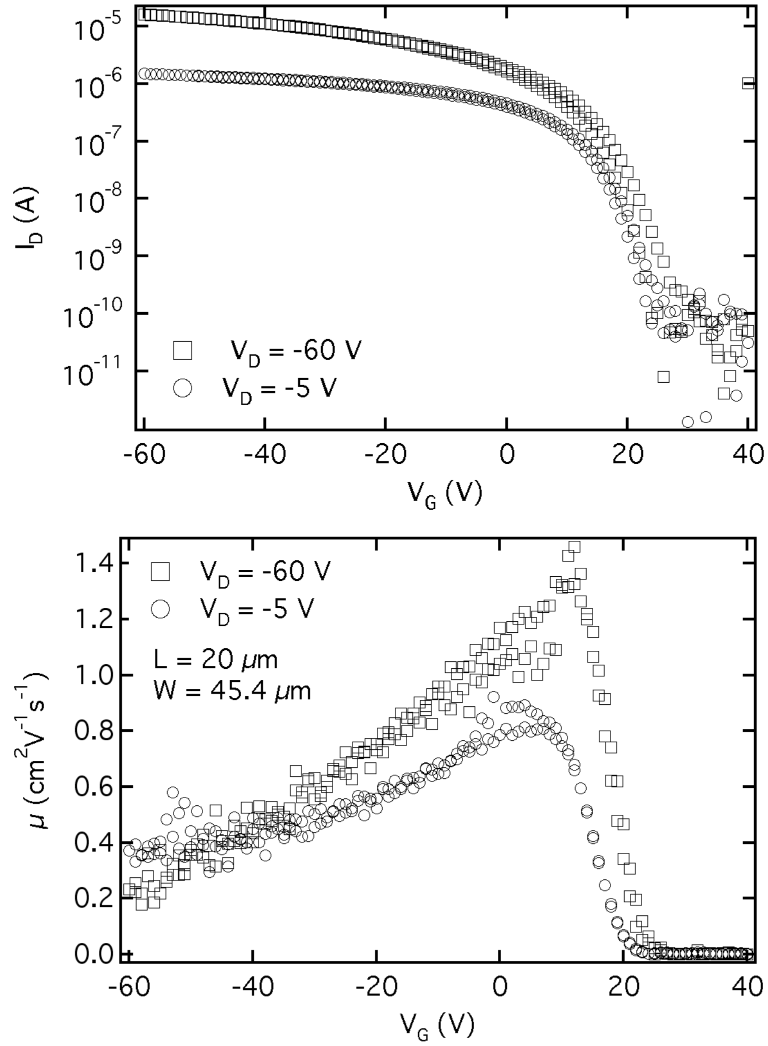

FIGURE 4.10: Linear and saturation transfer scans (top) for the TIPS pentacene device used in this section. V_T = 15.9 V in the linear regime and 20.6 V in saturation as estimated from linear fits to $I_{D,LIN}$ and $\sqrt{I_{D,SAT}}$ respectively. The corresponding mobility values (bottom) calculated from the transfer scans give peak values of 0.9 $cm^2V^{-1}s^{-1}$ in the linear regime and 1.4 $cm^2V^{-1}s^{-1}$ in saturation.

The optical image reveals several important details about the morphology of the device that will affect our estimates of the mobility. First, the contact edges are not smooth. There is a variation of around 1 μm in L across the width of the channel, meaning that the crystallites may have different effective L. However, these variations are only around 5% and will tend to average out over the whole device. The second detail is that, assuming only the contacted crystallites conduct, the effective W as measured across only those crystallites that contact both source and drain is actually only 50 μm, a reduction of 10 μm or 17%.

The third feature we must account for is that there are voids between the crystallites, which are more pronounced at the right contact edge. Assuming that the material between the crystallites does not conduct, a further adjustment must be made to W. In this device, removing the voids — at their widest points — from the channel width gives us an effective channel width of $W_{EFF} = 45.4 \mu m$, which is only 75% of the real width of the contacts. Finally, the crystallites are at an angle of 19° away from the direction of L, which has the effect of increasing the effective channel length from 20 μm to $L_{EFF} = 21.14$ μm. It is these new values of L and W that must be used in our calculations if we are to arrive at materially relevant values for μ_{LIN} and μ_{SAT}.

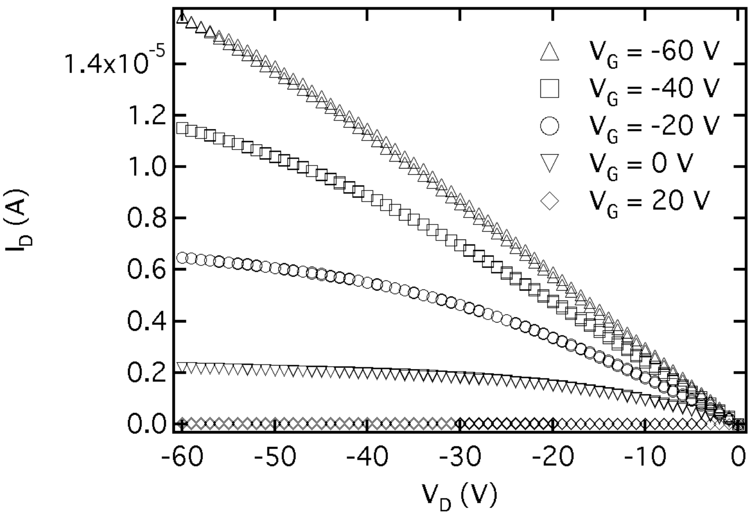

FIGURE 4.11: Output scans taken for 20 V intervals of V_G. The device does not fully saturate. In this case, $L = 20$ μm and the dielectric thickness, d is 1 μm. In terms of L/d, the ratio is very similar to that for the pBTTT devices described earlier.

The linear and saturation transfer scans and mobility calculated using L_{EFF} and W_{EFF} for the device shown in Figure 4.9 are presented in Figure 4.10. The measurements were taken under flowing nitrogen in the AFM stage immediately prior to AFM and KFGM measurements. The peak mobility values calculated from the transfer data are higher than any previously achieved in this work, $\mu_{LIN} = 0.9$ $cm^2V^{-1}s^{-1}$ and $\mu_{SAT} = 1.4$ $cm^2V^{-1}s^{-1}$. Unlike many of the pBTTT devices measured in the previous chapter, this TIPS pentacene device also exhibits a low hysteresis between the forward and reverse V_G sweeps. The gate leakage through the organic dielectric in this batch of devices was also very low, approximately

5×10^{-9} A at $V_G = -60$ V, corresponding to an electric field of up to 60 V/μm across the organic gate dielectric. This value represents around 3% of $I_{ON,LIN} = 1.5 \times 10^{-6}$ A. Output scans for the same device (see Figure 4.11) show fairly typical OTFT performance, although even in this longer channel TFT the current does not begin to saturate where we would expect.

Figure 4.12 shows the tapping mode AFM image of the same device, with the edges of the contacts - as estimated from the optical image – drawn in white. Even without the information from the optical images, the position of the contacts is indicated by lumps in the TIPS pentacene crystallites. Whether these are formed by increased thickness of the TIPS pentacene itself, by the binder, or – least likely – by underlying features of the organic dielectric or the evaporated metal cannot be determined from the AFM. The height of the crystallites is approximately 50 nm as estimated from Figure 4.12, which is comparable to the thickness of films spin-coated from formulations with a similar solids content.

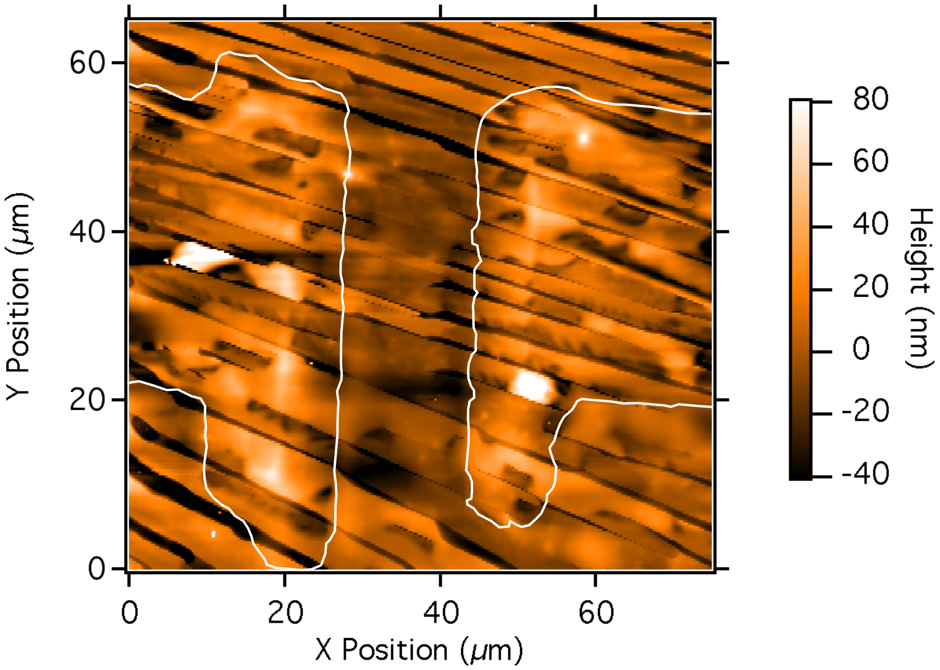

FIGURE 4.12: 75 μm tapping mode AFM topography image of the whole device with the outline of the contacts shown in white . Whilst the contacts are much more clearly visible in the optical in Figure 4.9 the raised contact regions can still be identified beneath the TIPS pentacene crystallites. Many of the features within the crystallites are also visible in the topography image. All of the crystallites crossing the channel can be clearly identified in both images.

Figure 4.13 is a KFGM image of the same device with $V_G = -40$ V and $V_D = -5$ V. From the potential map, it appears that there are 13 crystallites crossing the channel — as suggested by the optical image — and one further crystallite (labelled crystallite

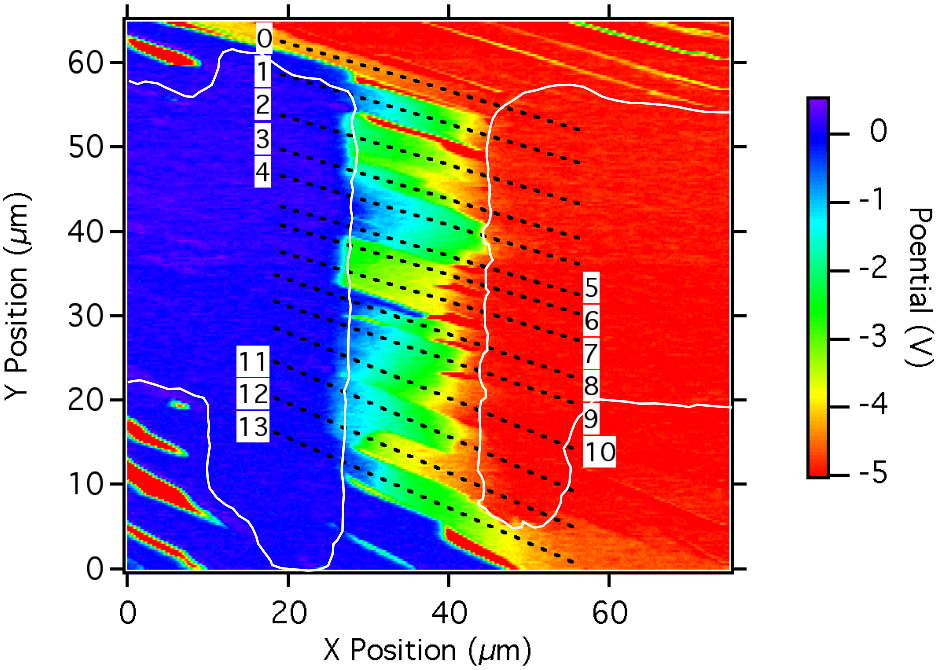

FIGURE 4.13: 75 μm KFGM potential image taken at 0.1 Hz with V_G = -40 V and V_D = -5 V with the outline of the contacts shown in white. The source (grounded) contact is on the left of the image. From this image it is easy to determine which crystallites are connected to the contacts and which are not as there is significant contrast between the two contact potentials. Numbers 1 - 13 have been assigned to the crystallites that cross the channel.

0) that appears to be partially contacted to the source (left) contact, as indicated by the gradual potential drop across it. Of the fully contacted crystallites, the image suggests that different crystallites drop the bulk of the applied potential at different positions within the channel. For example, crystallite 10 clearly drops more potential in the centre of the channel whilst its neighbours drop more at the drain contact edge.

Figure 4.13 is one of a series of KFGM potential images that were taken of Device 1 with V_G = 0, -20, -40 and -60 V and V_D = -5 V. Potential line-scans were extracted parallel to the crystallite long axis – as indicated by the dashed lines in Figure 4.13 – for each of the 13 crystallites crossing the channel and for crystallite 0 at each voltage. Due to problems with the KFGM imaging, line-scans for V_G = -60 V could only be extracted for crystallite 1 and for crystallites 3 to 7. The line-scan for crystallite 1 at V_G = 0 V is also truncated due to an error in positioning the AFM. Given the time taken to produce the images and the possibility of device degradation during imaging it was decided not to repeat the missing images for Device 1. In this case, the loss of these data points does not diminish the overall picture of the device performance.

In addition, one KFGM image was taken, covering crystallites 1 to 5 with V_G = -60 V and V_D = +5 V. This image provides a comparison of the potential drops across the channel when the source and drain contacts are reversed. This should allow us to confirm whether the features observed in the potential are related to charge injection from the source contact side of the channel or whether they are confined to localised areas of the crystallites, which would indicate local variations in conductivity.

The extracted line-scans across all the measured voltages are shown in Figures 4.15, 4.16 and 4.17 in the following sections. For each crystallite, all the available line-scans for $V_D = -5\ V$ are presented with additional plots showing the potential line-scan for $V_D = +5\ V$ and also the estimated resistance of selected regions of the channel. Where practical, the line-scans were divided into regions of constant conductivity, labelled "R" with linear fits shown, and regions with sharp potential drops indicating a resistive barrier, labelled "V." Some regions within crystallites, such as the 7 μm adjacent to the drain (right) contact of crystallite 3 could not be fitted with a linear. This was also the case for the whole of crystallites 8 and 13.

The crystallites have been grouped by Domain, as determined from their optical axes and shown in Figure 4.9, as it was initially assumed that the electrical behaviour of the crystallites would be Domain dependent. Whilst there may be some very general similarities between the crystallites within each domain, the variation between individual crystallites tends to be higher. Estimates of resistance were calculated assuming that the total current is split evenly between the 13 crystallites, allowing for a small estimated current flowing in crystallite 0.

4.2.1 Contribution of crystallite 0 to Device 1

Crystallite 0, shown in Figure 4.13, completely overlaps the right contact and appears to be electrically connected to it. It does not, however, overlap or appear to connect directly to the left contact. The potential profile parallel to the long-axis in crystallite 0 is shown in Figure 4.14. Studying both the KFGM and optical images, it seems most likely that crystallite 0 makes contact with crystallite 1, over 100 μm to the left the channel edge. There is one possible point of contact with crystallite 1 immediately above the edge of the left contact and there may be a change of the potential gradient associated with this, although the level of noise makes this impossible to confirm.

The potential gradient estimated from a linear fit – shown in Figure 4.14 – is 0.026 $V/\mu m$. Assuming that the gradient remains constant and that there is no significant resistive barrier at the far end of crystallite 0, the point of contact can be estimated to be 193 μm away from the drain contact. If the conductivity of the TIPS pentacene is uniform – which is a major assumption – then we might expect the resistance of Crystallite 0 to be 9.6 times higher than any of the crystallites crossing

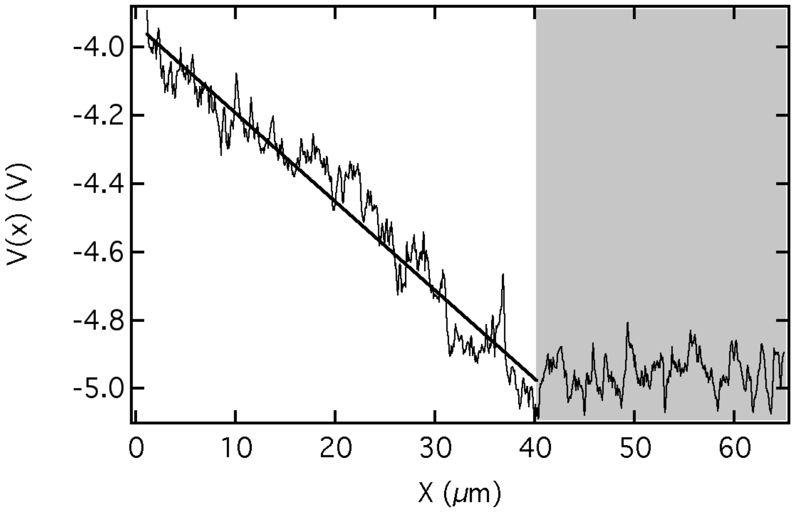

Figure 4.14: KFGM potential line-scan extracted parallel to the crystallite long-axis for crystallite 0 of Device 1, as indicated in Figure 4.13. There is no significant potential drop associated with the contact at $X = 40\ \mu m$. The potential to the left of the drain contact has been fitted with a linear, gradient $= 0.026\ V/\mu m$ (heavy black line).

the channel, which would lead to a current flow 9.6 times lower than in any other individual crystallite. If this is the case, then the contribution of crystallite 0 to the total current passing through the device is around 0.8% at $V_G = -40\ V$. This estimated contribution is accounted for in later discussions of the crystallite potential profiles.

There is a similar long range potential drop associated with crystallite 13 as it passes the right contact at the bottom of Figure 4.13. In this case, it appears as though crystallite 13 makes contact with an adjacent crystallite, which connects it to the back side of the contact. This will be taken into account in the discussion of Domain 3.

4.2.2 Potential line-scans of crystallites in Domain 1 of Device 1

The potential line-scans for the crystallites in Domain 1 are shown in Figure 4.15. Various crystallite behaviours are present within this domain. Crystallite 1 exhibits no potential drop at the source (left) contact and contains two regions, $R1$ and $R2$ that are well fitted by a linear. The resistance values calculated using the current estimated above (Figure 4.15 inset (b) for all crystallites) show that, whilst $V_G < 0\ V$, the resistance of $R1$ ($W = 16.8\ \mu m$) remains approximately a factor of two higher than that of $R2$ ($W = 3.4\ \mu m$). Since most of the potential is dropped in $R1$ – $2.87\ V$ at $V_G = -20\ V$ compared to $1.33\ V$ in R2 – it will have the greatest influence on device performance. However, the difference in width results in the conductivity of $R2$ being around a factor of four lower than that of $R1$. The line-scan taken with $V_D = +5\ V$

(Figure 4.15 inset (c) for all crystallites) shows a region of lower conductivity corresponding to R2. Interestingly, there appears to be a further subdivision of $R1$ into regions of differing conductivity with $W = 6.1$ and 10.7 μm respectively.

Crystallite 2 can be divided into a potential drop $V1$ at the source contact and the channel region $R1$. Aside from some deviations for $V_G = 0$ V, the potential along the channel is well approximated by a linear fit. The potential drop at $V1$ accounts for approximately 40% of the total potential across the channel. The line-scan for $V_D = +5$ V does not show such a pronounced potential drop at the left contact. There is, instead, a broader region of reduced conductivity extending for approximately 2.5 μm into the channel.

Crystallite 3 exhibits a sharp potential drop, $V1$, at the source contact, accounting for 1.7 V of the dropped potential. Immediately adjacent to $V1$ is a region 3 μm wide with a much higher conductivity than the rest of the channel, which drops less than 0.1 V. In the centre of the channel is a region, $R1$, with a constant conductivity ($W = 10$ μm). The 7 μm of the channel adjacent to the drain contact shows either a small potential drop and a region of higher conductivity or a region with variable conductivity. It is difficult to tell from the negative line-scans which is the case. The line-scan for $V_D = +5$ V shows a potential drop equivalent to $V1$ at the source (right) contact with an associated region of higher conductivity. The region $R1$ is still well defined, whilst the region adjacent to the left contact shows a similar potential profile to the region next to the right contact in crystallite 3(a).

Although the data is limited, we might infer that the channel in crystallite 3 is divided into 3 regions: the two regions adjacent to the contacts, which appear to behave as a traditional OTFT channel with a significant barrier to charge injection at the source and a central region, $R1$, with a gate dependent conductivity. One might model such a crystallite as three channels in series with a common V_G.

The final crystallite in Domain 1, crystallite 4, is more similar to crystallite 1 than to the others. There is a small potential drop at the source, a region, R1, of constant conductivity ($W = 16$ μm) and a large potential drop, V1, at the drain contact. In this case, the contributions of R1 and V1 are very similar, showing similar values for the estimated resistance. The positive line-scan shows that the potential drop is clearly associated, not with the polarity of the source and drain, but with the right contact itself. The AFM data shows what appears to be a very fine crack in this crystallite at the same position as the potential drop, so this is the most probable explanation for the high contact resistance.

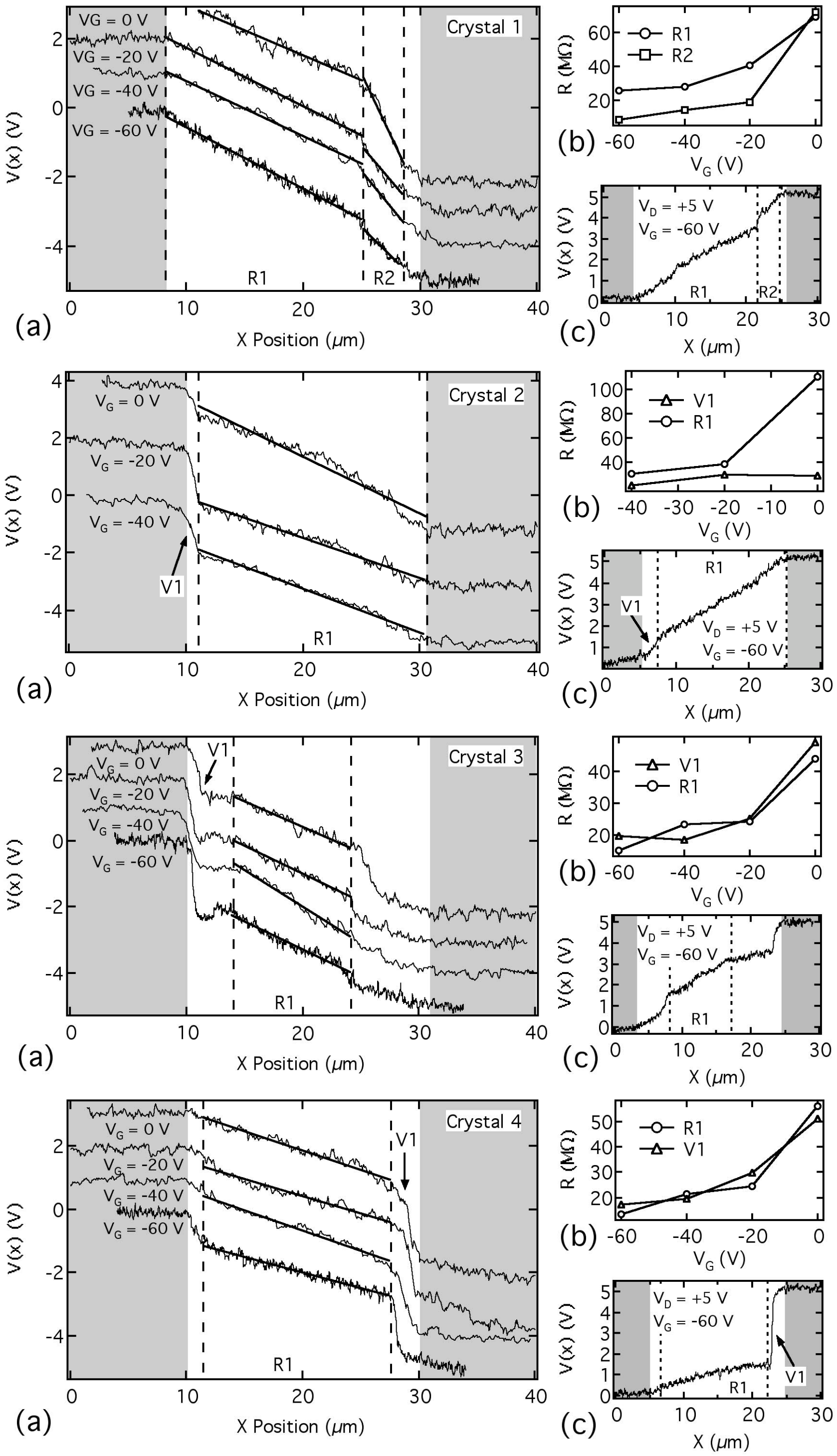

FIGURE 4.15: KFGM potential line-scans extracted from the images of the whole device taken at varying V_G for the crystallites in Domain 1 (a) along with the estimated resistance of selected regions of the channel (b) and the potential line-scan for V_D = +5 V (c). Crystallites 2 and 3 show pronounced potential drops at the source (left) contact, whilst crystallite 4 drops the bulk of V_D at the drain (right) contact. Crystallite 1 does not exhibit sharp potential drops at either contact, instead having two regions with differing conductivity. Where possible, the potential lines have been broken into regions, either with different linear slopes or sharp potential drops.

Within Domain 1 we have already seen a range of different electrical behaviours within the crystallites. Crystallite 1 contains two domains of varying conductivity and shows no significant contact resistance. Crystallite 2 has a contact resistance associated with the left contact regardless of source-drain orientation. Crystallite 3 may contain as many as three domains and shows a pronounced contact resistance associated with the source contact. Finally, crystallite 4 is dominated by contact resistance at the right contact, associated with a defect in the TIPS pentacene crystal. From four crystallites we have already observed four different behaviours

4.2.3 Potential line-scans of crystallites in Domain 2 of Device 1

The six crystallites that make up Domain 2 in Figure 4.16 are as varied as those described in Domain 1, although there are some features that these crystallites have in common. For example, crystallites 5, 6, 7 and 9 each have a region near the right contact with lower conductivity that tends to dominate when V_G is close to V_T. Crystallites 6 and 7 show a very strong potential drop at the left contact whilst crystallites 8 and 10 show no significant potential drop at either contact.

The behaviour of crystallites 5 and 9 is so similar that, despite their spatial separation, they can be discussed together. Each has a region, $R2$, at or close to the drain contact that is of much lower conductivity than the bulk of the channel, $R1$. This region has a similar extent in both crystallites – 2.8 μm in crystallite 5 and 3.1 μm in crystallite 9 – and, given the similar slope of the potential profiles, similar values for the resistance, varying by less than 20% for $V_G = 0$ to $-40\ V$. $R2$ in both cases also initially provides the greatest contribution to the total resistance of the device, falling below the resistance of $R1$ for more negative V_G. The line-scan for positive V_D in crystallite 5 shows the same regions with similar sizes and slopes. No comparable line-scan was taken for crystallite 9 but it is likely to be the same due to morphology rather than source-drain polarity. The fact that crystallites 5 and 9 are separated by three adjacent crystallites and spatially by 9.9 μm rules out any electrical connection between them that might explain the similarities.

Crystallites 6 and 7, on the other hand, are immediately adjacent to each other with a surface topography that implies they are in physical contact. The potential profiles are almost identical, further suggesting that crystallites 6 and 7 may behave as a single unit. Here they have been treated separately as they join the drain contact separately. Both show a strong potential drop, V1, at the source contact for all negative values of V_G and can be split into two regions; $R1$ in the bulk of the channel and $R2$ near the drain contact. The widths of $R1$ and $R2$ vary by less than 0.5 μm between the two

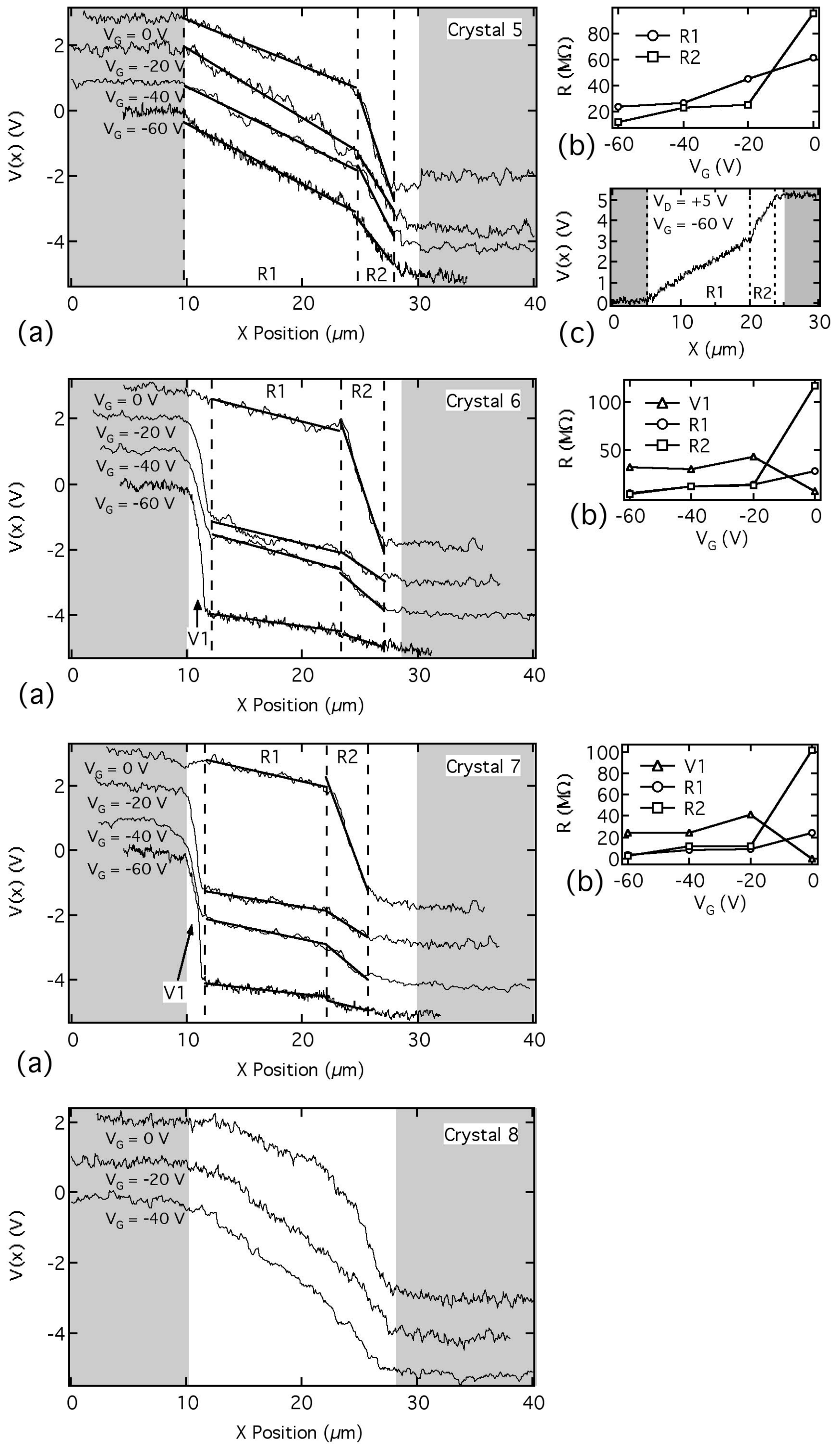

FIGURE 4.16: KFGM potential line-scans extracted from the images of the whole device taken at varying V_G for the crystallites in Domain 2. Continued on following page.

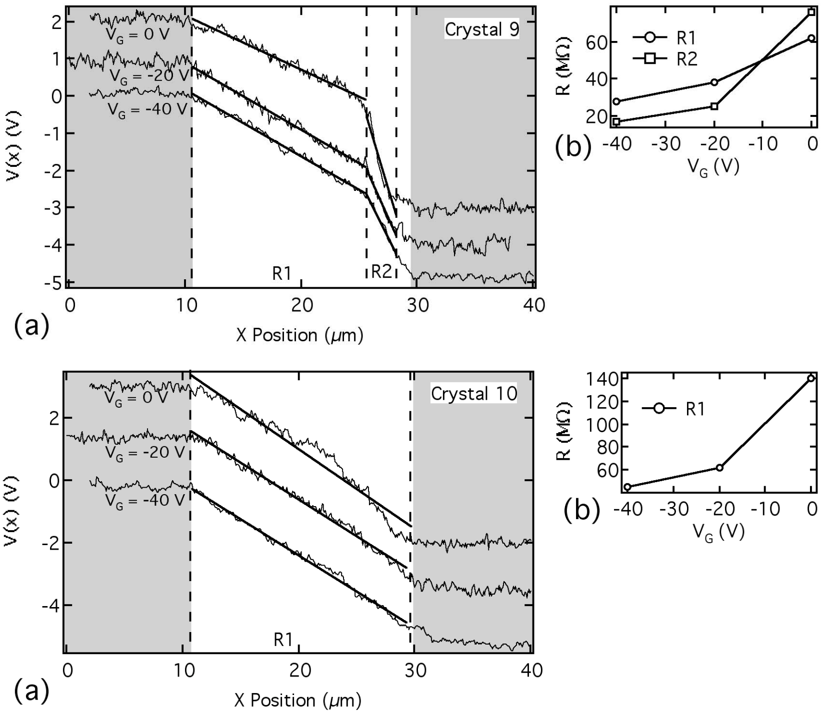

FIGURE 4.16: Here, crystallite 10 shows a linear potential profile across the channel with no obvious contact resistances. Crystallites 5, 6, 7 and 9 can be divided easily into regions R1 and R2 with R2, near the drain (right) contact, having a width of $2.5 - 4\ \mu m$. Crystallites 6 and 7 also exhibit a very strong potential drop at the source (left) contact, accounting for as much as 75% of the potential dropped. The potential profile of crystallite 8 is the only one not easily separable into linear regions. The potential profile here more closely resembles that of a device operating in saturation, as discussed in the previous chapter.

crystallites and their behaviour is the same. The resistance of $V1$ is initially effectively 0, rising to a fairly constant value for negative V_G. The resistance of $R2$ is around five times $R1$ at $V_G = 0\ V$, and drops to almost the same value as $R1$ for negative V_G. These two crystallites, whilst clearly separate at the drain contact have appear to have grown together such that they are so well connected they behave as one entity. This fact is further confirmed by the lack of any visible potential steps along the region where the crystallites are in contact.

Crystallite 8 is something of an odd one out in Device 1 as the potential profile within the channel more closely resembles that of a TFT operating in the saturation regime. The slope of the potential varies smoothly from source to drain contact, suggesting a conductivity that varies with position, and with a more pronounced curvature when V_D is closer to $V_G - V_T$. However, the device should be operating in the linear regime, as evidenced by the linear potential profiles observed in most of the other crystallites. Attempts were made, using the models described in the previous chapter, to fit this supra-linear potential profile, however none returned a good fit with plausible fitting parameters V_T and μ_{LIN}.

Crystallite 10 shows a linear, or close to linear, potential drop across the channel for all values of V_G and no sharp potential drop at either contact. The slope of the potential varies by less than 10% as V_G is increased so the resistance is determined by V_G. Aside from some deviation from the fit for $V_G = 0\ V$, crystallite 10 appears to be an ideal TFT showing no contact resistance at all.

Again, within a small number of crystallites we have observed a wide range of electrical behaviours, although for crystallites 6 - 10 we have no line-scans for positive V_D so cannot determine, for example, whether the high contact resistances at the left contact in crystallites 6 and 7 are caused by the polarity of the source and drain contact or by some physical defect in the TIPS pentacene crystal itself.

4.2.4 Potential line-scans of crystallites in Domain 3 of Device 1

Finally, we discuss the three crystallites from Domain 3 that cross the channel, shown in Figure 4.17. These crystallites are also very varied, exhibiting three distinct behaviours in their potential profiles. Crystallite 11 resembles crystallites 5 and 9 in the general shape of the potential, with some key differences. Crystallite 12 is the most complicated in the whole device in terms of fitting the potential profile if not in its general behaviour, whilst crystallite 13 is possibly the most difficult to categorise.

As mentioned above, crystallite 11 is split into two linear regions, analogous to crystallites 5 and 9. The bulk of the channel makes up a higher conductivity region R1, whilst the 2.4 μm adjacent to the drain contact makes up the lower conductivity R2. Unlike crystallites 5 and 9, the resistance of R1 initially dominates the device performance. The behaviour of the resistance values is similar to Crystallites 5 and 9 for negative V_G with the fractional potential dropped in both regions remaining almost the same.

Dividing crystallite 12 into linear regions and sharp potential drops is no more challenging than the others, excepting that there are more of them. In this case there is a region, R1, adjacent to the source contact with a width of 4.5 μm and a linear potential drop followed by a potential drop V1. To the right of V1 are two further regions with linear potential drops; the lower conductivity R2 ($W = 3\ \mu m$) and higher conductivity R3 ($W = 10.7\ \mu m$). At $V_G = 0\ V$, R2 makes the greatest contribution to the total resistance of the crystallite, followed by R3 and then V1 and R1. As V_G is increased, the resistances of the various regions move closer together, differing by less than 20% at $V_G = -40\ V$.

Crystallite 13 is the most difficult to categorise since it looks divisible into sections with similar behaviour with varying V_G but these regions show varying curvatures. It is also difficult to determine the position of the drain contact in the line-scans for crystallite 13 as it most likely connects to the adjacent crystal and then to the back side of the right contact. This makes determining the effective width of the crystallite very difficult.

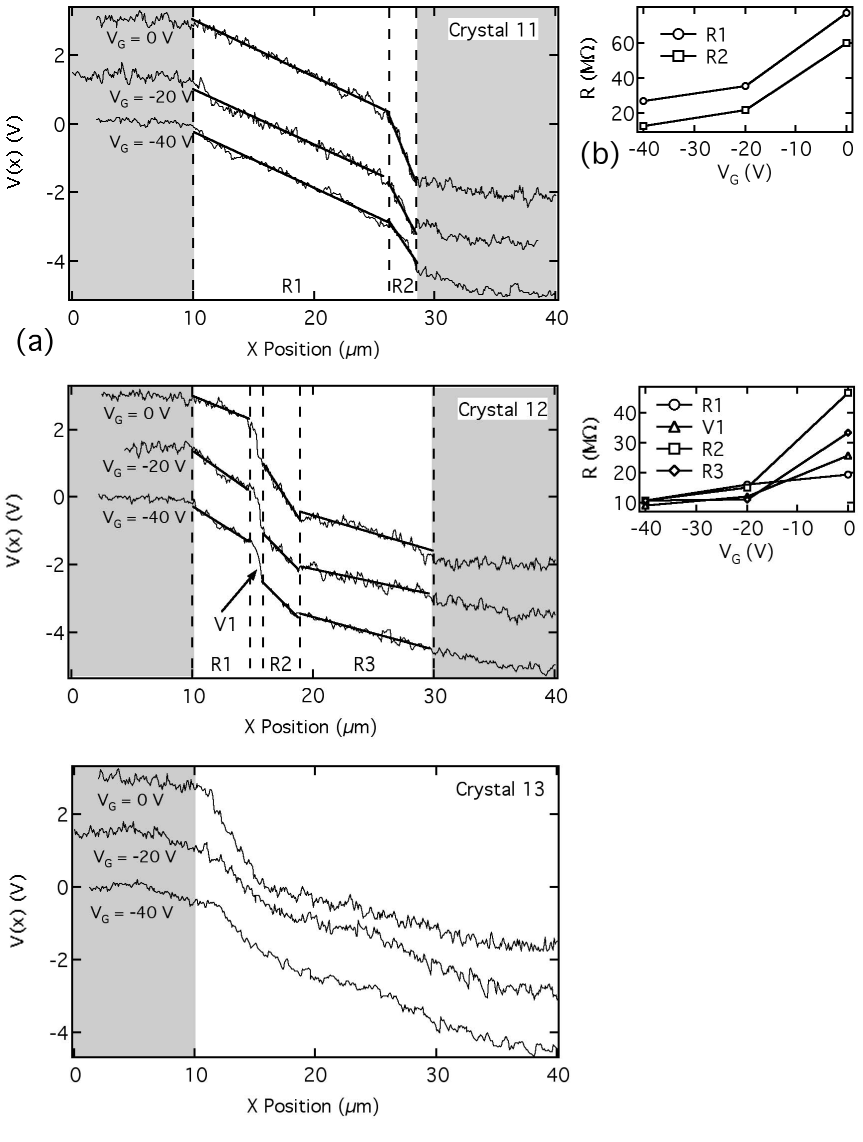

FIGURE 4.17: KFGM potential line-scans extracted from the images of the whole device taken at varying V_G for the crystallites in Domain 3. Crystallite 11 can be easily divided into two linear regions as shown in the preceding figures. Crystallite 12 appears to be divided into three linear regions, R1, R2 and R3 with a sharp potential drop between R1 and R2. The behaviour of crystallite 13 is more difficult to model.

4.2.5 Scanned gate microscopy of Device 1

A further modification of the EFM technique is scanned gate microscopy (SGM). In this technique, phase EFM is performed as normal, except that an $AC + DC$ bias is applied to the tip as the EFM scan is performed. The frequency of the AC component is typically around 500 Hz. The magnitude of the bias is set high enough that, when brought into close proximity to the surface, it will significantly affect the local gate voltage under the tip further turning the device either on or off. A lock-in amplifier can be used to pick out the signal in the current and an image is produced that shows the local susceptibility to changes in gate field.

Figure 4.18 is an AC-SGM image of Device 1 with a tip DC bias of 8 V and AC bias of 2 V and with $V_G = 0\ V$ and $V_D = -5\ V$. The current in this image varies significantly from the top to the bottom of the image, so a quantitative analysis will be difficult. However, a qualitative analysis will show whether the technique has any validity. Strikingly, there are regions with higher current associated with many of the crystallites, particularly at the right hand (drain) side of the channel. In many cases, the regions of increased current correlate with either sharp potential drops or with regions of lower conductivity that may be more susceptible to variations in $V_{G,EFF}$. However, there are also instances of high current regions not associated with features in the potential and vice-versa.

In this case it appears that the AC-SGM image cannot be used as a quick guide to the behaviour of different crystallites. However, it might reasonably be assumed that the crystallites showing the largest variation in I_D for the same change in $V_{G,EFF}$ might be those that carry the most current. For example, crystallite 2 shows an increase of more than 10% in I_D for the whole device for a tip bias of $8 \pm 2\ V$. By applying the correct biases to the device and to the AFM tip it might be possible to ‘turn off’ individual crystallites in order to determine the fraction of the total $_D$ passing through them.

4.2.6 Conclusions from device measurements

The data presented above on KFGM measurements of a complete TIPS pentacene device provide us with strong conclusions about how we must go about assessing the performance of organic semiconductors in situ, as well as highlighting some of the difficulties associated with interpreting the results of the KFGM in this context.

The first conclusion is very clear: there is no way the performance of the TIPS pentacene itself could be realistically determined using non-SPM techniques. Electrical measurements will provide only an average performance for the whole device, which

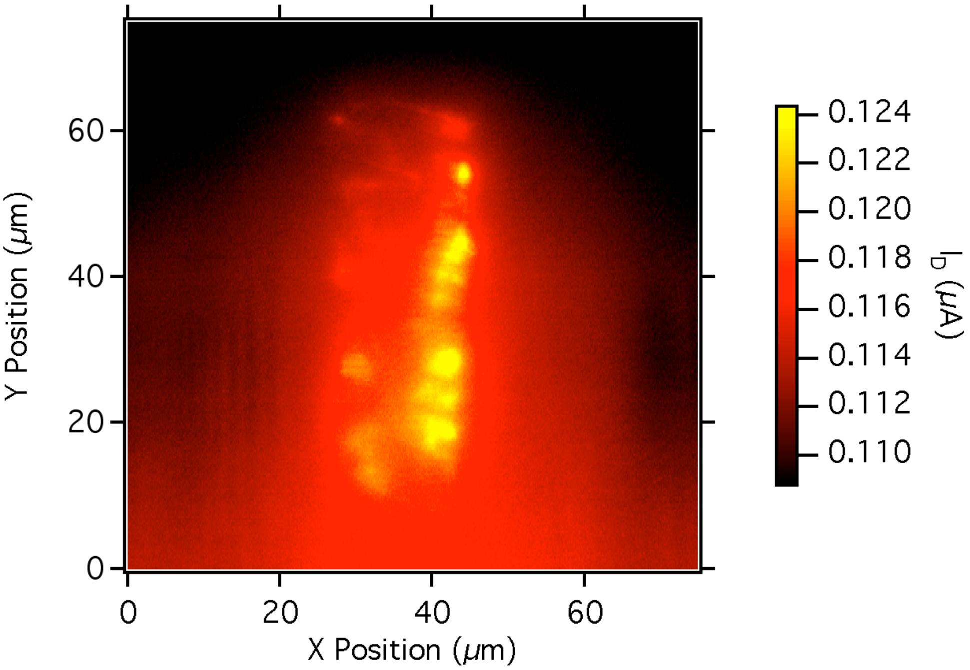

FIGURE 4.18: 75 μm SGM image of the whole device taken at V_G = 0 V and V_D = -5 V. The potential applied to the tip was +5 V and the lift-height was 50 nm. In this image, the regions most strongly affected by the presence of the tip potential correlate well with the positions of the strongest potential drops in the crystallites.

will be made up of crystallites with different mobilities, contact resistances and even different threshold voltages. Four point resistance measurements might produce reliable data if they could be applied to single crystallites and then only to those with behaviour closer to ideal TFT performance. By using KFGM, we can assess the range of different crystallite behaviours and begin to understand the local variations within the device.

Some crystallites are clearly contact limited, whether by resistive barriers at crystal defects or by injection barriers at the source electrode. Others appear saturated at linear voltages, whilst many are subdivided into up to three domains with differing conductivity. In addition to this, we have seen that the crystallites at the edges of the channel may connect source and drain by much more convoluted routes than we expect. None of this information could have been provided by the other commonly used techniques.

That said, there are limitations to KFGM as applied in this section. Without a quantitative way to determine what proportion of the device current flows through each crystallite, we can only estimate the electrical parameters of each. SGM may show us which areas are most sensitive to variations in V_G and cAFM might differentiate between conductive and non-conductive regions of the sample but neither these nor KFGM can provide a local measurement of the current.

In the following section we address this problem by producing a single crystallite device, allowing us to determine the material performance quantitatively. With the problems of localising the current addressed, the full power of KFGM to show us how every part of the channel responds to changes in V_G is realised.

4.3 SPM Measurements of a Single Crystal TIPS pentacene TFT

In section 4.2.6 the uniformity of the crystallites was highlighted as the greatest obstacle to characterising zone-cast TIPS pentacene devices. In the following section KFGM measurements on a single crystal TIPS pentacene device are presented.

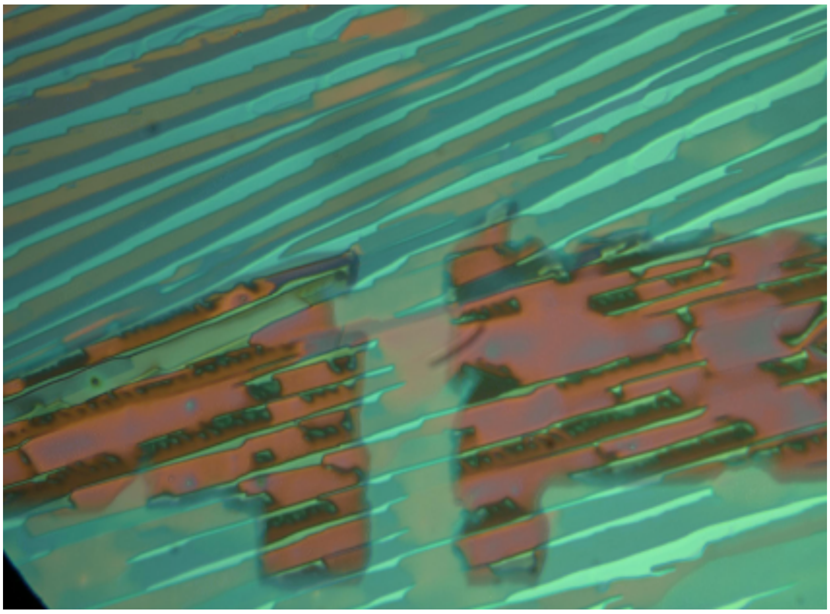

FIGURE 4.19: Optical microscope image of the TIPS pentacene device used in this section. The intact device was estimated to have $L = 17$ μm and $W = 42$ μm for the purpose of initial calculations of μ_{DEV}. The crystallites cross the channel at an angle of approximately 20°. The brown material in and around the TIPS pentacene crystallites is visible in AFM topography and could be the inert polymer binder.

A second device was prepared following the same procedure as in the previous section. This device, pictured in Figure 4.19 was produced using a source-drain contact mask with approximately the same dimensions as previously. In this device, the crystallites crossing the channel are contained within two domains with different orientations, but with the same molecular alignment relative to the crystallite long axis. The majority of the crystallites cross the channel at an angle of 20°. From an inspection of Figure 4.19 there appear to be 9 or 10 crystallites crossing the channel.

Adjusting for the width of the crystallites that cross the channel and for the channel length using the AFM data in Figure 4.20, the effective dimensions for this device, hereafter referred to as Device 2, are $L = 17$ μm and $W = 42$ μm. The value of L is estimated from the distance between a linear fit to the left and right contact edges and is a good estimate for all but one of the crystallites. One crystallite at the top of the channel appears to have length approximately 5 μm longer than the others due to a defect in the left contact

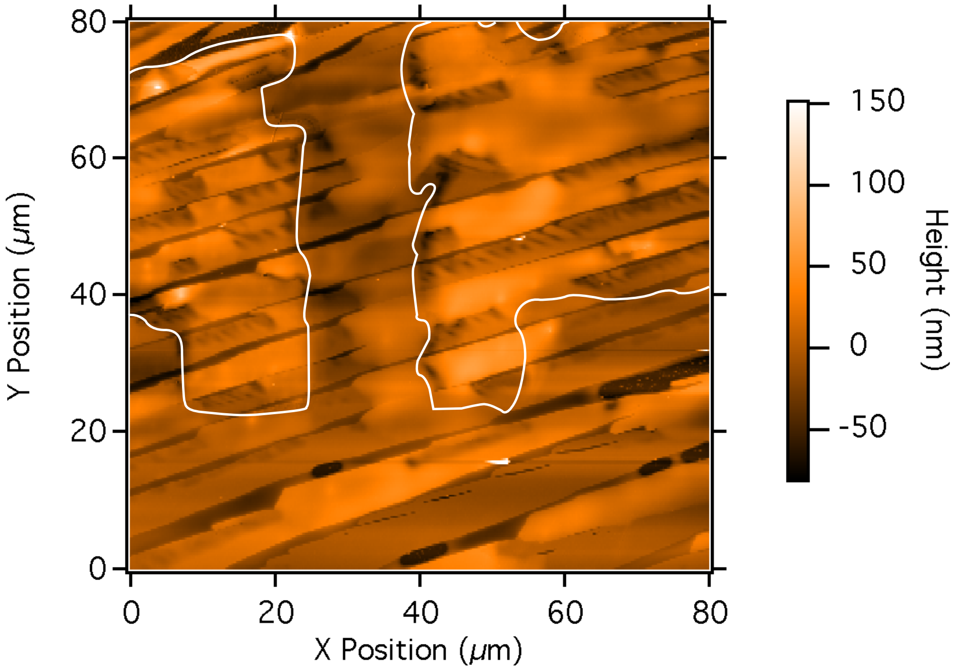

Figure 4.20: 80 μm tapping mode AFM topography image of the whole device. As with the previous device, the contacts are less easy to see than in the optical image, although they can be discerned as raised regions beneath the TIPS pentacene crystallites and have been outlined in white. Some cracks are visible in the crystallite surfaces, corresponding to similar features in the optical.

Both the optical and the AFM image of Device 2 show accumulations of material between and around the TIPS pentacene crystallites. In the optical image these appear as brown regions, which correspond to raised regions in the AFM image. These are commonly seen in films zone-cast from formulations containing an inert polymer binder such as those used in this chapter.

Figure 4.21 shows the linear and saturation transfer scans for Device 2 and the corresponding mobilities calculated using the values of W and L estimated above from the optical and AFM images. The transfer scans are within the range of device-to-device variation expected for zone-cast devices with low channel width. In the linear regime, Device 2 has a peak $\mu_{LIN} = 0.9\ cm^2V^{-1}s^{-1}$ at $V_G = 0\ V$, implying good charge injection from the source contact, and $V_T = 7.4\ V$. The corresponding values for the saturation regime are $\mu_{SAT} = 0.6\ cm^2V^{-1}s^{-1}$ and $V_T = 17.4\ V$. Interestingly, the saturation transfer scan exhibits a “double turn-on” but only in the forward scan. This form of hysteresis is unusual, possibly caused by short-lived traps confined to a localised area within the channel. The saturation mobility plot shows a small peak in the reverse scan that is not significant enough to be visible on the log plot.

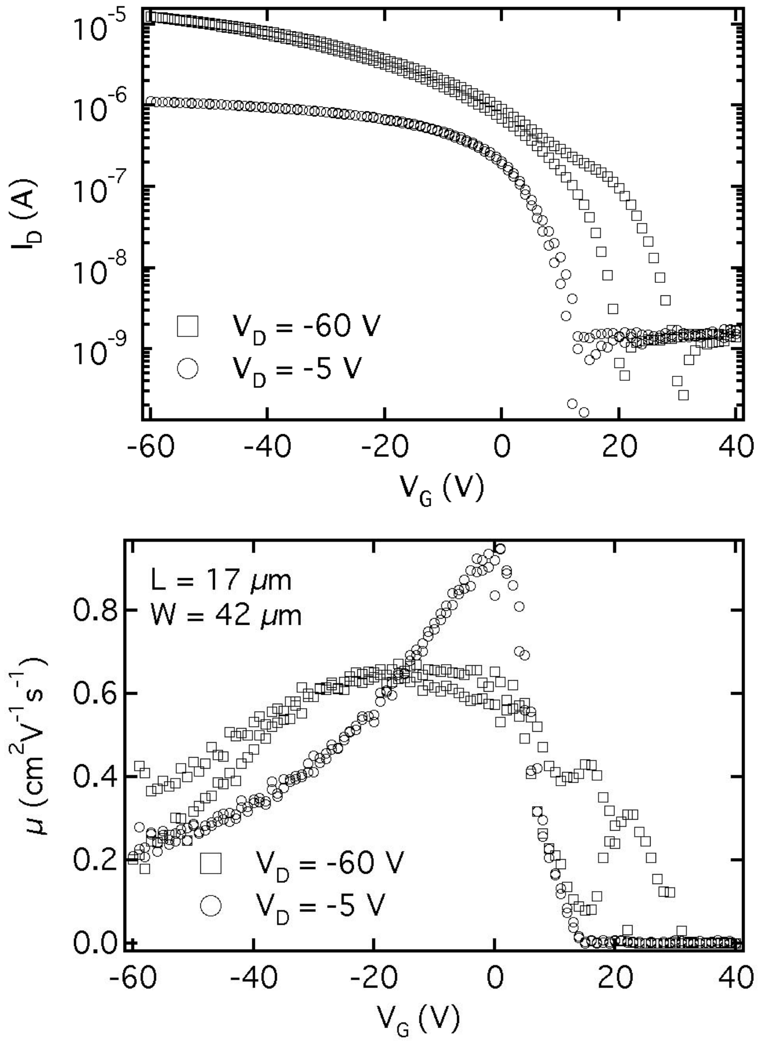

FIGURE 4.21: Transfer scans (top) and mobility (bottom) for the device used in this section. The device performance is in many ways similar to that of the device used in the previous section. The values of V_T estimated using a linear fit to the current were 7.4 V in the linear regime and 17.4 V in the saturation regime There is significant hysteresis in the form of a “double turn-on” in the saturation regime transfer scan. μ_{LIN} shows a strong peak of 0.9 $cm^2V^{-1}s^{-1}$ at $V_G = 0\ V$ in the linear regime and $\mu_{SAT} = 0.6\ cm^2V^{-1}s^{-1}$.

Figure 4.22 is the corresponding output scan for Device 2 taken at values of V_G from +20 to -60 V. The points at which saturation begins to occur are close to those we might expect if the value of V_T estimated in the saturation regime is correct, although Device 2 still does not appear to fully saturate, as indicated by attempts to fit the output scans using the long channel FET model described in the previous chapter. The closest fits to the output data were only achieved by using very high values of V_T and low values of μ.

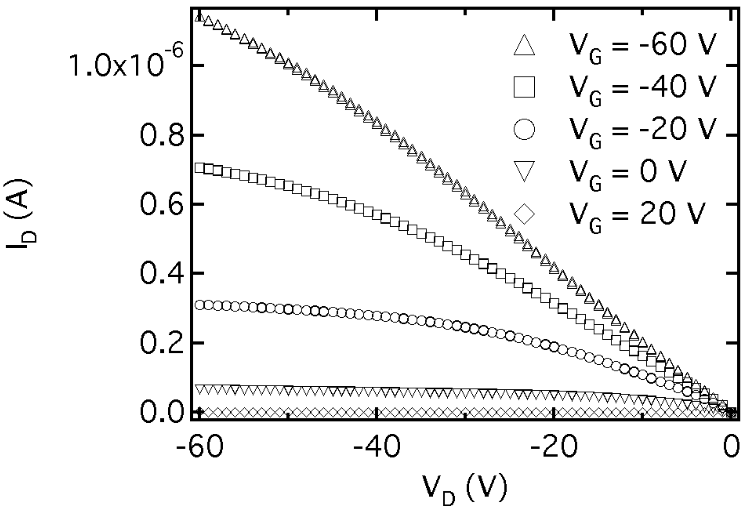

FIGURE 4.22: Output scans taken for 20 V intervals of V_G. This device, with $L = 20\ \mu m$, shows a lack of saturation at higher V_G, similar to that of the 5 μm pBTTT devices described earlier. In order to produce even approximate fits to the output current using the long channel FET model, very high values of V_T (approximately 90 V) and low values of μ (≤ 0.02) must be used.

4.3.1 Cutting TIPS pentacene crystallites with the AFM

In order to reduce Device 2 to a single crystal TFT, the AFM was used to cut through the unwanted crystallites. The refined approach to this technique is generally referred to as nanolithography although here we employ a more "brute force" – though no less effective – approach. In order to perform a cut, the desired area is first imaged in tapping mode using a tapping mode tip and the image width and AFM scanning direction aligned with the desired cutting position. The slow scan axis is disabled so that the AFM continually scans the cutting position and the AFM is re-engaged in contact mode. The deflection setpoint can then be set to a high value, 2 V in this case, to push the tip hard into the sample. The tip is then scanned back and forth along this line at around 50 μms^{-1} for several scans to ensure that the cut is deep enough to completely break the crystallite.

Figure 4.23 shows Device 2 imaged in tapping mode after all of the unwanted crystallites were cut using this technique (for confirmation see Figures 4.26 and 4.27 later on). The debris from the cutting is visible along the cuts used to isolate the single crystal. This image and the associated phase EFM image in Figure 4.24 also both show the image defects associated with imaging after cutting organic material with the AFM tip. The bad lines and changes in image height, and corresponding EFM signal, in the y direction are probably caused by material either adhering to or

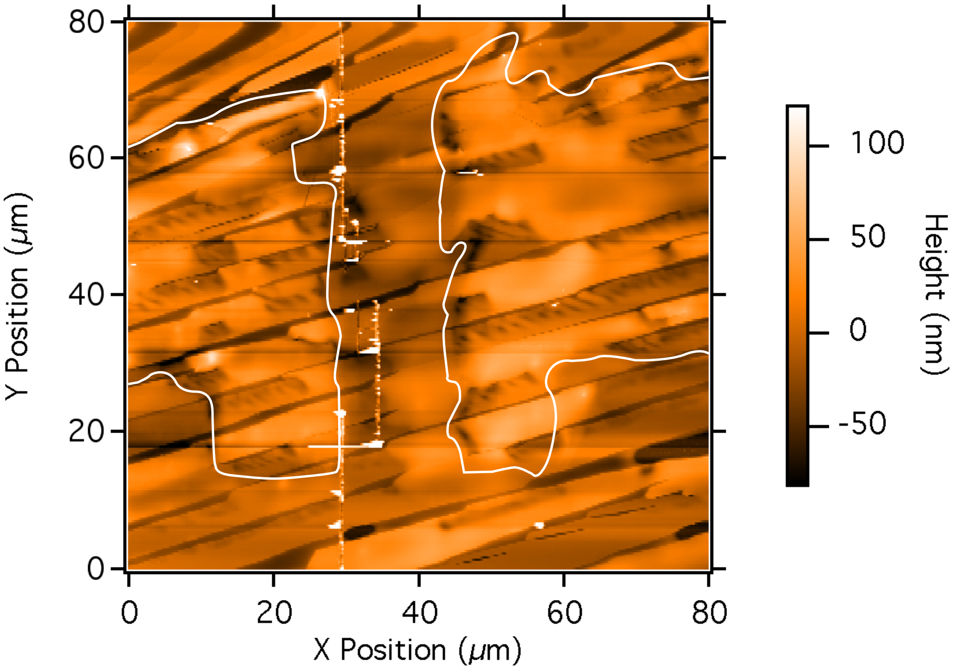

FIGURE 4.23: 80 μm tapping mode AFM topography image of the device after being cut using the AFM. The two long cuts were first used to disconnect most of the channel, with two further short cuts used to more carefully separate the chosen crystallite. The reduction in image quality is most likely due to the tip either becoming damaged by the cutting or picking up material from the resultant debris during imaging.

being pulled away from the tip. This will have the effect of altering both the effective length of the tip and the curvature of the tip apex, causing the observed artefacts.

In total, five separate cuts were required to isolate the single crystal, as shown in Figures 4.23 and 4.24. The first two cuts, at 50 μm long, cover the majority of the channel and extend approximately 20 μm beyond the channel edges. It was shown in the previous section that the crystallites at the edges of the channel can be electrically connected to the contacts through adjacent crystallites (see Figure 4.13) and by more convoluted paths. By cutting through many of the adjacent crystallites we reduce the chances of this happening. A further three shorter cuts were made with more precision to sever the crystallites immediately adjacent to the target crystallite, marked on Figure 4.24. As the EFM phase image shows, the EFM phase signal drops very sharply at each of the cuts.

Line-scans taken across the cut, as in Figure 4.25 show potentials on each side of the cuts that are fairly flat, separated by a sharp potential drop, which strongly suggests that the TIPS pentacene crystallites have been broken and that there is no electrical contact through the OSC between source and drain. It is still possible, of course, that

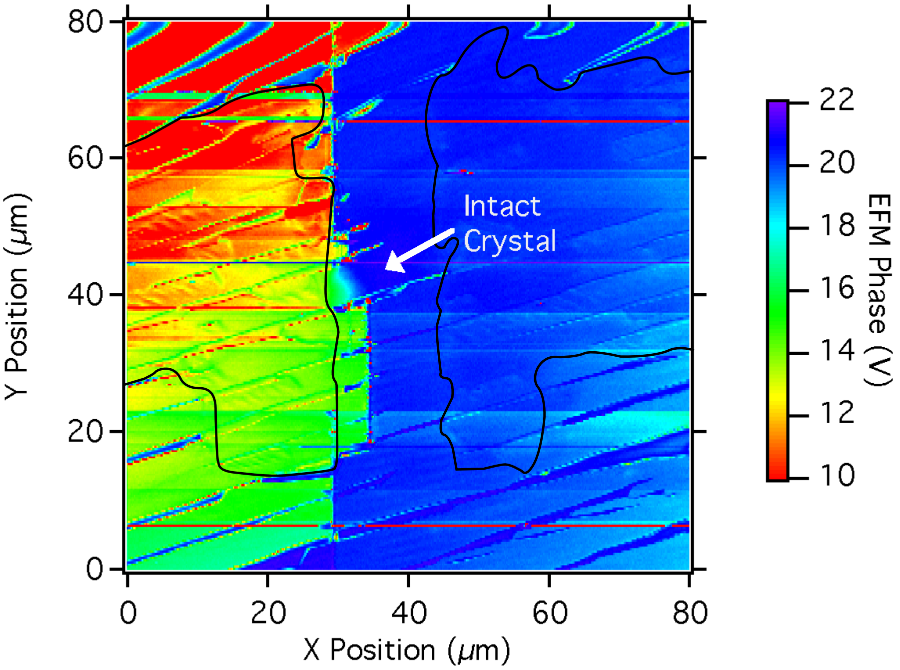

Figure 4.24: 80 μm EFM phase image of the device after being cut. Although there is significant variation in the observed phase at the left side of the channel, the sharp potential drops at the sites of the cuts (see Figure 4.25) strongly suggest that contact between the source and drain electrodes has been broken.

some current can flow elsewhere in the device, either through any uncut material or across the cuts themselves, which may just have a very high resistance.

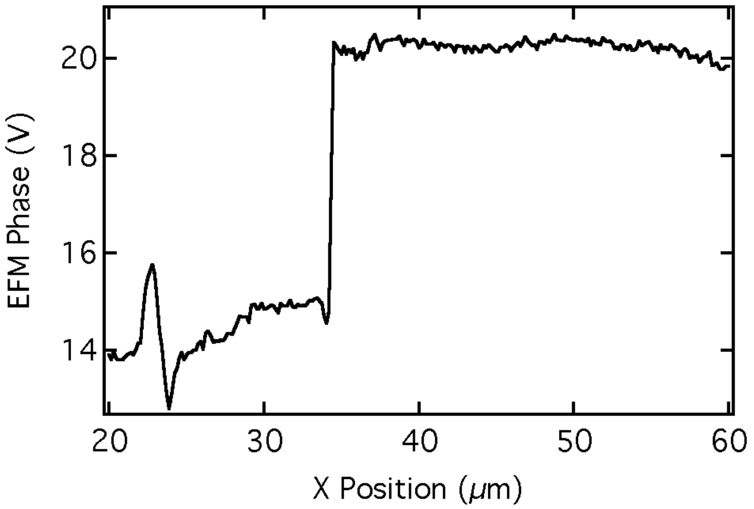

Figure 4.25: EFM phase line-scan taken at the point indicated in Figure 4.24. The majority of the potential is clearly dropped at the site of the cut.

In order to further investigate the effects of cutting the crystallites using the AFM, the device was remeasured after returning from KFGM measurements using an Agilent

4155C parameter analyser. This allowed for the measurement of the gate leakage current during the transfer scans, which could be expected to play a more significant role given the reduced current flowing through a single crystallite. It should be noted that, as previously observed with pBTTT TFTs, there are some changes in the overall device performance associated with transit between sites and with different equipment. These problems should, however, have no bearing on the following results.

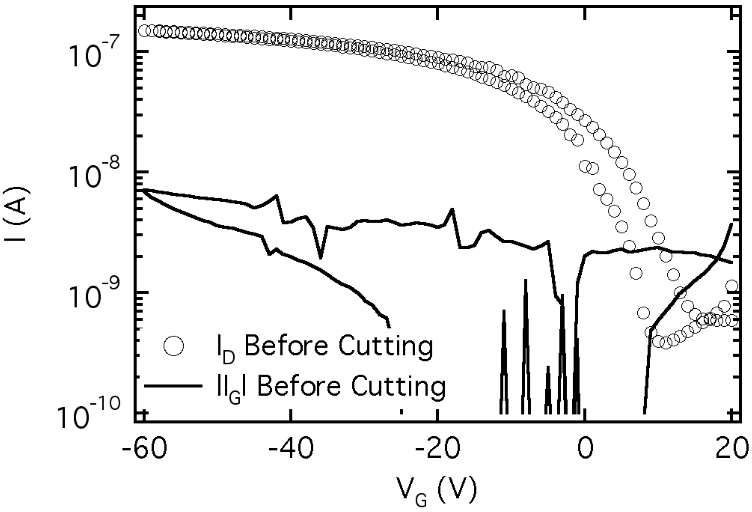

FIGURE 4.26: Linear transfer scan for Device no. 2 taken using the parameter analyser so that the gate leakage I_G could be recorded in addition to I_D. I_G is shown using absolute values so that the curves can be compared on a log scale and is 7.1 nA at V_G = -60 V, or 5% of $I_{D,ON}$.

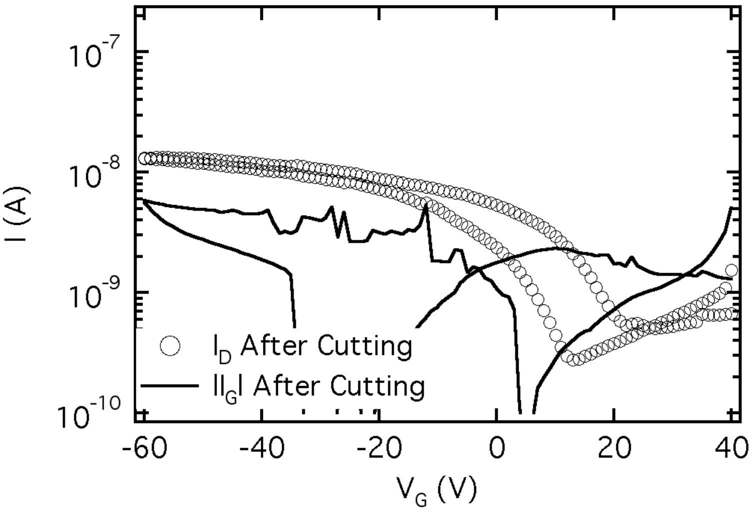

FIGURE 4.27: Linear transfer scan for Device no. 2 measured immediately after the final crystallite was cut using the AFM. In this case I_G = 5.8 nA, which is 44.27% of $I_{D,ON}$.

A transfer scan was first taken of Device 2 as shown in Figure 4.26. The remaining crystallite was then cut using a Veeco Dimension Icon AFM and a tapping mode AFM tip and a second transfer scan taken, as shown in Figure 4.27. As expected, the gate leakage current, I_G remains fairly constant with peak values of 6.9 nA before cutting and 5.8 nA after cutting. This is equivalent to around 5% of $I_{ON,UNCUT}$ and 44% of $I_{ON,CUT}$. The most significant change caused by the cutting is in the on current as expected. Before cutting $I_{ON,UNCUT} = 151\ nA$, dropping to 13 nA after cutting, which accounts for around 8.5% of $I_{ON,UNCUT}$. An attempt was made to produce a transfer scan for just the single crystallite itself, however the differences in threshold and hysteresis observed, rendered the final output unusable.

From these measurements, we can assume that over 90% of the current flowing through the device when it is on is flowing through the uncut TIPS pentacene crystallite. This introduces an error of around 8.5% into our measurements of current flowing through the device and into any values of mobility, resistances and so forth that we derive therefrom. However, this error is not significant enough to change the overall conclusions about device performance that we can draw from the KFGM data presented next.

4.3.2 A single crystal TIPS pentacene device

The transfer scans and derived mobilities for the single crystal TIPS pentacene TFT are shown in Figure 4.28. In this case the mobility was calculated using the dimensions of the crystallite, $L = 17\ \mu m$ and $W = 5\ \mu m$, with peak values of $\mu_{LIN} = 1.1\ cm^2V^{-1}s^{-1}$ and $\mu_{SAT} = 1.9\ cm^2V^{-1}s^{-1}$. These values are significantly higher than those calculated for the uncut device. It is likely that the crystallite selected is one of the more conductive in the channel, or that some unknown factor is influencing the calculated mobility. A small peak is still visible in $\mu_{SAT,CUT}$ at $V_G = 13\ V$, which is close to the position of the similar peak in μ_{SAT}. V_T has also shifted significantly to the positive with values of 18.6 V in the linear and 23.3 V in the saturation regime. The double turn-on effect observed in Figure 4.21 is also no longer present, suggesting that it was caused by one or more of the crystallites that were cut.

The output scans for the single crystallite device, in Figure 4.29, show less saturation than before Device 2 was cut. For $V_G = -60\ V$ the curvature of the output current even appears to be in the opposite direction. It is expected that with the shift in V_T there should be a corresponding shift in the saturation point, however the effect appears more pronounced than expected.

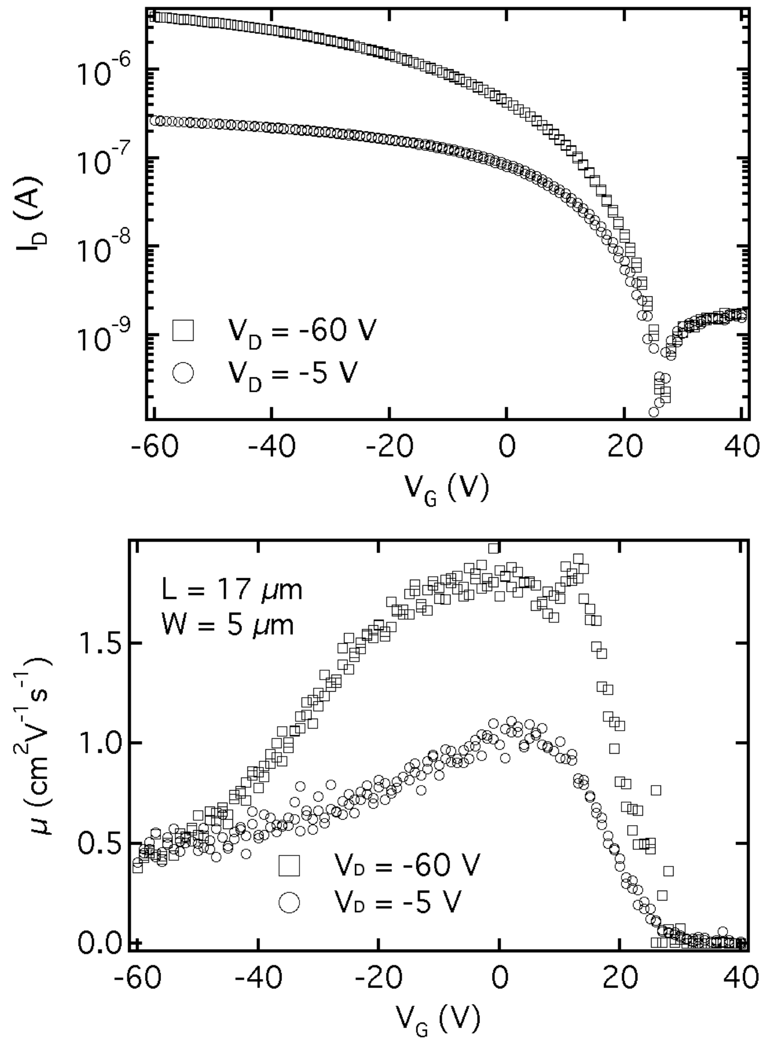

FIGURE 4.28: Transfer scans (top) and mobility (bottom) for the device after being cut with the AFM. As a result of the cutting, I_{ON} has been reduced by a factor of 4.2 in the linear regime and 3.2 in the saturation regime. Additionally, V_T has shifted to 18.6 V in the linear and 23.3 V in the saturation regimes. If the mobility is recalculated using channel dimensions estimated from the KFGM images ($L = 5\ \mu m$ and $W = 17\ \mu m$) then $\mu_{LIN} = 1.1$ and $\mu_{SAT} = 1.9\ cm^2V^{-1}s^{-1}$.

The AFM topography and the KFGM potential at $V_G = 0\ V$ and $V_D = -5\ V$ are shown in Figure 4.30. From the topography it is clear that the AFM cuts were somewhat less precise than intended, as they extend approximately 1 μm into the crystallite on each side. However, in this case it is better to cut slightly too far than not to cut far enough and leave the adjacent crystals able to carry current. There is also what appears to be a hairline crack visible in the crystallite, extending diagonally from around $x = 17\ \mu m$ and parallel to the “knee” feature visible on the top edge of the crystallite. This is further evidence, if rather circumstantial, that the TIPS pentacene molecules are aligned parallel to these features as we would expect the

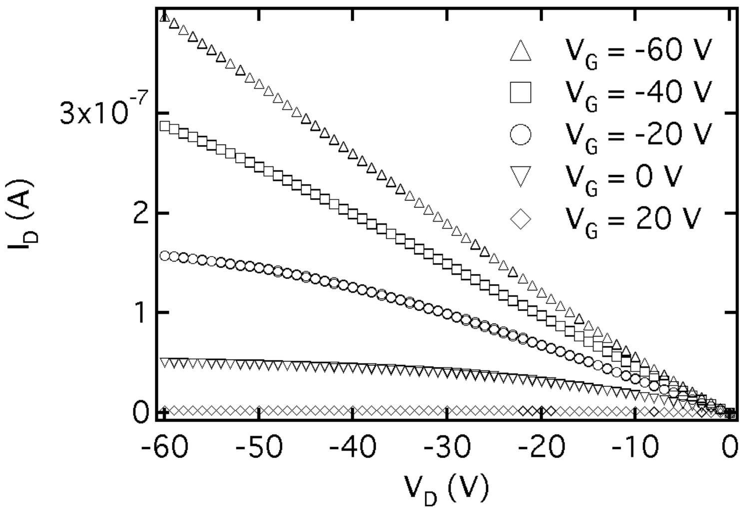

FIGURE 4.29: Output scans taken at 20 V intervals of V_G for the cut device. The lack of saturation in the output scans is more pronounced than in Figure 4.22 before the device was cut. The positive threshold shift caused by the cutting will have the effect of pushing the saturation region further to the negative V_D, although only by 6 - 10 V if the fitted values are correct.

crystallite to fracture along its crystal axes. The KFGM potential varies relatively smoothly along the crystallite, so we can be confident that it is intact, in marked contrast to the sharp potential steps in the cut crystallite shown previously in Figure 4.25. The approximate position, allowing for drift, of the line-scans used in this section is shown on the KFGM image (dashed line).

With the single crystallite isolated, we can take a similar approach to the KFGM measurements as in the previous chapter. In this case, KFGM potential images were taken of the whole crystallite at different values of V_G and V_D with only 16 lines and with 1,024 pixels per line. The resolution in the y direction in this case only needs to be high enough to pick out the correct line-scan, whilst the resolution in the x direction should be as high as possible. Line-scans for $V_D = -5\ V$ at $VG = +40$ to -60 V are shown in Figure 4.31. It is obvious from these line-scans that the crystallite selected from Device 2 is similar to the more complex crystallites in Device 1, and there is not a simple linear potential drop with R_S and R_D at the contacts. Whilst this may complicate the analysis, it is actually ideal as it highlights the strengths of the KFGM over other techniques in a way that linear measurements of pBTTT in the previous chapter did not.

The crystallite can be divided into three sections as shown in Figure 4.31. The 6 μm of the crystallite adjacent to the source (left) contact, here labelled region (a), has a lower conductivity and appears to behave almost as an independent short channel with a more pronounced potential drop at the left (source) side of the region, particularly for

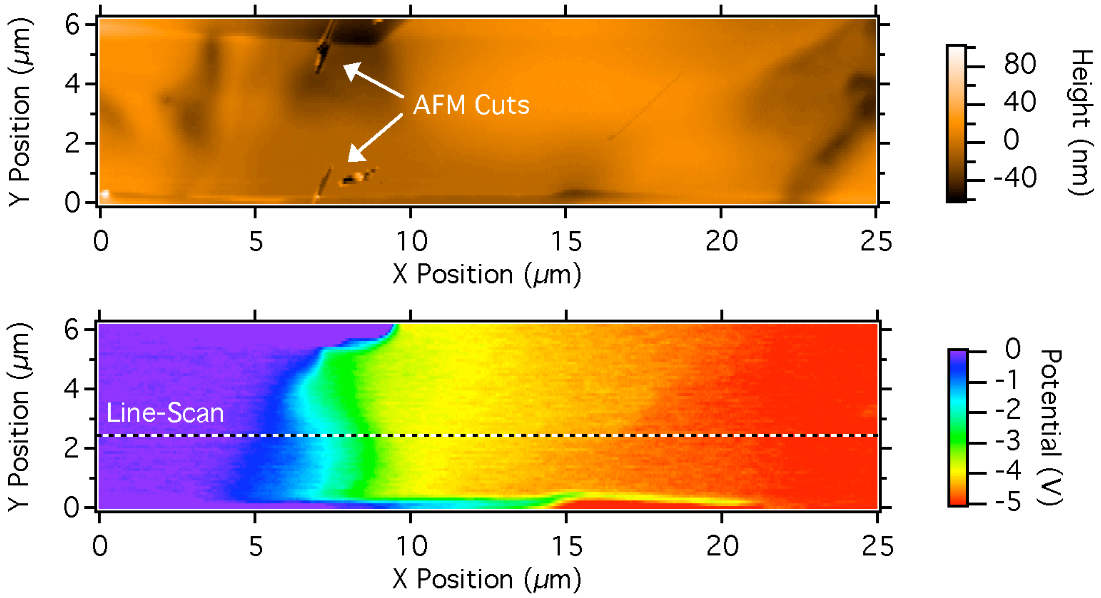

FIGURE 4.30: Tapping mode topography (top) and KFGM potential (bottom) images of the single crystallite. It can clearly be seen at the top and bottom edges of the crystallites that the cuts made using the AFM extend 1 μm into the crystallite edges. There is also a shallow crack visible towards the right side of the topography image. The locations of the cuts, and also the crack, are also visible in the potential image. Between the cuts, however, the potential drop is continuous, suggesting that no damage has been done to this region. The position of the potential line-scans used in Figure 4.31 is shown.

more negative V_G. The rest of the crystallite consists of regions (b) and (c), which appear to have a comparable conductivity in most of the line-scans and may in fact be one single region divided by the crack that is visible in Figure 4.30. There is also a sharp potential drop at the drain (right) contact when V_G is less than V_T which is not reproduced when $V_D = +5\ V$.

To confirm that the behaviour observed is consistent, and not simply the effect of source-drain polarity, a comparable set of line-scans – albeit for a smaller number of different V_G – were taken with $V_D = +5\ V$. These line-scans, shown in Figure 4.32, confirm that the same region (a) adjacent to the left (now drain) contact maintains a lower conductivity than regions (b) and (c). In the positive line-scans, the potential seems to be dropped more strongly at the right (source) side of region (a). This is consistent with region (a) behaving as an independent channel within the crystallite that will tend to dominate the performance of the single crystallite device as it drops the bulk of the potential.

As in the previous chapter, I_D was recorded during the KFGM scans. The mean value of the current in each image was plotted against V_G in Figure 4.33. This transfer scan is very similar to the one measured before KFGM imaging, shown in Figure 4.28. I_{ON}

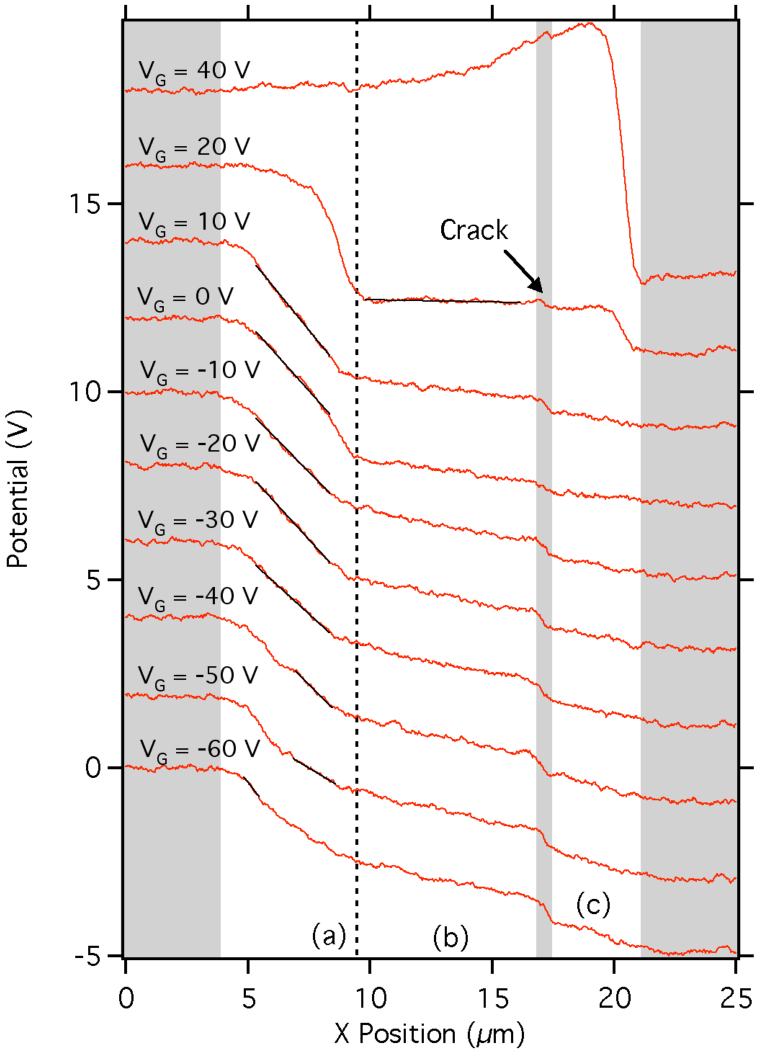

FIGURE 4.31: KFGM potential line-scans through the middle of the crystallite, taken for varying values of V_G. The channel has been divided into three regions based on the potential drops observed. Most of the potential is dropped in region (a) adjacent to the source contact, which seems to behave as a separate TFT channel. Regions (b) and (c) show a similar slope in the potential, and so have similar conductivity, but are divided by the sharp potential drop at the crack seen in Figure 4.30.

is reduced by around 10%, which is consistent with the differences observed during KFGM on the devices discussed previously. V_T calculated from the linear fit is 16.2 V, which is in good agreement with the linear threshold obtained prior to AFM measurement, especially allowing for the limited number of points for a linear fit in this case. It should be noted that, due to problems with the current data, values are not available for $V_G = -30$ and -50 V.

Using the potential drops extracted from the KFGM line-scans and the values of I_D in Figure 4.33 the resistances of the three regions within the channel were calculated. These are plotted in Figure 4.34 and follow a familiar form. The resistance is strongly

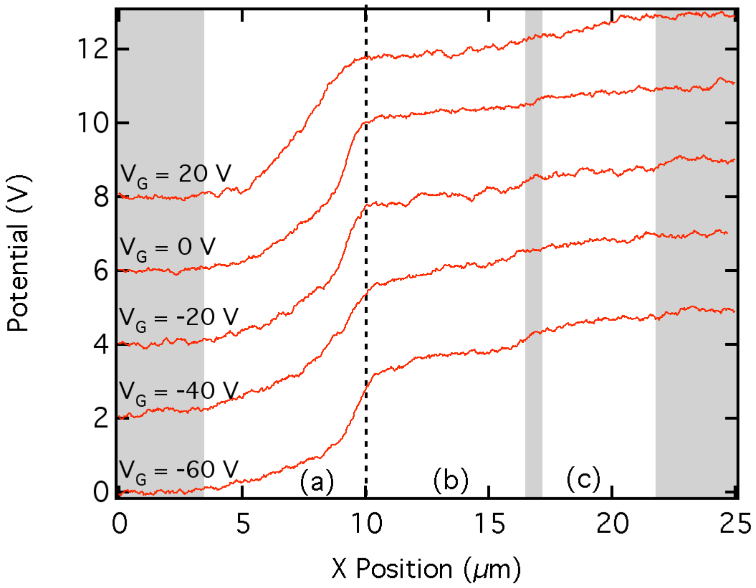

FIGURE 4.32: Potential line-scans through the middle of the crystallite, taken for a reduced set of V_G values. The channel has been divided into the same regions (a), (b) and (c) as in Figure 4.31. In general the behaviour is the same, with region (a) behaving as a smaller channel within the crystallite. The effect of the crack also appears less pronounced for positive V_D.

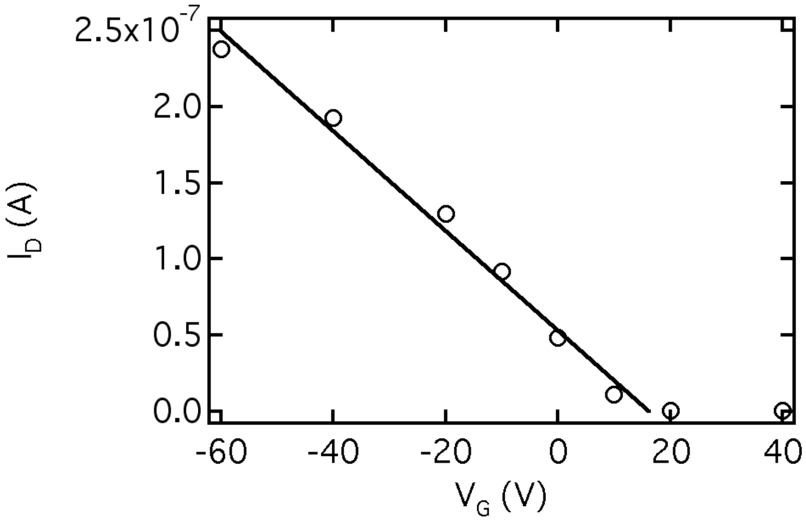

FIGURE 4.33: Linear transfer scan at V_D = -5 V taken during imaging. V_T = 16.2 V from a linear fit to the current (black line). The current closely matches that of the device measured when not being imaged.

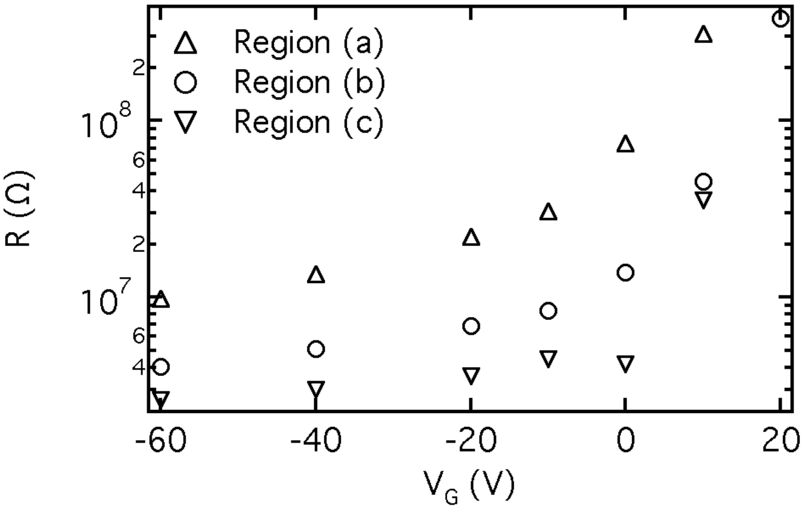

FIGURE 4.34: Resistance of the three regions shown in Figure 4.31 and also estimates for the resistance of the crack. As implied by the KFGM potential, region (a) dominates the performance of the single crystal device.

V_G dependent as we would expect, with the resistance of region (a) greater than those of regions (b) and (c) combined. Device 2 can thus be thought of as two channels in series, one with a much higher conductivity than the other.

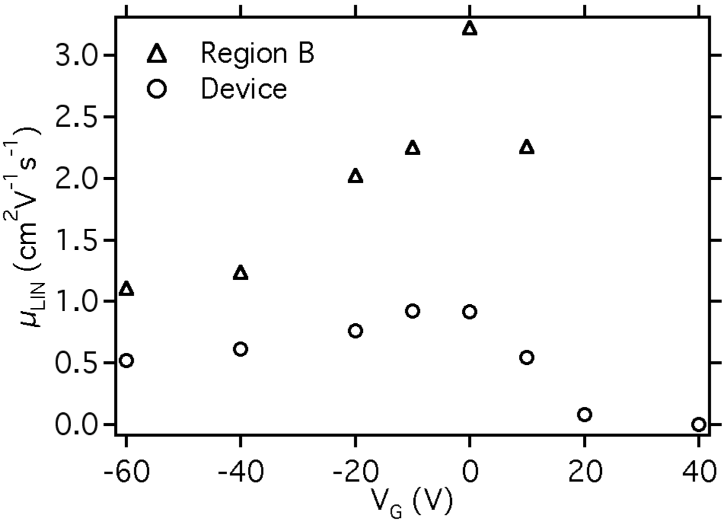

FIGURE 4.35: $\mu_{DEV,LIN}$ for Device 2 (circles) calculated using the KFGM current plotted against $\mu_{B,LIN}$ for Region B (triangles) of Device 2. The peak $\mu_{DEV,LIN} = 0.92\ cm^2V^{-1}s^{-1}$ corresponds reasonably well with the value obtained from the initial transfer scan (1.1 $cm^2V^{-1}s^{-1}$). The high peak value of $\mu_{B,LIN}$ may be an artefact, however taking the values either side gives a value of 2.25 $cm^2V^{-1}s^{-1}$, which is more than twice $\mu_{DEV,LIN}$.

As we have shown in Figures 4.31 and 4.34, the device mobility, μ_{DEV} is caused by a combination of the local mobilities in the different regions of the device. With the local potential data that the KFGM provides, we are able to extract the local mobility for the highest conductivity region of the device, Region B. Using the width of Region B, $W = 6.6\ \mu m$, and the potential dropped across it extracted from the KFGM line-scans, the local linear mobility, $\mu_{B,LIN}$, for Region B can be determined. In Figure 4.35 $\mu_{B,LIN}$ (circles) is plotted alongside $\mu_{DEV,LIN}$ (triangles) calculated using the values of I_D recorded during the KFGM scan. $\mu_{B,LIN}$ is, as we might expect, higher than $\mu_{DEV,LIN}$ by more than a factor of two and produces a realistic peak mobility value for Region B of 2.25 $cm^2V^{-1}s^{-1}$. Disregarding the very highest value, which is likely to be an artefact, this gives a much higher estimate of the theoretical maximum material mobility of the TIPS pentacene than device measurements alone.

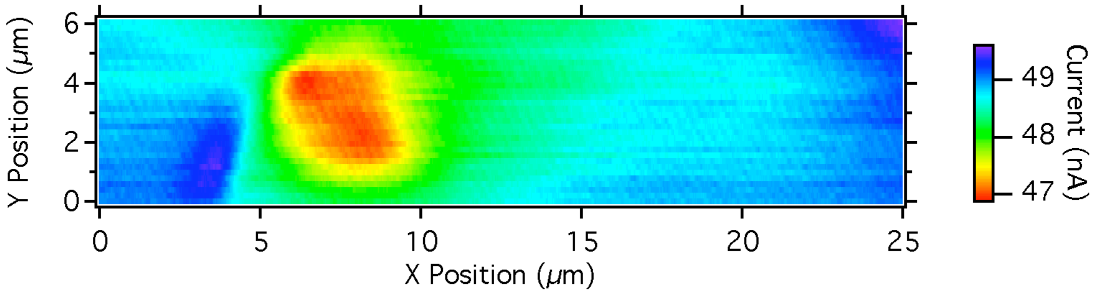

Figure 4.36: SGM image of the crystallite for V_D = -5 V, V_G = 0 V with a tip potential of 5 V and a lift-height of 50 nm. The area of strongest variation in the current corresponds directly to region (a). It was not possible to perform AC-SGM as the response of the SGM signal was too slow for frequencies above $\sim 100\ Hz$. It is possible that this was caused by a build-up of material on the tip during the day's imaging. The spread of the response in the y-direction could be due to some influence of the AFM cantilever in addition to the tip.

In the previous chapter, the material mobility values were significantly higher than the device mobility values because the devices were effectively contact limited, with 90% of the potential dropped at the contacts. In this case, there is no significant contact limitation but rather a material mobility that varies from region to region within the crystallites. The higher mobility gives an insight into the theoretical maximum performance of the TIPS pentacene, a value which is closer at least to the mobility that can be achieved with evaporated pentacene. There is no theoretical reason why, under ideal conditions, solution processed TIPS pentacene may not achieve similar material mobilities to its unsubstituted counterpart.

As with Device 1, SGM images were taken of the single crystal Device 2. Figure 4.36 shows an image comparable to that in Figure 4.18 shown in the previous section taken with a tip bias of +5 V. The SGM image shows that the region that most strongly influences the current corresponds to region (a), which is consistent with our expectations given that the majority of the potential is dropped across this region.

There is a sharp boundary to the left side of the region, corresponding to the source contact edge. The area of strongest influence is constrained both within the length of region (a) and between the two AFM cuts that overlap the edges of the crystallite. Regions (b) and (c) show a much smaller and more diffuse signal in the SGM, indicating a less strongly localised influence on the current.

As suggested in the previous section SGM and AC-SGM may provide a way to determine which crystallites have the strongest influence on the device current and may allow for selection of crystallites based on their general behaviour. However, even though the correlation is good in this image, they may not provide a way to quantitatively determine the crystallite behaviour without performing KFGM. As a tool for determining the extent of the active channel for similar devices, SGM may prove useful.

4.3.3 Conclusions from Single Crystallite Measurements

The data presented in this section confirms our initial conclusions about KFGM as a technique. With the right device preparation it is possible to obtain detailed quantitative data about local variations in mobility within a single crystallite TIPS pentacene TFT. Indeed, the AFM itself becomes an essential tool in the experimenter's arsenal when defining new device geometries. The simplicity of the nano-lithography approach and its flexibility in allowing the experimenter to choose which parts of a device to isolate makes it indispensible. The same instrument can then be used to produce potential profiles confirming the success of the procedure.

By doing this, we have shown that what appears, optically, to be a single uniform crystallite contains several regions with significantly different mobility. When combined with the crystallite-to-crystallite variability observed in Section 4.2, we find a massive range of variability in the TIPS pentacene film performance at all scales. It is clear that any macroscopic electrical characterisation would merely provide the average over all observed variability, concealing the true behaviour of the crystallites.

We have used KFGM to extract the dependence of the resistances and mobility on V_G for the different regions within the single TIPS pentacene crystallite, providing quantitative values for individual regions as small as 5×5 μm. We show that the performance of the crystallite is limited by a region of much lower mobility within the crystallite, suggesting that if the crystal growth could be more carefully controlled, we might greatly increase the mobility of our zone-cast devices, by at least a factor of two. No such similar measurements are to be found in the literature for such linear crystallites

However, in this chapter we have only scratched the surface in terms of data acquisition. Time permitting, the range of applied V_G and V_D could be covered in as much detail as desired. Chapter 3 on pBTTT demonstrated the effectiveness of KFGM in the saturation regime so those measurements would be a logical next step. After that, the range of potential experiments is vast, from investigating the effects of deposition parameters (speed, temperature) and composition of the OSC solution (solvent, cosolvent, polymer binder) to varying the contact metals, dielectric material and device geometry.

The need to make single crystallite measurements in the case of zone-cast TIPS pentacene is clear and it is the AFM that allowed for the creation of such a device using nano-lithography, once again proving the versatility of the instrument. Initial measurements using the cAFM and SGM techniques also hint at a significant increase in the versatility of the AFM in investigation of OTFTs.

We have identified significant variations in the behaviour of the OSC within the crystallite itself along the channel, demonstrating that more traditional and simpler four-point measurements or transfer scans are insufficient to infer material behaviour. In this regard, we have shown KFGM to be a proven technique for establishing the local performance of the OSC in these devices. However, more time than was available would be required to fully understand the behaviour we observed. Measurements on more single crystallite devices and further efforts to correlate electrical behaviour, surface potential and even SGM signal are needed to fully interpret the behaviour of zone-cast TIPS pentacene TFTs.

Chapter 5

Conclusions and the Future

There is no doubt that many questions remain unanswered regarding the operation of OTFTs made with both polymer and small molecule OSCs, so the broad purpose of this project was to increase our understanding of their operation. We were chiefly concerned with trying to understand the operation of OTFTs within the channel itself as an alternative to the results obtained with the more commonplace electrical characterisation. We have successfuly shown that purely electrical techniques will tend to produce oversimplified results and that only by using KFGM can we truly reveal how an OTFT is operating. In polymer TFTs made from C_{16} pBTTT, we have shown that, due to contact resistance, the mobility of the channel is ten times that of the device in the linear regime. By fitting to the local potential we have found that the mobility in the saturation regime is not contact limited, but is a factor of four less than the linear mobility, a result not reported elsewhere but made compelling by the internal consistency of the data.

The KFGM images have also shown us many details that we would never have seen otherwise. In the saturation regime we have placed an upper bound on channel length modulation if this is occurring. We have also shown that the source contact resistance in particular extends into the channel by up to 800nm suggesting that the OSC near the electrodes behaves differently to that within the channel, probably due to a disruption in the morphology caused by the gold electrode.

We have also used KFGM to greatly increase our knowledge of zone-cast TIPS pentacene TFTs, even if we have created as many new questions as we have answered. KFGM, along with conducting AFM was used to determine which parts of the TIPS pentacene/binder film were conductive and which were not, distinguishing between the OSC itself and the insulating binder. By applying this knowledge to whole devices we were able to use polarised optical microscope images to make more accurate estimates of W, and thus produce mobility values closer to that of the TIPS pentacene crystallites themselves. KFGM imaging of a complete TFT showed that the measured electrical characteristics were caused by averaging many crystallites with wildly differing electrical behaviours, as determined from their potential profiles. We also showed some intriguing preliminary results of scanned gate microscopy that hint at another way of determining which crystallites contribute most to the device performance.

Finally, by realising the full utility of the AFM, we have produced and characterised a single crystal TIPS pentacene OTFT, finding its mobility to be as high as 1.1 $cm^2V^{-1}s^{-1}$ in the linear regime, with localised areas showing a mobility as high as 2.5 $cm^2V^{-1}s^{-1}$, pushing the value much closer to that of its unsubstituted counterpart. The crystallites, themselves far from uniform in electrical behaviour, were found to contain areas of different mobility. Further scanned gate microscopy also showed that the regions of highest resistivity are also those that responded most strongly to the local gating effects of the tip.

The reults summarised here are a valuable contribution to our knowledge of the operation of OTFTs, even if we cannot fully explain everything we have observed. We have shown that by utilising the uniformity of amorphous and semicrystalline materials, one can easily extrapolate from $2D$ KFGM line profiles to whole-device models. The technique could easily be applied to any of the other polymer OSCs currently available or under development, with the major advantage that individual or anomalous devices can be imaged and compared to one another relatively quickly. In the case of crystalline small molecule materials, individual crystals can be rapidly compared to one another and, if necessary, isolated for individual characterisation. SGM also offers the possibility of determining where the key bottlenecks are in the OSC film.

In this project we have barely scratched the surface of what could be achieved using KFGM. In polymer devices, the effects of different surface treatments, SAMs and contact materials on the potential profiles could greatly add to our understanding of charge injection and film formation. By examining a wider range of materials we could determine if the phenomenon we observed – whereby the linear mobility is higher than saturation after accounting for the contacts – is present in other materials, and build up some understanding of how this relates to the structure and morphology of the material. Also of interest would be an examination of shorter channel length devices, of particular relevance to display manufactureres.

Insofar as small molecule OSCs are concerned, simply characterising more zone-cast TIPS pentacene single crystals would allow us to analyse the full range of behaviours they exhibit and subsequently to develop models to apply to whole-devices. Where with the polymer we used KFGM to "zoom in" on the small details in a broadly uniform device, with the small molecule we may extrapolate back from an understanding of the single crystal to the macroscopic device. An obvious next step, for example, would be to use KFGM to image TIPS pentacene devices with varying deposition angles relative to the channel and perhaps to determine the mobility relative to the π-stacking direction. The technique could also be applied to other crystalline OSCs deposited using different techniques.

As has probably already been made clear, the over-riding conclusion to be taken from this project is an affirmation of the power and versatility of electrical characterisation using the AFM as the only way to truly decipher the goings on within the TFT channel. This is particularly exciting when viewed in the context of the rapid expansion of the field pace at which new OSCs and deposition techniques are being developed.

Appendix A

Stability of pBTTT Thin-film Transistors

Much time at the outset of this project was devoted to the stability of the C_{16} pBTTT TFTs, as described in Chapter 3, under exposure to ambient conditions (water, oxygen, light and ozone) and under bias-stress. This work was originally undertaken as a research project in itself, although the lack of reproducible results and the difficulties encountered in performing certain experiments relegate the bulk of the work to this appendix. Some of the stability studies, in relation exposure of the TFTs to ambient conditions during transport and imaging, remain in the main body of this thesis. The key results will be described below, if only to highlight some of the difficulties inherent in studying TFTs that are unstable in ambient conditions. It should be noted that more recently developed OSCs have been designed with ambient stability in mind, which eliminates the need for expensive manufacturing under dry nitrogen and places lower requirements on the barrier properties of any passivation or encapsulation materials with regards to oxygen and water.

A.1 Bias stress stability of pBTTT TFTs

Bias stress describes any change in the performance of a TFT caused by application of a bias to the device. So long as the gradual channel approximation hoolds true, and the vertical field across the dielectric is much larger than the lateral field within the channel, it is generally assumed that the gate bias is the main cause of bias stress effects in OTFTs. Bias stress effects in polymeric TFTs are typically divided into two types, which are generally ascribed two different trapping processes within the dielectric, the OSC or at the interface between the two. [5]

The first is a straightforward shift of the whole transfer curve in the direction of the applied gate bias, creating a threshold shift, ΔV_T but producing no degradation in μ_{DEV}, I_{OFF} or S. It is this form of stress that is observed in Figure A.1, with an applied bias of $V_G = -40\ V$ over 12 hours. If the transfer curves in this case were offset by ΔV_T they would lie on top of each other. This form of stress is ascribed to charge carriers trapped in states that do not affect charge-transport - ie.those within the dielectric, highly localised states at the interface or particularly deep states within the OSC - and simply results in a shielding of V_G, and increasing the bias required to turn the device on.

The second form of stress typically results in a reduction in S and in μ_{DEV} and is ascribed to the formation of new states near the top of the HOMO level. These shallow traps must be filled before fully mobile charges can be injected into the channel and they contribute only partially to I_D since their charges must be thermally excited into conducting states in order to become mobile.

The time-scales of bias stress effects also change their effect on TFT performance. If the bias stress occurs on short enough timescales to occur during standard device measurements (1 to 30 s) then hysteresis is often observed, as with our pBTTT devices in Chapter 3. This behaviour was common, with varying extent, to all the pBTTT devices produced during this project. It has been shown that applying a pulsed bias during measurements rather than sweeping from one value to the next can significantly reduce bias stress during measurement. [105] The recovery time for such fast stress effects also tends to be short. In the case of our pBTTT devices, hysteresis may be observed in sequential forward and reverse transfer scans with no accumulated stress effects over multiple measurements, showing that the recovery time is on the same order as the measurement time.

Long-lived stress effects tend to be confined to a ΔV_T in polymeric TFTs and may occur over a period of many days [106] and have a recovery time of hours to days. [5] In the paper mentioned above, Salleo and Street show that in F8T2 TFTs, the application of light significantly reduces the recovery time of stressed devices, with the speed of recovery increasing both for longer exposure and for increased light intensity. We have seen a similat effect in our pBTTT TFTs, as discussed below.

Figure A.1 compares the bias stress behaviour of two pBTTT TFTs with $L = 20\ \mu m$ and stressed with $V_G = -40\ V$ and $V_D = -40\ V$ for 12 hours under dry nitrogen ($< 1\ pm$ water, $< 1\ ppm\ O_2$). In the first experiment (top) the stress was performed in a dark box and in the second (bottom) the stress was performed under ambient yellow-light conditions. The device stressed in the dark cleart exhibits a significant ΔV_T over the stress period, whilst the device stressed in the light undergoes a small initial shift and remains relatively stable thereafter. It should be clarified that the single outlying result for the device stressed in the light occurs midway through the measurement and may be a measurement artefact.

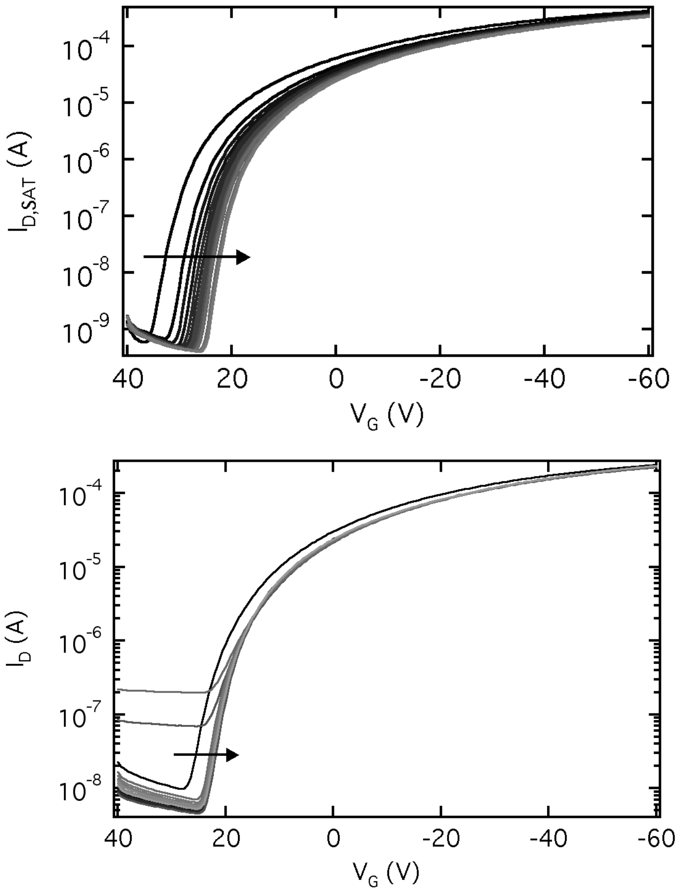

FIGURE A.1: Bias stress measurements comparing pBTTT TFTs with $L = 20\ \mu m$ stressed in a dark box (top) and under clean-room yellow-light conditions (bottom), both in a dry nitrogen atmosphere. In this case the device was stressed with $V_G = -40\ V$ and $V_D = -40\ V$ for 12 hours and measured every hour. The V_T shift over the course of the measurement is indicated with the arrows. In general, the shape of the transfer curve remains the same with the device stressed in the dark exhibiting a much greater V_T shift than the device exposed to light. of $-10\ V$ compared to $-3\ V$ for the device exposed to light.

This general behaviour is what we would expect if light exposure causes the detrapping of charges in long-lived trap states. The application of the light during stress may detrap charges at the same rate as they are trapped. However, one unusual feature of this experiment is highlighted in Figure A.2, which compares the absolute values of V_T throughout the experiment. The initial values of V_T in light and dark differ by around $8\ V$ but as the device in the dark is stressed, its V_T approaches that of the stable device. Measured under the same light conditions prior to stress, these devices showed similar values of V_T. Exposure to ambient light pushes V_T closer to zero, perhaps suggesting that the dielectric contains long-lived immobile charges that are freed by exposure to light.

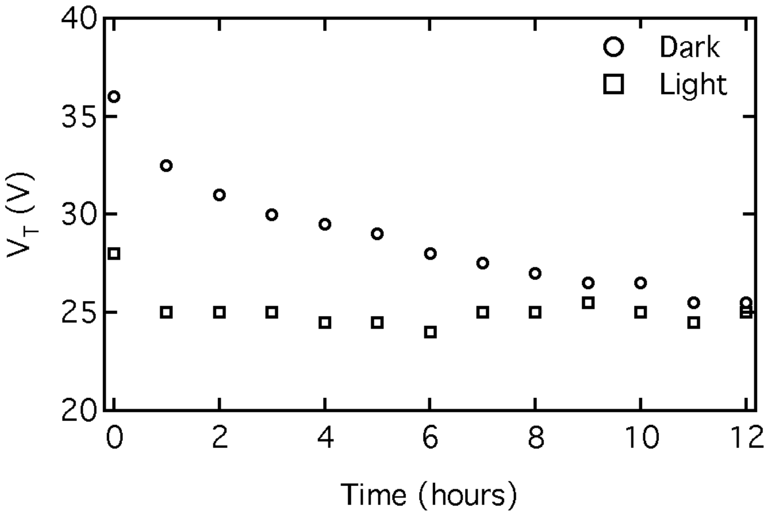

FIGURE A.2: V_T shift over time for the pBTTT devices measured in dark (circles) and light (squares). The device measured in light is much more stable over the 12 hour stress period, with a V_T shift of -3 V compared to -10.5 V the device measured in the dark. Interestingly, the V_T of both devices is very similar at the end of the stress period.

A.2 Environmental stability of pBTTT TFTs

The stability of polymer TFTs under exposure to typical ambient conditions (oxygen, water) is of great interest as more stable materials reduce the need for encapsulation or processing in dry or oxygen-free onditions. The effects of exposure to ambient conditions can be broken down into two categories: degradation of the film structure resulting in breaking of conjugation and doping of the OSC with oxygen or water. [5]

It has been suggested that OSCs may be particularly susceptible to singlet states of oxygen, which can be created by photo-excitation. In the case of polythiophene, $^1O_2$ may result in conjugation-breaking by formation of sulfine or diketone groups by way of an intermedaite transient endoperoxide. [107] Breaking the conjugation reduces the number of states that may contribute to conduction, reducing the mobility of the film. Also, as described in Chapter 1, reducing the conjugation length of the molecules increases the HOMO-LUMO gap.

Oxygen has long been known to act as a dopant in OSCs, and its interaction with polyacetylene and polythiophene has been studied. [108] The formation of states within the band-gap of the OSC causes a reduction in S and a genearl “smoothing” of the transfer curve. This may also lead to a bulk current within the OSC film, potentially increasing I_{OFF}, although this may have little effect on I_{ON}.

Salleo and Chabinyc[5] report very high stability in I_{ON} and I_{OFF} for P3HT and PQT-12 TFTs stored in dry air over a period of three months, whilst others have observed a wide range of variation in the behaviour of OTFTs exposed to ambient conditions, perhaps due to variations between the ambient conditions in different laboratories.

Water has also been shown to reduce the μ_{DEV} in poly(thiophene) TFTs. In this case, Chabinyc et al. show that increased humidity leads to a reduction in the mobility of the OSC, linking this the the rate of bipolaron formation caused by uptake of water in to the OSC film.[109] Qiu et al. link the presence of water in the film to the long-term degradation of pentacene TFTs over hundreds of hours [110] and suggest that water-related traps at grain boundaries cause a mobility reduction, whilst the adsorbed water increases the off-state conductivity of the film.

Our first results on pBTTT TFTs with $L = 20\ \mu m$ stored in the dark under ambient laboratory conditions are shown in Figure A.3. Devices from two identically processed substrates were measured automatically every day, using an automated probe stage, and compared to a reference device stored under dry nitrogen. The I_{ON} and I_{OFF} values are shown and the trend is clear. The device stored under nitrogen (black line) shows a reduction in I_{ON} of $\sim 25\%$ over the twelve days compared to reductions of anything between three and six orders of magnitude for the test devices (substrate 1: red lines, substrate 2: blue lines). The form of the degradation varies significantly from substrate to substrate and from device to device. Three of the devices on substrate 1follow a very similar trend in I_{ON}, whilst the other devices vary wildly.

The trend in I_{OFF} is also downwards, suggesting that the irreversible degradation by oxidative conjugation-breaking is responsible, reducing the overal conductivity of the film, although in this case there was little light available to excite the oxygen to ${}^1O_2$. It is possible that trace amounts of much more reactive ozone may be the cause of this degradation. There is less device-to-device variation in I_{OFF} with devices on the same substrate showing similar trends. The agreement between the location of the peaks is suggestive of an environmental cause in this case at least.

In order to examine correlations between the degradation of the pBTTT devices and the ambient conditions, the temperature and relative humidity (RH) in the laboratory were recoreded automatically during the experiment. It should be noted that the experiment was performed during a period when the laboratory was closed, in order to minimise the effects of people entering and leaving the lab and to eliminate the

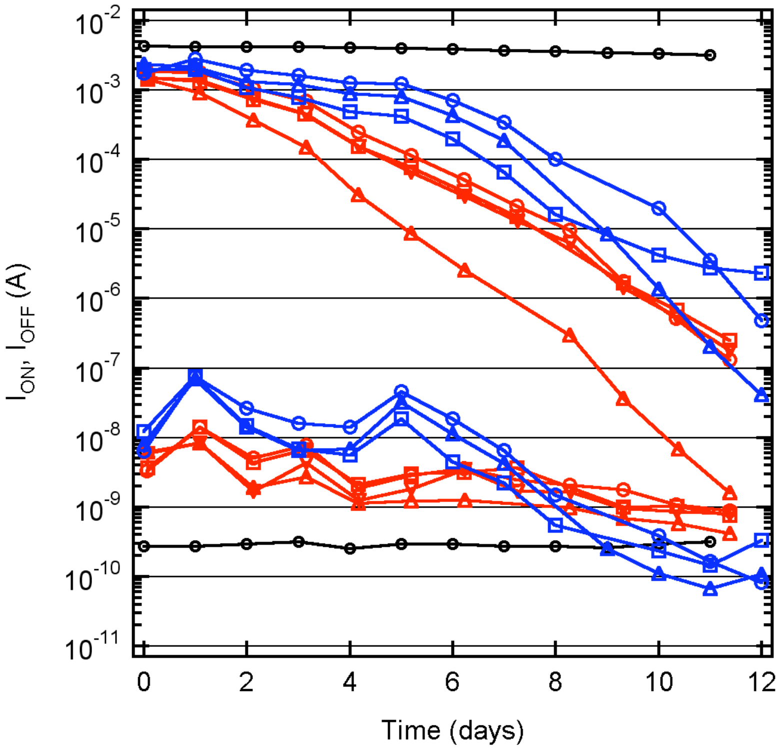

FIGURE A.3: I_{ON} and I_{OFF} measurements of a set of pBTTT device with $L = 20\ \mu m$ taken every day for 12 days in the dark. The control device (black line) measured under dry nitrogen remains comparatively stable over the course of the experiment, showing a 25% reduction in I_{ON}. In comparison, devices from substrate 1 (red lines) and substrate 2 (blue lines) measured under ambient laboratory conditions all show very large drops in I_{ON} of between three and six orders of magnitude. Both substrates also show a drop in I_{OFF} over the 12 days, although to different degrees and with differences in the pattern. This data illustrates both the substrate-to-substrate variation and the device-to-device variation within substrates that was commonly observed.

possiblity of contamination from other experiments. The recorded values are shown in Figure A.4. Aside from some small fluctuations over the first two days, the temperature remains at a constant 19 $°C$ for the duration of the experiment, whilst RH shows a gradually increasing trend from 30% to 40% over the experiment with some spikes as high as 58% seen in the latter half of the period. The rate of degradation of I_{ON} for substrate 2 does appear to increase as RH increases, however this is not really seen for device 1. In general, there is nothing in this data that can be directly correlated to changes in temperature or RH.

As seen in Figure A.3 long term TFT stability measurements, as the name implies, take a long time to perform. In order to speed this up, it was decided to perform stability measurements at higher temperature. Devices were kept on a Linkam hot stage under ambient conditions at a fixed temperature and measured periodically. The equipment was not available to perform these measurements so the data points are a

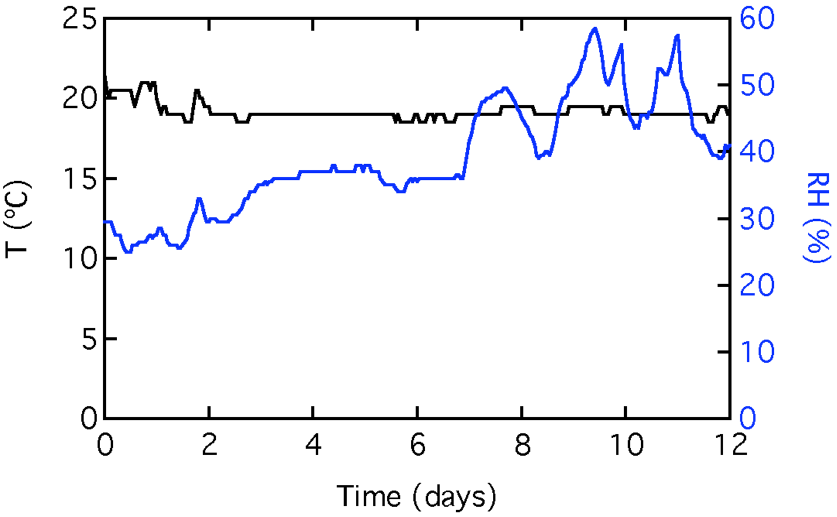

FIGURE A.4: Temperature and relative humidity (RH) data for the ambient laboratory conditions to which the devices in Figure A.3 were exposed during the experiment. The temperature is quite stable, deviating little from its mean value of 19.2 °C over the whole experiment. RH, on the other hand, exhibits a steady increase from an initial value of 30% to 41% at the end, with fluctuations as high as 58% seen in the period from days 7 to 11. There doesn't appear to be a strong correlation between humidity and device degradation in this case.

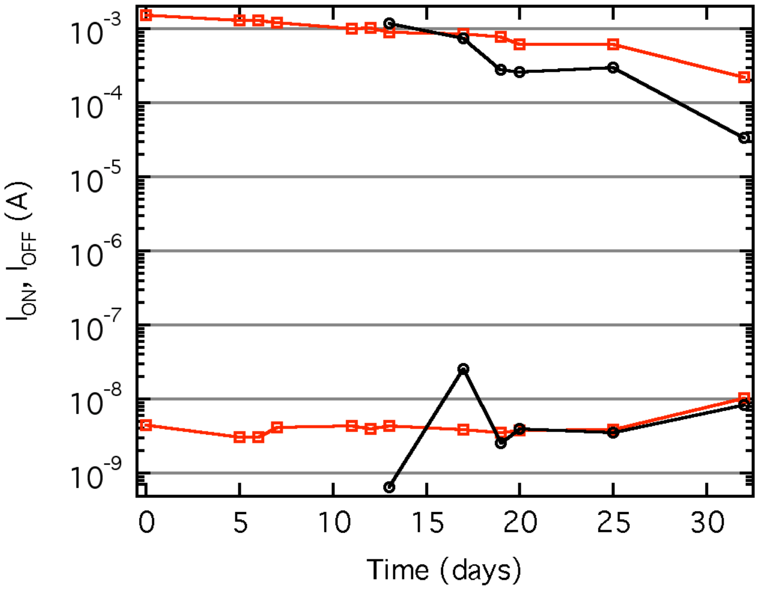

FIGURE A.5: I_{ON} and I_{OFF} measurements of a pBTTT device with $L = 20\ \mu m$ taken over a 32 day period at an elevated temperature of 60 °C and under ambient laboratory conditions (red squares). The rate of degradation is much slower than that observed in Figure A.3, with I_{ON} dropping by 1 order of magnitude over the entire duration. Due to the unexpectedly slow rate of degradation, on day 13 a second experiment was begun at room temperature (black squares). This device showed a reduction in I_{ON} by a factor of 36 over the remaining 20 day period. Comparing the data side-by-side, we might speculate that there are similarities in the trends suggesting a link to changes in the laboratory atmosphere.

little more sporadic, but this does not impact significantly on the outcome. Figure A.5 shows the degradation in I_{ON} and I_{OFF} for a pBTTT TFT with $L = 20\ \mu m$ over a 32 day period (red squares). Over the first 13 days of the experiment there was a reduction of only 40% in I_{ON}, much less than observed at room temperature in Figure A.3. I_{OFF} showed no significant reduction over this period. As a result, it was decided to begin monitoring a control sample under the same conditions but at room temperature (black circles). Unexpectedly, the device kept at room temperature shows a much stronger degradation, with a reduction in I_{ON} of 96% over the remaining period, during which the device held at 60 $°C$ showed a reduction of 70%.

The results of this experiment run counter to our expectations. It is generally assumed that the reaction rate for any chemical process increases with temperature, with the rule of thumb being a doubling of rate for every 10 $°C$. We had therefore assumed that increasing the temperature by $\sim 40\ °C$ would result in a significant increase in degradation rate where in fact we observed enhanced stability at higher temperatures. We do, however, observe enough similarity between the shape of the degradation in both I_{ON} and I_{OFF} to imply that some aspect of the laboratory environment is responsible for the degradation.

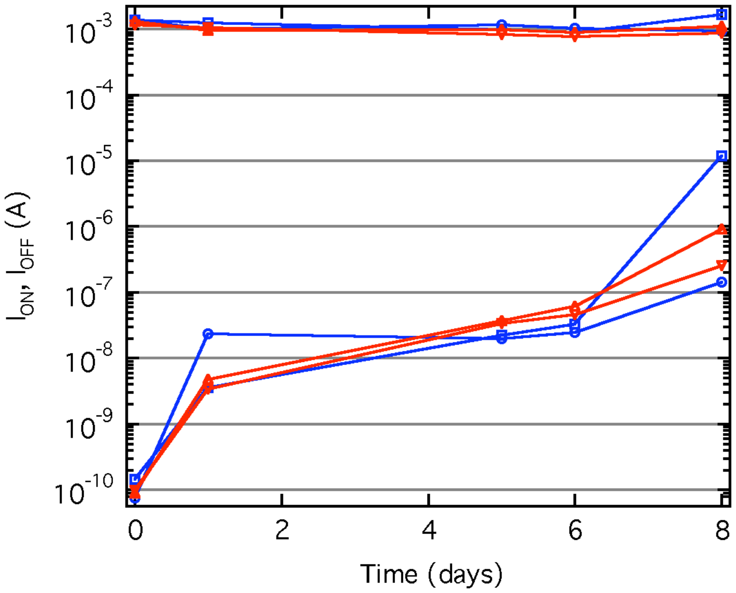

FIGURE A.6: I_{ON} and I_{OFF} over time for four pBTTT devices with $L = 20\ \mu m$ measured at room temperature under ambient laboratory conditions for eight days. Measurements were taken of two devices each on two substrates (red and blue lines). The device degradation takes a much different form in this case, with I_{ON} remaining stable over the whole period. Instead, we see an increase in I_{OFF} of between 3 and 5 orders of magnitude. Whilst this form of degradation has no significant effect on device mobility, the increase in I_{OFF} and reduction in on/off ratio makes the devices too unstable for use in any driving applications.

The results of a later repeat of the stability experiment shown in Figure A.3 are shown in Figure A.6. In this case two pBTTT TFTs, with $L = 20\ \mu m$, each from two substrates were measured over an 8 day period at room temperature and in the dark. In this case, I_{ON} remains stable or increases slightly over the observation period, whilst I_{OFF} shows a marked increase of between 3 and 5 orders of magnitude. This is much more in agreement with the expected behaviour in the presence of doping by oxygen. The increased I_{OFF} implies an increased bulk conductivity, which is masked in the on region as the on/off ratio remains above 100. This result is in stark contrast to our previous experiments and there were no significant changes in ambient temperature and RH in the laboratory that might explain the difference. The only major difference is that the first test was performed in December and that this one was carried out in June. It was suggested that since there was no change in temperature or RH in the laboratory between the two experiment, some long term flucuation in ozone levels might be responsible, although the expected differences would be on the parts-per-trillion (*ppt*) level. The proximity of the laboratory to a major motorway was suggested as a possible source of ozone, with changing atmospheric conditions outside the building responsible for modulating the concentration with the changing seasons. Unfortunately, there are no concurrent measurements of ozone levels to confirm or contradict this hypothesis.

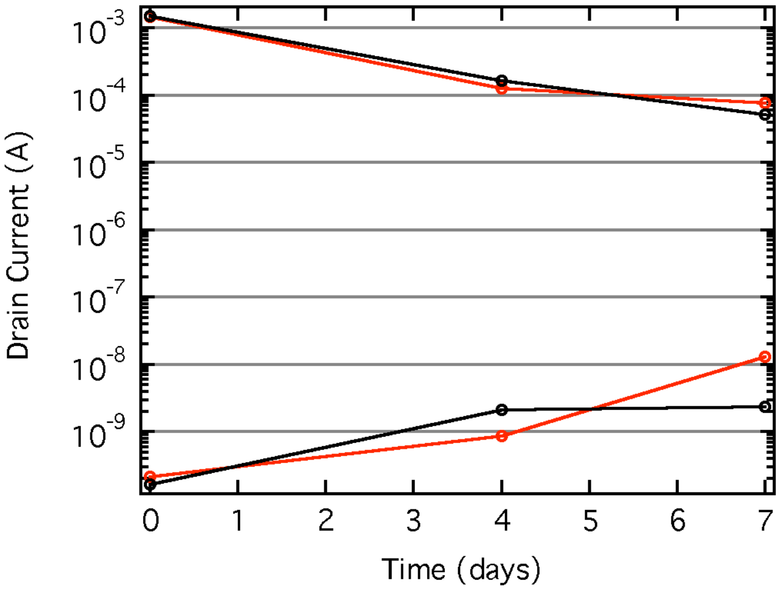

FIGURE A.7: I_{ON} and I_{OFF} over time for a pBTTT device measured under ambient laboratory conditions at 40 $^{\circ}C$ (red circles) compared to a control device at room temperature (black circles). In this experiment the behaviour of the two devices is quite similar. I_{ON} degrades by a factor of 19 for the test device compared to a factor of 29 for the control device. I_{OFF} increases by a factor of 61 for the test device and 14 for the control device.

The final stability measurement, presented here for completeness, is shown in Figure A.7. In this case, a device held at 40 °C was compared to a control device kept at room temperature, in the dark and under ambien laboratory conditions. In this case, both devices show a decrease in I_{ON} and an increase in I_{OFF} over a 7 day period. The trend is similar, although the heated device shows a significantly larger increase in I_{OFF}. However, the rate of the degradation is greater than that observed for the device held at 60 °C in Figure A.5.

In performing multiple stability experiments, we have observed multiple degradation behaviours and seen that the degradation rate does not increase with temperature as we might reasonably expect. Salleo and Chabinyc point out that the degradation of P3HT TFTs varies significantly between different laboratories [5], so we can at least confirm that there is some component of the ambient environment, even in the same laboratory, that may result in wildly different degradation rates and even mechanisms. In our experiments, we have ruled out ambient water and oxygen as the likely causes of the degradation, leading to speculation that ozone may be the culprit.

In order to investigate the effects of ozone on device performance, attempts were made to produce a glove-box system in which the ozone levels could be controlled. We found that this was relatively easy to do, either through a PID controlled system or by pulsed ozone production combined with a controlled air flow through the box. However, it proved impossible to control the ozone at the low levels required (typically tens of *ppt*). Some control was found to be possible in the range of 200 to 500 *ppt* but at these levels the devices were seen to degrade within hours. This it to be expected as ozone is routinely used to remove organic materials from substrates.

A.3 Conclusions on the ambient stability of pBTTT TFTs

As a result of the preceding study, we are able to suggest a hypothesis for the degradation observed in our pBTTT TFTs under ambient laboratory conditions, although we have been unable to test it. It is for this reason that this work is included as an appendix rather than a complete chapter. We have observed what appear to be multiple different forms of device degradation in pBTTT TFTs and shown no strong correlation to ambient RH or temperature. The effect of heating the devices was the opposite of that which we expected, a result that remains unexplained.

The main conclusion from the work carried out in this appendix is that the stability of polymer TFTs under ambient conditions is a difficult area to study, which perhaps explains the small number of studies performed in this area. It should be noted that the improvements are being made in the stability of polymer OSCs by synthesis without the use of exhaustive stability measurements. It has been shown that materials with increased ionisation potential have a better ambient stability, although often at the cost of a reduced mobility. In one case, this has been achieved with the addition of a thieno[2,3-*b*]thiophene unit (not to be confused with the thieno[3,2-*b*]thiophene in our pBTTT) into the polymer backbone.[111] It seems, then, that the problem of stability in polymer OSCs will be solved by synthetic means, with only a general understanding of the degradation processes involved.

Bibliography

[1] H Minemawari, T Yamada, H Matsui, J Tsutsumi, S Haas, R Chiba, R Kumai, and T Hasegawa. Inkjet printing of single-crystal films. *Nature*, 475(7365): 364–367, Jul 2011. doi: 10.1038/nature10313.

[2] A L Briseno, S C B Mannsfeld, M M Ling, S Liu, R J Tseng, C Reese, M E Roberts, Y Yang, F Wudl, and Z Bao. Patterning organic single-crystal transistor arrays. *Nature*, 444:913–917, Dec 2006. doi: 10.1038/nature05427.

[3] H Sirringhaus. Device physics of solution-processed organic field-effect transistors. *Adv Mater*, 17(20):2411–2425, Jan 2005. doi: 10.1002/adma.200501152.

[4] A C Arias, J D MacKenzie, I McCulloch, J Rivnay, and A Salleo. Materials and applications for large area electronics: Solution-based approaches. *Cheimical Reviews*, 110(1):3–24, 2010. doi: 10.1021/cr900150b.

[5] H Klauk. Organic electronics. *Wiley-VCH, Weinheim*, 2006.

[6] G Malloci, G Mulas, G Cappellini, and C Joblin. Time-dependent density functional study of the electronic spectra of oligoacenes in the charge states -1, 0, and +2. *Chemical Physics*, 340(1-3):43–58, Nov 2007. doi: 10.1016/j.chemphys.2007.07.046.

[7] P V Necliudov, M S Shur, D J Gundlach, and T N Jackson. Contact resistance extraction in pentacene thin film transistors. *Solid State Electron*, 47(2):259–262, Jan 2003. doi: 10.1016/S0038-1101(02)00204-6.

[8] N Koch, A Khan, J Ghijsen, J Pireaux, J Schwartz, R L Johnson, and A Elschner. Conjugated organic molecules on metal versus polymer electrodes: Demonstration of a key energy level alignment mechanism. *Appl Phys Lett*, 82 (1):70–72, 2003. doi: 10.1063/1.1532102.

[9] C Tanase, E J Meijer, P W M Blom, and D M de Leeuw. Local charge carrier mobility in disordered organic field-effect transistors. *Org Electron*, 4:33–37, 2003. doi: 10.1016/S1566-1199(03)00006-5.

[10] S M Sze. Semiconductor devices: Physics and technology. *John Wiley & Sons; 2nd edition*, 2001.

[11] G Horowitz, R Hajlaoui, H Bouchriha, R Bourguiga, and M E Hajlaoui. The concept of ”threshold voltage” in organic field-effect transistors. *Adv Mater*, 10 (12):923–+, Jan 1998. doi: 10.1002/(SICI)1521-4095(199808).

[12] K P Pernstich, S Haas, D Oberhoff, C Goldmann, D J Gundlach, B Batlogg, A N Rashid, and G Schitter. Threshold voltage shift in organic field effect transistors by dipole monolayers on the gate insulator. *J Appl Phys*, 96(11): 6431–6438, Jan 2004. doi: 10.1063/1.1810205.

[13] M Shtein, J Mapel, J B Benzige, and S R Forrest. Effects of film morphology and gate dielectric surface preparation on the electrical characteristics of organic-vapor-phase-deposited pentacene thin-film transistors. *Appl Phys Lett*, 81(2):268–270, 2002. doi: 10.1063/1.1491009.

[14] A F Stassen, R W I de Boer, N N Iosad, and A F Morpurgo. Influence of the gate dielectric on the mobility of rubrene single-crystal field-effect transistors. *Appl Phys Lett*, 85(17):3899–3901, 2004. doi: 10.1063/1.1812368.

[15] S K Park, J E Anthony, and T N Jackson. Solution-processed tips-pentacene organic thin-film-transistor circuits. *Ieee Electr Device L*, 28(10):877–879, Jan 2007. doi: 10.1109/LED.2007.905374.

[16] D Braga and G Horowitz. High-performance organic field-effect transistors. *Adv Mater*, 21(14-15):1473–1486, Jan 2009. doi: 10.1002/adma.200802733.

[17] P Stallinga, H L Gomes, F Biscarini, M Murgia, and D M de Leeuw. Electronic transport in field-effect transistors of sexithiophene. *J Appl Phys*, 96(9): 5277–5283, Jan 2004. doi: 10.1063/1.1789279.

[18] B H Hamadani, D J Gundlach, I McCulloch, and M Heeney. Undoped polythiophene field-effect transistors with mobility of 1 cm(2) v-1 s(-1). *Appl Phys Lett*, 91(24):243512, Jan 2007. doi: 10.1063/1.2824845.

[19] L Wang, D Fine, D Basu, and A Dodabalapur. Electric-field-dependent charge transport in organic thin-film transistors. *J Appl Phys*, 101(5):054515, Jan 2007. doi: 10.1063/1.2496316.

[20] B H Hamadani and D Natelson. Gated nonlinear transport in organic polymer field effect transistors. *J Appl Phys*, 95(3):1227–1232, Jan 2004. doi: 10.1063/1.1635979.

[21] E J Meijer, G H Gelinck, E van Veenendaal, B H Huisman, D M de Leeuw, and T M Klapwijk. Scaling behavior and parasitic series resistance in disordered organic field-effect transistors. *Appl Phys Lett*, 82(25):4576–4578, Jan 2003. doi: 10.1063/1.1581389.

[22] R J Chesterfield, J C McKeen, C R Newman, C D Frisbie, P C Ewbank, K R Mann, and L L Miller. Variable temperature film and contact resistance measurements on operating n-channel organic thin film transistors. *J Appl Phys*, 95(11):6396–6405, Jan 2004. doi: 10.1063/1.1710729.

[23] P V Pesavento, R J Chesterfield, C R Newman, and C D Frisbie. Gated four-probe measurements on pentacene thin-film transistors: Contact resistance as a function of gate voltage and temperature. *J Appl Phys*, 96(12):7312–7324, Jan 2004. doi: 10.1063/1.1806533.

[24] I Yagi, K Tsukagoshi, and Y Aoyagi. Direct observation of contact and channel resistance in pentacene four-terminal thin-film transistor patterned by laser ablation method. *Appl Phys Lett*, 84(5):813–815, Jan 2004. doi: 10.1063/1.1645316.

[25] L Burgi, H Sirringhaus, and R H Friend. Noncontact potentiometry of polymer field-effect transistors. *Appl Phys Lett*, 80(16):2913–2915, Jan 2002. doi: 10.1063/1.1470702.

[26] K Puntambekar, P V Pesavento, and C D Frisbie. Surface potential profiling and contact resistance measurements on operating pentacene thin-film transistors by kelvin probe force microscopy. *Appl Phys Lett*, 83(26):5539–5541, Jan 2003. doi: 10.1063/1.1637443.

[27] V Palermo, M Palma, and P Samori. Electronic characterization of organic thin films by kelvin probe force microscopy. *Adv Mater*, 18(2):145–164, Jan 2006. doi: 10.1002/adma.200501394.

[28] P G Le Comber and W E Spear. Electronic transport in amorphous silicon films. *Phys Rev Lett*, 25(8):509–511, Aug 1970. doi: 10.1103/PhysRevLett.25.509.

[29] A Miller and E Abrahams. Impurity conduction at low concentrations. *Physical Review*, 120(3):745–755, 1960. doi: 10.1103/PhysRev.120.745.

[30] M C J M Vissenberg and M Matters. Theory of the field-effect mobility in amorphous organic transistors. *Phys Rev B*, 57(20):12964–12967, May 1998. doi: 10.1103/PhysRevB.57.12964. Hopping Transport Model.

[31] G Horowitz, M E Hajlaoui, and R Hajlaoui. Temperature and gate voltage dependence of hole mobility in polycrystalline oligothiophene thin film transistors. *J Appl Phys*, 87(9):4456–4463, Jan 2000. doi: 10.1063/1.373091.

[32] Z Bao and J Locklin. Organic thin-film transistors. *CRC Press, Boca Raton*, 2007.

[33] N Sato, H Inokuchi, and E A Silinsh. Reevaluation of the electronic polarization energies in organic molecular crystals. *Chemical Physics*, 115(2):269–277, 1987. doi: 10.1016/0301-0104(87)80041-1.

[34] A R Brown, C P Jarrett, D M de Leeuw, and M Matters. Field-effect transistors made from solution-processed organic semiconductors. *Synthetic Met*, 88(1): 37–55, 1997. doi: 10.1016/S0379-6779(97)80881-8.

[35] H Bässler. Charge transport in disordered organic photoconductors a monte carlo simulation study. *Physica Status Solidi B*, 175(1):15–56, 1993. doi: 10.1002/pssb.2221750102.

[36] A R Völkel, R A Street, and D Knipp. Carrier transport and density of state distributions in pentacene transistors. *Phys Rev B*, 66(19):195336, 2002. doi: 10.1103/PhysRevB.66.195336.

[37] G Horowitz, R Hajlaoui, and P Delannoy. Temperature dependence of the field-effect mobility of sexithiophene. determination of the density of traps. *Journal de Physique III*, 5(4):355–371, 1995. doi: 10.1051/jp3:1995132.

[38] J W Orton and M J Powell. The hall effect in polycrystalline and powdered semiconductors. *Reports on Progress in Physics*, 43(11):1263, 1980. doi: 10.1088/0034-4885/43/11/001.

[39] J Chen, C K Tee, M Shtein, J E Anthony, and D C Martin. Grain-boundary-limited charge transport in solution-processed 6,13 bis(tri-isopropylsilylethynyl) pentacene thin film transistors. *J Appl Phys*, 103 (11):114513, Jan 2008. doi: 10.1063/1.2936978.

[40] B H Hamadani and D Natelson. Nonlinear charge injection in organic field-effect transistors. *J Appl Phys*, 97(6):064508, Jan 2005. doi: 10.1063/1.1858874.

[41] L Burgi, T J Richards, R H Friend, and H Sirringhaus. Close look at charge carrier injection in polymer field-effect transistors. *J Appl Phys*, 94(9):6129–6137, Jan 2003. doi: 10.1063/1.1613369.

[42] J P Hong, A Park, S Lee, J Kang, N Shin, and D Y Yoon. Tuning of ag work functions by self-assembles monolayers of armoatic thiols for an efficient hole injection for solution processed triisopropylsilylethynyl pentacene organic thin film transistors. *Appl Phys Lett*, 92:143311, Apr 2008. doi: 10.1063/1.2907691.

[43] J Zaumseil, K W Baldwin, and J A Rogers. Contact resistance in organic transistors that use source and drain electrodes formed by soft contact lamination. *J Appl Phys*, 93(10):6117–6124, Jan 2003. doi: 10.1063/1.1568157.

[44] P V Pesavento, K Puntambekar, C D Frisbie, J C McKeen, and P P Ruden. Film and contact resistance in pentacene thin-film transistors: Dependence on film thickness, electrode geometry, and correlation with hole mobility. *J Appl Phys*, 99(9):094504, Jan 2006. doi: 10.1063/1.2197033.

[45] P West. Introduction to atomic force microscopy: Theory, practice, applications. *Pacific Nanotechnology*, 2008. URL http://www.afmuniversity.org/download.html.

[46] R Young, J Ward, and F Scire. The topagrafiner: An instrument for measuring surface microtopography. *Rev Sci Instrum*, 43(7):999–1011, Jul 1972. doi: 10.1063/1.1685846.

[47] G Binnig, H Rohrer, Ch Gerber, and E Weibel. Tunneling through a controllable vacuum gap. *Appl Phys Lett*, 40(2):178–180, 1982.

[48] G Binnig, H Rohrer, Ch Gerber, and E Weibel. Surface studies by scanning tunneling microscopy. *Phys Rev Lett*, 49:57–61, Jul 1982. doi: 10.1103/PhysRevLett.49.57.

[49] G Binnig, C F Quate, and Ch Gerber. Atomic force microscope. *Phys Rev Lett*, 56:930–933, Mar 1986. doi: 10.1103/PhysRevLett.56.930.

[50] Y Martin, C C Williams, and H K Wickramasinghe. Atomic force microscope-force mapping and profiling on a sub 100-å scale. *J Appl Phys*, 61 (10):4723–4729, 1987. doi: 10.1063/1.338807.

[51] E Meyer, H J Hug, and R Benewitz. Scanning probe microscopy: The lab on a tip. *Springer-Verlag, Berlin*, 2003.

[52] Y Martin and H K Wickramasinghe. Magnetic imaging by ”force microscopy” with 1000 å resolution. *Appl Phys Lett*, 50(20):1455–1457, May 1987. doi: 10.1063/1.97800.

[53] C Schönenberger, S F Alvarado, S E Lambert, and I L Sanders. Separation of magnetic and topographic effects in force microscopy. *J Appl Phys*, 67(12): 7278–7280, 1990. doi: 10.1063/1.344511.

[54] Y Martin, D W Abraham, and H K Wickramasinghe. High-resolution capacitance measurement and potentiometry by force microscopy. *Appl Phys Lett*, 52(13):1103–1105, 1988. doi: 10.1063/1.99224.

[55] M Nonnemacher, M P Oboyle, and H K Wickramasinghe. Kelvin probe force microscopy. *Appl Phys Lett*, 58(25):2921–2923, 1991. doi: 10.1063/1.105227.

[56] F J Giessibl. Advances in atomic force microscopy. *Reviews of Modern Physics*, 75(3):949–983, 2003. doi: 10.1103/RevModPhys.75.949.

[57] R García and R Pérez. Dynamic atomic force microscopy methods. *Surface Science Reports*, 47:197–301, 2002. doi: 10.1016/SO167-5729(02)00077-8.

[58] R García and A San Paulo. Amplitude curves and operating regimes in dynamic atomic force microscopy. *Ultramicroscopy*, 82:79–83, 2000. doi: 10.1016/S0304-3991(99)00132-1.

[59] T R Albrecht, P Grütter, D Horne, and D Rugar. Frequency modulation detection using high-q cantilevers for enhanced force microscopy sensitivity. *J Appl Phys*, 69(2):668, 1991. doi: 10.1063/1.347347.

[60] H Hölscher, U D Schwarz, and R Wiesendanger. Calculation of the frequency shift in dynamic force microscopy. *Appl Surf Sci*, 140(3-4):344–351, 1999. doi: 10.1016/S0169-4332(98)00552-2.

[61] C Loppacher, M Bammerlin, F Battiston, M Guggisberg, D Müller, H R Hidber, R Lüthi, E Meyer, and H J Güntherodt. Fast digital electronics for application in dynamic force microscopy using high-q cantilevers. *Applied Physics A*, 66: S215, 1998. doi: 10.1007/s003390051132.

[62] P Girard. Electrostatic force microscopy: principles and some applications to semiconductors. *Nanotechnology*, 12:485–490, Nov 2001. doi: 10.1088/0957-4484/12/4/321.

[63] Th Glatzel, S Sadewasser, and M C Lux-Steiner. Amplitude or frequency modulation-detection in kelvin probe force microscopy. *Appl Surf Sci*, 210:84–89, 2003. doi: 10.1016/S0169-4332(02)01484-8. Amplitude vs Frequency modulation in KFGM.

[64] C C Williams, J Slinkman, W P Hough, and H K Wickramasinghe. Lateral dopant profiling with 200 nm resolution by scanning capacitance microscopy. *Appl Phys Lett*, 55(16):1662–1664, 1989. doi: 10.1063/1.102312.

[65] J Colchero, A Gil, and A M Baro. Resolution enhancement and improved data interpretation in electrostatic force microscopy. *Phys Rev B*, 64(24):245403, Jan 2001. doi: 10.1103/PhysRevB.64.245403.

[66] J M R Weaver and D W Abraham. High resolution atomic force microscopy. *Journal of Vacuum Science and Technology B*, 9(3):1559–1561, 1991. doi: 10.1116/1.585423.

[67] S Bain, D C Smith, N R Wilson, and M Carrasco-Orozco. Kelvin force gradient microscopy of pbttt transistors in both the linear and saturation electrical regimes. *Appl Phys Lett*, 95(14), 2009. doi: 10.1063/1.3242001.

[68] D J Gundlach, Y Y Lin, T N Jackson, S F Nelson, and D G Schlom. Pentacene organic thin-film transistors - molecular ordering and mobility. *Ieee Electr Device L*, 18(3):87–89, Jan 1997. doi: 10.1109/55.556089.

[69] F Biscarini, R Zamboni, P Samori, P Ostoja, and C Taliani. Growth of conjugated oligomer thin films studied by atomic-force microscopy. *Phys Rev B*, 52(20):14868–14877, 1995. doi: 10.1103/PhysRevB.52.14868.

[70] G Horowitz and M E Hajlaoui. Grain size dependent mobility in polycrystalline organic field-effect transistors. *Synthetic Met*, 122(1):185–189, Jan 2001. doi: 10.1016/S0379-6779(00)01351-5.

[71] R J Kline, M D McGehee, E N Kadnikova, J S Liu, and J M J Frechet. Controlling the field-effect mobility of regioregular polythiophene by changing the molecular weight. *Adv Mater*, 15(18):1519–+, Jan 2003. doi: 10.1002/adma.200305275.

[72] A Bolognesi, M Berliocchi, M Manenti, A Di Carlo, P Lugli, K Lmimouni, and C Dufour. Effects of grain boundaries, field-dependent mobility, and interface trap states on the electrical characteristics of pentacene tft. *Ieee T Electron Dev*, 51(12):1997–2003, Jan 2004. doi: 10.1109/TED.2004.838333.

[73] D Knipp, P Kumar, A R Völkel, and R A Street. Influence of organic gate dielectrics on the performance of pentacene thin film transistors. *Synthetic Met*, 155(3):485–489, Jan 2005. doi: 10.1016/j.synthmet.2005.06.018.

[74] K C Dickey, J E Anthony, and Y Loo. Improving organic thin-film transistor performance through solvent-vapor annealing of solution-processable

triethylsilylethynyl anthradithiophene. *Adv Mater*, 18(13):1721–+, Jan 2006. doi: 10.1002/adma.200600188.

[75] F Dinelli, M Murgia, F Biscarini, and D M de Leeuw. Thermal annealing effects on morphology and electrical response in ultrathin film organic transistors. *Synthetic Met*, 146(3):373–376, Jan 2004. doi: 10.1016/j.synthmet.2004.08.016.

[76] N Zhao, G A Botton, S P Zhu, A Duft, B S Ong, Y L Wu, and P Liu. Microscopic studies on liquid crystal poly(3,3”’-dialkylquaterthiophene) semiconductor. *Macromolecules*, 37(22):8307–8312, Jan 2004. doi: 10.1021/ma048434s.

[77] K Seshadri and C D Frisbie. Potentiometry of an operating organic semiconductor field-effect transistor. *Appl Phys Lett*, 78(7):993–995, Jan 2001. doi: 10.1063/1.1345805.

[78] P Annibale, C Albonetti, P Stoliar, and F Biscarini. High-resolution mapping of the electrostatic potential in organic thin-film transistors by phase electrostatic force microscopy. *J Phys Chem A*, 111(49):12854–12858, Jan 2007. doi: 10.1021/jp709590p.

[79] L Burgi, R H Friend, and H Sirringhaus. Formation of the accumulation layer in polymer field-effect transistors. *Appl Phys Lett*, 82(9):1482–1484, Jan 2003. doi: 10.1063/1.1556564.

[80] L Burgi, T Richards, M Chiesa, R H Friend, and H Sirringhaus. A microscopic view of charge transport in polymer transistors. *Synthetic Met*, 146(3):297–309, Jan 2004. doi: 10.1016/j.synthmet.2004.08.009.

[81] J A Nichols, D J Gundlach, and T N Jackson. Potential imaging of pentacene organic thin-film transistors. *Appl Phys Lett*, 83(12):2366–2368, Jan 2003. doi: 10.1063/1.1611278.

[82] T Miyazaki, K Kobayashi, K Ishida, S Hotta, T Horiuchi, H Yamada, and K Matsushige. Nanoscale electrical properties of molecular films in the vicinity of platinum ultrathin film electrode. *Japanese Journal of Applied Physics*, 42: 4852–4855, 2003. doi: 10.1143/JJAP.42.4852.

[83] S G J Mathijssen, M Cölle, A J G Mank, M Kemerink, P A Bobbert, and D M de Leeuw. Scanning kelvin probe microscopy on organic field-effect transistors during gate bias stress. *Appl Phys Lett*, 90(19):192104, Jan 2007. doi: 10.1063/1.2737419.

[84] I McCulloch, M Heeney, C Bailey, K Genevicius, I Macdonald, M Shkunov, D Sparrowe, S Tierney, R Wagner, W Zhang, M L Chabinyc, R J Kline, M D McGehee, and M F Toney. Liquid-crystalline semiconducting polymers with high charge-carrier mobility. *Nat Mater*, 5(4):328–333, Jan 2006. doi: 10.1038/nmat1612.

[85] F Zhang, M Funahashi, and N Tamaoki. High-performance thin film transistors from semiconducting liquid crystalline phases by solution processes. *Appl Phys Lett*, 91(6):063515, Jan 2007. doi: 10.1063/1.2768307.

[86] A Salleo, M L Chabinyc, M S Yang, and R A Street. Polymer thin-film transistors with chemically modified dielectric interfaces. *Appl Phys Lett*, 81(23): 4383–4385, Jan 2002. doi: 10.1063/1.1527691.

[87] R J Kline, D M DeLongchamp, D A Fischer, E K Lin, L J Richter, M L Chabinyc, M F Toney, M Heeney, and I McCulloch. Critical role of side-chain attachment density on the order and device performance of polythiophenes. *Macromolecules*, 40(22):7960–7965, Jan 2007. doi: 10.1021/ma0709001.

[88] D M DeLongchamp, R J Kline, E K Lin, D A Fischer, L J Richter, L A Lucas, M Heeney, I McCulloch, and J E Northrup. High carrier mobility polythiophene thin films: Structure determination by experiment and theory. *Adv Mater*, 19(6): 833–+, Jan 2007. doi: 10.1002/adma.200602651.

[89] I McCulloch, M Heeney, M L Chabinyc, D M DeLongchamp, R J Kline, M Cölle, W Duffy, D Fischer, D J Gundlach, B H Hamadani, R Hamilton, L Richter, A Salleo, M Shkunov, D Sparrowe, S Tierney, and W Zhang. Semiconducting thienothiophene copolymers: Design, synthesis, morphology, and performance in thin-film organic transistors. *Adv Mater*, 21(10-11):1091–1109, Jan 2009. doi: 10.1002/adma.200801650.

[90] D J Gundlach, L Zhou, J A Nichols, T N Jackson, P V Necliudov, and M S Shur. An experimental study of contact effects in organic thin film transistors. *J Appl Phys*, 100(2):024509, Jan 2006. doi: 10.1063/1.2215132.

[91] B H Hamadani, C A Richter, D J Gundlach, R J Kline, I McCulloch, and M Heeney. Influence of source-drain electric field on mobility and charge transport in organic field-effect transistors. *J Appl Phys*, 102(4):044503, Jan 2007. doi: 10.1063/1.2769782.

[92] B H Hamadani and D Natelson. Temperature-dependent contact resistances in high-quality polymer field-effect transistors. *Appl Phys Lett*, 84(3):443–445, Jan 2004. doi: 10.1063/1.1639945.

[93] M D Austin and S Y Chou. Fabrication of 70 nm channel length polymer organic thin-film transistors using nanoimprint lithography. *Appl Phys Lett*, 81(23): 4431–4433, Jan 2002. doi: 10.1063/1.1526457.

[94] M L Chabinyc, J P Lu, R A Street, Y L Wu, P Liu, and B S Ong. Short channel effects in regioregular poly(thiophene) thin film transistors. *J Appl Phys*, 96(4): 2063–2070, Jan 2004. doi: 10.1063/1.1766411.

[95] C Reese and Z Bao. Detailed characterization of contact resistance, gate-bias-dependent field-effect mobility, and short-channel effects with microscale elastomeric single-crystal field-effect transistors. *Adv Funct Mater*, 19 (5):763–771, Jan 2009. doi: 10.1002/adfm.200801019.

[96] J N Haddock, X H Zhang, S J Zheng, Q Zhang, S R Marder, and B Kippelen. A comprehensive study of short channel effects in organic field-effect transistors. *Org Electron*, 7(1):45–54, Jan 2006. doi: 10.1016/j.orgel.2005.11.002.

[97] P Stallinga and H L Gomes. Modeling electrical characteristics of thin-film field-effect transistors i. trap-free materials. *Synthetic Met*, 156(21-24): 1305–1315, Jan 2006. doi: 10.1016/j.synthmet.2006.09.015.

[98] A Salleo and R A Street. Kinetics of bias stress and bipolaron formation in polythiophene. *Phys Rev B*, 70(23):235324, Jan 2004. doi: 10.1103/PhysRevB.70.235324.

[99] J E Anthony, J S Brooks, D L Eaton, and S R Parkin. Functionalized pentacene: Improved electronic properties from control of solid-state order. *J Am Chem Soc*, 123(38):9482–9483, Jan 2001.

[100] M M Payne, S R Parkin, J E Anthony, C C Kuo, and T N Jackson. Organic field-effect transistors from solution-deposited functionalized acenes with mobilitites as high as 1 cm2/vs. *J Am Chem Soc*, 127:4986–4987, Mar 2005. doi: 10.1021/ja042353u.

[101] A Tracz, J K Jeszka, M D Watson, W Pisula, K Müllen, and T Pakula. Hexa-peri-hexabenzocoronene on untreated glass by simple solution processing. *J Am Chem Soc*, 125(7):1682–1683, 2003. doi: 10.1021/ja028945z.

[102] P Miskiewicz, M Mas-Torrent, J Jung, S Kotarba, I Glowacki, E Gomar-Nadal, D B Amabilino, J Veciana, B Krause, D Carbone, C Rovira, and J Ulanski. Efficient high area ofets by solution based processing of a pi-electron rich donor. *Chem Mater*, 18(20):4724–4729, 2006. doi: 10.1021/cm060675m.

[103] W Pisula, A Menon, M Stepputat, I Lieberwirth, U Kolb, A Tracz, H Sirringhaus, T Pakula, and K Müllen. A zone-casting technique for device fabrication of field-effect transistors based on discotic hexa-peri-hexabenzocoronene. *Adv Mater*, 17(6):684–689, 2005. doi: 10.1002/adma.200401171.

[104] R L Headrick, S Wo, F Sansoz, and J E Anthony. Anisotropic mobility in large grain size solution processed organic semiconductor films. *Appl Phys Lett*, 92: 063302, 2008. doi: 10.1063/1.2839394.

[105] A Salleo and R A Street. Light-induced bias stress reversal in polyfluorene thin-film transistors. *J Appl Phys*, 94(1):471–479, Jan 2003. doi: 10.1063/1.1581352.

[106] R A Street, M L Chabinyc, F Endicott, and B S Ong. Extended time bias stress effects in polymer transistors. *J Appl Phys*, 100(11):114518, Jan 2006. doi: 10.1063/1.2398798.

[107] M S A Abdou and S Holdcroft. Solid-state photochemistry of pi-conjugated poly(3-alkylthiophenes). *Canadian Journal of Chemistry*, 73(11):1893–1901, 1995. doi: 10.1139/v95-234.

[108] T A Skotheim, R L Elsenbaumer, and J R Reynolds. Handbook of conducting polymers. *Marcel Dekker Inc., New York*, 1998.

[109] M L Chabinyc, F Endicott, B D Vogt, D M DeLongchamp, E K Lin, Y L Wu, P Liu, and B S Ong. Effects of humidity on unencapsulated poly(thiophene) thin-film transistors. *Appl Phys Lett*, 88(11):113514, Jan 2006. doi: 10.1063/1.2181206.

[110] Y Qui, Y Hu, G Dong, L Wang, J Xie, and Y Ma. H2o effect on the stability of organic thin-film field-effect transistors. *Appl Phys Lett*, 83(8):1644–1647, 2003. doi: 10.1063/1.1604193.

[111] M Heeney, C Bailey, K Genevicius, M Shkunov, D Sparrowe, S Tierney, and I McCulloch. Stable polythiophene semiconductors incorporating thieno[2,3-b]thiophene. *JACS Communications*, 127(4):1078–1079, 2005. doi: 10.1021/ja043112p.